N_2 Splitting and Functionalization in the Coordination Sphere of Tungsten

Dissertation
zur Erlangung des mathematisch-naturwissenschaftlichen Doktorgrades
"Doctor rerum naturalium"
der Georg-August-Universität Göttingen

im Promotionsprogramm der
Georg-August University School of Science (GAUSS)

vorgelegt von:
Bastian Schluschaß
aus Frankfurt am Main

Göttingen, 2020

Betreuungsausschuss

Prof. Dr. Sven Schneider
Institut für Anorganische Chemie, Georg-August-Universität Göttingen

Prof. Dr. Franc Meyer
Institut für Anorganische Chemie, Georg-August-Universität Göttingen

Mitglieder der Prüfungskommission

Referent	**Prof. Dr. Sven Schneider** Institut für Anorganische Chemie, Georg-August-Universität Göttingen
Korreferent	**Prof. Dr. Franc Meyer** Institut für Anorganische Chemie, Georg-August-Universität Göttingen

Weitere Mitglieder der Prüfungskommission

Prof. Dr. Manuel Alcarazo
Institut für Organische und Biomolekulare Chemie,
Georg-August-Universität Göttingen

Prof. Dr. Dirk Schwarzer
Max-Planck-Institut für Biophysikalische Chemie, Göttingen

Dr. Michael John
Institut für Organische und Biomolekulare Chemie,
Georg-August-Universität Göttingen

Dr. Christian Sindlinger
Institut für Anorganische Chemie,
Georg-August-Universität Göttingen

Tag der mündlichen Prüfung: 22.09.2020

Acknowledgements

First of all, I would like to express my appreciation to my supervisor **Prof. Dr. Sven Schneider** for providing me not only with this interesting and challenging topic, but also with scientific support, inspiring discussions, excellent laboratory conditions as well as the opportunity to present my work at several conferences.
Furthermore, I want to express my gratitude to **Prof. Dr. Franc Meyer** for taking the part of my second supervisor and being referee for my thesis.
Moreover, I wish to show my gratitude to the following people and institutions:

- **Prof. Dr. Manuel Alcarazo, Prof. Dr. Dirk Schwarzer, Dr. Michael John** and **Dr. Christian Sindlinger** for their work within my thesis committee
- **Prof. Dr. Kenneth Caulton** and **Dr. Nicholas Maciulis** for the friendly acceptance in their work-group within my internship at Indiana University
- **Dr. Christian Würtele** for measuring X-ray crystal structures even sometimes with little chance of success
- **Prof. Dr. Vera Krewald**, **Dr. Markus Finger** and **Severine Rupp** for performing all theoretical calculations
- **Prof. Dr. Dirk Schwarzer** and **Jan-Hendrik Borter** for running and analyzing the pump-probe spectroscopy experiments
- **Dr. Claudia Stückl** and **Prof. Dr. Joshua Telser** for measuring and simulating EPR spectra
- **Prof. Dr. Christian Limberg, Dr. Christian Herwig** and **Dr. Sebastian Dechert** for recording the Raman-spectra
- **Prof. Dr. Ivana Ivanovic-Burmazovic** and **Dr. Alicja Franke** for their help and support in analyzing and interpreting the UVvis kinetic studies
- **Dr. Michael John** and **Ralf Schöne** for their help and assistance with NMR spectroscopy
- **Dr. Serhiy Demeshko** for measuring and simulating SQUID magnetometry
- **Sebastian Kopp** for his ambitious support in maintaining our laboratory as well as synthesizing my ligand, which saved me a lot of time
- My bachelor- and internship students, **Patricia-Marie Padonou**, **Jessica Schneider**, **Katharina Wenderoth** and **Annemarie Kehl**, for their effort in supporting my research and the great time in the lab
- The **European Research Council** (ERC Grant Agreement 646747) for funding

My special thanks go to the whole **AK Schneider** for a fantastic and unforgettable time both inside and outside the lab. Additionally, I want to acknowledge my former office-collegues (and friends), **Richt Van Alten**, **Dr. Josh Abbenseth**, **Dr. Jan Gerkens**, **Sebastian Kopp** and **Dr. Florian Wätjen** for the inspiring discussions and cooperative atmosphere.

Last but not least, I want to thank my family for their support and patience within the last years.

Contents

1 Introduction **1**

1.1 Bonding of N_2 to transition metals . . . 3
  1.1.1 General aspects of N_2-binding . . . 3
  1.1.2 End-on bridging N_2 . . . 4
  1.1.3 Side-on bridging N_2 . . . 15
1.2 N_2-Functionalization . . . 19
  1.2.1 Ammonia Formation . . . 19
  1.2.2 Thermal N_2-cleavage into terminal nitrides . . . 27
  1.2.3 Photolytic N_2-cleavage . . . 34
1.3 Nitride-Functionalization . . . 42
  1.3.1 Bonding of terminal transition metal nitrides . . . 42
  1.3.2 Reactivity of N_2-derived nitrides . . . 46
  1.3.3 Generation of cyanate from N_2-derived nitrides . . . 52
1.4 Scope of this work . . . 57

2 Results and Discussion **59**

2.1 Synthesis and Characterization of N_2-bridged Ditungsten-PNP-Complexes 59
  2.1.1 Redox-series $[(N_2)\{WCl(PNP)\}_2]^{n+}$ (n = 0-2) . . . 59
  2.1.2 Synthesis and characterization of $[(N_2)\{W(CO)(PNP)\}_2]$ (**4**) . . . 66
2.2 Proton induced N_2-cleavage *versus* proton reduction . . . 72
2.3 N_2-cleavage of $[(N_2)\{W(CO)(PNP)\}_2]$ (**4**) . . . 83
  2.3.1 Thermal N_2-cleavage . . . 84
  2.3.2 Photolytic N_2-cleavage . . . 89
2.4 Functionalization of tungsten-nitrido-complexes . . . 96
  2.4.1 Alternative synthesis of [W(N)(CO)(PNP)] (**16**) *via* an azide route . . 96
  2.4.2 Functionalization of [W(N)(CO)(PNP)] (**16**) using π-acceptor ligands 100
  2.4.3 Mechanistic investigations on CN-bond coupling . . . 102
  2.4.4 Liberation of cyanate and closure of the synthetic cycle . . . 105
2.5 Summary and Outlook . . . 110

3 Experimental **115**

3.1 General Working Techniques . . . 115
3.2 Analytical Methods . . . 115
  3.2.1 Crystallographic details . . . 115
  3.2.2 Cyclic voltammetry . . . 116
  3.2.3 Electron Paramagnetic Resonance . . . 116
  3.2.4 Elemental Analysis . . . 116
  3.2.5 Head Space Analysis . . . 116
  3.2.6 Irradition . . . 117
  3.2.7 Magnetic measurements . . . 117
  3.2.8 Mass spectrometry . . . 117
  3.2.9 Nuclear magnetic resonance . . . 117

3.2.10 Quantum yield determination 118
3.2.11 Transient UVvis spectra 119
3.2.12 Transient IR spectra 119
3.2.13 UVvis spectroscopy 120
3.2.14 Vibrational spectroscopy 120
3.3 Synthesis 121
3.3.1 [WCl$_3$(PNP)] (**5**) 121
3.3.2 [(N$_2$){WCl(PNP)}$_2$] (**1**) 122
3.3.3 [(N$_2$){WCl(PNP)}$_2$]$^+$ (**2**) 123
3.3.4 [(N$_2$){WCl(PNP)}$_2$]$^{2+}$ (**3**) 124
3.3.5 [W(N)Cl(^{H}PNP)]$^+$ (**11**) 125
3.3.6 *in situ* [(^{H}PNP)ClW-(N$_2$)-WCl(PNP)]$^+$ (**12**) 125
3.3.7 *in situ* [{(^{H}PNP)ClW}(μ—N$_2$)]$^{2+}$ (**13**) 126
3.3.8 [(N$_2$){WCl(CO)(PNP)}$_2$] (**8**) 126
3.3.9 [(N$_2$){W(CO)(PNP)}$_2$] (**4**) 127
3.3.10 [W(N)(CO)(PNP)] (**16**) 128
3.3.11 [W(CO)$_3$(^{H}PNP)] (**9**) 129
3.3.12 [WI(CO)$_2$(PNP)] (**18**) 130
3.3.13 [WCl(CO)$_2$(PNP)] (**10**) 131
3.3.14 [W(N$_3$)(CO)$_2$(PNP)] (**19**) 132
3.3.15 [W(N)(CO)(^{H}PNP)]$^+$ (**20**) 133
3.3.16 [W(NCO)(CO)$_2$(PNP)] (**21**) 134
3.3.17 [W(NCO)(CN^{t}Bu)$_2$(PNP)] (**22**) 135
3.3.18 [W(NCO)(CN-C$_6$H$_4$-OMe)$_2$(PNP)] (**23**) 136
3.3.19 [WCl(CN^{t}Bu)$_2$(PNP)] (**6**) 137
3.3.20 Na[W(CO)$_2$(PNP)] (**24**) 138
3.4 Kinetic Analysis: Protonation of **1** with [HNEt$_3$][BAr$^F_{24}$] 139
3.4.1 Exemplary UVvis spectrum 139
3.4.2 Determination of equilibrium constant K_1 139
3.4.3 Determination of rate constants k_2 and k_3 140
3.4.4 Determination of rate constant k_3 via initial rate method 140
3.5 Kinetic Analysis: N$_2$-cleavage of [(N$_2$){W(CO)(PNP)}$_2$](**4**) 141
3.5.1 Reaction Monitoring 141
3.5.2 Kinetic Modelling 142
3.5.3 *Eyring* Analysis 143
3.5.4 *Van't Hoff* Analysis 143
3.6 Transient spectroscopy 144

4 List of compounds **147**

5 List of abbreviations **149**

6 Appendix **151**
6.1 Spectroscopic Results 151

6.1.1 [WCl_3(PNP)] (**5**) . . . 151
6.1.2 [(N_2){WCl(PNP)}$_2$](**1**) . . . 152
6.1.3 [(N_2){WCl(PNP)}$_2$]$^+$(**2**) . . . 155
6.1.4 [(N_2){WCl(PNP)}$_2$]$^{2+}$ (**3**) . . . 157
6.1.5 [W(N)Cl(^{H}PNP)]$^+$ (**11**) . . . 159
6.1.6 *in situ* [(^{H}PNP)ClW-(N_2)-WCl(PNP)]$^+$ (**12**) . . . 160
6.1.7 *in situ* [{(^{H}PNP)ClW}(μ—N_2)]$^{2+}$ (**13**) . . . 163
6.1.8 [(N_2){WCl(CO)(PNP)}$_2$](**8**) . . . 164
6.1.9 [(N_2){W(CO)(PNP)}$_2$](**4**) . . . 168
6.1.10 [W(N)(CO)(PNP)] (**16**) . . . 170
6.1.11 [W(N)(CO)(^{H}PNP)]$^+$ (**20**) . . . 173
6.1.12 [W$(CO)_3$(^{H}PNP)] (**9**) . . . 176
6.1.13 [WI$(CO)_2$(PNP)] (**18**) . . . 178
6.1.14 [WCl$(CO)_2$(PNP)] (**10**) . . . 180
6.1.15 Characterization of TMS—NCO . . . 182
6.1.16 [W(N_3)$(CO)_2$(PNP)] (**19**) . . . 183
6.1.17 [W(NCO)$(CO)_2$(PNP)] (**21**) . . . 185
6.1.18 [W(NCO)(CN^{t}Bu)$_2$(PNP)] (**22**) . . . 189
6.1.19 [W(NCO)(CN—C_6H_4—OMe)$_2$(PNP)] (**23**) . . . 191
6.1.20 [WCl(CN^{t}Bu)$_2$(PNP)] (**6**) . . . 193
6.1.21 Na[W$(CO)_2$(PNP)] (**24**) . . . 195
6.2 Crystal Structures . . . 198
6.2.1 [WCl_3(PNP)] (**5**) . . . 198
6.2.2 [(N_2){WCl(PNP)}$_2$] (**1**) . . . 199
6.2.3 [(N_2){WCl(PNP)}$_2$]$^+$ (**2**) . . . 200
6.2.4 [(N_2){WCl(PNP)}$_2$]$^{2+}$ (**3**) . . . 201
6.2.5 [W(N)Cl(^{H}PNP)]$^+$ (**11**) . . . 202
6.2.6 [(N_2){WCl(CO)(PNP)}$_2$] (**8**) . . . 203
6.2.7 [(N_2){W(CO)(PNP)}$_2$] (**4**) . . . 204
6.2.8 [WI$(CO)_2$(PNP)] (**18**) . . . 205
6.2.9 [W(N)(CO)(^{H}PNP)]$^+$ (**20**) . . . 206
6.2.10 [W(NCO)$(CO)_2$(PNP)] (**21**) . . . 207
6.2.11 [W(NCO)(CN^{t}Bu)$_2$(PNP)] (**22**) . . . 208
6.2.12 [W(NCO)(CN-C_6H_4-OMe)$_2$(PNP)] (**23**) . . . 209
6.2.13 [WCl(CN^{t}Bu)$_2$(PNP)] (**6**) . . . 210
6.2.14 Na[W$(CO)_2$(PNP)] (**24**) . . . 211

7 Curriculum Vitae **225**

List of Figures

1 Most frequently found coordination modes in N_2-complexes. 3
2 Orbital interactions between N_2 and a metal center in end-on bound N_2-complexes. 4
3 Structural and spectroscopic properties of the $[(N_2)\{Mo(N(R)Ar)_3\}_2]^{n+}$ (n = 0-2)-redox series (**I**, **II**, **III**) and the hetero-bimetallic Mo/Nb analogue (**IV**) by *Cummins*. 6
4 The PNP-pincer supported N_2-bridged Mo (**XI**) and Re (**XII**; **XIII**) dinuclear complexes reported by *Schneider*. 11
5 *Sita's* isostructural $[(N_2)(MCp^*am)_2]$ complexes 13
6 *left: Chirik*'s terpyridine supported Mo-N_2-dimer redox series **XVII**$^{n+}$ (n = 0-4). *right:* Qualitative FMO scheme of the redox series and the corresponding spin states and NN stretching frequencies. 14
7 Increased steric shielding of the supporting ligands results in linkage isomerization from side-on to end-on. 17
8 pK_a-dependence of the selectivity between N_2-reduction (NRR, blue) and H_2-evolution (HER, blue) of **XXVIa**. 23
9 Pincer-supported Mo-complexes by *Schrock* (**XXXIV**) and *Mezaillés* (**XXXV**) capable for N_2-cleavage under reductive conditions. 29
10 Pincer-supported, square-planar nitrido-complexes reported by *Caulton* (*left*), *Burger* (*middle*) and *Schneider* (*right*). 44
11 Molecular structure of **5** 59
12 Molecular structure of **1** 60
13 Comparison of the cyclic voltammograms of **1** (blue) and **XI** (red) 61
14 Molecular structure and EPR-spectrum of **2**. 62
15 Molecular structure and $\chi_M T$ vs. T-plot for **3**-$[Al(OC(CF_3)_3)_4]_2$ 63
16 Spin-density-plots for **2** (*left*) and **3** (*right*). 65
17 $^{31}P\{^1H\}$ NMR spectra of the reaction of **1** with CN-^{t}Bu. 66
18 Molecular structure and CV of **8** 69
19 Molecular structure and $\chi_M T$ vs. T-plot for **4** 70
20 *left*: qualitative MO-scheme for end-on N_2-bridged compound with idealized fourfold symmetry. *right:* Comparison of the structural and spectroscopic features of **4**, *Schneider's* ReCl-congener **XII** and *Cummins'* neutral **I**. 71
21 Molecular structure and EPR-spectrum of **11** 72
22 $^{31}P\{^1H\}$ (*left*) and $^{15}N\{^1H\}$ NMR spectra (*right*) of **12** in THF—d_8 at -35 °C. 75
23 Examplary UVvis spectrum of the protonation of **1** and K_1-determination 77
24 abs (607nm) *vs* time and $k_{obs(2)}$ *vs* c(H^+) plots 77
25 Plot of the concentration of **4** *vs.* time at different temperatures. 84
26 *Van't Hoff*- and *Eyring*-plots for the conversion of **4** into **16** 85
27 Computed structures of the two isomers found for **16**. 86
28 Experimental UVvis spectrum of **4** in THF. 89

29 *left:* Transient UVvis difference spectra of **4** in THF at selected pump-probe delays (pump wavelength: 475 nm). The black line shows the scaled linear absorption spectrum. *right:* Time-dependence of the integrated absolute absorption changes (red line is a bi-exponential fit with $\tau_1 = 1.5 \pm 0.2$ ps and $\tau_2 = 9.2 \pm 0.5$ ps). 90
30 Transient IR difference spectra of **4** in THF at selected pump-probe delays (pump wavelength: 400 nm). 91
31 Simplified energy surfaces for a diabatic photoreaction (*left*) and a reaction proceeding *via* a hot-ground state (*right*). 92
32 Comparison of the experimental (black) and TD-DFT computed (blue: $S = 0$; red: $S = 1$) electronic absorption spectra of **4**. The inset shows the potentially active transitions. 94
33 *left*: Difference density plots (loss in yellow,gain in red) for the transitions S15, S16, T13 and T14 calculated for **4**. *right*: Simplified MO-scheme for **4** with the electronic excitation assigned to productive in photolytic N_2-cleavage. 95
34 Molecular structures of **9** and **18** in the crystal obtained by single crystal X-ray diffraction. 97
35 Molecular structure of **20** in the crystal obtained by single crystal X-ray diffraction. 99
36 NMR signature of ^{15}N-**21** 101
37 Molecular structure of **21** in the crystal obtained by single crystal X-ray diffraction. 101
38 NMR signature of ^{13}CO-**21** 103
39 Molecular structures of **22** (*left*) and **23** (*right*) 104
40 Cyclic voltammogram of the reduction of **21**. 105
41 Molecular structure of **24** in the crystal obtained by single crystal X-ray diffraction. 106
42 Molecular structure of **10** in the crystal obtained by single crystal X-ray diffraction. 108
43 Quantum yield determination of the photosplitting of **4** by 427 nm LED lamp. 118
44 Exemplary UVvis spectrum of the protonation of **1** with [HNEt$_3$][BAr$^F_{24}$]. . 139
45 K_1-determination 139
46 Absorbance at 607 nm vs time plot. 140
47 c(**4**) *vs.* time plot at different temperatures. 141
48 ln(k_1/T) vs. 1/T plot (*Eyring-plot*) for the thermal splitting of **4** into **16**. . . 143
49 ln(K/T) vs. 1/T plot (*Van’t Hoff-plot*) for the thermal splitting of **4** into **16**. 143
50 *left:* Transient UVvis difference spectra of **4** in THF at selected pump-probe delays (pump wavelength: 530 nm). The black line shows the scaled linear absorption spectrum. *right:* Time-dependence of the integrated absolute absorption changes (red line is a bi-exponential fit with $\tau_1 = 1.8$ ps and $\tau_2 = 11.1$ ps). 144

51 *left:* Transient UVvis difference spectra of **4** in THF at selected pump-probe delays (pump wavelength: 475 nm). The black line shows the scaled linear absorption spectrum. *right:* Time-dependence of the integrated absolute absorption changes (red line is a bi-exponential fit with $\tau_1 = 1.5$ ps and $\tau_2 = 9.2$ ps). 144
52 *left:* Transient UVvis difference spectra of **4** in THF at selected pump-probe delays (pump wavelength: 380 nm). The black line shows the scaled linear absorption spectrum. *right:* Time-dependence of the integrated absolute absorption changes (red line is a bi-exponential fit with $\tau_1 = 1.1$ ps and $\tau_2 = 8.3$ ps). 145
53 *left:* Transient UVvis difference spectra of **4** in THF at selected pump-probe delays (pump wavelength: 330 nm). The black line shows the scaled linear absorption spectrum. *right:* Time-dependence of the integrated absolute absorption changes (red line is a bi-exponential fit with $\tau_1 = 1.3$ ps and $\tau_2 = 9.9$ ps). 145
54 Transient IR difference spectra of **4** in THF at selected pump-probe delays (pump wavelength: 400 nm). 146
55 ^{1}H NMR Spectrum of **5** in C_6D_6 at r.t. 151
56 ^{1}H NMR Spectrum of **1** in THF—d_8 at r.t. 152
57 ^{13}C{^{1}H} NMR Spectrum of **1** in THF—d_8 at r.t. 152
58 ^{15}N{^{1}H} NMR Spectrum of ^{15}N-**1** in THF—d_8 at r.t. 153
59 ^{31}P{^{1}H} NMR Spectrum of **1** in THF—d_8 at r.t. 153
60 CV of **1** in 0.1 M solution of $[^n\text{Bu}_4\text{N}][\text{PF}_6]$ in THF (WE = GC, RE = Ag/Ag$^+$, CE = Pt) at different scan rates. 154
61 rRaman Spectrum (457 nm) of ^{14}N/^{15}N-**1** in frozen THF—d_8. 154
62 ^{1}H NMR Spectrum of **2**-[BPh$_4$] in THF—d_8 at r.t. 155
63 rRaman Spectrum (457 nm) of ^{14}N/^{15}N-**2**-[BPh$_4$] in frozen THF—d_8. 155
64 Comparison of the EPR-Spectra of ^{14}N/^{15}N-**2**, both in THF at r.t. 156
65 χ_MT vs. T plot for **2**-[BAr$^F_{24}$] 156
66 ^{1}H NMR Spectrum of **3**-$[\text{Al(OC(CF}_3)_3)_4]_2$ in THF—d_8 at r.t. 157
67 rRaman Spectrum (514.5 nm) of ^{14}N/^{15}N-**3**-$[\text{Al(OC(CF}_3)_3)_4]_2$ in THF—d_8 at -100 °C. 157
68 χ_MT vs. T plot for **2**-$[\text{Al(OC(CF}_3)_3)_4]_2$ 158
69 EPR-Spectrum of **11** in THF at r.t. 159
70 ATR-IR-Spectrum ^{14}N/^{15}N-**11**. 159
71 ^{31}P{^{1}H} NMR Spectrum of **12**-OTf in THF—d_8 at -35 °C. 160
72 ^{15}N{^{1}H} NMR Spectrum of ^{15}N-**12**-OTf in THF—d_8 at -35 °C. 160
73 ^{1}H COSY NMR Spectrum of **12**-OTf in THF—d_8 at -35 °C. 161
74 ^{1}H -^{15}N HSQC NMR Spectrum of **12**-OTf in THF—d_8 at -35 °C. 161
75 ^{1}H -DOSY NMR Spectrum of **12**-OTf in THF—d_8 at -35 °C. 162
76 *left*: ^{19}F{^{1}H} -DOSY NMR Spectrum of **12**-OTf, *right*: ^{19}F{^{1}H} -DOSY NMR Spectrum of HOTf; both in THF—d_8 at -35 °C. 162
77 ^{1}H NMR Spectrum of **13**-(OTf)$_2$ in THF—d_8 at -65 °C. 163

78 ^{1}H NMR Spectrum of **8** in C_6D_6 at r.t. 164
79 ^{13}C{^{1}H} NMR Spectrum of **8** in C_6D_6 at r.t. 164
80 ^{15}N{^{1}H} NMR Spectrum of **8** in C_6D_6 at r.t. 165
81 ^{31}P{^{1}H} NMR Spectrum of **8** in C_6D_6 at r.t. 165
82 ^{1}H-^{31}P-HMBC NMR Spectrum of **8** in C_6D_6 at r.t. showing a cross-peak for all four ^{t}Bu-groups to only one ^{31}P-signal. 166
83 rRaman Spectrum (457 nm) of ^{14}N/^{15}N-**8** in frozen THF—d_8. 166
84 ATR-IR Spectrum of **8**. 167
85 CV of **8** in 0.1 M solution of [^{n}Bu$_4$N][PF$_6$] in THF (WE = GC, RE = Ag/Ag^{+}, CE = Pt) at different scan rates. 167
86 rRaman Spectrum (633 nm) of ^{14}N/^{15}N-**4** in frozen THF—d_8. 168
87 ATR-IR Spectrum **4**. 169
88 χ_MT vs. T plot for **4** 169
89 ^{1}H NMR Spectrum of **16** in C_6D_6 at r.t. 170
90 ^{13}C{^{1}H} NMR Spectrum of **16** in C_6D_6 at r.t. 170
91 ^{15}N{^{1}H} NMR Spectrum of **16** in C_6D_6 at r.t. 171
92 ^{31}P{^{1}H} NMR Spectrum of **16** in C_6D_6 at r.t. 171
93 ATR-IR Spectrum of **16**. 172
94 ^{1}H NMR Spectrum of **20** in C_6D_6 at r.t. 173
95 ^{13}C{^{1}H} NMR Spectrum of **20** in C_6D_6 at r.t. 173
96 ^{15}N{^{1}H} NMR Spectrum of **20** in C_6D_6 at r.t. 174
97 ^{31}P{^{1}H} NMR Spectrum of **20** in C_6D_6 at r.t. 174
98 ATR-IR Spectrum of **20**. 175
99 ^{1}H NMR Spectrum of **9** in CD_2Cl_2 at r.t. 176
100 ^{13}C{^{1}H} NMR Spectrum of **9** in CD_2Cl_2 at r.t. 176
101 ^{31}P{^{1}H} NMR Spectrum of **9** in CD_2Cl_2 at r.t. 177
102 ATR-IR Spectrum of **9**. 177
103 ^{1}H NMR Spectrum of **18** in C_6D_6 at r.t. 178
104 ^{13}C{^{1}H} NMR Spectrum of **18** in C_6D_6 at r.t. 178
105 ^{31}P{^{1}H} NMR Spectrum of **18** in C_6D_6 at r.t. 179
106 ATR-IR Spectrum of **18**. 179
107 ^{1}H NMR Spectrum of **10** in C_6D_6 at r.t. 180
108 ^{13}C{^{1}H} NMR Spectrum of **10** in C_6D_6 at r.t. 180
109 ^{31}P{^{1}H} NMR Spectrum of **10** in C_6D_6 at r.t. 181
110 ATR-IR Spectrum of **10**. 181
111 *left:* Comparison of the ^{13}C{^{1}H} NMR Spectra of TMS—^{15}NCO (*top*) and TMS—NCO (*bottom*). *right:* Comparison of the ^{29}Si{^{1}H} NMR Spectra of TMS—NCO (*top*) and TMS—^{15}NCO (*bottom*). 182
112 ^{15}N{^{1}H} NMR Spectrum of TMS—^{15}NCO in C_6D_6 at r.t. 182
113 ^{1}H NMR Spectrum of **19** in C_6D_6 at r.t. 183
114 ^{13}C{^{1}H} NMR Spectrum of **19** in C_6D_6 at r.t. 183
115 ^{31}P{^{1}H} NMR Spectrum of **19** in C_6D_6 at r.t. 184
116 ATR-IR Spectrum of **19**. 184

117 ^{1}H NMR Spectrum of **21** in C_6D_6 at r.t. 185

118 ^{13}C{^{1}H} NMR Spectrum of **21** in C_6D_6 at r.t. 185

119 ^{15}N{^{1}H} NMR Spectrum of ^{15}N-**21** in C_6D_6 at r.t. 186

120 ^{31}P{^{1}H} NMR Spectrum of **21** in C_6D_6 at r.t. 186

121 ^{13}C{^{1}H} (*left*) and ^{31}P{^{1}H} (*right*) NMR spectra of ^{15}N-**21** in C_6D_6 at r.t. 187

122 ATR-IR spectrum of **21**. The red line represents the ATR-IR spectrum of ^{15}N-**21**, the blue line shows the spectrum of (^{13}CO)$_2$-**21**. 187

123 CV of the reduction of **21** in 0.1 M solution of [$^{n}Bu_4N$][PF_6] in THF (WE = GC, RE = Ag/Ag^{+}, CE = Pt) at different scan rates. 188

124 ^{1}H NMR Spectrum of **22** in C_6D_6 at r.t. 189

125 ^{13}C{^{1}H} NMR Spectrum of **22** in C_6D_6 at r.t. 189

126 ^{31}P{^{1}H} NMR Spectrum of **22** in C_6D_6 at r.t. 190

127 ATR-IR Spectrum of **22**. 190

128 ^{1}H NMR Spectrum of **23** in C_6D_6 at r.t. 191

129 ^{13}C{^{1}H} NMR Spectrum of **23** in C_6D_6 at r.t. 191

130 ^{31}P{^{1}H} NMR Spectrum of **23** in C_6D_6 at r.t. 192

131 ATR-IR Spectrum of **23**. 192

132 ^{1}H NMR Spectrum of **6** in D_6D_6 at r.t. 193

133 ^{13}C{^{1}H} NMR Spectrum of **6** in D_6D_6 at r.t. 193

134 ^{31}P{^{1}H} NMR Spectrum of **6** in D_6D_6 at r.t. 194

135 ATR-IR Spectrum of **6**. 194

136 ^{1}H NMR Spectrum of **24** in THF—d_8 at r.t. 195

137 ^{13}C{^{1}H} NMR Spectrum of **24** in THF—d_8 at r.t. 195

138 ^{31}P{^{1}H} NMR Spectrum of **24** in THF—d_8 at r.t. 196

139 ATR-IR Spectrum of **24**. 196

140 CV of the first oxidation event of **24** in 0.1 M solution of [$^{n}Bu_4N$][PF_6] in THF (WE = GC, RE = Ag/Ag^{+}, CE = Pt) at different scan rates. 197

141 CV of the first two oxidation events of **24** in 0.1 M solution of [$^{n}Bu_4N$][PF_6] in THF (WE = GC, RE = Ag/Ag^{+}, CE = Pt) at different scan rates. 197

142 Thermal ellipsoid plot of **5** with the anisotropic displacement parameters drawn at the 50% probability level. The asymmetric unit contains one complex molecule. 198

143 Thermal ellipsoid plot of **1** with the anisotropic displacement parameters drawn at the 50% probability level. The asymmetric unit contains a half disordered complex molecule. The disordered complex molecule was refined with population of 0.670(3) on the main domain using some restraints (SADI, RIGU). 199

144 Thermal ellipsoid plot of **2** with the anisotropic displacement parameters drawn at the 50% probability level. The asymmetric unit contains one complex molecule, one benzene solvent molecule and one disordered $CF_3SO_3^-$ anion with a population of 0.67(1) on the main domain. The structure was refined as twin using the twin law -100 010 00-1 (BASF: 0.47(1)) and some restraints and constrains (SADI, RIGU, EADP). 200

145 Thermal ellipsoid plot of **3** with the anisotropic displacement parameters drawn at the 50% probability level. The asymmetric unit contains a half complex molecule, a half THF solvent molecule, one BPh_4 anion and one disordered THF solvent molecule. The disordered THF molecule was refined with population of 0.506(6) on the main domain using some restraints (SADI, RIGU).. 201

146 Thermal ellipsoid plot of **11** with the anisotropic displacement parameters drawn at the 50% probability level. The asymmetric unit contains one cationic complex molecule, one CF_3COO^- anion and one benzene solvent molecule. The N-H hydrogen atom was found from the residual density map and isotropically refined. 202

147 Thermal ellipsoid plot of **8** with the anisotropic displacement parameters drawn at the 50% probability level. The asymmetric unit contains one disordered complex molecule. The disordered complex molecule was refined with population of 0.845(5) and 0.724(8) on their main domains using some restraints and constraints (SADI, EADP). The structure was refined as an inversion twin using the twin law -100 0-10 00-1 (BASF: 0.307(4)). Reflection 0 2 1 was removed from the refinement using OMIT commands. 203

148 Thermal ellipsoid plot of **4** with the anisotropic displacement parameters drawn at the 25% probability level. The asymmetric unit contains a half disordered complex molecule. The disordered complex molecule was refined with population of 0.799(6) on the main domain using some restraints (SADI, RIGU). 204

149 Thermal ellipsoid plot of **18** with the anisotropic displacement parameters drawn at the 50% probability level. The asymmetric unit contains one disordered complex molecule. The disordered complex molecule was refined with population of 0.9311(9) on the main domain using some restraints and constraints (SADI, EADP). 205

150 Thermal ellipsoid plot of **20** with the anisotropic displacement parameters drawn at the 50% probability level. The asymmetric unit contains one complex molecule one $CF_3SO_3^-$ anion and one toluene solvent molecule. The N-H hydrogen atom was found from the residual density map and isotropically refined. 206

151 Thermal ellipsoid plot of **21** with the anisotropic displacement parameters drawn at the 50% probability level. The asymmetric unit contains one complex molecule. The reflections 2 0 0 and 8 9 16 are removed from the refinement using OMIT commands. 207

152 Thermal ellipsoid plot of **22** with the anisotropic displacement parameters drawn at the 50% probability level. The asymmetric unit contains one disordered complex molecule. The disordered complex molecule was refined with population of 0.67(1) on the main domain using some restraints (RIGU, SADI). The structure was refined as an inversion twin using the twin law -100 0-10 00-1 (BASF: 0.03(1)). 208

153 Thermal ellipsoid plot of **23** with the anisotropic displacement parameters drawn at the 50% probability level. The asymmetric unit contains one complex molecule and a half disordered diethyl ether solvent molecule. The disorder was refined using PART -1 command. 209

154 Thermal ellipsoid plot of **6** with the anisotropic displacement parameters drawn at the 50% probability level. The asymmetric unit contains two complex molecules. 210

155 Thermal ellipsoid plot of **24** with the anisotropic displacement parameters drawn at the 50% probability level. The asymmetric unit contains one complex molecule. The reflections -5 5 6 and -5 5 8 are removed from the refinement using OMIT commands. 211

List of Schemes

1 Proposed mechanism of reduction of dinitrogen at the {FeMo}-nitrogenase. 1

2 Mechanism of ammonia formation *via* the *Haber-Bosch-process*. 2

3 Influence of the supporting ligands in formation of end-on bridging N_2-complexes. 5

4 Qualitative Molecular Orbital scheme for S_6-symmetric N_2-bridged dinuclear species. 6

5 *left*: *Floriani's* N_2-bridged dinuclear vanadium dimer **V**. 7

6 Trigonal bipyramidal N_2-bridged dinuclear species with π^{10}-configuration reported by *Schrock* and *Copéret*. 8

7 Trigonal bipyramidal N_2-bridged Ti-complexes with different π-electron count reported by *Liddle*. 9

8 Qualitative Molecular Orbital scheme for D_{4h}-symmetric N_2-bridged dinuclear complexes. 10

9 *left:* Qualitative MO-diagramm for D_{2h}- or D_{2d}-symmetric end-on N_2-bridged dinuclear compounds. *right:* Generalized structure of **XIV** and **XV**. 12

10 Qualitative Molecular Orbital scheme for D_{2h}-symmetric side-on N_2-bridged dinuclear species. The symmetry of the resulting molecular orbitals (MOs) is indicated by the color with black π-, purple δ-symmetry. 15

11 Linkage isomerization from side-on to end-on by exchange of Cl^- *vs.* Cp^-. 16

12 Different reactivity upon reaction with H_2 depending on the coordination mode of the bridging N_2-ligand. 17

13 NN-bond cleavage upon addition of CO to a side-on N_2-bridged *ansa*-hafnocene-complex **XXIII**. 18

14 *left:* Schematic of the FeMo-cofactor of the {FeMo}-nitrogenase. *right:* Overall reaction for the transformation of N_2 into NH_3 mediated by the {FeMo}-nitrogenase. 19

15 *left:* Structure of $[(N_2)\text{-Mo(HIPTN}_3\text{N)}]$ (**XXVa**). *right:* Proposed mechanism for the catalytic formation of NH_3 upon successive protonation/reduction of **XXVa** (*Schrock-cycle*). 20

16 *left:* Structures of $[\text{Fe(TBP)}]^-$ (**XXVIa**) and $[(N_2)\text{-Fe(SiP}_3^{iPr})]^-$ (**XXVIIa**). *right:* Proposed mechanistic pathways for the transformation of **XXVIb** into **XXVIk** *via* **XXVId**, either *via* an distal (top) or alternating (bottom) pathway. The dotted arrows illustrate a hybrid pathway between distal and alternating. 21

17 Possible reactions of **XXVIc**, either leading to NH_3 formation or to H_2 formation. 23

18 *left*: Reduction of **XXVIII** results in the formation of end-on N_2 bridged **XXVIIIb**. *right*: A proposed key intermediate within the catalytic formation of NH_3. 24

19 *left*: *Nishibayashi's* [MoCl$_3$(^{carb}PCP)] (**XXIX**) complex. *right*: Reduction of [MoX$_3$(^{pyr}PNP)] **XXVIII** with SmI$_2$ results in N$_2$-cleavage and formation of [Mo(N)I(^{pyr}PNP)] **XXVIIIc**. 25
20 *left:* The proposed distal mechanism for N$_2$-fixation. *right*: The proposed mechanism for N$_2$-fixation *via* NN-bond cleavage. 26
21 The first example for N$_2$-cleavage reported by *Cummins*. 27
22 Molecular orbital scheme for the thermal splitting of **I** into **XXXI** *via* an *zig-zag*-transition state. 28
23 The end-on N$_2$-bridged dinuclear complexes of *Floriani* (**XXXIIa**) and *Schrock* (**VIa**), which are not both capable to cleave the NN-bond thermally. 29
24 *Top:* Re-mediated N$_2$-cleavage *via* end-on N$_2$-bridged dinuclear **XII**. *Bottom:* Postulated EC^{N_2}C^{Cl}EC^{Dim}-mechanism for the formation of **XII**. 30
25 Proposed mechanism of proton induced N$_2$-splitting. 31
26 Qualitative frontier molecular orbitals diagramm for **XI** (*left*), **XL** (*middle*) and the calculated *zig-zag*-transition state from **XL** to **XXXVIII** (*right*). . . 31
27 Oxidative N$_2$-cleavage as presented by *Masuda*. 32
28 Calculated energies for N$_2$-cleavage for **XII** (black) and **XIII** (green) *via* a *zig-zag*-transition state. 33
29 Proposed mechanism for the formation of **XXXIIb** upon irradiation of **XXXIIa**. 34
30 Irradiation of **I** or **XXXIIa** leads to competitive N-N- and M-N$_2$-cleavage and in case of **XXXIIa** to recombination of **XXXIIc** and **XXXIIe** to give nitride bridged **XXXIIb**. 35
31 Photolytical (R^1 = ^{i}Pr; R^2 = Me) and thermal (R^1 = Et; R^2 = Ph) N$_2$-cleavage of *Sita's* η^5-cyclopentadienyl/η^2-amidinate complexes (M = Mo **XVIg**, **XLVa** and W **XVIh**, **XLV**). 36
32 Photolytical splitting of **XLVIIa** gives terminal nitride **XLVIII**, whose oxidation yields in **XLVIIb** *via* nitride coupling. 37
33 Irradition of **XLIXa** yields in **La** and **Lb**, which subsequently react further to give two equivalents of **Lc**. 38
34 Molecular orbital scheme for the cleavage of **XLIXa** into **La** and **Lb** upon elongation of the NN-bond distance. 39
35 Formation of the N$_2$-bridged dinuclear Re-PONOP-species **LII** and their interconversion into **LIIIa** upon photolysis. 40
36 *left*: Qualitative orbital interactions within octahedrally coordinated L$_5$MN. *right:* Qualitative frontier molecular orbital scheme for metal nitrido complexes in tetrahedral, octahedral and square-planar coordination geometries. 43
37 Simplified molecular orbital schemes for the π-interaction within the metal-nitride-bond. 44
38 Ligand influence on the nucleophilicity of an Tp-supported Os-nitride. . . . 45
39 Oxidation of the PNP-pincer-ligand and the Re-center in nucleophilic **XXXVII** change the nitride-philicity to electrophilic in **LXVI**. 46

40 Photolytic cleavage of **XLIXa** generates a unstable Os(V)-nitride **Ld**, which subsequently disproportionates and starts a cascade reaction, which finally gives **LXVIII**. 47
41 *Top:* Sequential methylation of N_2-derived **XXXI** forms the ethylimido **LXXI**. *Bottom:* Generation of CN^- from **XXXI**. 48
42 Synthetic cycle to generate organic nitriles from N_2. 48
43 Synthetic cycle for the formation of nitriles from N_2 and acyl chlorides using N_2-bridged heterobimetallic **IV** 49
44 Synthetic cycle for the generation of acetonitrile from N_2 using a Re-PNP-pincer-platform. 50
45 Three step synthetic cycle for the formation of benzamide, benzonitrile and benzoic acid from benzoylchloride and N_2, including photolytic N_2-cleavage and electrochemical re-reduction of the ligand-backbone. 51
46 *left:* An idealized cycle for the formation of cyanate from N_2 and CO. *right:* Overall equations for the formation of potassium cyanate and cyanate 52
47 *Top:* Coupling of a non-N_2-derived V(V)-nitride **LXXXIX** with CO results in formation of NaOCN. *Bottom:* Reduction of the Nb(IV)-cyanate **XCII** results in decarbonylation and formation of the Nb(V)-nitride **XCI**. 53
48 *left:* Carbonylation of **XCIV** results in CN-coupling to give **XCV** on different time-scales depending on the oxidation state. *right:* The proposed transition state of CN-coupling. 54
49 Carbonylation of *Agapie's* Mo(IV)-nitride **XCVIIa** results in CO coordination, while carbonylation of the corresponinding Mo(II)-nitride **XCVIIa** gives NaOCN. 54
50 Synthetic cycle for the transformation of N_2 and CO into cyanate mediated by a V(ONO)-platform. 55
51 Synthesis of **1** and its further one or two electron oxidation to **2** and **3**, respectively. 61
52 Qualitative molecular orbital scheme of **1** (*left*), **2** (*middle*) and **3** (*right*) . 64
53 *left*: Reaction of **1** with CN-^{t}Bu. *right*:Molecular structure of **6** in the crystal obtained by single crystal X-ray diffraction. 67
55 Protonation of **1** leads either to N_2-cleavage and formation of **11** or to proton-reduction and formation of **3**. 73
56 Anion dependence upon protonation of **1** with different $[HNEt_3{}^+]X$ salts. . 74
57 Protonation of **1** with one equiv. $[H(OEt_2)_2][BAr^F_{24}]$ or HOTf at low temperatures. 75
58 Proposed mechanism of tungsten mediated proton induced N_2-splitting. . 76
59 Proposed mechanistic pathways for proton reduction at high (Path A) and low (Path B) concentrations of acid. 78

60 Computed energy profile for proton induced N_2-cleavage (*left branch*) and proton reduction (*right branch*) both *via* double protonation of **1** at 25 °C in the absence (solid line) and in the presence (dashed line) of triflate as counteranion. The italic energies represent the calculated barriers for N_2-splitting from **13** and **13**^{OTf_2} to give **11** and **11**^{OTf}, respectively. 79
61 Computed energy profile for proton induced N_2-cleavage (*left branch*) and proton reduction (*right branch*) both *via* double protonation of **1** with triflic acid at 25 °C (black) and -80 °C (green). The italic energies represent the calculated barriers for N_2-splitting from **13**^{OTf_2} to give **11**^{OTf}. . . 81
62 Thermal and photolytical N_2-cleavage of **4** to give **16**. 83
63 The equilibrium of **4** and **16** and the resulting rate law for the decay of **4** used to fit the kinetic curves. 84
64 *left*: Energy-profile for the N_2-splitting of **4** to give **16** including the experimental and computed values. *right*: Structure of the calculated singlet-transition-state, **^{S}TS**. 86
65 Qualitative molecular orbital diagram for the splitting of **4** into **16** *via* a *zig-zag*-transition state. 87
66 The two possible synthetic pathways for the synthesis of **16**. 97
67 Protonation of **19** liberates CO and N_2 and gives **20**. 98
68 Carbonylation of **16** leads to formation of **21**. 100
69 Possible pathways for the formation of **21** *via* carbonylation of **16**, either following an intramolecular (*left*) or an intermolecular (*right*) pathway for C-N coupling to give **21a** or **21b**, respectively. 102
70 Functionalization of **16** using isocyanides. 103
71 Formation of **24** *via* reduction of **18** or **21** or *via* deprotonation of **9**. . . . 106
72 Liberation of NCO from **21** *via* salt-metathesis with TMS-Cl giving **10** and TMS-NCO in quantitative yields. 107
73 Oxidation of **10** under photolytic conditions with NCS (*N*-chloro-succinimide) reforms **5**. 109
74 Synthetic cycle for the formation of TMS-NCO from N_2 and CO using a W(PNP)-platform. 109
75 Comparison of the electronic structures of **3**, **2**, **1** and **4**. 110
76 Protonation of **1** leads either to N_2-cleavage and formation of **11** or to proton-reduction and formation of **3**. 111
77 The experimentally derived kinetic and thermodynamic parameters for N_2-cleavage in **4** yielding **16**. 111
78 Synthetic cycle for the formation of TMS-NCO from N_2 and CO using a W(PNP)-platform. 113
79 Proposed Lewis-acid induced N_2-cleavage of **1**. 113
80 The equilibrium of **4** and **16** and the resulting rate law for the decay of **4** used to fit the kinetic curves. 142

List of Tables

1 Bond lengths and stretching frequencies of free and coordinated N_2-species. . . . 3
2 Comparison of the structural and electronic properties of several nacnac-supported N_2-bridged dinuclear compounds. . . . 12
3 NN-bond-distances in the N_2-bridged η^5-cyclopentadienyl/η^2-amidinate complexes **XVI** reported by *Sita*. . . . 13
4 Acid influence on the selectivity (NH_3/H_2) and activity (equiv.(NH_3+H_2) per catalyst) upon usage of **XXVIIIb** under catalytic conditions. . . . 24
5 Photolysis (λ = 405 nm) of different mixtures of **LIIa**, **LIIb** and **LIIc** gives different quantum yields (Φ, obtained after 2 h) and yields of **LIIIa**. . . . 40
6 Comparison of the structural and spectroscopic features of the bridging N_2 ligand in **1**, **2** and **3** with the Mo-congener **XI** and Cummins' dicationic **III**. . . . 64
7 Comparison of the spectroscopic and structural parameters of the synthesized tungsten-biscarbonyl-complexes. . . . 107
8 The derived rate constants k_1 and k_2 and the so obtained equilibrium constants K and ΔG-values. . . . 142
9 Crystal data and structure refinement for **5**. . . . 198
10 Crystal data and structure refinement for **1**. . . . 199
11 Crystal data and structure refinement for **2**. . . . 200
12 Crystal data and structure refinement for **3**. . . . 201
13 Crystal data and structure refinement for **11**. . . . 202
14 Crystal data and structure refinement for **11**. . . . 203
15 Crystal data and structure refinement for **4**. . . . 204
16 Crystal data and structure refinement for **18**. . . . 205
17 Crystal data and structure refinement for **20**. . . . 206
18 Crystal data and structure refinement for **21**. . . . 207
19 Crystal data and structure refinement for **22**. . . . 208
20 Crystal data and structure refinement for **23**. . . . 209
21 Crystal data and structure refinement for **6**. . . . 210
22 Crystal data and structure refinement for **24**. . . . 211

1 Introduction

Along with carbon, hydrogen and oxygen, nitrogen is one of the main elements found in organic compounds. Although nitrogen is the most abundant gas in the atmosphere, comprising 78%, it exists in its biologically and chemically most stable dinuclear gaseous form, N_2, making it hard to manipulate and convert into useful chemicals. Its conversion into a more reactive nitrogen source, ammonia (NH_3), by biological, enzymatic "nitrogen fixation" was an essential step in development of life.[1,2]
Industrially, atmospheric dinitrogen is transformed into ammonia *via* the so-called *Haber-Bosch-process* upon reaction with hydrogen in the presence of iron or ruthenium at high pressures (50-200 atm) and temperatures (700-850 K).[3,4] Nowadays, millions of tons of NH_3 are produced of which the major part (approx. 80%) is used for the production of fertilizers setting the foundation for modern agriculture. The remaining part of the so generated ammonia is used for the production of nitrogen-containing industrially relevant organic molecules, building blocks and fine chemicals.[4–6]
For both, the industrial and the biological ammonia production, fundamentally different pathways are proposed. Enzymatic N_2-fixation is supposed to occur *via* a successive protonation/reduction route (Scheme 1).[2] For this route two possible pathways, either following a distal or an alternating mechanism, are proposed. While in the distal mechanism the terminal N-atom is hydrogenated first and released as NH_3, in the alternating mechanism both N-atoms are hydrogenated simultaneously.[7]
Inspired by this, homogeneous biomimetic catalysts, which are capable for the transformation of N_2 into ammonia *via* successive protonation/reduction at ambient conditions, have been developed.[8–10]

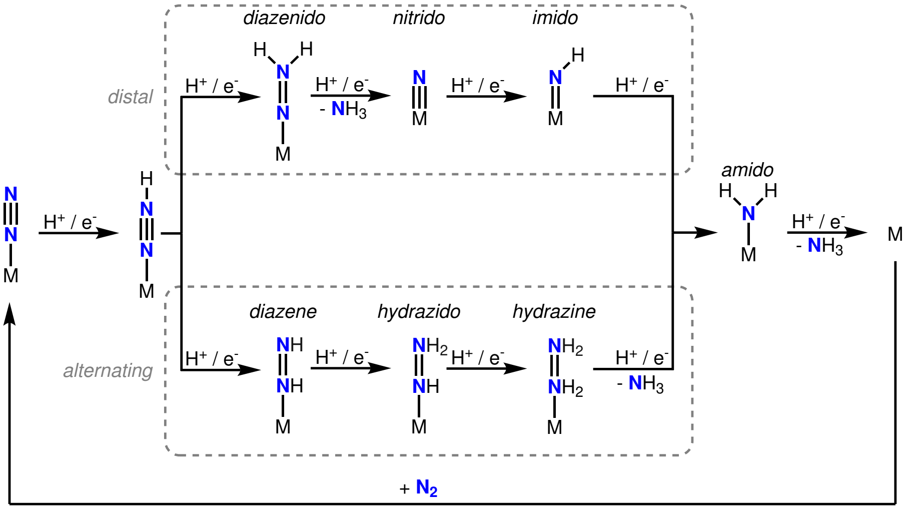

Scheme 1: Proposed mechanism of reduction of dinitrogen at the {FeMo}-nitrogenase.[7]

In the *Haber-Bosch-process* dinitrogen is initially cleaved on the catalyst surface into two surface bound N-atoms followed by successive N-H bond formation (Scheme 2). At not too low temperatures and under “normal” N_2/H_2 partial pressure ratios the rate limiting step within this transformation is the cleavage of the NN-bond at the surface of the Fe catalyst ($N_{2(ad)} \longrightarrow 2\ N_{(ad)}$).[4,11]

$$
\begin{gathered}
H_2 \rightleftharpoons 2\ H_{(ad)} \\
N_2 \rightleftharpoons N_{2(ad)} \rightleftharpoons 2\ N_{(ad)} \\
N_{(ad)} + H_{(ad)} \rightleftharpoons NH_{(ad)} \\
NH_{(ad)} + H_{(ad)} \rightleftharpoons NH_{2(ad)} \\
NH_{2(ad)} + H_{(ad)} \rightleftharpoons NH_{3(ad)} \\
NH_{3(ad)} \rightleftharpoons NH_3
\end{gathered}
$$

Scheme 2: Mechanism of ammonia formation *via* the *Haber-Bosch-process*.[4]

Mimicking this mechanism several homogeneous systems capable for full cleavage of the NN-triple bond under formation of a metal-bound nitride, of which some of them can be further functionalized to give ammonia, have been developed.[12–21]
Additionally, full cleavage of N_2 to give a metal-bound nitride holds the promise of direct and therefore more atom efficient functionalization of N_2 by avoiding full reduction to ammonia and subsequent re-oxidation to nitrogen-containing higher value molecules.[6,22]

For both pathways understanding of N_2-binding to transition metals is essential. This topic will be covered in chapter 1.1. The functionalization of N_2 to give ammonia will be described in chapter 1.2.1 focusing on the parameters influencing the selectivity between competing nitrogen- and proton-reduction.
Afterwards the thermal and photolytical splitting of N_2 and the functionalization of the so derived metal-bound nitrides, with focus on CN-coupling, will be discussed.
In order to illustrate the origin of a *N*-functionality within a compound, all nitrogen-atoms, which could be derived from N_2, are given in blue.

1.1 Bonding of N_2 to transition metals

1.1.1 General aspects of N_2-binding

Molecular dinitrogen N_2, the most common form of all global nitrogen, is both thermodynamically and kinetically a very stable molecule. It features a high bond dissociation energy (941 $kJ\cdot mol^{-1}$), a high ionization potential (-15.6 eV) and low proton (5.1 eV) and electron (-1.9 eV) affinities. Additionally, N_2 provides no dipole moment, which makes it a rather poor ligand.[23–25]

Nevertheless, since the first published N_2-complex in 1965, $[Ru(NH_3)_5N_2]^{2+}$, there have been many examples for transition metal complexes bearing dinitrogen as ligand, typically in one of the four most frequently reported coordination modes depicted in Figure 1: (**A**) mononuclear end-on (η^1-N_2), (**B**) dinuclear end-on (μ^2:η^1:η^1-N_2) , (**C**) dinuclear side-on (μ^2:η^2:η^2-N_2) and (**D**) dinuclear side-on-end-on (μ^2:η^1:η^2-N_2), with (**A**) being predominant.[22,26]

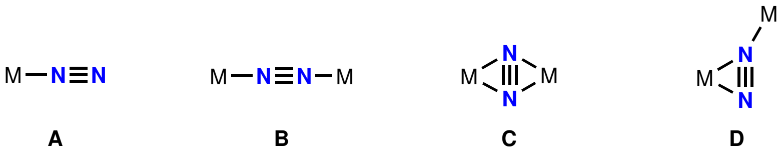

Figure 1: Most frequently found coordination modes in N_2-complexes.[22]

Due to donation of electron density from the metal center into appropriate antibonding orbitals of the N_2 ligand, the coordination to a metal center leads to weakening (or "activation") of the NN-bond. The degree of activation can be rationalized by the NN stretching frequency and the NN bond length, which should be, according to *Badger's* rule, inversely proportional (Table 1). Additional information about the redox state of the N_2 ligand can be derived by its spin-state due to magnetic coupling to the metal ion(s).[27–29]

Table 1: Bond lengths (d_{NN}) and stretching frequencies ($\tilde{\nu}_{NN}$) of free and coordinated N_2-species.[22]

	S	d_{NN} [Å]	$\tilde{\nu}_{NN}$ [cm^{-1}]
free N_2	-	1.10	2331
[N≡N]	0	~1.10-1.20	1700-2331
$[N{\equiv}N]^-$	1/2	n.a.	n.a.
free H_2N_2	-	1.25	1583 / 1529
$[N{=}N]^{2-}$	1	~1.20-1.35	1200-1700
$[N{=}N]^{3-}$	1/2	1.40	989-1040
free H_4N_2	-	1.45	885
$[N{-}N]^{4-}$	0	~1.40-1.60	700-1100

The degree of N_2 activation for reported complexes ranges from nearly unactivated neutral N_2 up to highly activated hydrazide (N_2^{4-}). Notably, while there are many examples for complexes carrying a diazenide (N_2^{2-}) or hydrazide (N_2^{4-}) ligand, there are only few examples bearing a N_2^{3-}-ligand. Furthermore, the monoanionic N_2^- was only detected in solid matrices at low temperatures emphasizing the importance of initial multi electron reduction for N_2-activation.[30–33]

Splitting of N_2 into molecular nitrides requires overall six electrons and typically proceeds *via* the formation of end-on N_2-bridged complexes (Figure 1, **B**) as key intermediates, which will be discussed in the next chapter.[22]

1.1.2 End-on bridging N_2

The formation of end-on bridging N_2-complexes typically proceeds in a two step process *via* the coordination of a second metal center to a end-on bound N_2-moiety. Initial binding of N_2 to one metal center is similar to other diatomic ligands like CO and can be understood as a combination of σ-donation of the lone pair of the N_2-unit into an empty metal d-orbital with suitable symmetry and π-backdonation from a filled metal d-orbital into an empty π^*-orbital of the N_2 ligand. Differences arise from the much higher HOMO-LUMO gap of N_2 (10.82 eV) compared to other diatomic ligands like CO (9.34 eV), which results in a smaller orbital overlap and weaker activation of the N_2-moiety.[24] Nevertheless, binding to a metal center increases the electron density on the N_2 ligand and its affinity for binding a second metal ion.[34] Independent studies by the groups of *Cummins* and *Schneider* have shown, that reduction of the end-on bound N_2-complex can promote and accelerate the formation of end-on N_2 bridged complexes.[35,36]

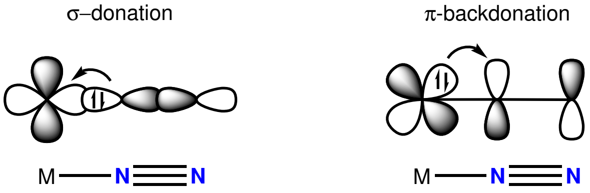

Figure 2: Orbital interactions between N_2 and a metal center in end-on bound N_2-complexes.

Another possibility for the formation of such N_2-bridged compounds is the coupling of two terminal nitrides, the microscopic reverse to N_2-splitting into terminal nitrides, which is mainly found for late transition metals.[16,37–51]

Since both metal ions get in close proximity the formation of N_2-bridged dinuclear species can be inhibited by usage of too sterically demanding supporting ligands (Scheme 3, **A**). However, a certain shielding of the metal ion(s) is required to prevent the formation of strong metal-metal bonds, as it has been demonstrated by *Cummins* for a series of differently substituted molybdenum(III) triamide and molybdenum(III) trialkoxide complexes (Scheme 3, **B**).[35,52–56]

In this context, the group could also show that reversible cyclometalation can be used as a strategy to prevent metal-metal bond formation (Scheme 3, **C**).[57]

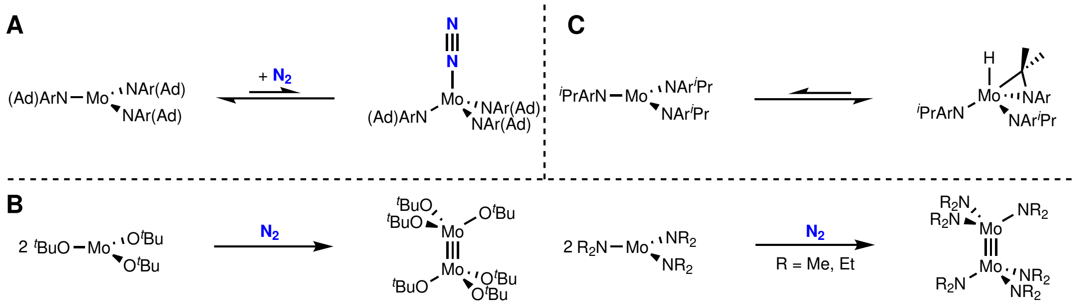
A
(Ad)ArN–Mo NAr(Ad) NAr(Ad)
+ N_2
N N Mo (Ad)ArN NAr(Ad) NAr(Ad)
C
^{i}PrArN–Mo NAr^{i}Pr NAr^{i}Pr
H Mo NAr ^{i}PrArN NAr^{i}Pr
B
2 ^{t}BuO–Mo O^{t}Bu O^{t}Bu
N_2
^{t}BuO ^{t}BuO Mo O^{t}Bu Mo ^{t}BuO O^{t}Bu O^{t}Bu
2 R_2N–Mo NR_2 NR_2
N_2
R = Me, Et
R_2N R_2N Mo NR_2 Mo R_2N NR_2 NR_2

Scheme 3: Influence of the supporting ligands in formation of end-on bridging N_2-complexes.[35,52–57]

Once formed, the degree of N_2-activation and therefore the stability of the obtained N_2 bridged complexes can be achieved by consideration of orbital interactions, as first discussed by *Gray* and *Chatt*.[58,59] Thereby, the molecular orbitals are generated from linear combination of the metal d-orbitals and nitrogen p-orbitals. The symmetry of the N_2-bridged complex has a strong influence on the energetic order of the resulting frontier molecular orbitals (FMOs).

In N_2-bridged dinuclear species with S_6-symmetry, linear combination of the d_{xz} and d_{yz} with the two π and the two π^*-orbitals of the N_2-ligand results in four sets of π-orbitals ($1e_u$, $1e_g$, $2e_u$, $2e_g$) each set consisting of two degenerate orbitals (Scheme 4, black). Additionally, M-N_2-σ-orbitals (a_u, Scheme 4, green) are generated by overlap between the d_{z^2} orbitals of the two metal centers with the σ^*-orbital of the bridging N_2-ligand. Due to the lack of N_2-molecular orbitals with appropriate symmetry, the two remaining d-orbitals of each metal center, d_{xy} and $d_{x^2-y^2}$, give two sets of NN-non-bonding δ-orbitals ($3e_g$ and $3e_u$) again each set consisting of two degenerate orbitals (Scheme 4, purple).
Taking these simple and qualitative MO considerations to account, the degree of N_2-activation can be correlated to population of π and π^*-orbitals. A very illustrative example stems from the group of *Cummins*, who investigated the degree of N_2-activation in a series of Mo-triamido-complexes, $[(N_2)\{Mo(N(R)Ar)_3\}_2]^{n+}$, (R = ^{t}Bu; Ar = 3,5-$C_6H_3Me_2$; n = 0 **I**, n = 1 **II**, n = 2 **III**). By comparing the NN-bond lengths and NN-stretching frequencies, an increase of the degree of N_2-activation was observed with neutral **I** bearing the weakest activated bridging N_2-ligand within this redox-series (Figure 3). The observed trend can be correlated to the number of π-electrons within the {MoNNMo}-manifold.

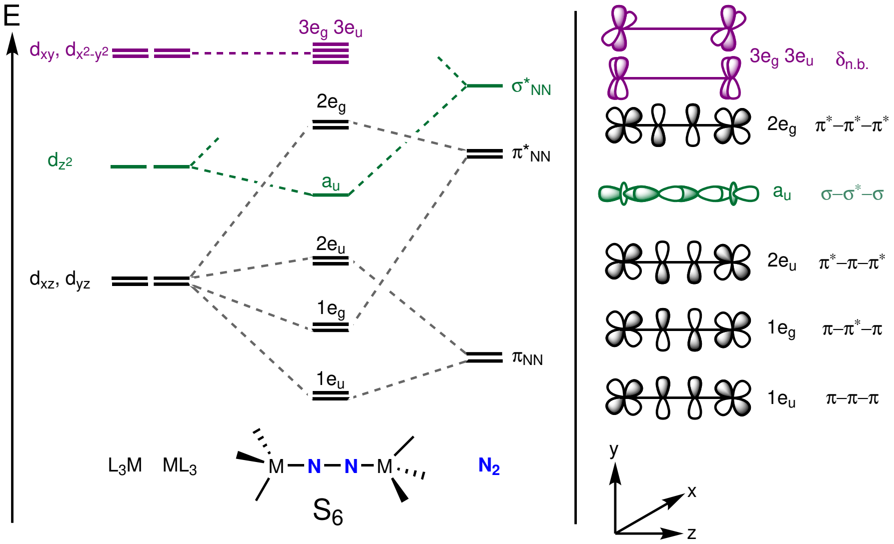
E
d_{xy}, $d_{x^2-y^2}$
$3e_g$ $3e_u$
σ^*_{NN}
$2e_g$
d_{z^2}
π^*_{NN}
a_u
d_{xz}, d_{yz}
$2e_u$
$1e_g$
π_{NN}
$1e_u$
L_3M ML_3
M–N–N–M
S_6
N_2
$3e_g$ $3e_u$ $\delta_{n.b.}$
$2e_g$ π^*–π^*–π^*
a_u σ–σ^*–σ
$2e_u$ π^*–π–π^*
$1e_g$ π–π^*–π
$1e_u$ π–π–π
y
x
z

Scheme 4: Qualitative Molecular Orbital scheme for S_6-symmetric N_2-bridged dinuclear species. The symmetry of the resulting molecular orbitals (MOs) is indicated by the color with green σ-, black π- and purple δ-symmetry.[59]

Neutral **I** features overall ten π-electrons, assuming the bridging N_2 ligand to be neutral, both Mo(III)-ions deliver three π-electrons, while the remaining four π-electrons stem from the N_2 ligand itself. Consequently, this electron count results in a $1e_u^4 1e_g^4 2e_u^2$-configuration within the {MoNNMo}-manifold with a NN-bonding and M-N_2-antibonding HOMO ($2e_u$; Scheme 4). Upon oxidation to a $1e_u^4 1e_g^4 2e_u^1$- (**II**) or $1e_u^4 1e_g^4 2e_u^0$-configuration (**III**), this MO gets depleted, which explains the observed increase in the degree of N_2-activation upon oxidation.[60,61]

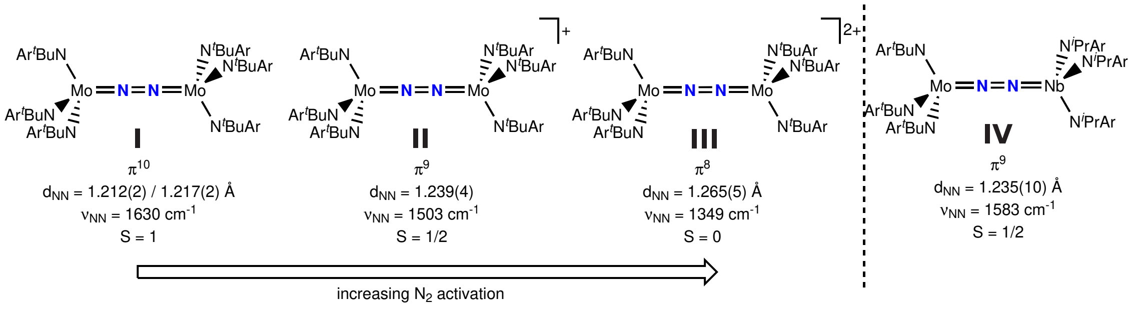
Ar^{t}BuN
N^{t}BuAr
N^{t}BuAr
Mo=N=N=Mo
Ar^{t}BuN
Ar^{t}BuN
N^{t}BuAr
I
π^{10}
d_{NN} = 1.212(2) / 1.217(2) Å
ν_{NN} = 1630 cm^{-1}
S = 1
+
II
π^9
d_{NN} = 1.239(4)
ν_{NN} = 1503 cm^{-1}
S = 1/2
2+
III
π^8
d_{NN} = 1.265(5) Å
ν_{NN} = 1349 cm^{-1}
S = 0
Mo=N=N=Nb
N^{i}PrAr
N^{i}PrAr
N^{i}PrAr
IV
π^9
d_{NN} = 1.235(10) Å
ν_{NN} = 1583 cm^{-1}
S = 1/2
increasing N_2 activation

Figure 3: Structural and spectroscopic properties of the $[(N_2)\{Mo(N(R)Ar)_3\}_2]^{n+}$ (n = 0-2)-redox series (**I**, **II**, **III**) and the hetero-bimetallic Mo/Nb analogue (**IV**) by *Cummins*.[60–62]

This picture gains further support by magnetic measurements. Neutral **I** features a magnetic moment of $\mu_{\mathrm{eff}} = 2.85\ \mu_B$ in agreement with a triplet ground state.[60] The magnetic moment of monocationic **II** was determined to $\mu_{\mathrm{eff}} = 1.96\ \mu_B$ in line with the expected doublet ground state, while dicationic **III** is diamagnetic.[61]
The group of *Cummins* was also able to prepare a Nb/Mo hetero-bimetallic analogue (**IV**), which has a π^9-configuration isoelectronic to monocationic **II**. Accordingly, the NN-bond length ($d_{NN} = 1.235(10)$ Å) as well as the NN-stretching frequency of **IV** ($\tilde{\nu}_{NN} = 1583\ \mathrm{cm}^{-1}$) are almost invariant from homobimetallic **II**. Nevertheless, combined DFT and EPR studies showed valence delocalisation of the odd electron over the whole {MoNNNb}-core, further supporting a covalent bonding picture.[62]

The σ- and π-donating abilities of the supporting ligands can have a strong influence on the energetic order of the MO's shown in Scheme 4. This was demonstrated by *Floriani* upon a redox-series of N_2-bridged dinuclear vanadium compounds (**V**). Neutral **V** has a diamagnetic ground state and features a relatively long NN-bond ($d_{NN} = 1.222(4)$ Å) in line with eight π-electrons fully populating the $1e_u$- and $1e_g$-orbitals of the {VNNV}-core (Scheme 4). Further reduction giving monoanionic **V**$^-$ or dianionic **V**$^{2-}$ does not lead to significant changes in the NN-bond lengths as it would have been expected by populating the NN-antibonding $2e_u$-orbital following the MO-scheme shown in Scheme 4.[63–65]

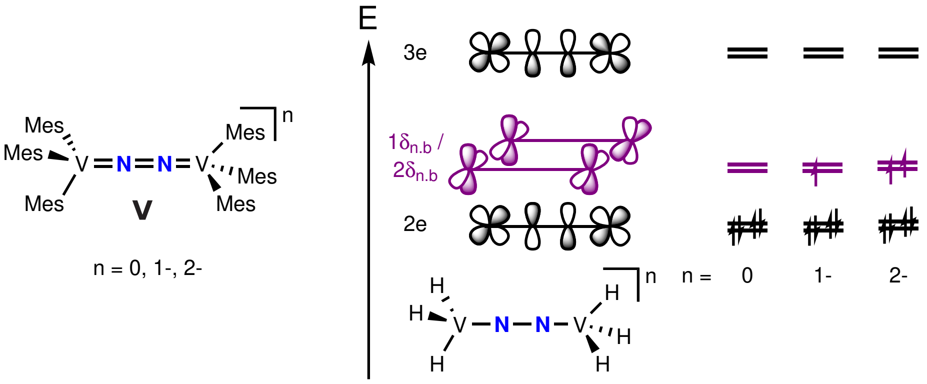

Scheme 5: *left*: *Floriani's* N_2-bridged dinuclear vanadium dimer **V**. *Right:* Qualitative MO-scheme for the truncated $[(N_2)\text{-}\{VH_3\}_2]$-model.[63–65]

These differences were rationalized computationally using a truncated $[(N_2)\{VH_3\}_2]$-model.[63–65] The calculations on the neutral compound revealed a diamagnetic ground state in which the HOMO consists of a set of two degenerate orbitals (2e, Scheme 5), which are both fully occupied. The LUMO is only about 1 eV higher in energy and features mostly metal δ-character. The relatively small energy gap leads to an accessible exited triplet state and second order contributions in the magnetic susceptibility, in agreement with the observed TIP (temperature independent paramagnetism) for **V**. Single electron reduction of **V** leads to population of the δ-orbital and a doublet magnetic ground state. The NN-non-bonding character of this orbital is expressed by a nearly unchanged NN-bond length. Further reduction leads to a $(1\delta^1/2\delta^1)$-configuration. Again the metal-based character of these orbitals leads to insignificant changes in the NN-bond lengths. The missing contribution of the bridging N_2 ligand in the δ-orbitals results in very weak antiferromagnetically coupling of both $S = 1/2$ centers, in agreement with the observed magnetic behavior of $\mathbf{V}^{2-}$.

A fourth auxiliary ligand at the metal center can lead to two different symmetries depending on the coordination sphere around the metal ion. Addition of a ligand *trans* to the bridging N_2-ligand results in a trigonal bipyramidal coordination sphere around the metal, which can have a strong impact on the stability of the N_2-bridge with respect to N_2-cleavage (see chapter 1.2.2). Nevertheless, the fourth ligand *trans* to the N_2-bridge does not lead to significant changes in the degree of N_2-activation. For example, both trigonal bipyramidal π^{10}-electron complexes reported by *Schrock* (**VIa**) and *Copéret* (**VII**) feature almost identical NN-bond lengths, very close to those of isoelectronic **I** (Scheme 6).[66,67]

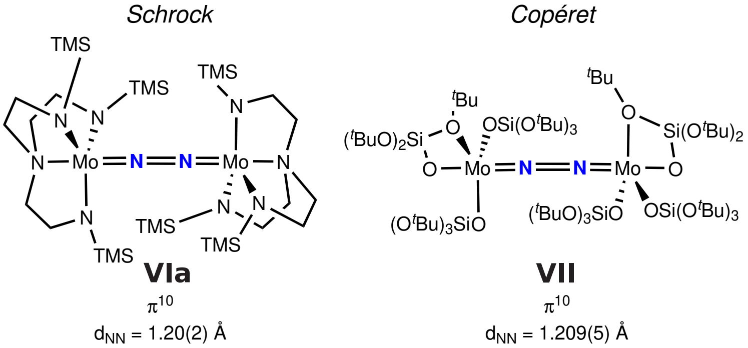
Schrock
TMS
TMS
TMS
N
Mo
N
Mo
N
TMS
TMS
TMS
VIa
π^{10}
d_{NN} = 1.20(2) Å
Copéret
^{t}Bu
^{t}Bu
O
OSi(O^{t}Bu)$_3$
(^{t}BuO)$_2$Si
Si(O^{t}Bu)$_2$
Mo
N
N
Mo
(O^{t}Bu)$_3$SiO
(^{t}BuO)$_3$SiO
OSi(O^{t}Bu)$_3$
VII
π^{10}
d_{NN} = 1.209(5) Å

Scheme 6: Trigonal bipyramidal N_2-bridged dinuclear species with π^{10}-configuration reported by *Schrock* and *Copéret*.[66,67]

The group of *Liddle* reported several Ti-congeners to *Schrock's* **VIa** with different π-electron counts (Scheme 7). The bridging N_2 ligand of neutral congener **VIII** with six π-electrons shows only very weak activation ($d_{NN} = 1.121(6)$ Å; $\tilde{\nu}_{NN} = 1701\ cm^{-1}$), due to only two electrons occupying the NN-antibonding $1e_u$-orbital. In line with the described MO-picture, further reduction to the potassium supported π^8-configurated **IX** results in further population of the $1e_u$-orbital and an increased degree of N_2-activation as indicated by the NN-bond length ($d_{NN} = 1.315(3)$ Å) and the NN-stretching frequency ($\tilde{\nu}_{NN} = 1201\ cm^{-1}$). Abstraction of the two supporting potassium ions yields in the formation of dianionic **X** with an increased NN-bond distance as well as an slightly increased NN-stretching frequency. Notably, usage of Mg insted of KC_8 as reducing agent does not result in formation of N_2-bridged species, which illustrates the influence of the used reducing agent and the obtained cation.[68,69]

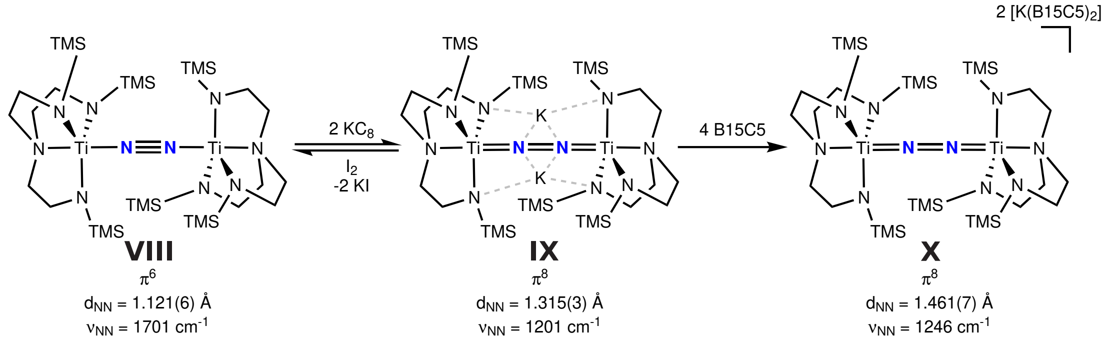

Scheme 7: Trigonal bipyramidal N_2-bridged Ti-complexes with different π-electron count reported by *Liddle* (B15C5 = benzo-15-crown-5-ether).[68]

The addition of a fourth auxiliary ligand can also result in square-pyramidal coordination of the metal ions, typically with the N_2-bridge on the apical side. As a result of the changed symmetry from threefold to fourfold, the orbital overlap with the supporting ligands changes and the b_{1u}- and b_{2g}-orbitals drop in energy. Since these orbitals are generated by linear combination of the two metal d_{xy}-orbitals with δ-symmetry, they provide NN-non-bonding character, which has to be taken into account when correlating the overall electron count to the degree of N_2-activation (Scheme 8).

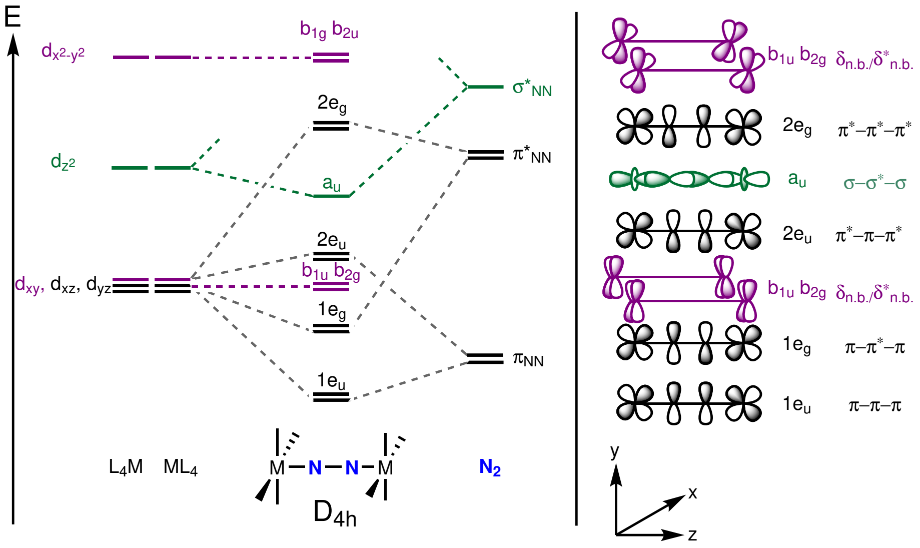
E
$d_{x^2-y^2}$
d_{z^2}
d_{xy}, d_{xz}, d_{yz}
b_{1g} b_{2u}
$2e_g$
a_u
$2e_u$
b_{1u} b_{2g}
$1e_g$
$1e_u$
σ^*_{NN}
π^*_{NN}
π_{NN}
L_4M
ML_4
M−N−N−M
D_{4h}
N_2
b_{1u} b_{2g} $\delta_{n.b.}/\delta^*_{n.b.}$
$2e_g$ $\pi^*-\pi^*-\pi^*$
a_u $\sigma-\sigma^*-\sigma$
$2e_u$ $\pi^*-\pi-\pi^*$
b_{1u} b_{2g} $\delta_{n.b.}/\delta^*_{n.b.}$
$1e_g$ $\pi-\pi^*-\pi$
$1e_u$ $\pi-\pi-\pi$
y
x
z

Scheme 8: Qualitative Molecular Orbital scheme for D_{4h}-symmetric N_2-bridged dinuclear complexes. The symmetry of the resulting molecular orbitals (MOs) is indicated by the color with green σ-, black π- and purple δ-symmetry.[59]

Such (idealized) D_{4h}-symmetric compounds are often observed, when pincer complexes are used. For example, the group of *Schneider* reported two PNP^{tBu}-pincer (PNP^{tBu} = $[N(CH_2CH_2P^tBu_2)_2]^-$ supported N_2-bridged dinuclear complexes containing either Mo (**XI**) or Re (**XII**) and therefore different electron counts within the {MNNM}-core (Figure 4).[36,70]

The Mo-compound **XI** contains overall twelve electrons within the {MoNNMo}-core, four steming from the N_2 ligand itself and two times four electrons from the (formal) Mo(II)-centers. Following the MO-picture (Scheme 8) this results in a $1e_u^4 1e_g^4 b_{1u}^2 b_{2g}^2$ configuration with a π-electron count of eight. The degree of N_2-activation is very close to **III** as judged by the NN-bond-length ($d_{NN} = 1.258(9)$ Å) and NN-stretching frequency ($\tilde{\nu}_{NN} = 1343$ cm^{-1}).[70] Moving from group 6 to group 7, two additional electrons are introduced, which leads to occupation of the $2e_u$-orbitals and an overall $1e_u^4 1e_g^4 b_{1u}^2 b_{2g}^2 2e_u^2$-configuration with an π-electron count of ten. Accordingly, the degree of N_2-activation in **XII** is smaller compared to **XI**, as indicated by the shorter NN-bond-length ($d_{NN} = 1.202(10)$ Å), which is very similar to the one of *Cummins'* neutral **I**.[36]

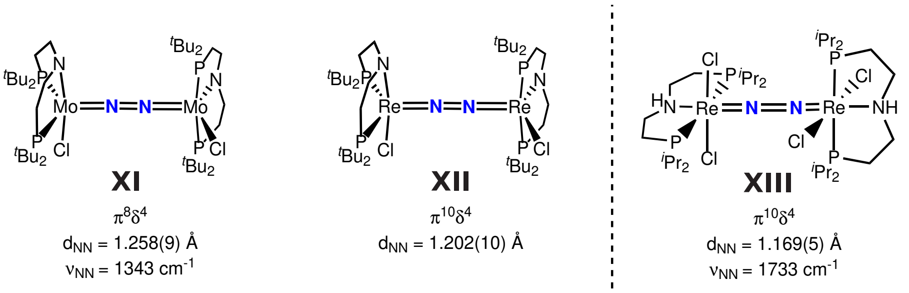

XI $\pi^8\delta^4$ $d_{NN} = 1.258(9)$ Å $\nu_{NN} = 1343$ cm^{-1}

XII $\pi^{10}\delta^4$ $d_{NN} = 1.202(10)$ Å

XIII $\pi^{10}\delta^4$ $d_{NN} = 1.169(5)$ Å $\nu_{NN} = 1733$ cm^{-1}

Figure 4: The PNP-pincer supported N_2-bridged Mo (**XI**) and Re (**XII**; **XIII**) dinuclear complexes reported by *Schneider*.[36,70,71]

An additional fifth auxiliary ligand *trans* to the N_2-bridge does not effect the energetic order of the MOs with π- and δ-symmetry within the described MO-scheme (Scheme 8). It can therefore be used to rationalize the degree of N_2-activation in octahedrally coordinated N_2-bridged dinuclear complexes, like for the weakly activated $[(N_2)\{Ru(NH_3)_3\}_2]^{4+}$ ($\pi^{12}\delta^4$; $d_{NN} = 1.12$ Å; $\tilde{\nu}_{NN} = 2100$ cm^{-1}) or the strong activated $[\{(PhMe_2P)_4ClRe\}(N_2)\{MoCl_4(OMe)\}]$ ($\pi^8\delta^3$; $d_{NN} = 1.21$ Å; $\tilde{\nu}_{NN} = 1660$ cm^{-1}).[72,73] Nevertheless, the stability of such N_2-bridged dinuclear species with respect to N_2-cleavage is increased compared to the square pyramidal analogues. For example, features ^{i}Pr-substituted and octahedrally coordinated **XIII** (Figure 4) the same electron count and degree of N_2-activation as its ^{t}Bu-substituted analogue **XII**, but is thermally stable with respect to N_2 cleavage. A more detailed discussion about the influence of a ligand *trans* to the N_2-bridge regarding N_2-cleavage will be given in chapter 1.2.2.[71]

Upon usage of β-diketiminate (nacnac) ligands, several end-on N_2-bridged dinuclear complexes, bearing late transition metals (Fe, Co, Ni), have been reported.[74–79] Depending on the steric encumbrance of the nacnac-substituents, both {M(nacnac)}-moieties are either coplanar or perpendicular oriented, resulting in an idealized D_{2h}- or D_{2d}-symmetry, respectively. Furthermore, a distortion from linearity of the {M-N-N-M} is often found, indicating low bending potentials of the core within these type of compounds. The degree of N_2-activation can be rationalized using the MO-diagramm depicted in Scheme 9.

Assuming the x-axis to be oriented along the {M-N-N-M}-bond, linear combination of the d_{xy}- and d_{xz}-orbitals with the respective N_2-π-orbitals results in four sets of π-orbitals each set consisting of two degenerate orbitals. The remaining d_{yz}, d_{z^2} and $d_{x^2-y^2}$-orbitals form three sets of NN-non-bonding orbitals each consisting of two (nearly) degenerate orbitals, which are all located between the π_2- and π_3-level.[80] These considerations are in line with detailed spectroscopic and computational analysis of $[(N_2)\{Fe(nacnac^{tBu})\}_2]$ (**XIVa**), whose overall $S = 3$ ground state was rationalized by two high-spin Fe(II)-centers ($S = 2$), which are each antiferromagnetically coupled to the bridging N_2^{2-}-ligand ($S = 1$), leading to an overall {↑↑↑↑↓↓↑↑↑↑}-three-spin model.[75,80] Accordingly, the relative strong degree of N_2-activation within

XIVa and its Me-substituted congener $[(N_2)\{Fe(nacnac^{Me}\}_2]$ (**XVa**) (Table 2, entries 1 and 2) can be explained by a two electron transfer to the N_2-bridge and a $(\pi_1)^4(\pi_2)^4(d_{yz}/d_{z^2})^6(d_{x^2-y^2})^2(\pi_3)^2$-configuration with an overall π-electron count of ten.[74,75,80]

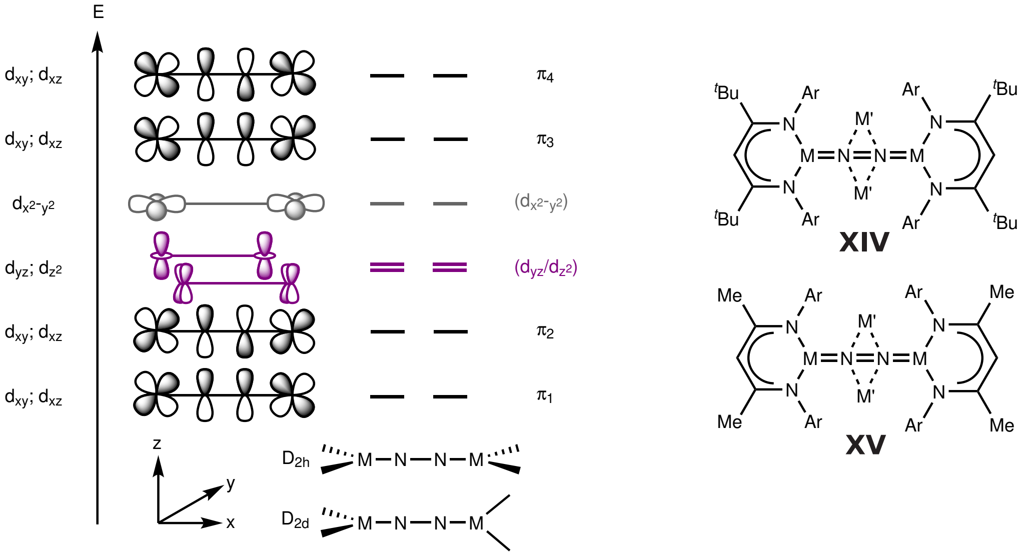

Scheme 9: *left:* Qualitative MO-diagramm for D_{2h}- or D_{2d}-symmetric end-on N_2-bridged dinuclear compounds.[80] *right:* Generalized structure of **XIV** and **XV**.

Further reduction is metal centered and leads to full occupation of the d_{yz}/d_{z^2}-orbitals. However, increased Fe→N2-backbonding leads to further weakening of the N_2-bond (Table 2, entries 3 and 4).[74,75] The same trend was observed for the group 9-congener (Table 2, entries 6 and 7). Compared to the Fe-analogue the degree of N_2-activation is smaller due to the lower energy of the d-orbitals, which is even more expressed for the Ni-analogue (Table 2, entry 8).[76,77]

Table 2: Comparison of the structural and electronic properties of several nacnac-supported N_2-bridged dinuclear compounds, $M_2'[(N_2)\{M(nacnac^R)\}_2]^X$, and their N_2-activation parameters.[74–77,79]

No	compound	M	R	M’	X	d_{yz}/d_{z^2}	$d_{x^2-y^2}$	d_{NN} [Å]	$\tilde{\nu}_{NN}$ [cm^{-1}]	ref.
1	**XIVa**	Fe	^{t}Bu	-	0	6	2	1.19	1778	75
2	**XVa**	Fe	Me	-	0	6	2	1.19	1810	74
3	**XIVb**	Fe	^{t}Bu	K	0	8	2	1.24	1589	75
4	**XVb**	Fe	Me	K	0	8	2	1.22	1625	74
5	**XVc**	Fe	Me	-	2-	8	2	1.19	1683	79
6	**XIVc**	Co	^{t}Bu	-	0	8	2	1.14	-	76
7	**XVd**	Co	^{t}Bu	K	0	8	4	1.22	1599	76
8	**XVe**	Ni	^{t}Bu	-	0	8	4	1.12	2164	77

The group of *Holland* was also able to abstract the potassium-cations from **XVb**. Thereby the N_2-bond grows short accompanied by a hypsochromic shift of the NN-stretching frequency, indicating a weaker activation in the absence of a counter-cation within the complex (Table 2, entry 5).[79] However, variation of the alkali-metal in **XVb** showed no significant changes in the degree of N_2-activation.[74,78] The only difference arises from the different size of the alkali-metal-ions, which leads to twisting and a larger torsion-angle between the {Fe(nacnac^{Me})}-moieties (Na = 0°; Cs = 50.6°).[78]
Notably, upon usage of a sterically less encumbered nacnac-ligand, $[MeC(CMeNC_6H_3\text{-}2,6\text{-}Me_2)_2]^-$, full cleavage of the NN-bond into tetra- or trinuclear bis-μ-nitride complexes was observed.[13,81]

Besides by the number of electrons and the coordination sphere of the metal centers the degree of N_2-activation is also influenced by the metal itself. This was demonstrated by the group of *Sita* for a series of group 4-6 N_2-bridged η^5-cyclopentadienyl/η^2-amidinate complexes **XVI** (Figure 5). Moving down within a group the degree of N_2-activation increases as indicated by significantly elongated NN-bond-distances (Table 3). This trend can be explained by the cathodic shift of the oxidation potentials of the metal ions and therefore increased backbonding from the metal to the N_2-ligand. Similarly, a correlation between the degree of activation and the oxidation potential of the respective metal was also found within a row.[82–85]
Notably, within group 4 the Ti-complex **XVIa** is the only one featuring a end-on bridging $\mu^2{:}\eta^1{:}\eta^1$-N_2-ligand, best described as N_2^{2-}. In contrast, both higher homologes, Zr (**XVIb**) and Hf (**XVIc**), feature a highly activated side-on bound $\mu^2{:}\eta^2{:}\eta^2$-N_2-ligand, which is best described as an N_2^{4-}-ligand. The higher degree of activation was assigned to the different oxidation potentials, which renders further oxidation of Ti(III) to Ti(IV), while the side-on coordination was attributed to the larger covalent radii of Zr and Hf (both 1.75 Å) compared to Ti (1.60 Å).[83,86]

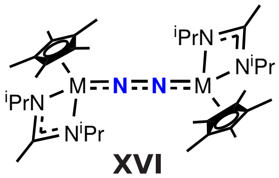

XVI

M = Ti, V, Nb, Ta, Mo, W

Figure 5: *Sita's* isostructural $[(N_2)(MCp^*am)_2]$ complexes (am = $[N(^iPr)C(Me)N(^iPr)]^-$).

Table 3: NN bond distances in the N_2-bridged η^5-cyclopentadienyl/η^2-amidinate complexes reported by *Sita*. [a]exchange of methyl group in amidinate with NMe_2. [b]exchange of methyl group in amidinate with phenyl.[82–85]

metal	coord. mode	d_{NN} [Å]	Ref.
Ti **XVIa**	$\mu^2{:}\eta^1{:}\eta^1$	1.270(2)	83
Zr[a] **XVIb**	$\mu^2{:}\eta^2{:}\eta^2$	1.518(2)	86
Hf **XVIc**	$\mu^2{:}\eta^2{:}\eta^2$	1.611(4)	86
V **XVId**	$\mu^2{:}\eta^1{:}\eta^1$	1.225(2)	84
Nb[b] **XVIe**	$\mu^2{:}\eta^1{:}\eta^1$	1.300(3)	84
Ta **XVIf**	$\mu^2{:}\eta^1{:}\eta^1$	1.313(4)	82
Mo **XVIg**	$\mu^2{:}\eta^1{:}\eta^1$	1.267(2)	83
W **XVIh**	$\mu^2{:}\eta^1{:}\eta^1$	1.277(8)	83

The group of *Chirik* illustrated the influence of the supporting ligands based on a redox-series of overall five end-on N_2-bridged terpyridine supported dinuclear Mo-complexes, $[(N_2)\{Mo(Tpy^{Ph})(PMe_2Ph)_2\}]^{n+}$ (**XVII**$^{n+}$; n = 0-4; Typ^{Ph} = 4’-Ph-2,2’,6,6’2”-terpyridine) (Figure 6, *left*). Computional analysis describe dicationic **XVII**$^{2+}$ as two Mo(II)-ions bridged by an N_2^{2-}-ligand, which is in good agreement with the observed NN-stretching frequency ($\tilde{\nu}_{NN}$ = 1563 cm^{-1}) and NN-bond length (d_{NN} = 1.203(2) Å). Due to mixing with the π-system of the terpyridine ligand, the degeneracy of the M$\overset{\pi^*}{-}$N$\overset{\pi}{-}$N$\overset{\pi^*}{-}$M orbitals is lifted, which results in a singlet ground state for **XVII**$^{2+}$. Accordingly, due to removal of an electron from an NN-bonding orbital, oxidation of **XVII**$^{2+}$ to **XVII**$^{3+}$ results in a significant increase of the degree of N_2-activation ($\tilde{\nu}_{NN}$ = 1482 cm^{-1}). Interestingly, the double oxidation product **XVII**$^{4+}$ features an almost identical NN-stretching frequency ($\tilde{\nu}_{NN}$ = 1477 cm^{-1}), which was rationalized by removal of an electron from a metal centered b_{1u}-orbital in agreement with the observed triplet ground state for **XVII**$^{4+}$. Intriguingly, reduction of **XVII**$^{2+}$ also leads in weakening of the NN-bond, which was substantiated by the mainly Typ^{Ph}-π^*-character of its LUMO ($2b_{2g}$) and therefore mostly ligand-centered reduction in line with EPR measurements of **XVII**$^{+}$ (Figure 6, *right*).[87]

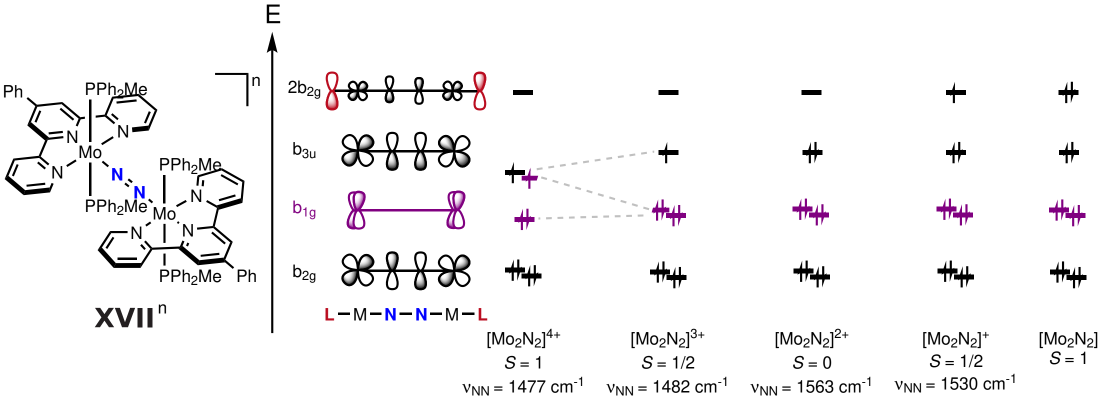

Figure 6: *left: Chirik*’s terpyridine supported Mo-N_2-dimer redox series **XVII**$^{n+}$ (n = 0-4). *right:* Qualitative FMO scheme of the redox series and the corresponding spin states and NN stretching frequencies.[87]

1.1.3 Side-on bridging N_2

Another, but much less common, binding motif of N_2 is the side-on (μ^2:η^2:η^2-N_2) coordination mode (Figure 1, **C**).[28,59,88] First evidence for such a binding mode originate from linkage isomerization studies of $[\{(NH_3)_5Ru\}(^{14/15}N_2)]^{2+}$, which are too fast to occur from initial N_2-dissoziation.[37] In 1973 the first structurally characterized side-on bridging N_2-complex was published.[89,90] Since than various other examples bearing a side-on bridging N_2 ligand have been reported, especially for early transition metals and f-block elements.[18,91–97]

Side-on bridging of N_2 is more complex compared to end-on coordination and often leads to distortion of the $\{M_2N_2\}$-core from planarity. Similar to the already described end-on bridging mode, the molecular orbitals for the side-on bridging mode can be derived from linear combination of the π-MOs of the N_2 ligand with metal d-orbitals of appropriate symmetry.

Assuming a D_{2h}-symmetry with the z-axis oriented along the M-M axis the d_{z^2} and $d_{x^2-y^2}$-orbitals are used for σ-bonding with the ligands of the ML_4-fragment and with the N_2 ligand. Linear combination of the d_{yz}-orbitals with the respective π^*_h-orbital of the N_2 ligand results in formation of two MOs with π-symmetry (Scheme 10, *black*). The d_{xy}-orbitals form together with the π^*_v-orbital of the N_2 ligand two MOs with δ-symmetry (Scheme 10, *purple*), while the remaining d_{xy}-orbitals are non-bonding because of the lack of N_2-MOs with suitable symmetry (Scheme 10, *grey*).[59]

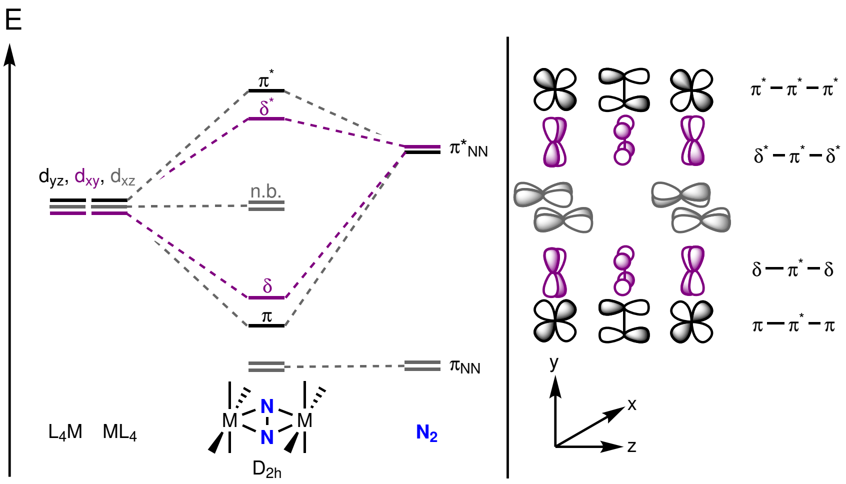

Scheme 10: Qualitative Molecular Orbital scheme for D_{2h}-symmetric side-on N_2-bridged dinuclear species. The symmetry of the resulting molecular orbitals (MOs) is indicated by the color with black π-, purple δ-symmetry.[59]

Overall, the weaker orbital overlap of the δ- compared to the π-interactions should result in a energetic preference for end-on coordination. The formation of side-on bridging N_2 ligands can be explained by the absence of an accessible d-orbital suitable to from a second π-bond. This was demonstrated by *Fryzuk* and coworkers with an pincer supported Zr-N_2-complex $[(N_2)\{Zr(X)N(SiMe_2CH_2P^iPr_2)_2\}_2]$ (**XVIII**). The chloro-substituted ($X = Cl^-$, **XVIIIa**) features a side-on bridging N_2 ligand, while the Cp^--substituted ($X = Cp^-$, **XVIIIb**) undergoes linkage isomerization to an end-on bridging N_2 ligand (Scheme 11). The side-on coordination in **XVIIIa** originates from strong interaction of the PNP-amide π- and the chloride σ-orbital with the d_{yz}-orbital. Therefore, this orbital is raised in energy and too high to form a π-bond with the N_2 ligand, which results in δ-bonding between the d_{xy}- and the π_v^*-orbital to stabilize the system. Exchange of the chloro ligand with Cp^- changes the energetic order of the d-orbitals. The d_{yz}-orbital drops in energy and becomes available for π-bonding. On the other hand the energy of the d_{xy}-orbital required for δ-bonding is lifted, due to strong interaction with the Cp^- ligand. The overlap of the PNP-amide *p*-orbital is also decreased since the appropriate d-orbital is involved in π-bonding with the N_2 ligand, which leads to significant lengthening of the Zr-N^{PNP} bond.[59]

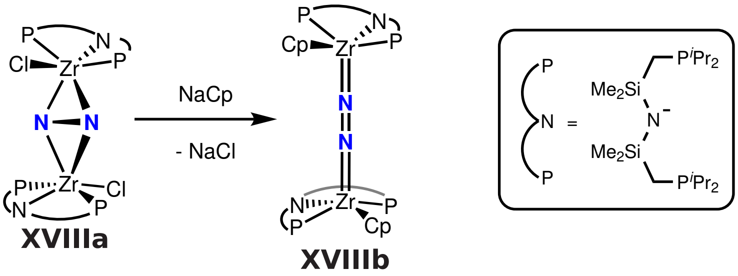

Scheme 11: Linkage isomerization from side-on to end-on by exchange of Cl^- *vs.* Cp^-.[59]

Since both metal centers are in much closer proximity, compared to the end-on bridging mode, the steric shielding of the metal centers plays another important role in the formation of side-on bridging N_2 complexes. Notably, the size of the metal ion itself can also influence coordination mode, as shown by the already mentioned N_2-bridged η^5-cyclopentadienyl/η^2-amidinate complexes **XVI** by *Sita* (Figure 5). Within group 4, end-on coordination of the bridging N_2-ligand was only found for the Ti-complex **XVIa**, while both higher homologues, Zr (**XVIb**) and Hf (**XVIc**), feature a side-on bridging N_2-ligand (Table 3), which was attributed to the larger covalent radii of Zr and Hf (both ~1.75 Å) compared to Ti (1.60 Å).[83,86]

Furthermore, the series of differently substituted zirconocenes (**XIX**, Figure 7) by *Chirik* and *Bercaw* demonstrates how the steric encumbrance of the auxiliary ligands can dictate the coordination mode of the bridging N_2-unit, with bulky substituents prefering the formation of an end-on bridging mode.[98–101]

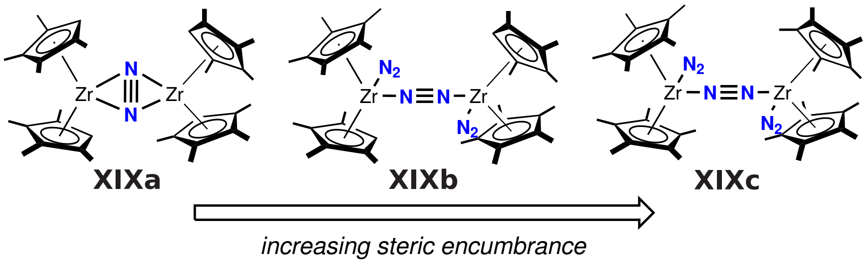
Zr
N
N
Zr
N2
Zr
N≡N
Zr
N2
XIXa
XIXb
XIXc
increasing steric encumbrance

Figure 7: Increased steric shielding of the supporting ligands results in linkage isomerization from side-on to end-on.[98–101]

Notably, the reactivity of the compounds changes depending on the coordination mode of the bridging N_2 ligand. Reaction of side-on coordinated **XIXa** with 1 atm of H_2 results in formation of the zirconocene hydrazido complex $[(\mu\text{-}N_2H_2)\{Zr(H)Cp'_2\}_2]$ (**XX**), which upon heating under H_2-atmosphere releases NH_3 giving bishydride $[Zr(H)_2Cp'_2]$ (**XXIa**). Heating of **XX** in the absence of H_2 yields in cleavage of the NN-bond and formation of $[(\mu\text{-}N)(\mu\text{-}NH_2)\{ZrCp'_2\}_2]$ (**XXII**) (Scheme 12). In contrast, reaction of end-on bridged **XIXb** with H_2 leads to loss of the bridging N_2 ligand and formation of a bishydride-complex $[Zr(H)_2Cp^*C']$ (**XXIb**).[101,102]

Similar hydrogenation behavior to **XIXa** was also reported for other complexes bearing a side-on bound N_2-moiety.[86,103] Furthermore, computational studies imply, that side-on binding is essential for N_2-hydrogenation.[104]

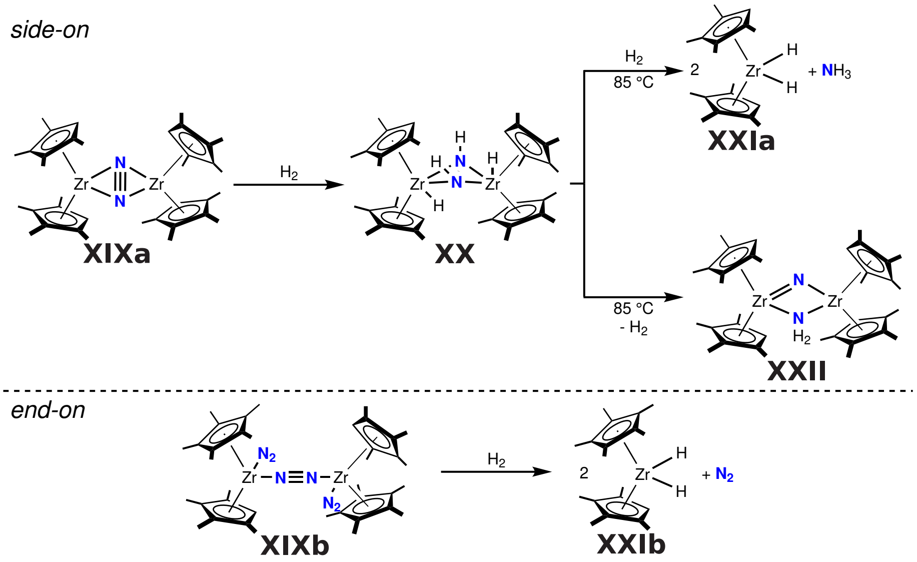
side-on
end-on
Zr
N
N
Zr
XIXa
H2
H
H
N
H
N
H
Zr
Zr
XX
H2
85 °C
2
Zr
H
H
+ NH3
XXIa
85 °C
- H2
Zr
N
N
H2
Zr
XXII
N2
Zr
N≡N
Zr
N2
XIXb
H2
2
Zr
H
H
+ N2
XXIb

Scheme 12: Different reactivity upon reaction with H_2 depending on the coordination mode of the bridging N_2-ligand.[101,102]

Besides hydrogenation, (partial) N_2-cleavage under the formation of N-E-bonds (E = B, C, Si) has also been reported.[86,103,105–109] In this respect, the group of *Chirik* presented the full cleavage of side-on bound N_2 ligand upon addition of CO to a *ansa*-hafnocene-complex (**XXIII**) (Scheme 13). The first equivalent of CO is proposed to insert into the Hf-N bond. After a retro [2+2]-cycloaddition cyanate (NCO^-) as well as a reactive vacant coordination site are formed (**XXIV**). This vacant coordination site undergoes intramolecular C-H activation (**XXIVa**), which can be prevented upon addition of a suitable substrate such as H_2 (**XXIVb**). Remarkably, addition of excess CO to **XXIII** results in C-C-bond formation and the oxamidide complex (**XXIVc**). Acidic work-up of **XXIVc** releases oxamide ($H_2NC(O)-C(O)NH_2$).[107,108,110]

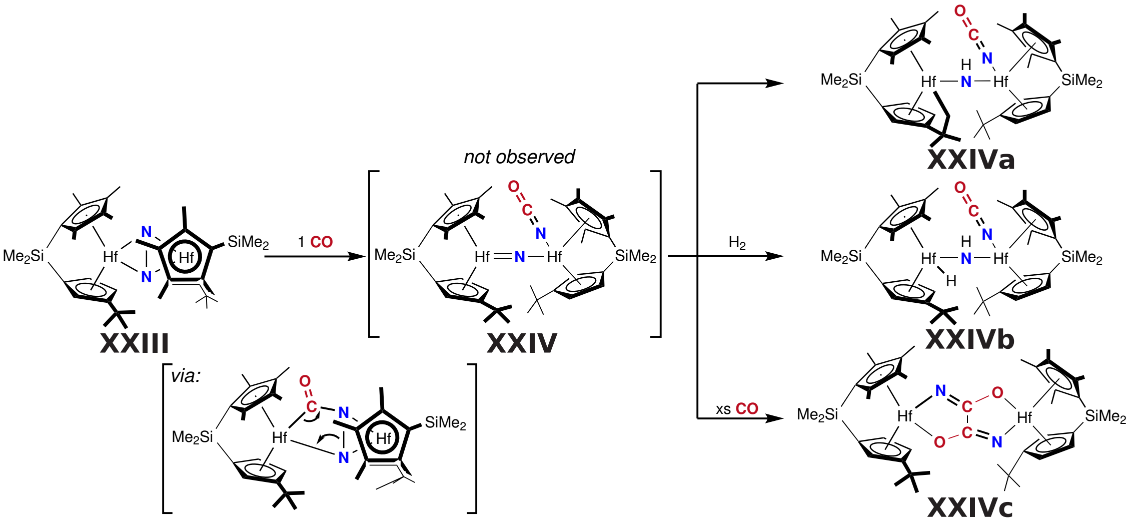
Me2Si
Hf
N
N
Hf
SiMe2
XXIII
1 CO
not observed
Me2Si
Hf=N—Hf
O
C
N
SiMe2
XXIV
via:
Me2Si
Hf
O
C
N
N
Hf
SiMe2
H2
xs CO
Me2Si
Hf—N—Hf
H
SiMe2
XXIVa
XXIVb
Me2Si
Hf
N
C
O
O
C
N
Hf
SiMe2
XXIVc

Scheme 13: NN-bond cleavage upon addition of CO to a side-on N_2-bridged *ansa*-hafnocene-complex **XXIII**.[107,108,110]

1.2 N_2-Functionalization

1.2.1 Ammonia Formation

Even though, N_2 is a very stable and inert molecule, there are some conversions, which are thermodynamically feasible. The most prominent example is the conversion into ammonia.[28]

$$N_{2(g)} + 3\,H_{2(g)} \longrightarrow 2NH_{3(g)} \qquad \Delta H° = -46.2\ kJ \cdot mol^{-1} \tag{1.1}$$

In nature, this transformation is done at ambient temperature and pressure by three different so-called nitrogenase enzymes, which differ in the composition of their active sites. The most common one, the {FeMo}, employs an iron-molybdenum-sulfur cluster {7Fe-9S-Mo-C-homocitrate} as the active site (Scheme 14), while in the two other less common ones, {FeV} and {Fe-only}, the Mo is replaced by V or Fe, respectively. Under optimal conditions, N_2 is transformed into 2 equiv. NH_3 in a $6H^+/6e^-$ process under the consumption of overall 16 ATP, which underlines the high energy demand to overcome the kinetic barrier for N_2-fixation. Furthermore, two additional electrons and protons are required for reductive activation of the FeMo-cofactor and initial N_2-binding under the release of one equivalent of H_2.[28,29]

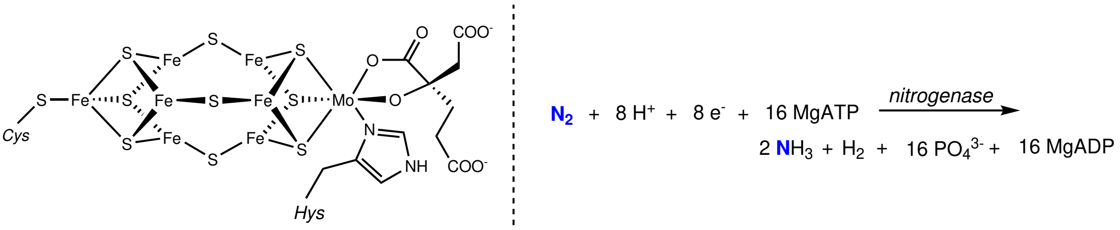

Scheme 14: *left:* Schematic of the FeMo-cofactor of the {FeMo}-nitrogenase. *right:* Overall reaction for the transformation of N_2 into NH_3 mediated by the {FeMo}-nitrogenase.[28,29]

Inspired by this, many transition metal catalysts have been developed that are capable for ammonia production upon addition of electrons and protons. Their mechanisms are often not fully understood and/or under current investigation. Two distinct different pathways are proposed, either (similar to the mechanism of the *Haber-Bosch-process*) *via* initial cleavage of the NN-bond under formation of a metal-nitride (see chapter 1.2.2) or *via* successive reduction/protonation of the N_2-moiety mimicking the reactivity of the nitrogenase.

The first stoichiometric examples for these type of mechanism date back to reports by *Chatt*, who first reported the formation of diazine (N_2H_2) upon protonation of *trans*-[$M(N_2)_2(dppe)_2$] (M = Mo or W; dppe = $Ph_2PCH_2CH_2PPh_2$) and later the almost quantitative formation of NH_3 upon protonation of *cis*-[$M(N_2)_2(PMe_2Ph)_4$] (M = Mo or W). These discoveries lead to the postulation of the so-called *Chatt-cycle* (Chapter 1, Scheme 1), which is also proposed to be the actual mechanism for ammonia formation within the {FeMo}-nitrogenase.[7,111–114]

In 2003, *Schrock* reported the first example for catalytic reduction of N_2 to ammonia using a single site molybdenum catalyst supported by a tetradentate $[HIPTN_3N]^{3-}$ triamidoamine ligand ($[\{3,5\text{-}(2,4,6\text{-}iPr_3C_6H_2)_2C_6H_3NCH_2CH_2\}_3N]^{3-}$; **XXV**) (Scheme 15), whose sterically demanding ligands prevent the formation of N_2-bridged-dinuclear complexes.[8]

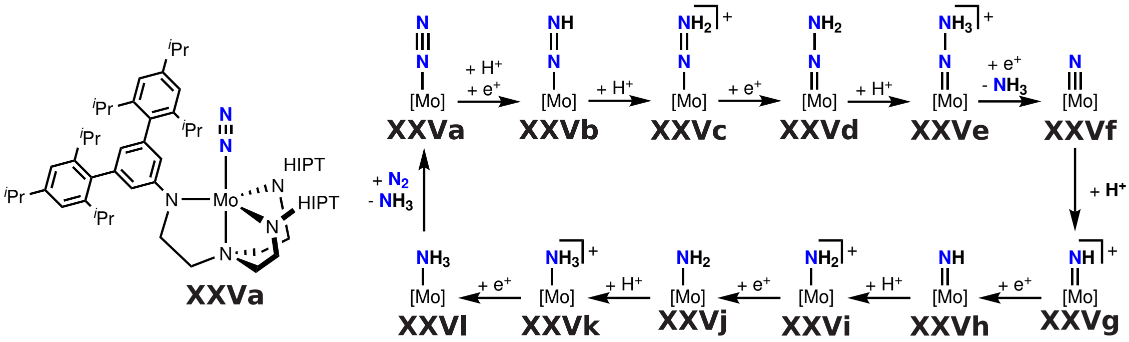

Scheme 15: *left:* Structure of [(N_2)-Mo($HIPTN_3N$)] (**XXVa**). *right:* Proposed mechanism for the catalytic formation of NH_3 upon successive protonation/reduction of **XXVa** (*Schrock-cycle*).[8]

Usage of [LutH][BAr^F_{24}] ([LutH] = 2,6-lutidinium, $[2,6\text{-}Me_2C_5H_3NH]^+$; [$BAr^F_{24}$] = $[B(3,5\text{-}(CF_3)_2\text{-}C_6H_3)_4]^-$) as proton source and $CrCp^*_2$ as reductant gives ammonia in 66% yield (relative to the reductant) in four turn-overs. It was also possible to prepare and characterize several intermediates (**XXVa**, **XXVb**, **XXVc**, **XXVf**, **XXVg**, **XXVk**, **XXVl**) and therefore postulate the so-called *Schrock-cycle* (Scheme 15), which is in agreement with the *Chatt-cycle* (Chapter 1, Scheme 1), although favoring a distal pathway.[8,115]

The nature of the used acid has a large influence on the catalytic activity and can even inhibit ammonia-formation at all. For example, usage of $[2,6\text{-}Et_2C_5H_3NH]^+$ gives only 23% of ammonia, while with $[2,6\text{-}Ph_2C_5H_3NH]^+$ or $[3,5\text{-}Me_2C_5H_3NH]^+$ no ammonia is obtained. This effect is attributed to the steric hindrance of the [$HIPTN_3N$]-ligand preventing the acid from protonation at the N_yH_x-moiety. Too little steric hindrance can lead to side reactions, like proton-reduction, and/or lower the soluablity of the acid in unpolar solvents.[115–117]

The group of *Schrock* also prepared the other two group 6 as well as the V-congener of [Mo(HIPTN$_3$N)] (**XXV**), all showing no catalytic activity in nitrogen reduction to ammonia, although due to different reasons.
Binding of N_2 to the Cr-analogue, [Cr(HIPTN$_3$N)], was not observed, most likely due to its high-spin character and the anodic shifted reduction potential of Cr(III) compared to Mo(III).[118] In contrast, the W-analogue [(N$_2$)W(HIPTN$_3$N)] and several other W-analogues of the proposed intermediates within the *Schrock-cycle* could be prepared. Although most of these intermediates show less stability compared to their Mo-congeners, the first half of the catalytic cycle, the transformation of [(N$_2$)W(HIPTN$_3$N)] into [N≡W(HIPTN$_3$N)] and NH_3, could be achieved. Catalytic turn-over is believed to be suppressed by the last steps within the cycle. Reduction of [(H$_3$N)W(HIPTN$_3$N)]$^+$ even with two equivalents of $CoCp^*_2$ does not result in full conversion to [(H$_3$N)W(HIPTN$_3$N)], which also does not exchange its NH_3 ligand with N_2.[119] The reason for the lack of catalytic turn-over with the V-congener are attributed to one less overall charge of each intermediate.[120] Overall, these studies illustrate, how certain parameters, like acid-size and -strength, redox-potentials and overall charge, can have a large impact on the catalytic activity of such systems.

Using a structurally related ligand framework, the group of *Peters* presented a single-site Fe-TPB-complex, [Fe(TBP)]$^+$ (TBP = tris(phosphine)borane; **XXVIa**; Scheme 16, *left*), capable for the reduction of N_2 into ammonia.[10]

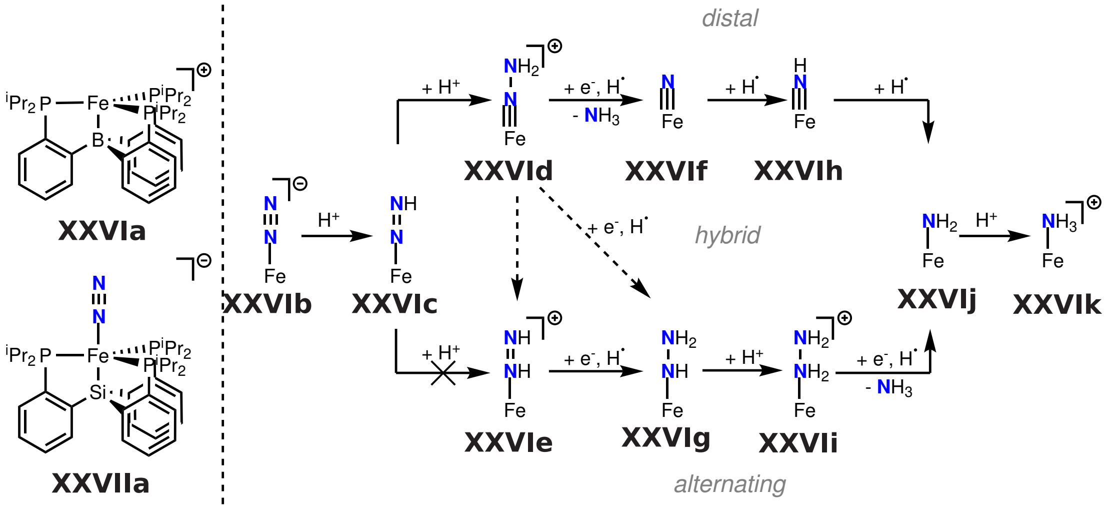

Scheme 16: *left:* Structures of [Fe(TBP)]$^-$ (**XXVIa**) and [(N$_2$)-Fe(SiP$^{iPr}_3$)]$^-$ (**XXVIIa**). *right:* Proposed mechanistic pathways for the transformation of **XXVIb** into **XXVIk** *via* **XXVId**, either *via* an distal (top) or alternating (bottom) pathway. The dotted arrows illustrate a hybrid pathway between distal and alternating.[121]

Mechanistic studies showed that the initial protonation of $[(N_2)Fe(TBP)]^-$ (**XXVIb**) gives [(HNN)Fe(TBP)] (**XXVIc**), followed by a second protonation of the β-nitrogen to give $[(H_2NN)Fe(TBP)]^+$ (**XXVId**), hinting towards a distal mechanism, which is supported by the characterization the terminal Fe(IV)-nitride $[(N{\equiv}Fe(TBP)]^+$ (**XXVIf**; see also chapter 1.3).[121–123]
However, the mechanistic scenario changes if a more rigid ligand is used. Double protonation of isostructural $[(N_2)Fe(SiP_3^{iPr})]^-$ (SiP_3^{iPr} = tris(2-(diisopropylphosphino) phenyl)silyl$^-$; **XXVIIa**), in which the linking borane is exchanged with silyl, gives rise to the structurally characterized $[(H_2NN)Fe(SiP_3^{iPr})]^+$ (**XXVIIb**), in line with a distal pathway. Notably, **XXVIIb** disproportionates with its neutral, one electron reduced congener $[(H_2NN)Fe(SiP_3^{iPr})]$ (**XXVIIc**) to give $[(N_2)Fe(SiP_3^{iPr})]$ (**XXVIId**) and $[(H_2NH_2N)Fe(SiP_3^{iPr})]^+$ (**XXVIIe**), a typical intermediate within a alternating pathway, which was rationalized with a hybrid mechanism. The different mechanistic pathways are attributed to the high rigidity of the silyl-bridge, which does not allow the formation of an tetrahedrally coordinated Fe(IV)-nitride.[123,124]

In the first reports for catalytic ammonia formation using **XXVIb** as catalyst $[H(OEt_2)_2][BAr^F_{24}]$ (p$K_a \approx 0$) and KC_8 ($E° \leq$ -3.0 V vs. Fc^+/Fc) were used as proton- and electron-source, respectively. In this way up to 7.0 equivalents of ammonia (per Fe) could be obtained.[10] Later, it was discovered that metallocene based reductands can be protonated and that these protonated species feature low CH-bond dissoziation energies (BDE's) (*endo/exo*-$[CoCp^*(\eta^4\text{-}C_5Me_5H)]^+ = 31$ kcal·mol^{-1}; *endo*-$[CrCp^*(\eta^4\text{-}C_5Me_5H)]^+ = 37$ kcal·mol^{-1}; *exo*-$[CrCp^*(\eta^4\text{-}C_5Me_5H)]^+ = 30$ kcal·mol^{-1}) making them potential proton-coupled-electron-transfer (PCET) reagents. In this way, the selectivity over competitive H_2-evolution (due to proton reduction) and the yield of ammonia could be increased, even though the overall driving force was lowered due to usage of a weaker reductant ($CoCp^*_2$, $E° \leq$ -1.96 V vs. Fc^+/Fc) and acid ($[Ph_2NH_2]OTf$, p$K_a = 3.2$).[125]
Additionally, different anilinium acids over a wide pK_a-range were tested revealing a correlation of the selectivity between N_2-reduction (NRR) and H_2-evolution (HER) with the pK_a of the used acid (Figure 8). The weakest acid ($[^{4-OMe}PhNH_3][OTf]$, p$K_a = 8.8$) was found to be inactive in the formation of NH_3, while slightly stronger acids ($[PhNH_3][OTf]$, p$K_a = 7.8$; $[^{2.6-Me}PhNH_3][OTf]$, p$K_a = 6.8$ or $[^{2-Cl}PhNH_3][OTf]$, p$K_a = 5.6$) showed an increase of the selectivity for NH_3 by lowering the pK_a. The selectivity and yield for ammonia with even stronger acids ($[^{2.5-Cl}PhNH_3][OTf]$, p$K_a = 4.3$; $[^{2.6-Cl}PhNH_3][OTf]$, p$K_a = 3.4$ or $[^{2.4.6-Cl}PhNH_3][OTf]$, p$K_a = 2.1$) is high and almost independent to the acid strength within this range. Notably, the yield and selectivity for ammonia drops again for the strongest acid within this study ($[^{per-Cl}PhNH_3][OTf]$, p$K_a = 1.3$), which was explained by an outer sphere electron transfer (ET), that is preferred over a potential protonation of the $CoCp^*_2$.[126]

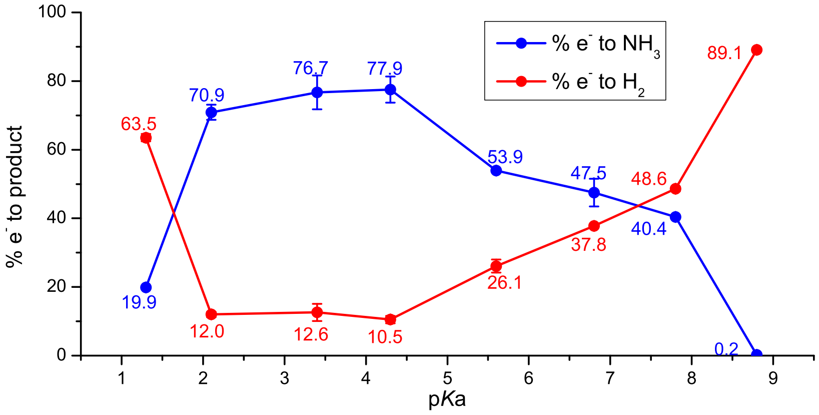

Figure 8: pK_a-dependence of the selectivity between N_2-reduction (NRR, blue) and H_2-evolution (HER, blue) of **XXVIa**.[126]

For all other acids a competitive branch within their postulated mechanism for NH_3-formation, which can lead to H_2-evolution, is postulated (Scheme 17). Hence, initially formed $[(NN)Fe(TBP)]^-$ (**XXVIb**) is protonated once to give very unstable, neutral [(HNN)Fe(TBP)] (**XXVIc**). In the absence of another proton (due to bad solubility of the acid) to form more stable $[(H_2NN)Fe(TBP)]^+$ (**XXVId**), **XXVIc** reacts bimolecularly to give H_2 and [(NN)Fe(TBP)] (**XXVII**) (Scheme 17, *bottom*). Accordingly, addition of only one equivalent of acid to **XXVIb** results exclusively in H_2-evolution. Furthermore, usage of excess $[^{2.6-Cl}PhNH_3]^+$ to **XXVIb** results depending on the anion and solubility of the acid in different products. While upon protonation with excess of good soluble $[^{2.6-Cl}PhNH_3][BAr^F_{24}]$ **XXVId** and fixed-*N*-products could be detected, such species are absent with badly soluble $[^{2.6-Cl}PhNH_3][OTf]$. However, these findings are in contradiction to the observed high yields of ammonia with $[^{2.6-Cl}PhNH_3][OTf]$ under catalytic conditions in the presence of $CoCp^*_2$ (13.8±0.9 equiv. NH_3/Fe, Figure 8) implying that the $CoCp^*_2$ or its protonated form, $[CoCp^*(\eta^4\text{-}C_5Me_5H)]^+$, are involved in the formation of NH-bonds.[126]

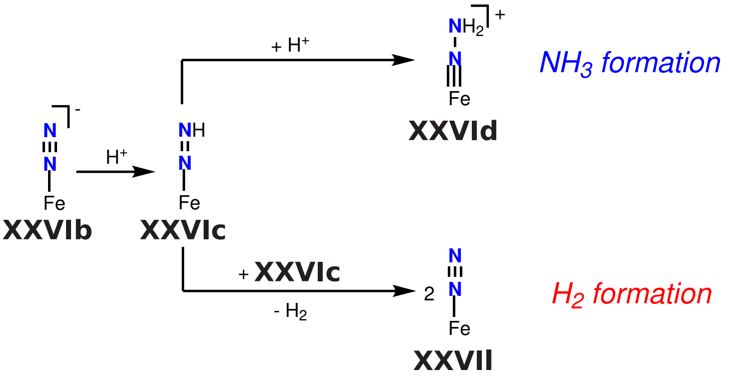

Scheme 17: Possible reactions of **XXVIc**, either leading to NH_3 formation or to H_2 formation.[126]

Another example for the influence of the anion on the selectivity, either giving H_2 or NH_3, was reported by the group of *Nishibayashi* using molybdenum supported by a pyridine based PNP-pincer ligand (**XXVIII**). Reduction of the Mo(III) precursor, $[MoX_3(^{pyr}PNP)]$ (**XXVIIIa**, X = Cl, Br, I), in the presence of N_2 results in the formation of end-on N_2 bridged dinuclear **XXVIIIb** (Scheme 18).[9]

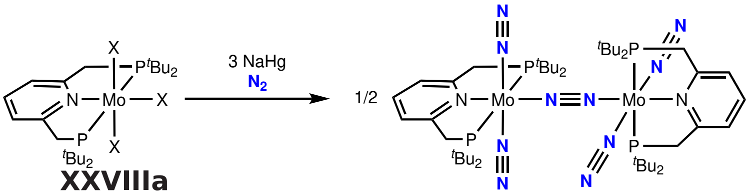

XXVIIIa **XXVIIIb**

Scheme 18: *left*: Reduction of **XXVIII** results in the formation of end-on N_2 bridged **XXVIIIb**. *right*: A proposed key intermediate within the catalytic formation of NH_3.[9]

XXVIIIb is capable for the catalytic formation of ammonia in the presence of a reductant and a proton source. Upon variation of the acid, while keeping the reductant ($CoCp_2$) constant, a large influence of the acid on the activity (equiv.(NH_3+H_2) per catalyst) and selectivity (NH_3/H_2) was observed. Similar to the report of *Peters* an influence of the pK_a was found, although without any clear trend. The strongest used acid (HOTf, Table 4, entry 1) features only low activity, but with a relatively high selectivity for ammonia. Upon usage of weaker acids, [pyrH]OTf, [2-picH]OTf or [LutH]OTf (Table 4, entries 2-4), the selectivity for NH_3 drops, while the overall activity is increased.[9]

Notably, both selectivity and activity are not only depending on the acid strength, but also on the corresponding acid-anion, as demonstrated upon usage of different lutidinium salts (Table 4, entries 4-6). Within this series, [LutH][BAr^F_{24}] provides the lowest preference for ammonia, although the overall activity is high. Compared to that, [LutH]OTf gives a slightly increased overall activity with a almost equal amounts of NH_3 and H_2. The highest NH_3 to H_2 ratio was found upon usage of [LutH]Cl. Nevertheless, the overall activity is the lowest of all used acids within this study.[9]

Table 4: Acid influence on the selectivity (NH_3/H_2) and activity (equiv.(NH_3+H_2) per catalyst) upon usage of **XXVIIIb** under catalytic conditions. (pyr = pyridine, 2-pic = 2-methyl pyridine, Lut = 2.6-dimethyl pyridine).[9]

$$N_2 + CoCp_2 + HX \xrightarrow[\text{tol, r.t.}]{\text{cat.}} NH_3 + H_2$$

entry	HX	pK_a(in MeCN)	NH_3 / H_2	NH_3 + H_2 [mol. equiv. / cat.]
1	HOTf	2.6	1.55	2.8
2	[pyrH]OTf	12.6	0.19	24.3
3	[2−picH]OTf	13.9	0.55	25.7
4	[LutH]OTf	14.4	0.88	25.2
5	[LutH][BAr^F_{24}]	14.4	0.14	21.7
6	[LutH]Cl	14.4	7.0	0.8

Similar to the reports by *Peters*, a huge increase of the catalytic activity was observed upon usage of PCET-reagents. But instead of protonated metallocenes the group of *Nishibayashi* utilized a combination of SmI_2 and alcohols or water, which feature low OH-bond strengths due to coordination to the Sm(II)-center. For example, the OH-bond strength of free water (111 kcal·mol^{-1}) drops in $[Sm(OH_2)_n]^{2+}_{(aq)}$ to only 26 kcal·mol^{-1}.[127] In this way the group of *Nishibayashi* was able to increase the yield of ammonia up to 42.8 equiv. (per **XXVIIIa**). The yield was even more increased upon usage of a related carbene supported catalyst, $[MoCl_3(^{carb}PCP)]$ (**XXIX**, Scheme 19, *left*). Together with a combination of SmI_2 and H_2O (both 14400 equiv. based on **XXIX**) 4350 equiv. of ammonia together with only 150 equiv. of H_2 (per **XXIX**) could be obtained, which sets today's record for the most effective homogeneous catalyst for ammonia formation from N_2.[19]

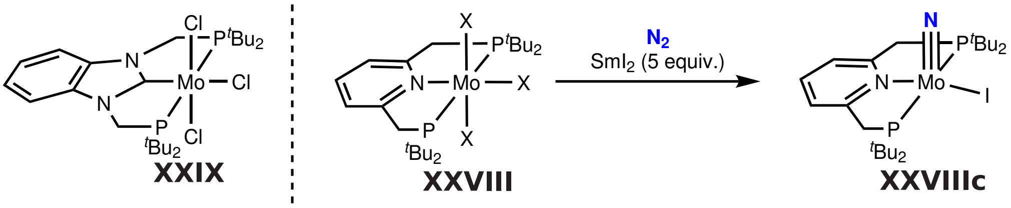

Scheme 19: *left*: *Nishibayashi's* $[MoCl_3(^{carb}PCP)]$ (**XXIX**) complex. *right*: Reduction of $[MoX_3(^{pyr}PNP)]$ **XXVIII** with SmI_2 results in N_2-cleavage and formation of $[Mo(N)I(^{pyr}PNP)]$ **XXVIIIc**.[19]

The catalytic cycle is not fully understood, but two distinct different pathways have been discussed. Early studies of **XXVIII** proposed a distal mechanism, similar to the ones already discussed, in which a thermally bound N_2-moiety is successively protonated and reduced to give the corresponding nitride (**XXVIIIc**) and one equivalent NH_3. Further protonation and reduction gives a second equivalent of NH_3 and closes the cycle upon N_2-binding (Scheme 20, *left*).[9,128,129]

Novel studies demonstrated that reduction of [MoI$_3$(^{pyr}PNP)] (**XXVIIId**) in the presence of N_2 results in N_2-cleavage and formation of [Mo(N)I(^{pyr}PNP)] (**XXVIIIc**). These findings lead to the formulation of an alternative, *Haber-Bosch*-type, mechanism in which the bridging N_2 ligand is initially cleaved followed by successive protonation and reduction of the formed nitride to give ammonia (Scheme 20, *right*).[19,130]

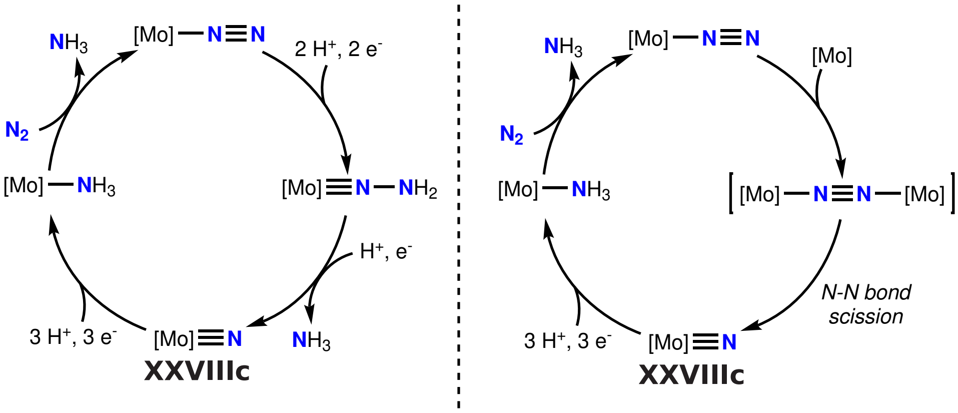
NH3
[Mo]—N≡N
2 H+, 2 e-
N2
[Mo]—NH3
[Mo]≡N—NH2
H+, e-
3 H+, 3 e-
[Mo]≡N
NH3
XXVIIIc
NH3
[Mo]—N≡N
[Mo]
N2
[Mo]—NH3
[[Mo]—N≡N—[Mo]]
N-N bond scission
3 H+, 3 e-
[Mo]≡N
XXVIIIc

Scheme 20: *left:* The proposed distal mechanism for N_2-fixation.[9,128,129] *right*: The proposed mechanism for N_2-fixation *via* NN-bond cleavage.[130]

Besides its potential role within catalytic ammonia formation, dinitrogen splitting into molecular nitrides holds also the promise of direct incorporation of N_2 into organic molecules. Even though, metal nitrides are well known compounds and their reactivity has been widely studied, their direct synthesis from N_2 remains a challenging task, which will be discussed in the next chapter.[131]

1.2.2 Thermal N_2-cleavage into terminal nitrides

Splitting of dinitrogen into terminal molecular nitrides typically occurs *via* formation of end-on bridged dinuclear complexes. The first example for such a reaction was presented by *Cummins* in 1996. Reaction of $[Mo(N(R)Ar)_3]$ (R = ^{t}Bu; Ar = 3,5-$C_6H_3Me_2$, **XXX**) with N_2 at low temperatures gives the already mentioned end-on N_2-bridged $[(N_2)\{Mo(N(R)Ar)_3\}_2]$ (**I**). Upon warming to r.t. the NN-bond is cleaved to give the respective Mo(VI)-nitride $[Mo(N)(N(R)Ar)_3]$ (**XXXI**) in almost quantitative yield (Scheme 21).[12] Counterintuitively, even though the mono- and dioxidized analogues, **II** and **III**, are more activated, they are both stable with respect to N_2-cleavage due to the lack of electrons to form stable Mo(VI)-nitrides.[60,61]

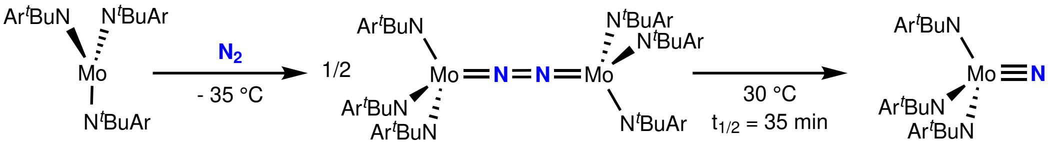

XXX **I** **XXXI**

Scheme 21: The first example for N_2-cleavage reported by *Cummins*.[12]

Further rationalization of the N_2-splitting process can be achieved by comparing the electronic configurations of the N_2-bridged species with the ones of the respective nitrides (Scheme 22). As already described in chapter 1.1.2, the molecular orbitals of end-on N_2-bridged dinuclear complexes can be obtained by linear combination of the metal d-orbitals and nitrogen p-orbitals. In case of *Cummins'* S_6-symmetric **I** this results in a π^{10}-configuration and a triplet ground state (Scheme 22, *left*). In comparison, the formed nitrides are diamagnetic with eight electrons populating the π-manifold. Furthermore the former $\{\sigma\text{-}\sigma^*\text{-}\sigma\}$-orbital ($a_u$) drops in energy, becomes populated and forms the σ-bond of the nitride moiety (Scheme 22, *right*). Accordingly, N_2-splitting occurs *via* electron transfer from a π- into a σ-bonding framework. Since such an electron transfer should be symmetry forbidden, breakage of the NN-bond cannot occur on a linear trajectory. Instead distortion to a C_{2h}-symmetric *zig-zag*-transition state should lift the degeneracy of the orbital sets and enable σ/π-transfer by avoided crossing.[60,132]

These consideration are supported by computational analysis by *Morokuma* using truncated $[(N_2)\{Mo(NH_3)_3\}_2]$, which characterize the *zig-zag*-transition state as a singlet with NN-single-bond character.[132]

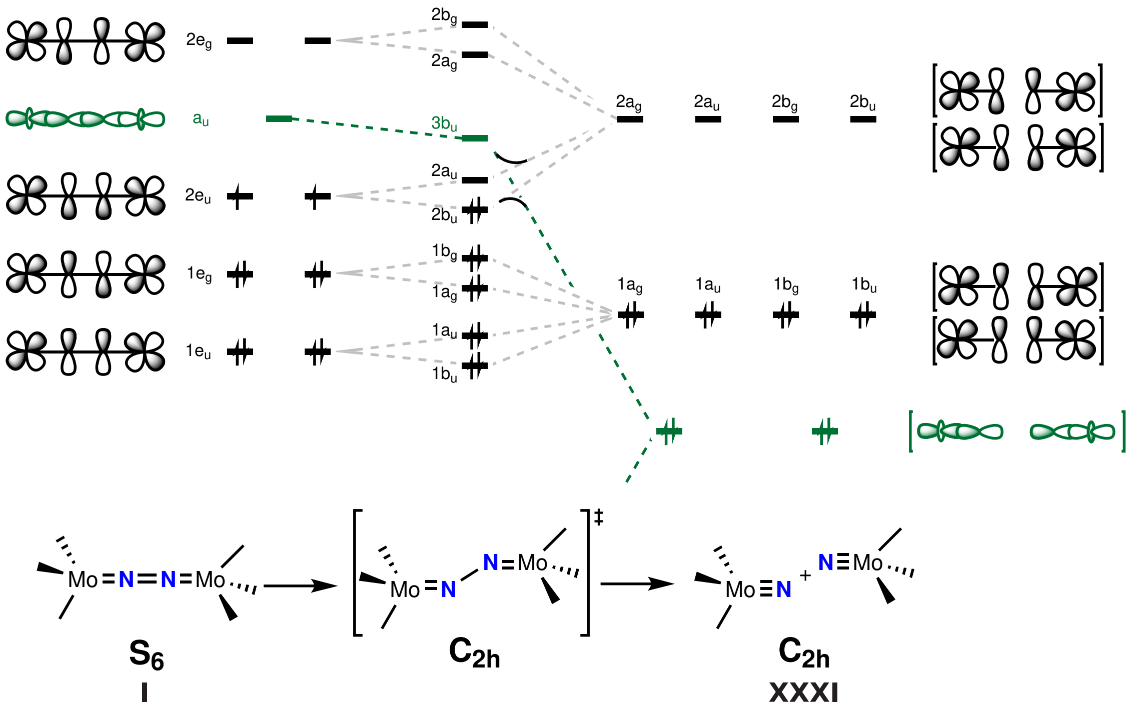

Scheme 22: Molecular orbital scheme for the thermal splitting of **I** into **XXXI** *via* an *zig-zag*-transition state.[60]

The (thermal) stability with respect to N_2-cleavage does not only rely on the number of electrons within the {MNNM}-π-system, but also on the energy gap between the $2e_u$- and a_u-orbitals. One possibility to tune this gap is by exchanging the supporting ligands, as shown by *Floriani*. $[(N_2)\{Mo(Mes)_3\}_2]$ (Mes = 2,4,6-C_6H_2, **XXXIIa**) is isostructural to **I** and features also 10 π-electrons, nevertheless it does not cleave the NN-bond thermally to give the respective nitride **XXXIIb** (Scheme 23). This can be rationalized by the weaker σ- and π-donor abilities of the mesityl-ligands compared to the amide-ligands in **I**, which should lower the energy of the $2e_u$-orbital and thereby increase the energy gap to the a_u-orbital.[133]

The introduction of a fourth supporting ligand *trans* to the N_2-bridge has a similar effect. As already mentioned, *Schrock's* **VIa** features almost the same degree of N_2-activation as *Cummins'* **I** due to the similarity of the ancillary ligands and the same π-electron count. However, the fourth ligand *trans* to the N_2-bridge increases the energy of the a_u-orbital, which hampers mixing with the $2e_u$-orbitals. Besides this kinetic influence, splitting of **VIa** is also thermodynamically less favored and even calculated to be endothermic due to the amine donor *trans* to the formed nitride-ligand (**XXXIII**).[66,132,134]

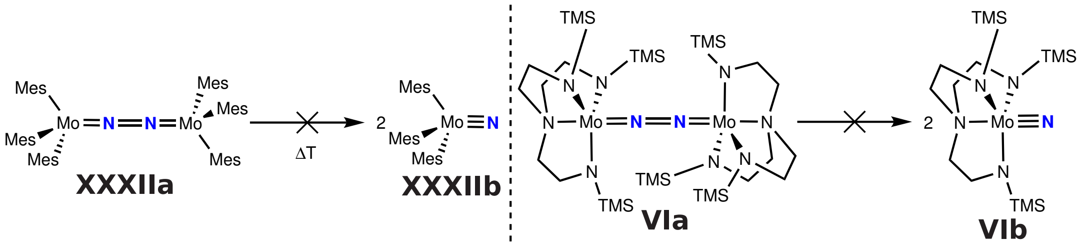

Scheme 23: The end-on N_2-bridged dinuclear complexes of *Floriani* (**XXXIIa**) and *Schrock* (**VIa**), which are not both capable to cleave the NN-bond thermally.[66,132–134]

Changing the symmetry from threefold to fourfold, which is (idealized) most commonly found for pincer-ligands, the overall number of electrons within the {MNNM}-manifold required for N_2-cleavage is increased. For example, feature both Mo-ions in *Nishibayashi's* already mentioned octahedral [$MoI_3(^{pyr}PNP)$] (**XXVIIId**) and *Cummins'* trigonal planar [$Mo(N(R)Ar)_3$] (**XXX**) formally the same oxidation state (+III), but only the latter is capable for direct N_2-binding and -cleavage. In contrast, **XXVIIId** requires the addition of two electrons to give the respective Mo(IV)-nitride **XXVIIIc** (Scheme 19).[130] Similar observations have been made for related pincer supported Mo(III)-complexes by the groups of *Schrock* (**XXXIV**), *Mezaillés* (**XXXV**, Figure 9).[14,17]

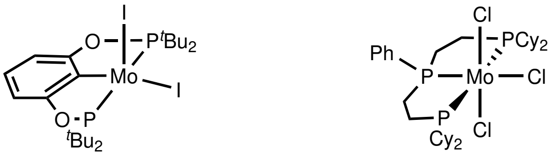

XXXIV **XXXV**

Figure 9: Pincer-supported Mo-complexes by *Schrock* (**XXXIV**) and *Mezaillés* (**XXXV**) capable for N_2-cleavage under reductive conditions.[14,17]

However, isolation and characterization of any N_2-bridged intermediate was not possible so far for any of those systems, which leaves the electronic configuration required for N_2-cleavage unsettled. Following the already discussed MO-scheme (Scheme 8), the energies of the NN-non-bonding b_{1u} and b_{2g}-δ-orbitals drop below the $2e_u$-orbital, due to the changed symmetry. Accordingly and under the assumption of a low spin configuration four additional electrons are required to reach a $\pi^{10}\delta^4$-configuration. Splitting would therefore occur from formal Mo(I)/Mo(I)-stage directly into the respective Mo(IV)-nitrides in all three cases.

These electronic considerations are supported by studies on N_2-binding and -cleavage using the already mentioned [$ReCl_2(PNP^{tBu})$] (**XXXVI**) by the groups of *Miller*, *Siewert* and *Schneider*. Combined electrochemical and computational analysis suggest an $EC^{N_2}C^{Cl}EC^{Dim}$-mechanism for the formation of the structurally characterized N_2-bridged **XII** (Scheme 24), which is capable for N_2-cleavage.

In the first step the Re(III)-starting complex (**XXXVI**) gets reduced to the Re(II)-stage accompanied by N_2-binding and chloride-loss. The so formed $[ReCl(N_2)(PNP)^{tBu}]$ has a less negative reduction potential ($\Delta E \approx 0.4$ V) compared to starting material **XXXVI** and is therefore reduced to $[ReCl(N_2)(PNP)^{tBu}]^-$. Binding of another $[ReCl_2(PNP^{tBu})]$ (**XXXVI**) leads to comproportionation of both Re-centers, loss of another chloride-ligand and formation of dinuclear **XII**, which finally gives the respective Re(V)-nitride (**XXXVII**) *via* N_2-cleavage. Accordingly, splitting occurs on a formal Re(II)/Re(II)-stage supporting the requirement of a $\pi^{10}\delta^4$-configuration in a fourfold symmetry for N_2-cleavage.[15,36]

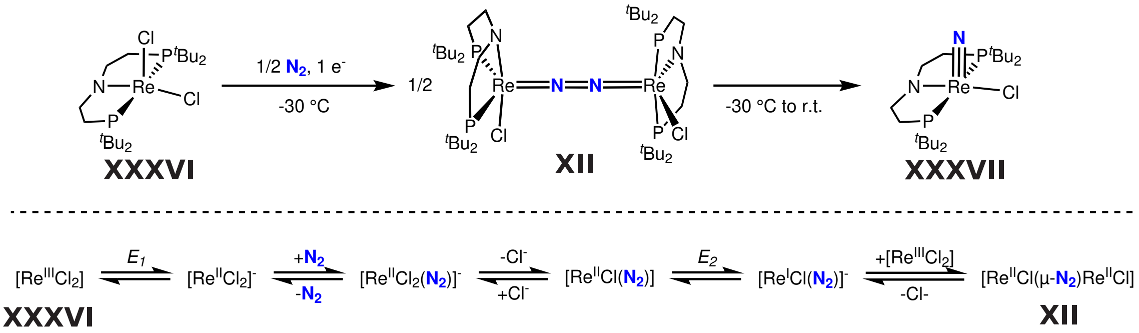

Scheme 24: *Top:* Re-mediated N_2-cleavage *via* end-on N_2-bridged dinuclear **XII**. *Bottom:* Postulated $EC^{N_2}C^{Cl}EC^{Dim}$-mechanism for the formation of **XII**.[15,36]

An alternative scenario, using the b_{1u} and b_{2g}-δ-orbitals as electron reservoir, was suggested by *Schrock*. In this case, splitting was proposed to occur from a formal Mo(II)/Mo(II)-stage into the respective Mo(V)-nitride, followed by subsequent reduction to the corresponding Mo(IV)-nitride. Hence, splitting is induced by a metal to ligand charge transfer from a singlet $\pi^8\delta^4$- into a quintet $\pi^{10}\delta^2$-configuration.[14]

A similar behavior was demonstrated experimentally by *Schneider* for the already mentioned $[(N_2)\{MoCl(PNP)\}_2]$(**XI**). As already discussed, **XI** features a $\pi^8\delta^4$-configuration and is thermally stable with respect to N_2-cleavage similar to *Cummins'* dicationic **III**. Counterintuitively, protonation of **XI** results in N_2-cleavage and formation of the corresponding Mo(V)-nitride, $[Mo(N)Cl(^{H}PNP)]^+$ (**XXXVIII**). It was shown that the first as well as the second protonation both occur on the amide of the pincer-ligand(s). While the monoprotonated intermediate **XXXIX** is diamagnetic, double protonation leads to a quintet ground state for **XL**, as expected for a $\pi^{10}\delta^2$-configuration.[70]

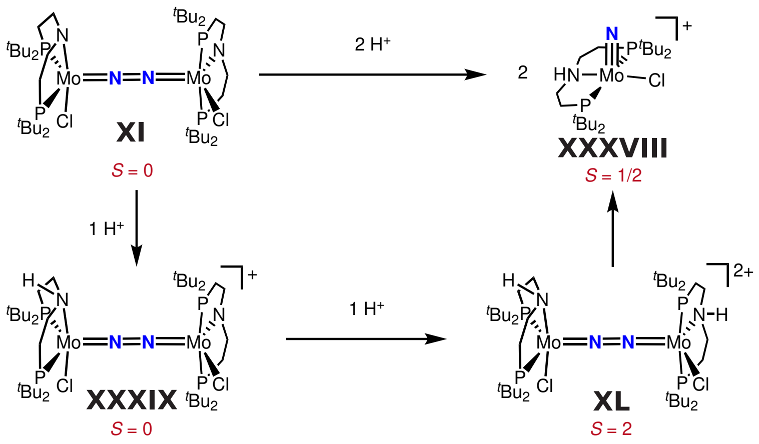
XI
S = 0
2 H+
2
XXXVIII
S = 1/2
1 H+
XXXIX
S = 0
1 H+
XL
S = 2

Scheme 25: Proposed mechanism of proton induced N_2-splitting.[70]

Computational analysis of the reaction revealed an interaction of the amide-p-orbital with the {MoNNMo}-core (Scheme 26, *left*). Therefore the $2e_u$-orbital is destabilized, which leads to a low-spin $\pi^8\delta^4$-configuration due to the large energy gap between the the b_{1u} and b_{2g}-δ-orbitals to the $2e_u$-orbitals . Additionally, the energy of the a_u is also enhanced, which results in a high kinetic barrier ($\Delta G^{\ddagger}_{calc}$ = 37 kcal·mol^{-1}) for N_2-cleavage.[70]

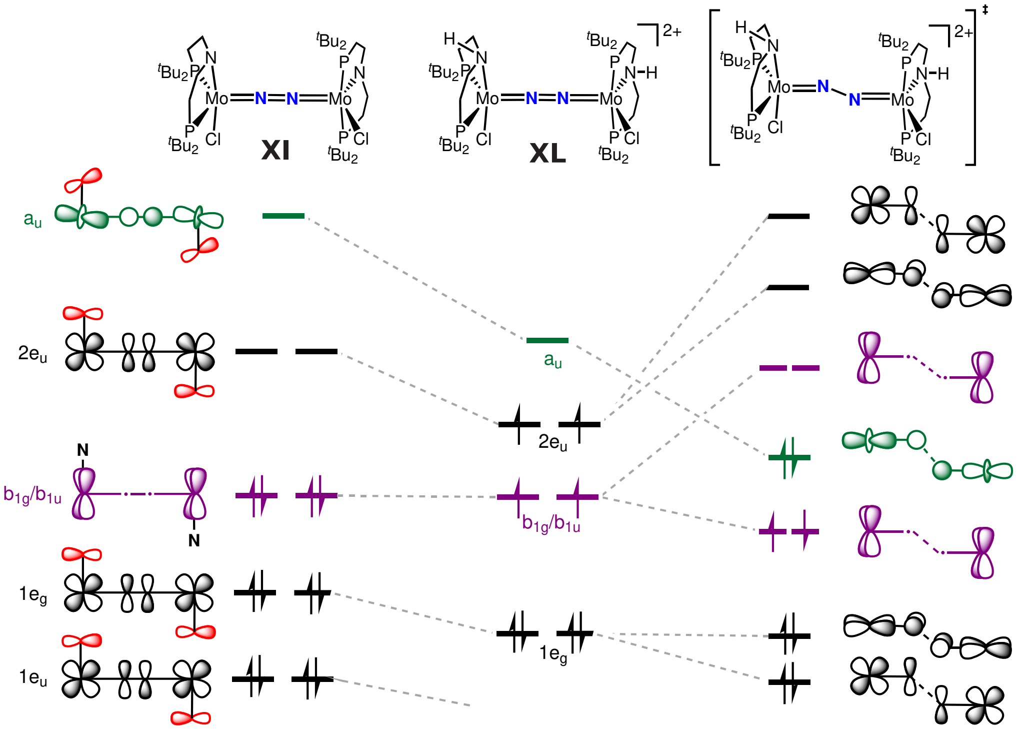
XI
XL
‡
a_u
$2e_u$
b_{1g}/b_{1u}
N
N
$1e_g$
$1e_u$
a_u
$2e_u$
b_{1g}/b_{1u}
$1e_g$

Scheme 26: Qualitative frontier molecular orbitals diagramm for **XI** (*left*), **XL** (*middle*) and the calculated *zig-zag*-transition state from **XL** to **XXXVIII** (*right*).[70]

Upon double protonation both amide-p-orbitals are engaged in covalent bonding to H and do not interact with the {MoNNMo}-core anymore (Scheme 26, *middle*). Accordingly, the $2e_u$-orbitals drop in energy and become populated to give a $\pi^{10}\delta^{2}$-configuration, in line with the observed quintet-ground state for **XL**. Furthermore, the energy of the a_u-orbital is also diminished, which results in a reduced kinetic barrier for N_2-cleavage ($\Delta G^{\ddagger}_{calc}$ = 21 kcal·mol^{-1}) in good agreement with the experimentally derived values ($\Delta H^{\ddagger}_{exp}$ = 17.8 kcal·mol^{-1}; $\Delta H^{\ddagger}_{calc}$ = 19 kcal·mol^{-1}).[70]

Another approach for N_2-cleavage was presented by *Masuda* (Scheme 27). Instead of reducing a Mo-precursor in a relatively high oxidation state, the group utilized zero-valent *trans*-[Mo(N_2)$_2$(depe)$_2$] (depe = $Et_2PCH_2CH_2PEt_2$, **XLIa**) for N_2-cleavage. One electron oxidation of **XLIa** gives the respective nitride, [Mo(N)(depe)$_2$]$^+$ (**XLIb**), *via* formation of intermediate [(N_2){Mo(depe)$_2$}$_2$]$^{2+}$ (**XLIc**) with a $\pi^{10}\delta^{4}$-configuration.[20]

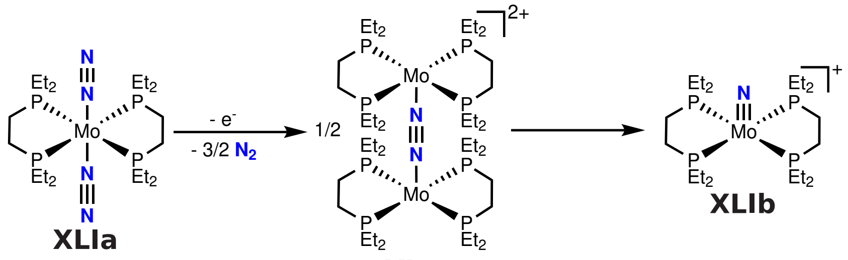

XLIa **XLIc** **XLIb**

Scheme 27: Oxidative N_2-cleavage as presented by *Masuda*.[20]

Overall, all these examples imply the requirement of ten electrons within the {MNNM}-π-manifold for NN-bond cleavage in such N_2-bridged complexes to form the respective nitride-complexes. The thermodynamic and kinetic parameters of N_2-splitting can be tuned by addition of a ligand *trans* to the N_2-bridge, which raises the kinetic barrier for N_2-cleavage by increasing the energy gap between the $2e_u$- and the a_u-orbital.
For instance, octahedrally coordinated [(N_2){ReCl$_2$(^{H}PNP^{iPr})}$_2$] (**XIII**) features the same electron count and degree of activation as **XII** (Scheme 28). Nevertheless, **XIII** is thermally stable and provides a high kinetic barrier for N_2-cleavage ($\Delta G^{\ddagger}_{calc}$ = 41.8 kcal·mol^{-1}), which is in contrast to the kinetic barrier for N_2-cleavage for **XII** ($\Delta G^{\ddagger}_{calc}$ = 20.2 kcal·mol^{-1}).[15,36,71]
Besides this kinetic influence, the thermodynamic driving force for N_2-cleavage is also affected. While splitting of **XII** into the respective five-coordinate [Re(N)Cl(PNP)] (**XXXVII**) is strongly exergonic ($\Delta G^{\circ}_{298\,K}$ = -40.3 kcal·mol^{-1}), splitting of **XIII** into the respective six-coordinate *trans*-[Re(N)Cl$_2$(^{H}PNP^{iPr})] (**XLIIa**) is calculated to be almost thermoneutral ($\Delta G^{\circ}_{298\,K}$ = 2.2 kcal·mol^{-1}). Additional driving force is added by isomerization into the *cis*-dichloro nitride **XLIIb**.

This difference can be rationalized by the strong σ- and π-donating properties of the nitride moiety, which compete with a ligand in *trans*-position. Accordingly, the lower thermodynamic driving force for **XIII** can be explained by a destabilization of **XLII**.[15,36,71]

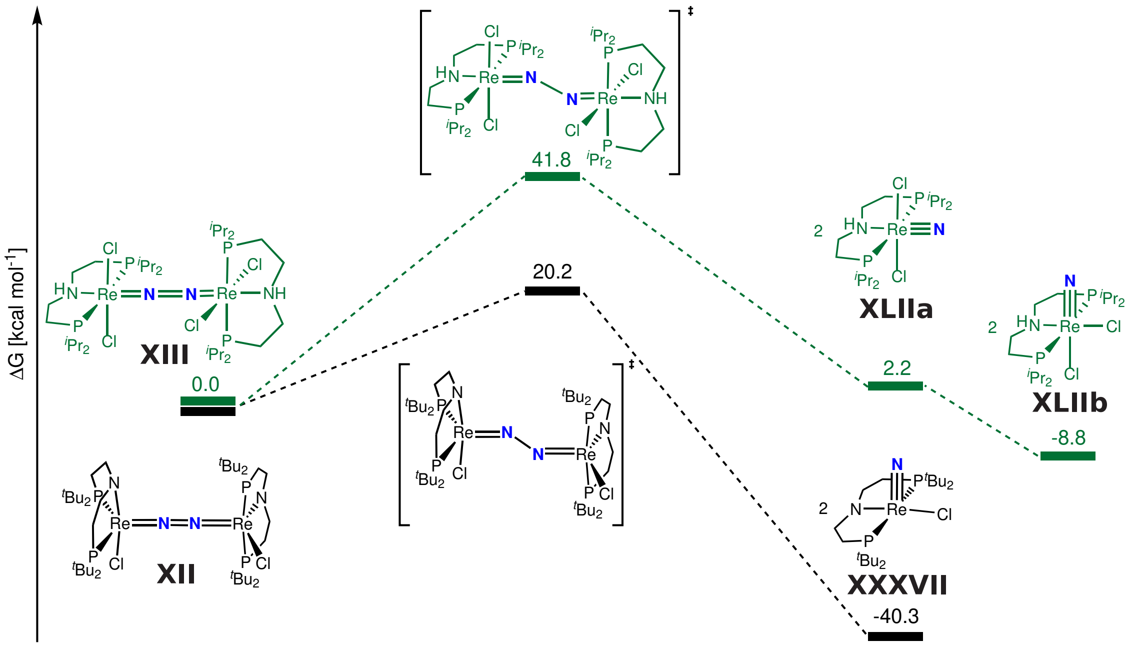

Scheme 28: Calculated energies for N_2-cleavage for **XII** (black) and **XIII** (green) *via* a *zig*-*zag*-transition state.[15,36,71]

Even though, N_2-splitting has a high kinetic barrier and only a low thermodynamic driving force, **XIII** can be transformed into **XLIIb** upon photolysis. In contrast to **XXXVII**, which is largely overstabilized, splitting into **XLIIb** is almost thermoneutral. As a consequence **XLIIb** can be functionalized with much weaker electrophiles compared to **XXXVII**.[71] This is one of the benefits of photolytical N_2-cleavage, which will be discussed in the next chapter.

1.2.3 Photolytic N_2-cleavage

Although first suggested by *Fischler* and *von Gustorf* in 1975,[135] the photolytic cleavage of N_2 is still by far less well established than the thermal N_2-cleavage, which is reflected by the low number of compounds capable for photolytic N_2-splitting. The first example was published in 2001 by the group of *Floriani* using a mesityl-ligated N_2-bridged dimolybdenum-complex, $[(N_2)\{Mo(Mes)_3\}_2]$ (Mes = 2,4,6-Me_3-C_6H_2, **XXXIIa**). Even though, **XXXIIa** features a π^{10}-configuration in a S_6-symmetry and is therefore isostructural and isoelectronic to *Cummins'* **I**, thermal N_2-cleavage has not been reported. These differences were assigned to the weaker σ- and π-donor properties of the mesityl ligands compared to the amido ligands used by *Cummins* (see chapter 1.2.2). Nevertheless, irradiation of **XXXIIa** with UV-light (λ = 365 nm) results in formation of nitride bridged $[(N)\{Mo(Mes)_3\}_2]$ (**XXXIIb**).[133] The group of *Floriani* postulated a mechanism in which the initially formed terminal nitride $[Mo(N)(Mes)_3]$ (**XXXIIc**) acts as a Lewis base which binds **XXXIIa** to give tetranuclear **XXXIId**. Loss of the N_2-bridge yields the final product **XXXIIb**, which was also observed upon reaction of independently prepared **XXXIIc** with **XXXIIa** (Scheme 29).[133]

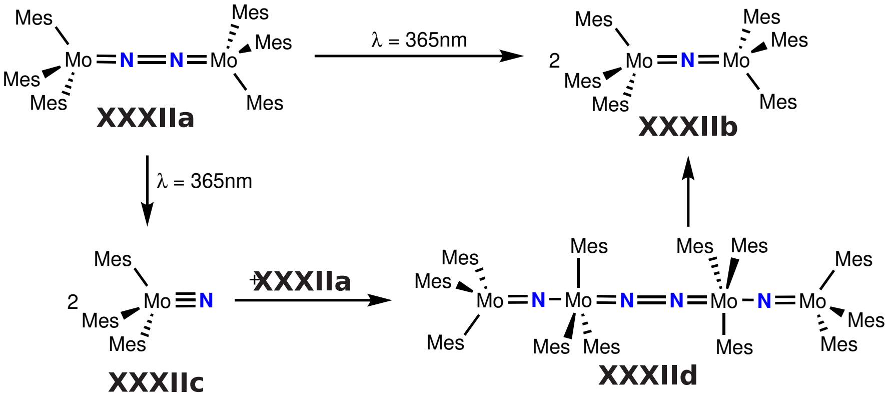

Scheme 29: Proposed mechanism for the formation of **XXXIIb** upon irradiation of **XXXIIa**.[133]

An alternative mechanism was later proposed by *Cummins* (Scheme 30). Upon irradiation of **I** at low temperatures, in order to prevent thermal N_2-splitting, an equimolar mixture of $[Mo(N(R)Ar)_3]$ (**XXX**) and $[Mo(N)(N(R)Ar)_3]$ (**XXXI**) was obtained, hinting towards competitive N_2-splitting and -extrusion pathways. Due to the steric bulk of the amido-ligands, the reaction of **XXX** and **XXXI** to give a nitride-bridged species is circumvented in *Cummins'* case, while the mesityl-ligands used by *Floriani* provide enough space for the formation of nitride-bridged **XXXIIb**.[61]

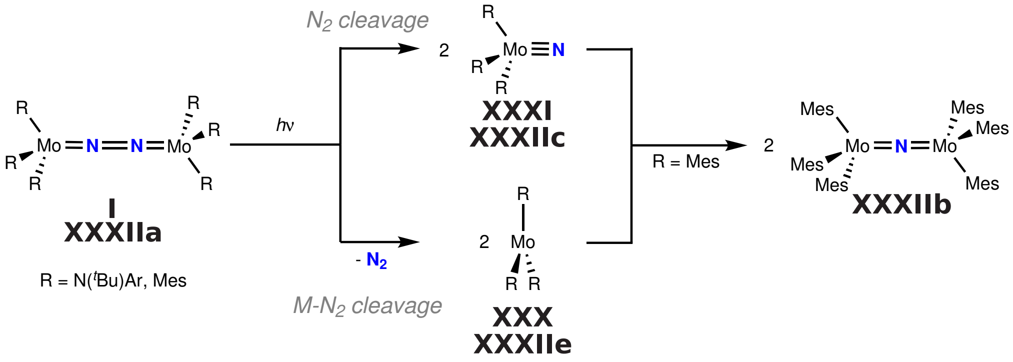

Scheme 30: Irradiation of **I** or **XXXIIa** leads to competitive N-N- and M-N_2-cleavage and in case of **XXXIIa** to recombination of **XXXIIc** and **XXXIIe** to give nitride bridged **XXXIIb**.[61]

The photoreactivity of **I** was examined by UVvis pump-probe spectroscopy in combination with extensive DFT-calculations by the groups of *Cummins* and *Blank*. Based on the used truncated DFT model with simple NH_2-ligands, the strong electronic absorption at 534 nm found for **I** was assigned to an excitation from the triplett ground state into the second excited triplet state ($e_g^4 e_u^2 \rightarrow e_g^3 e_u^3$). Such a transition implies charge transfer from an more metal based Mo-N_2-bonding and N-N-antibonding orbital (π-π^*-π) into an N_2-centered orbital with Mo-N_2-antibonding and N-N-bonding character (π^*-π-π^*) within the {MoNNMo}-core. The excited state is very short-lived and undergoes internal conversion back to the hot ground state within 300-800 fs. The small overall quantum yield ($\Phi = 5\%$) was used as an indicator for competitive unproductive vibrational cooling and productive Mo-N_2- or N-N-cleavage. The almost equally distributed amounts of Mo-N_2- and N-N-splitting products contrast their different thermal barriers, which should favor cleavage of the Mo-N_2-bond.[132] This observation was rationalized by a nonthermal vibrational energy distribution created by the internal conversion process due to coupling with {MoNNMo}-bending modes, which should add some bias to the NN-dissociation path. Overall, the photolytical cleavage of **I** was portrait as a reaction from a vibrationally hot ground state with a non-statistical energy distribution, which results in different selectivities for Mo-N_2 and N-N-cleavage compared to the thermal pathway.[136]

By now, **I** is the only system capable for photolytic N_2-cleavage whose photochemical and -physical properties have been experimentally probed. Another experimental study on the photophysics of an N_2-bridged dinuclear complex was reported by the groups of *Chirik* and *Scholes*.[137] Although the used $[(N_2)\{Mo(Tpy^{Ph})(PMe_2Ph)_2\}]^{2+}$ (**XVII**$^{2+}$; Typ^{Ph}=4’-Ph-2,2’,6,6’2”-terpyridine, Figure 6) does not show any photoreactivity, the study revealed some fundamental aspects and guidelines for effective photolytic N_2-cleavage. All probed excitations with wavelengths between 440 and 1150 nm showed strong MLCT character by populating a ^{1}MLCT-state with strong π^*-Typ^{Ph}-ligand character within 100 fs. Relaxation either *via* internal conversion or inter system crossing occurs within 2-3 ps. The inter system crossing from the excited ^{1}MLCT-state into the ^{3}MLCT-state results in migration of electron density from the Typ^{Ph}-ligand into the bridging N_2-unit, which could increase the nucleophilicity of the N_2-bridge and thereby increase its reactivity. However, relaxation into the ground state, either *via* direct decay (10-15 ps) or *via* indirect decay through an intermediate high-energy metal state (23-26 ps), occurs too fast for bimolecular reactivity. This drawback could potentially be overcome by increasing the exited state lifetime upon usage of a more electron deficient terpyridine-ligand or *via* subsequent intramolecular trapping of the exited state, as also suggested by *Reiher* and *Sellmann*.[138] Overall, this example demonstrates how supporting ligands can act as strong light harvesters that transfer energized electron density to the {MNNM}-core and thereby potentially increase its reactivity.[137] More recent studies of the system had shown, that this energy transfer from the chromophore to the N_2-bridge gains efficiency due to Fermi-resonance coupling of the vibrational modes of the Mo(Typ^{Ph})-moiety and the {MoNNMo}-core.[139]

Competitive M-N_2- and N-N-cleavage was also observed for another class of compounds capable for photolytical N_2-cleavage. Irradiation of *Sita's* already mentioned, thermally stable N_2-bridged η^5-cyclopentadienyl/η^2-amidinate complexes (M = Mo **XVIg**, W **XVIh**) yields bis-nitride bridged $[(N)_2(MCp^*am)_2]$ (M = Mo **XLIIIa**, W **XLIIIb**, Scheme 31). In case of the Mo-compound, **XVIg**, the formation of mono-nitride $[(N)(MoCp^*am)_2]$ (**XLIVa**) strongly hints towards competative M-N_2 and N-N-bond breakage, reminiscent to the examples by *Floriani* and *Cummins*.[140]
Upon variation of the substituents on the amidinate-ligand (am* = $[N(Et)C(Ph)N(Et)]^-$, **XLV**) thermal N_2-cleavage into the bis-nitrido-complexes $[(N)_2(MCp^*am^*)_2]$ (M = Mo **XLVIa**, W **XLVIb**) could be achieved, showcasing how relatively small changes on the ligand-framework can have a large impact on the reactivity of such N_2-bridged compounds.[85]

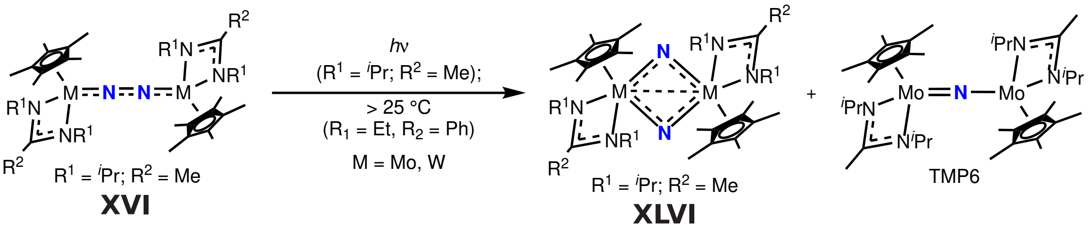

XVI

R^1 =Et; R^2 = Ph

XLIII

XLVI

R^1 =Et; R^2 = Ph

XLIV

Scheme 31: Photolytical (R^1 = ^{i}Pr; R^2 = Me) and thermal (R^1 = Et; R^2 = Ph) N_2-cleavage of *Sita's* η^5-cyclopentadienyl/η^2-amidinate complexes (M = Mo **XVIg**, **XLVa** and W **XVIh**, **XLV**).[85,140]

Using structurally related $[(N_2)\{MoCp^*(depf)\}_2]$ (depf = 1,1'-bisdiethylphosphino-ferrocene, **XLVIIa**) photolytical cleavage into a terminal nitride [Mo(N)Cp*(depf)] (**XLVIII**) was demonstrated by the group of *Nishibayashi* (Scheme 32). Remarkably, the splitting reaction could be reversed upon one electron oxidation of **XLVIII** giving dicationic $[(N_2)\{MoCp^*(depf)\}_2]^{2+}$ (**XLVIIb**) *via* nitride coupling. **XLVIIb** can be reduced again to give monocationic **XLVIIc** and neutral **XLVIIa** thereby closing the synthetic cycle.[16]

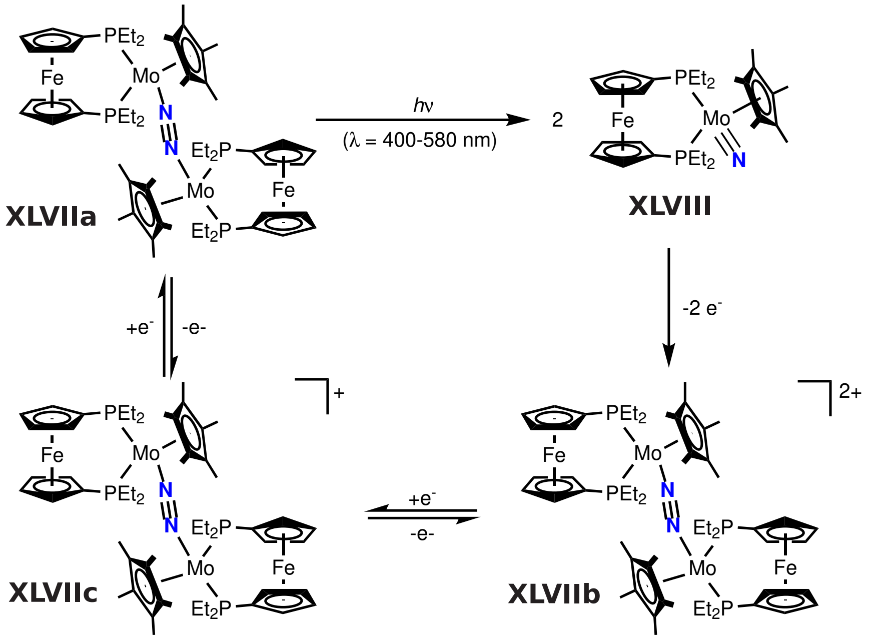

Scheme 32: Photolytical splitting of **XLVIIa** gives terminal nitride **XLVIII**, whose oxidation yields in **XLVIIb** *via* nitride coupling.[16]

Another example, which was later computationally studied by *González* and *Krewald*, was presented by *Kunkely* and *Vogler* (Scheme 33).[141] Irradiation of the mixed valent, valence localized Os^{II}/Os^{III}-N_2-bridged complex $[((NH_3)_5Os^{II})(N_2)(Os^{III}(NH_3)_5)]^{5+}$ (**XLIXa**) yields the respective Os^{V}- and Os^{VI}-nitride-complexes, $[Os^{V}(N)(NH_3)_5]^{2+}$ (**La**) and $[Os^{VI}(N)(NH_3)_5]^{3+}$ (**Lb**). The strong *trans*-influence of the nitride-ligand causes NH_3-liberation. Additionally, the Os(V)-nitride (**La**) gets subsequently oxidized to stabilize the Os≡N-bond and form another equivalent of $[Os^{VI}(N)(NH_3)_4]^{3+}$ (**Lc**, see also Scheme 40). Notably, direct cleavage into **Lb** upon irradiation of the corresponding Os^{III}/Os^{III} complex, $[((NH_3)_5Os^{III})(N_2)(Os^{III}(NH_3)_5)]^{6+}$ (**XLIXb**), was unsuccessful, since the latter liberates N_2 upon irradiation or at temperatures above 5 °C.[141]

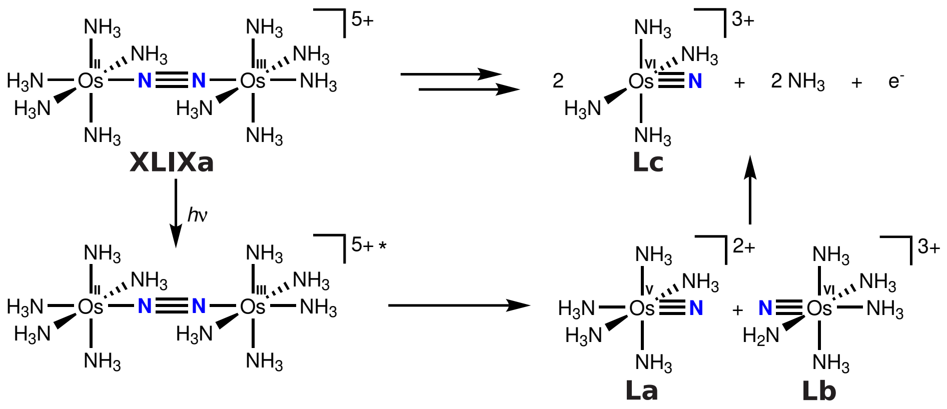

Scheme 33: Irradition of **XLIXa** yields in **La** and **Lb**, which subsequently react further to give two equivalents of **Lc**.[142]

González and *Krewald* calculated the effect of NN-bond elongation on the relative MO-energies of **XLIXa** to finally give **La** and **Lb** (Scheme 34). Elongation of the NN-bond decreases the overlap of the two N-p_z-orbitals leading to weaker seperation of the N-N σ/σ^*-levels and a stabilization of the σ-σ^*-σ-orbital. Once both nitrogen atoms are far enough separated, the σ-σ^*-σ-orbital becomes degenerate with the π^*-π-π^*-orbital. As a result the electronic configuration as well as the NN-bond strength change since electrons are transferred from the former HOMO (π^*-π-π^*), with NN-bonding and Os-N_2 antibonding-character, into an orbital with NN-antibonding and Os-N_2-bonding character (σ-σ^*-σ). Full cleavage into the two monomers, **La** and **Lb**, goes along with degeneration of the former σ-σ^*-σ- with the former σ-σ-σ-orbital.[142,143]

Taking these considerations into account, two possible scenarios for photolytical N_2-cleavage have been postulated. One possibility is the electronic excitation into an excited state with an distorted M-N-N-M core, which lowers the energy of the σ-σ^*-σ-orbital making it accessible for population and thereby lowering the kinetic barrier for N_2-cleavage. Another possibility would be the direct electronic excitation into the σ-σ^*-σ-orbital leading to a large decrease of the NN-bond strength. This effect would be maximized if the excited electron originates from an MN-π^*-orbital, since in this way the MN-bond-order would be increased while the NN-bond-order would be decreased.[142,143]

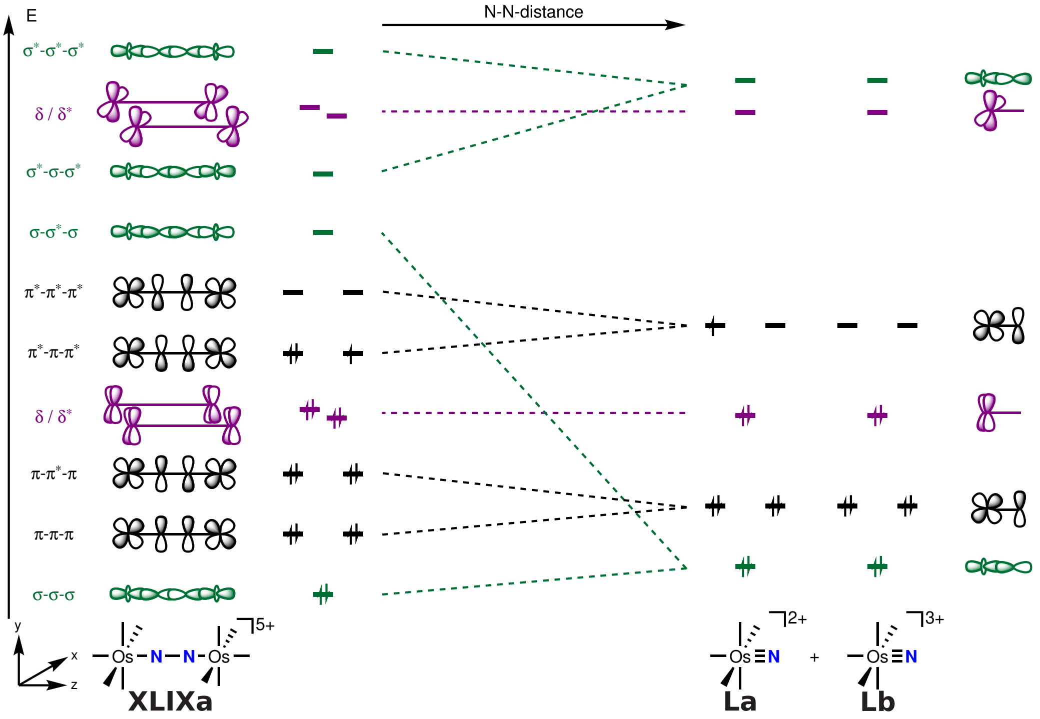

Scheme 34: Molecular orbital scheme for the cleavage of **XLIXa** into **La** and **Lb** upon elongation of the NN-bond distance.[142]

These proposed scenarios can also be applied to the already discussed photoactive systems by *Sita* (**XVIg**, **XVIh**), *Nishibayashi* (**XLVIIa**) and *Schneider* (**XIII**), although their photochemical and photophysical properties are not fully understood yet. For instance, computational analysis by *Krewald* of photoactive **XVIg** revealed an excitation with LMCT-character from the bridging N_2 ligand to the Mo-ions.[144] Such a transition should weaken the NN-bond and thereby increase the flexibility of the {MoNNMo}-core. Notably, such a transition is not predicted for the photoinactive analogue **XLVa**. Further comparison between both systems, **XVIg** and **XLVa**, also unveiled several LMCT transitions from both amidinate and Cp*, which were only present in photoactive **XVIg** and could induce ligand dissociation as initial step for isomerization into **XLIIIa** as it was also proposed by *Sita*.[85,144,145]

TD-DFT calculations of *Nishibayashi's* structurally related **XLVIIa** imply that the active transition also leads to a decrease of electron density between both nitrogen atoms resulting in a more flexible Mo-N-N-Mo unit.[16]

The active transitions within *Schneider's* **XIII** were attributed to have mainly $(\delta/\delta^*) \rightarrow (\pi^*\text{-}\pi^*\text{-}\pi^*)$-character, which could lead to distortions of the {ReNNRe}-core possibly promoting N_2-cleavage *via* a *zig-zag*-transition state.[71]

Another example, structurally related to already discussed **XIII**, was recently reported by the group of *Miller*. Reduction of [$ReCl_3$(PONOP)] (**LI**; PONOP = 2,6-(^{i}Pr_2PO)$_2$-NC_5H_3) in presence of N_2 forms the N_2-bridged dinuclear *trans, trans*-**LIIa**, which is thermally stable with respect to N_2-cleavage but isomerizes into the thermodynamically more favored *cis, trans*-**LIIb** and *cis, cis*-**LIIc** above 130 °C (Scheme 35). Each isomer transforms into *cis*-[Re(N)Cl_2(PONOP)] (**LIIIa**) upon irradiation (λ = 405 nm), although with very different quantum efficiencies and yields, with **LIIc** being most effective (Table 5).[21]

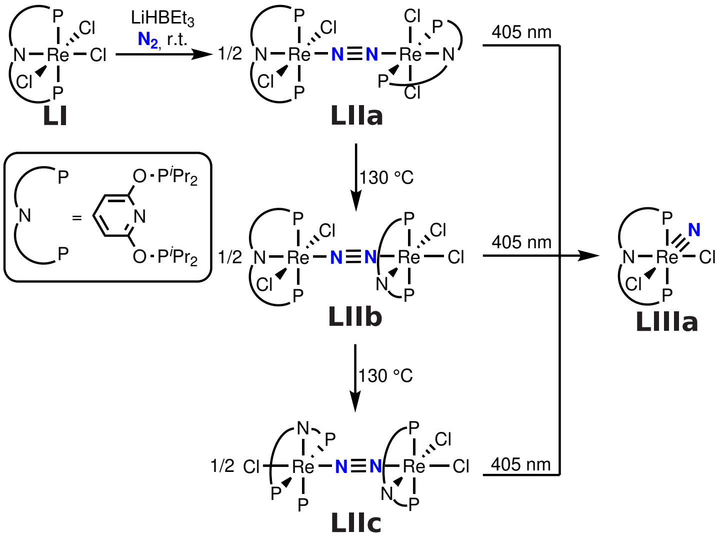

Scheme 35: Formation of the N_2-bridged dinuclear Re-PONOP-species **LII** and their interconversion into **LIIIa** upon photolysis.[21]

The incapability for thermal N_2-cleavage for all three dinuclear species was rationalized by a high kinetic barrier ($\Delta G^\ddagger$ = 51.3-53.2 kcal·mol^{-1}), furthermore cleavage of the NN-bond into the respective *cis/trans*-[Re(N)Cl_2(PONOP)] (**LIIIa**/**LIIIb**) was calculated to be endergonic ($\Delta G°$ = 10.5-13.9 kcal·mol^{-1}). Isomerization of *trans*-**LIIIb** into *cis*-**LIIIa** was calculated to be exergonic ($\Delta G°$ = -6.4 kcal·mol^{-1}) in line with the exclusive formation of **LIIIa** upon photolysis. However, the high barrier for N_2-cleavage circumvents nitride coupling of **LIIIa** to N_2-bridged **LIIc**, which was observed neither thermally nor photolytically.[21]

Table 5: Photolysis (λ = 405 nm) of different mixtures of **LIIa**, **LIIb** and **LIIc** gives different quantum yields (Φ, obtained after 2 h) and yields of **LIIIa**.[21]

LIIa	**LIIb**	**LIIc**	Φ (after 2 h)	Yield	time
8	1	0	0.003	<3%	9 d
0	7	1	0.06	24%	7.5 h
0	1	1	0.11	47%	7 h

Overall, the system of *Miller* represents another good example how photolysis enables N_2-splitting over a high kinetic barrier and without a thermodynamic driving force. Such thermoneutral (or even endergonic) reactions hold the promise of forming less stabilized and therefore easier to functionalize N_2-derived nitrides.[143] For example, requires thermally obtained [Re(N)Cl(PNP)] (**XXXVII**) strong electrophiles, like alkyltriflates, for functionalizations of the nitride moiety *via* C-N-coupling.[15,146] In contrast, $[Re(N)Cl_2(^{H}PNP^{iPr})]$ (**XLII**), generated photolytically, can be functionalized with milder electrophiles, such as benzoylchlorides, to give benzamide.[71] The functionalization of N_2-derived nitrides will be discussed in the next chapter.

1.3 Nitride-Functionalization

The cleavage of N_2 typically results in the formation of a transition metal nitride. However, such nitrides are mostly not prepared *via* N_2-scission and represent a long known class of compounds, which can be synthesized on various different routes.[131] The first report for a transition metal nitride dates back to the synthesis of $[OsO_3N]^-$ in 1847.[147] Since than the chemistry of transition metal nitrides has evolved and was covered in many review articles.[45,131,148–156]

This chapter will focus on more general bonding considerations and the resulting reactivity of transition metal nitrides. Afterwards, the reactivity of N_2-derived nitrides, with focus on C-N-coupling reactions, will be discussed.

1.3.1 Bonding of terminal transition metal nitrides

The metal-nitride bond is considered as a triple bond consisting of one σ- and two π-bonds, in which the nitride ligand acts as both a strong σ- and π-donor. Although, this description as well as the typical consideration as N^{3-} imply a rather nucleophilic character, the high covalent character of the M≡N-bond can also lead to electrophilic behavior, especially for late transition metals.[131]

To understand the stability and reactivity of such metal-nitride complexes it is important to understand their electronic structure. *Gray* and *Ballhausen* developed a bonding picture for octahedral $[VO(OH_2)_5]^{2+}$, which can be adopted for octahedral nitride complexes and translated into other geometries.[157] Considering the M≡N-bond to be oriented along the z-axis, linear combination of the metal d_{z^2}- with the nitrogen p_z-orbital results in σ-bond formation, while combination of the d_{xz}- and d_{yz}-orbitals with the p_x- and p_y-*N*-orbitals, respectively, results in π-interactions. Due to the lack of *N*-orbitals with suitable symmetry, the d_{xy}- and $d_{x^2-y^2}$-orbitals remain non-bonding with respect to the M≡N-bond. The nitride-ligand (formally considered as N^{3-}) adds six electrons to this scheme, which results in full occupation of all bonding-orbitals and a bond order of three (Scheme 36, *left*). The remaining orbitals can be populated with former metal d-electrons. Accordingly, the stability and reactivity of the metal-nitride bond relies on the number of remaining d-electrons. In case of a d^0-configuration only orbitals with MN-bonding character are populated, while upon addition of one or two more electrons the former d_{xy}-orbital with non-bonding character gets occupied. A higher number of electrons leads to population of MN-antibonding orbitals and weakening of the M≡N-bond. Furthermore, occupation of the $d_{x^2-y^2}$-orbital reduces the bond-order to the remaining supporting ligands. Hence, octahedrally coordinated metal-nitrido-complexes require a low number of d-electrons to be stable in line with the low number of late transition metal nitrides in this coordination mode.[155,158] Additionally, the strong σ- and π-donor properties of the nitride ligand have a strong *trans*-influence, which often prevent binding of a ligand in *trans*-position and foster the formation of square-pyramidal complexes with the nitrido-ligand on the apical position.[131]

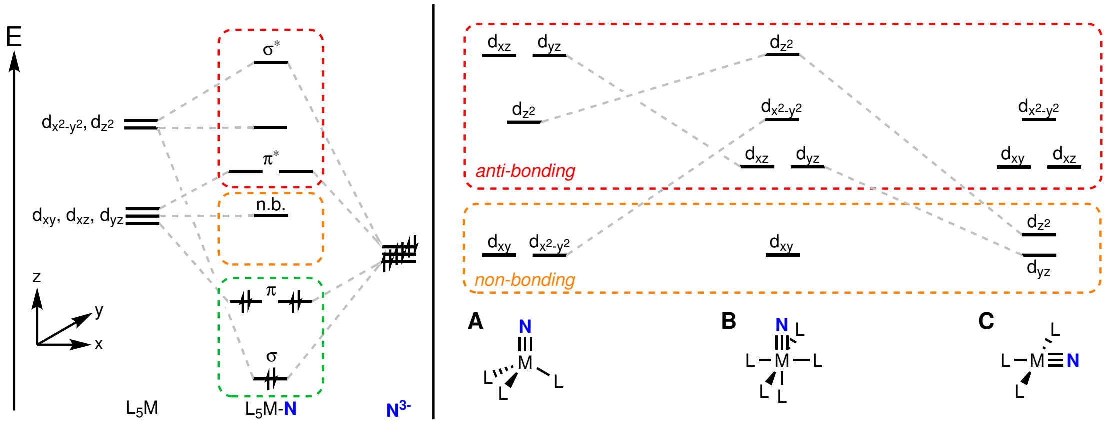

Scheme 36: *left*: Qualitative orbital interactions within octahedrally coordinated L_5MN. *right:* Qualitative frontier molecular orbital scheme for metal nitrido complexes in tetrahedral, octahedral and square-planar coordination geometries.[45,131,157,159]

Higher d-electron counts can be stabilized within different coordination geometries. Within a tetrahedral geometry the $d_{x^2-y^2}$-orbital becomes overall non-bonding and drops in energy, degenerate with the d_{yz}-orbital. Since both of these orbitals have an overall non-bonding character, a d-electron count up to four can be stabilized. This was first shown by *Peters*[45] for a pseudo-tetrahedral Fe(IV)-nitride, $[Fe(N)(P_3^{iPr}BPh)]$ (**LIV**, $P_3^{iPr}BPh = [PhB(CH_2P^iPr_2)_3]^-$) and later independently by *Meyer*[160] and *Smith*[161] with structurally related Fe(IV)-nitrides both supported by tripodal carbene-ligands. All three compounds exhibit a singlet ground state in agreement with the proposed MO-scheme shown in Scheme 36 (*right*, A), which was further corroborated by DFT-calculations.[45,160,161]

Square-planar coordination geometries can also stabilize higher d-electron counts. Considering the M≡N-bond to be oriented along the x-axis, the d_{z^2}-orbital drops in energy and becomes non-bonding, which should lead to the MO-diagram shown in Scheme 36 (*right*, C).[159] The first example for a square-planar d^4-nitride, $[Ru(N)(PNP^{Si})]$ (**LV**, $PNP^{Si} = [N(SiMe_2CH_2P^tBu_2)_2]^-$), was presented by the group of *Caulton*.[162] Notably, upon usage of this coordination geometry, the groups of *Burger* and *Schneider* were also able to stabilize the d^5-configurated nitrides, [Ir(N)(PDI)] (**LVI**; PDI = pyridinediimino) and [M(N)(PNP")] (M = Rh (**LVII**), Ir (**LVIII**); $PNP" = [N(CHCHP^tBu_2)_2]^-$), respectively (Figure 10).[46–48,163]

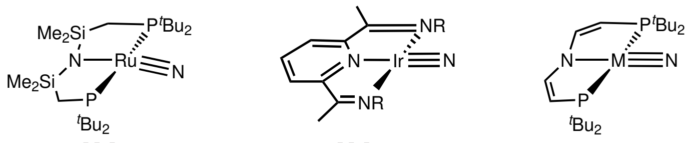

LV **LVI** M = Rh **LVII**
M = Ir **LVIII**

Figure 10: Pincer-supported, square-planar nitrido-complexes reported by *Caulton*[162] (*left*), *Burger*[46] (*middle*, R = di-isopropylphenyl) and *Schneider*[47,48] (*right*).

While these considerations give some insights into the stability of the M≡N-bond, the philicity of the nitride ligand itself depends on the relative energies of the metal-d- and nitrogen-p-orbitals forming one of the two π-bonds. Upon comparison two scenarios evolve: In one case, when the metal d-orbitals are energetically higher than the nitrogen p-orbitals, the two π-bonding electrons are mainly nitrogen-centered, making the nitride nucleophilic (Scheme 37, *left*). In the opposite scenario, when the metal d-orbitals are energetically below the nitrogen p-orbitals, the bonding π-orbital has mainly metal-character and the corresponding antibonding π^*-orbital is mainly nitrogen-centered resulting in a more electrophilic nitride (Scheme 37, *right*).[131,151]

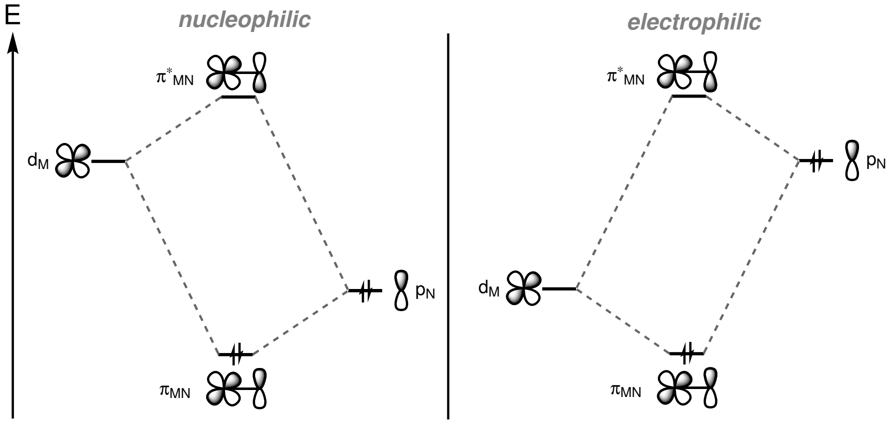

Scheme 37: Simplified molecular orbital schemes for the π-interaction within the metal-nitride-bond, either leading to a nucleophilic or electrophilic character of the nitride-ligand.[131]

Accordingly, the electrophilic character of the nitrido-ligand should increase moving right along the periodic table. This trend was also determined computationally *via* population analysis for a series of [M(N)(salen)] and $[M(N)Cl_4]^{2+}$ complexes (M = V, Cr, Mn, Fe; salen = *N,N'*-bis(salicylidene)ethyldiamine dianion) using DFT, which showed a decreasing negative charge at the nitride ligand moving right along the periodic table.[164]

However, the reactivity of the nitride does not only rely on the metal and electron count as the supporting ligands can also model its reactivity, as shown by the group of *Mayer* using a Tp-supported Os-nitride complex, $[Os(N)R_2(Tp)]$ **LIX**; Tp = trispyrazolylborate).[165–167] While the bis-chloro complex, $[Os(N)Cl_2(Tp)]$ (**LIXa**), reacts fast with *Grignard*-reagents, such as PhMgCl, under the formation of the respective imido-complex, the bis-phenyl complex, $[Os(N)Ph_2(Tp)]$ (**LIXb**), barely reacts with PhMgCl, implying different reactivity of the nitride-moiety.[165,166] Different reactivity was also found upon addition of triarylboranes (Scheme 38). Phenyl-ligated **LIXb** reacts as a nucleophile and forms N-B aducts, $[Os(NB(C_6F_5)_3)Cl_2(Tp)]$ (**LX**). In contrast, chloro-ligated **LIXa** inserts as an electrophile into the B-Ar-bond and forms the respective borylanilido compound (**LXI**).[166,167] The different reactivity was rationalized computationally. The nearly degenerate LUMO and LUMO+1 of **LIXa** are low lying, M-N π-antibonding and mainly nitrogen centered, in line with the observed electrophilic behavior. Upon exchange of Cl vs. more σ-donating Ph, both orbitals rise in energy, which explains the reduced electrophilicity of **LIXb** compared to **LIXa**.[166]

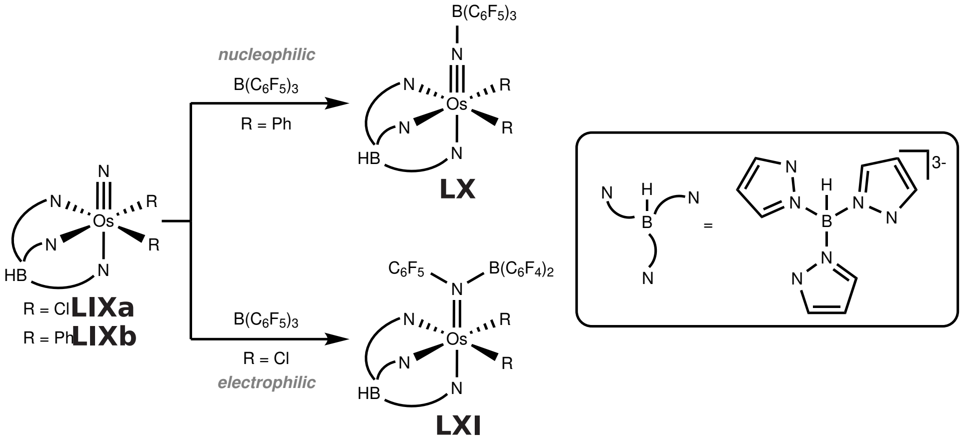

Scheme 38: Ligand influence on the nucleophilicity of an Tp-supported Os-nitride.[166,167]

All in all, these considerations as well as the high covalent character of the M≡N-bond demonstrate that the typical description of the nitride ligand as N^{3-} can be misleading. A very illustrative example was published by the group of *Wieghardt*. Comparison of the structural parameters of $[M(N)(CN)_4(OH_2)]^{2-}$ ($M = Re$ (**LXIIa**), Mn (**LXIIb**)) with the corresponding nitrosyl complexes $[M(NO)(CN)_4(OH_2)]^{2-}$ ($M = Re$ (**LXIIIa**), Mn (**LXIIIb**)) showed almost no difference in the M-CN distances, even though, upon considering the nitride-ligand as trianionic and the nitrosyl-ligand as monocationic, the oxidation state of the metal has changed from +V to +I.[168]
Therefore, a different notation, $\{M\text{-}N\}^n$, similar to the *Enemark-Feltham* notation[169] for {M-NO}-complexes, was proposed. Within this $\{M\text{-}N\}^n$-notation, n represents the number of d-electrons within the M≡N-fragment, considering the nitrido-ligand as a trianionic ligand. In this way, the actual distribution of the electrons within the M≡N-

bond remains undefined. Additionally, *n* can be correlated to the MO-schemes shown in Scheme 36 and can give some insights about the stability of the metal-nitride-bond.[168]

1.3.2 Reactivity of N_2-derived nitrides

Applying these bonding considerations to the N_2-generated terminal nitrides presented in the previous chapters it can be seen, that most of the pincer-supported nitrides as well as *Masuda's* $[Mo(N)(depe)_2]^+$ (**XLIb**) exhibit d^2-configurations. Accordingly, the MN-non-bonding HOMO of these nitrides is fully occupied and further reduction should lead to weakening of the M≡N-bond. One exception is *Schneider's* $[Mo(N)Cl(^{H}PNP)]^+$ (**XXXVIII**), which features a d^1-configuration. Nevertheless, all of these compounds contain early transition metals, which gives the respective nitride a nucleophilic character. In fact, functionalization of most of the mentioned nitrides has been achieved with electrophiles such as alkyltriflates,[15,146] boranes,[170] silanes[17,171,172] or benzoylchlorides.[71]
The group of *Holland* attempted the oxidation of N_2-derived [Re(N)Cl(PNP)] (**XXXVII**, $PNP = [N(CH_2CH_2P^tBu_2)_2]^-$).[173] While outer-sphere oxidents, like ferrocenium, lead to metal centered oxidation to give $[Re(N)Cl(PNP)]^+$ (**LXIV**), electrophilic O-atom-transfer reagents, like mCBPA (mCBPA = 3- chloroperbenzoic acid) lead to oxidation of the pincer-amide and formation of $[Re(N)Cl(P^{O}NP)]$ (**LXV**, $P^{O}NP = [ON(CH_2CH_2P^tBu_2)_2]^-$), which could not be synthesized upon usage of nucleophilic O-atom-transfer agents. **LXV** was successfully oxidized to give $[Re(N)Cl(P^{O}NP)]^+$ (**LXVI**), which could also be obtained upon reaction of **LXIV** with mCPBA. Although, the structural parameters of **LXVI** do not differ significantly from **XXXVII**, the M≡N-moiety reacts with phosphines to give the phosphinimide **LXVII**, which decomposes to **LXIV**, OPR_3 and other products. Hammett-analysis *via* variation of the phosphine substituents imply an electrophilic character of the nitride-ligand, showcasing how the ligand and oxidation-state of the metal influence the reactivity of the nitride-moiety.[173]

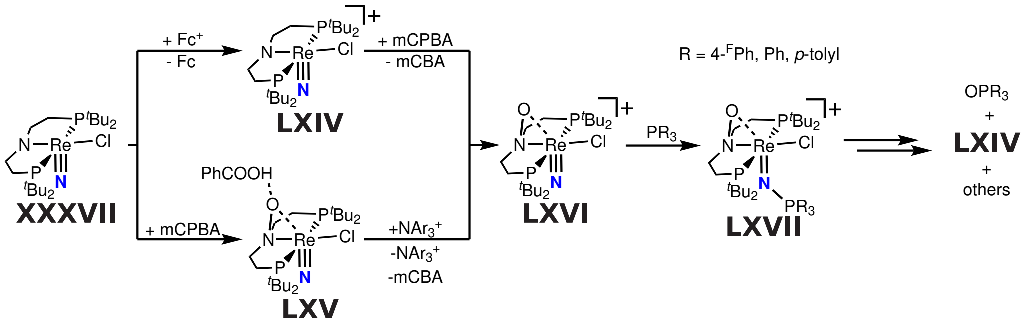

Scheme 39: Oxidation of the PNP-pincer-ligand and the Re-center in nucleophilic **XXXVII** change the nitride-philicity to electrophilic in **LXVI**.[173]

The described bonding considerations can also be used to rationalize the instability of the Os(V)-nitride $[Os(N)(NH_3)_5]^{2+}$ (**La**), which was proposed as one of the two initial N_2-splitting products upon photolysis of $[((NH_3)_5Os^{II})(N_2)(Os^{III}(NH_3)_5)]^{5+}$ (**XLIXa**) (Scheme 40, a). The strong *trans*-influence of the nitride ligand leads to liberation of one NH_3-ligand (Scheme 40, b). The d^3-configuration of the so formed $[Os(N)(NH_3)_4]^{2+}$ (**Ld**) destabilizes the Os≡N-bond due to occupation of an anti-bonding orbital. Disproportionation to $[Os(N)(NH_3)_4]^{+}$ (**Le**) and $[Os(N)(NH_3)_4]^{3+}$ (**Lc**) (Scheme 40, c), starts a cascade reaction, using $[Os(N)(NH_3)_4]^{2+}$ (**Ld**) as reductant, in which one nitride ligand is subsequently reduced and protonated to give $[(NH_3)_5Os(OH_2)]^{3+}$ (**LXVIII**) (Scheme 40, d).[141]

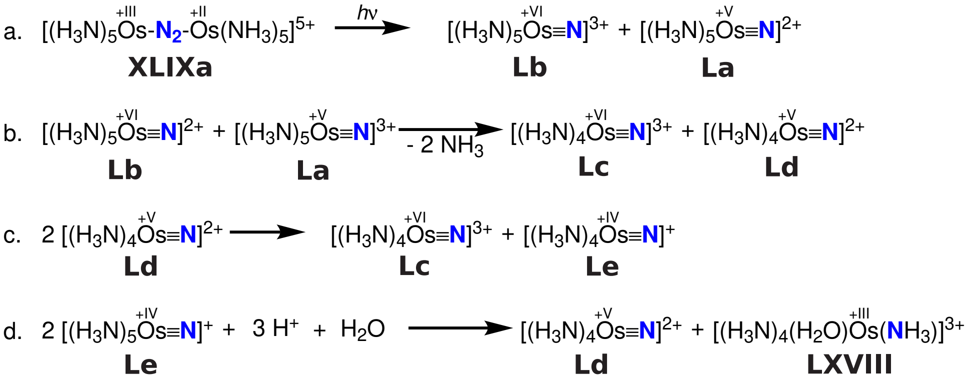
a. $[(H_3N)_5\overset{+III}{Os}\text{-}N_2\text{-}\overset{+II}{Os}(NH_3)_5]^{5+} \xrightarrow{h\nu} [(H_3N)_5\overset{+VI}{Os}{\equiv}N]^{3+} + [(H_3N)_5\overset{+V}{Os}{\equiv}N]^{2+}$
XLIXa
Lb
La
b. $[(H_3N)_5\overset{+VI}{Os}{\equiv}N]^{2+} + [(H_3N)_5\overset{+V}{Os}{\equiv}N]^{3+} \xrightarrow[-\,2\,NH_3]{} [(H_3N)_4\overset{+VI}{Os}{\equiv}N]^{3+} + [(H_3N)_4\overset{+V}{Os}{\equiv}N]^{2+}$
Lb
La
Lc
Ld
c. $2\,[(H_3N)_4\overset{+V}{Os}{\equiv}N]^{2+} \longrightarrow [(H_3N)_4\overset{+VI}{Os}{\equiv}N]^{3+} + [(H_3N)_4\overset{+IV}{Os}{\equiv}N]^{+}$
Ld
Lc
Le
d. $2\,[(H_3N)_5\overset{+IV}{Os}{\equiv}N]^{+} + 3\,H^{+} + H_2O \longrightarrow [(H_3N)_4\overset{+V}{Os}{\equiv}N]^{2+} + [(H_3N)_4(H_2O)\overset{+III}{Os}(NH_3)]^{3+}$
Le
Ld
LXVIII

Scheme 40: Photolytic cleavage of **XLIXa** generates a unstable Os(V)-nitride **Ld**, which subsequently disproportionates and starts a cascade reaction, which finally gives **LXVIII**.[141]

Cummins' N_2-derived nitride $[Mo(N)(N(R)Ar)_3]$ (**XXXI**) reacts as a nucleophile, as predicted for a d^0-configurated early transition metal nitride. Besides aduct formation with Lewis-acids, such as BX_3 (X = F, Cl), AlX_3 (X = F, Cl, Br, I), $GaCl_3$, $InCl_3$, $GeCl_2$ or $SnCl_2$, the formation of imido-complexes ($[Mo{=}N{-}R]^+$) with MeI, TMS-OTf or *in situ* prepared PhC(O)-OTf has also been observed.[174]

The methyl-imido complex **LXIX**, obtained upon reaction of **XXXI** with MeI, can be deprotonated to yield in the formation of the respective ketimido complex **LXX**, which can be *C*-methylated to give the ethylimido-complex **LXXI** (Scheme 41, *top*). Remarkably, direct synthesis of the ethylimido-complex upon reaction of **XXXI** with EtOTf, EtI or $[Et_3O]BF_4$, was not successful.[174] In a related study, the group of *Cummins* was able to transform the N_2-derived nitride-ligand into cyanide. Reacting a mixture of $MeOCH_2Cl$ and $^iPr_3SiOTf$ with **XXXI** leads to formation of methoxymethylimide **LXXII**, whose deprotonation gave the respective alkoxyketimide **LXXIII**. Addition of $SnCl_2$ as Lewis-acid and Me_2NSiMe_3 as Brønsted-base yields in the formation of *C*-bound $[Mo(CN)(N(R)Ar)_3]$ (**LXXIV**, Scheme 41, *bottom*) .[175]

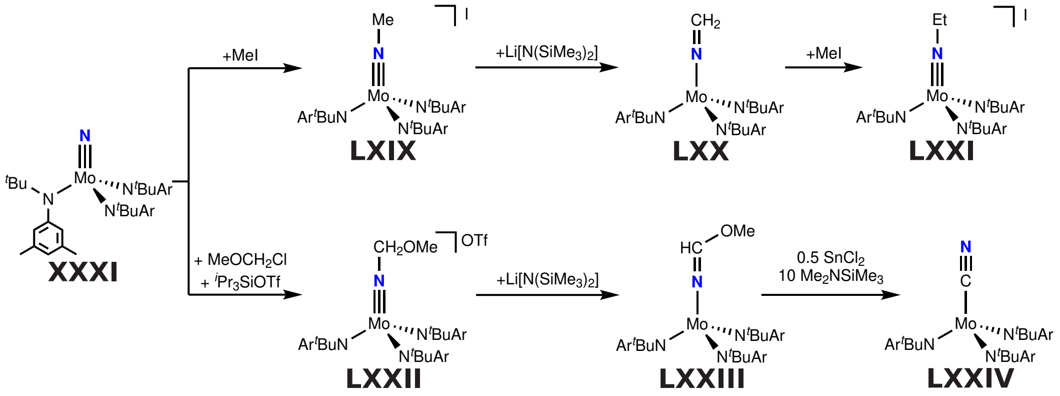
+MeI
+Li[N(SiMe3)2]
+MeI
+ MeOCH2Cl
+ iPr3SiOTf
+Li[N(SiMe3)2]
0.5 SnCl2
10 Me2NSiMe3
XXXI
LXIX
LXX
LXXI
LXXII
LXXIII
LXXIV

Scheme 41: *Top:* Sequential methylation of N$_2$-derived **XXXI** forms the ethylimido **LXXI**. *Bottom:* Generation of CN^- from **XXXI**.[174,175]

While reformation of **XXXI** from **LXXIV** was unsuccessful, the group of *Cummins* was able to generate organic nitriles R—C≡N from N$_2$ in a synthetic cycle (Scheme 42).[176] Acylation of N$_2$-derived **XXXI** using a RC(O)Cl/Me$_3$SiOTf-mixture (R = Me. Ph, ^{t}Bu) gives the respective acylimide complexe **LXXV**, which can be reduced with Mg/anthracene in the presence of Me$_3$SiOTf to give the respective trimethylsiloxyketimides **LXXVI**. Liberation of the respective nitrile was achieved *via* addition of a Lewis-acid, such as ZnCl$_2$ or SnCl$_2$, to give Mo(IV)-chloride **LXXVII**. Reduction of **LXXVII** gives [Mo(N(R)Ar)$_3$] (**XXX**), which binds and splitts N$_2$ to reform **XXXI**.[176]

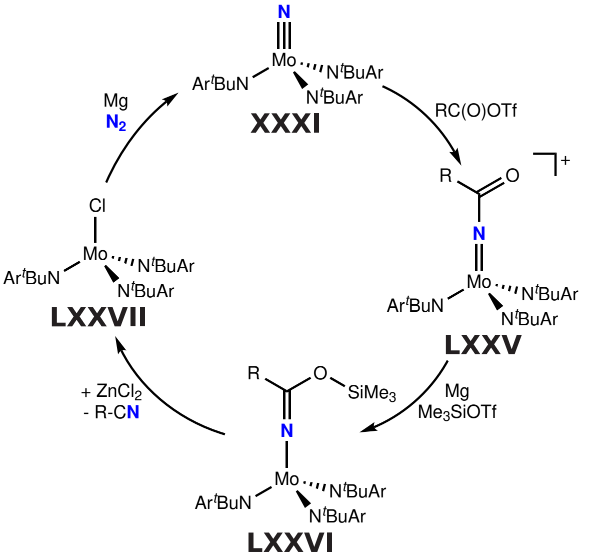
XXXI
RC(O)OTf
LXXV
Mg
Me3SiOTf
LXXVI
+ ZnCl2
- R-CN
LXXVII
Mg
N2

Scheme 42: Synthetic cycle to generate organic nitriles from N$_2$ (R = Me, Ph, ^{t}Bu).[176]

A similar synthetic cycle was achieved with already mentioned heterobimetallic **IV** (Figure 3), which cleaves the N_2-bond upon reduction to give Mo(VI)-nitride **XXXI** and anionic Nb(V) $[Nb(N)(N(R)Ar)_3]^-$ (**LXXVIII**, R = ^{i}Pr, Np, Scheme 43). The Nb-nitride **LXXVIII** is more reactive and releases the respective organic nitrile directly upon reaction with acyl chlorides under formation of a Nb(V) oxo-complex, $[Nb(O)(N(R)Ar)_3]$ (**LXXIX**). After reaction of **LXXIX** with trifluoromethanesulfonic anhydride giving $[Nb(OTf)_2(N(R)Ar)_3]$ (**LXXX**) and reduction with $CoCp_2$, the so obtained Nb(IV)-triflate $[Nb(OTf)(N(R)Ar)_3]$ (**LXXXI**) undergoes salt metathesis with $Na[Mo(N_2)(N(R)Ar)_3]$ (**LXXXII**) and reforms dinuclear **IV**.[62,177]

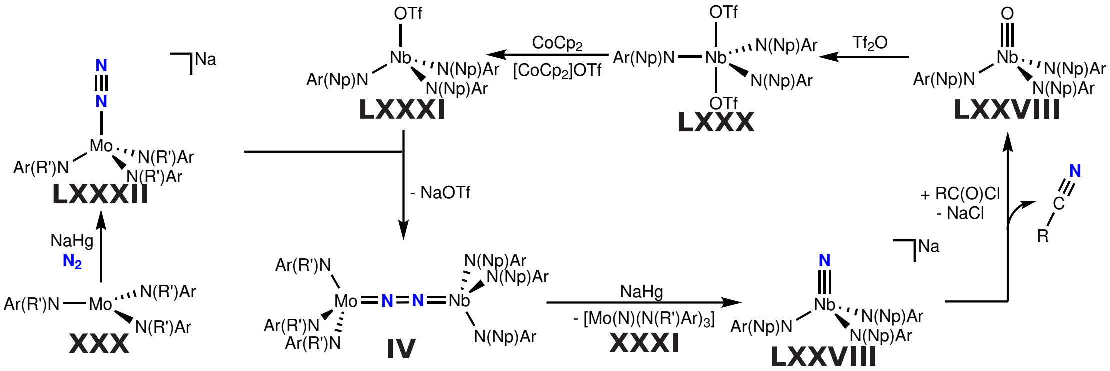
OTf
Nb
Ar(Np)N
N(Np)Ar
N(Np)Ar
LXXXI
CoCp2
[CoCp2]OTf
OTf
Ar(Np)N
Nb
N(Np)Ar
N(Np)Ar
OTf
LXXX
Tf2O
O
Nb
Ar(Np)N
N(Np)Ar
N(Np)Ar
LXXVIII
N
N
Na
Mo
Ar(R')N
N(R')Ar
N(R')Ar
LXXXII
- NaOTf
NaHg
N2
Ar(R')N
Mo
N(R')Ar
N(R')Ar
XXX
Ar(R')N
Mo
N
N
Nb
N(Np)Ar
N(Np)Ar
Ar(R')N
Ar(R')N
N(Np)Ar
IV
NaHg
- [Mo(N)(N(R')Ar)3]
XXXI
N
Nb
Na
Ar(Np)N
N(Np)Ar
N(Np)Ar
LXXVIII
+ RC(O)Cl
- NaCl
N
C
R

Scheme 43: Synthetic cycle for the formation of nitriles from N_2 and acyl chlorides using N_2-bridged heterobimetallic **IV** (R = Ad, Ph, ^{t}Bu; R' = Np, ^{t}Bu; Ar = 3,5-$Me_2C_6H_3$).[177]

The group of *Schneider* followed a different approach in which re-reduction of the metal-center does not rely on external reductants like in *Cummins'* case. In the first example, N_2-derived Re(V)-nitride **XXXVII** was used to produce acetonitrile in a synthetic cycle (Scheme 44).[146] In the first step, **XXXVII** is reacted with EtOTf to form the respective Re(V)-ethylimido **LXXXIII**, which can be deprotonated to give the respective ketimide **LXXXIV**. This deprotonation is accompanied by formal two electron reduction from Re(V) to Re(III) in which both electrons formally stem from the CH-bond of the α-carbon. Further deprotonation of this carbon-atom was reported to result also in two electron reduction of the Re-center and release of acetonitrile. However, the so formed Re(I)-species, **LXXXV**, requires strong acceptor-ligands, like iso-nitriles, for stabilization and does not activate N_2. Nevertheless, reaction of **LXXXIV** with two equivalents of *N*-chlorosuccinimide (NCS) liberates acetonitrile under formation of the Re(IV)-trichloro-complex **LXXXVI**. Closure of the synthetic cycle was achieved upon reduction of **LXXXVI** with NaHg in the presence of N_2 to reform nitride **XXXVII**.[146] Usage of *in situ* prepared $PhCH_2OTf$ instead of EtOTf yields in the formation of benzonitrile following a analogue mechanism.[178]

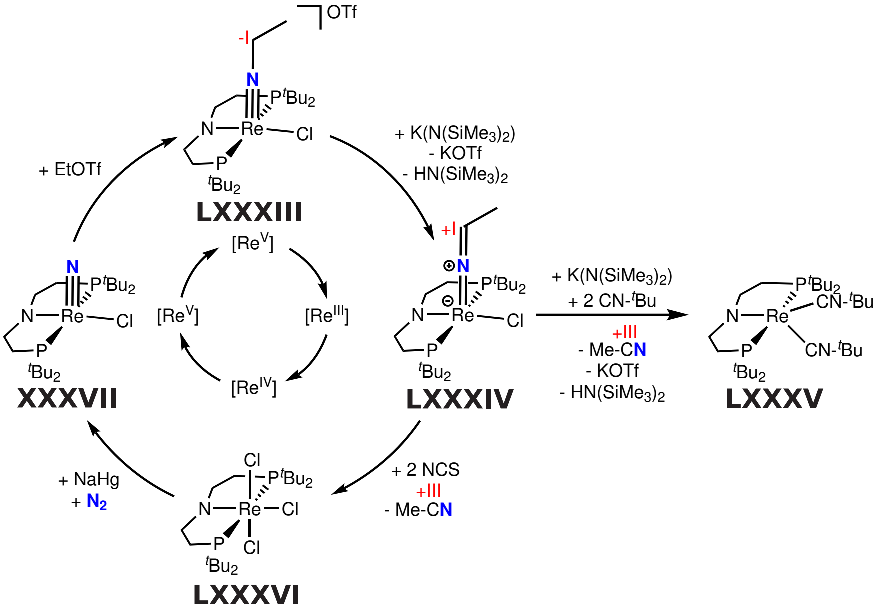

Scheme 44: Synthetic cycle for the generation of acetonitrile from N_2 using a Re-PNP-pincer-platform.[146]

Later the group of *Schneider* utilized [Re(N)Cl_2(^{H}PNP^{iPr})] (**XLIIb**) for C-N-coupling in a synthetic cycle (Scheme 45).[71] In contrast to **XXXVII**, functionalization of **XLIIb** does not rely on very strong electrophiles, like alkyltriflates. Therefore C-N-coupling could be achieved using benzoylchloride (PhC(O)Cl), which releases a mixture of benzamide ($PhC(O)NH_2$), benzoic acid ($PhCO_2H$) and benzonitrile (PhCN). The appearance of benzoic acid and benzonitrile is a result of a reaction of benzoylchloride with immediate formed benzamide. Interestingly, both protons, required for the formation of $PhC(O)NH_2$, stem from the ligand backbone, which serves as a $2H^+/e^-$-donor and is oxidized to give Re(III) imine-complex **LXXXVII**. Re-reduction of the ligand backbone was accomplished *via* stepwise addition of Li[$HBEt_3$] and [Ph_2NH_2]Cl. The so-formed Re(III)-trichloro-complex **LXXXVIII** can be reduced under N_2-atmosphere to yield the N_2-bridged dinuclear **XIII**. However, the yields following this route are relatively low most likely due to the formation of hydride-complexes. Therefore, the group of *Schneider* investigated the electrochemical reduction of the ligand-backbone using controlled potential electrolysis (CPE). CPE (E^{appl} = -1.65 V) of **LXXXVII** in the presence of a suitable acid (2,6-dichlorophenol) yielded **LXXXVIII** almost quantitatively, which allowed its subsequent electrochemical reduction to **XIII** *via* CPE using a lower potential (E^{appl} = -1.85 V). Irradiation of **XIII** cleaves to N_2-bond and reforms **XLIIb** to close the synthetic cycle.[71]

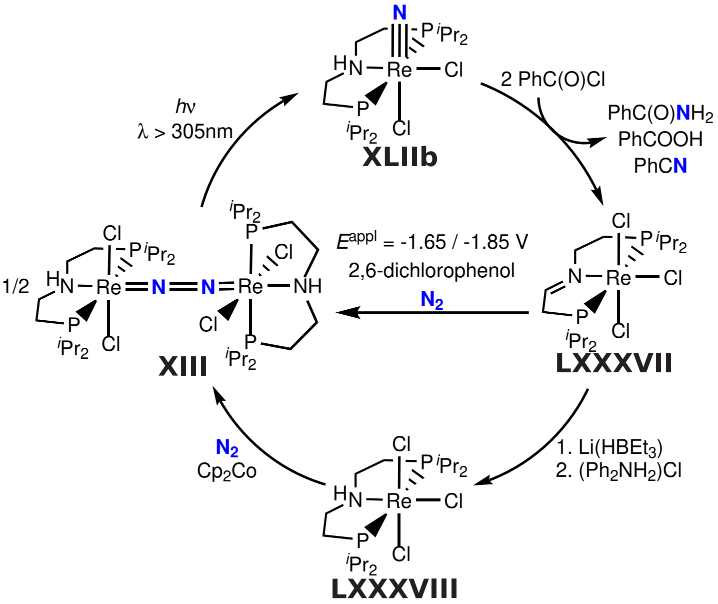
hν
λ > 305nm
XLIIb
2 PhC(O)Cl
PhC(O)NH2
PhCOOH
PhCN
E^appl = -1.65 / -1.85 V
2,6-dichlorophenol
N2
1/2
XIII
LXXXVII
1. Li(HBEt3)
2. (Ph2NH2)Cl
N2
Cp2Co
LXXXVIII

Scheme 45: Three step synthetic cycle for the formation of benzamide, benzonitrile and benzoic acid from benzoylchloride and N_2, including photolytic N_2-cleavage and electrochemical re-reduction of the ligand-backbone.[71]

All above discussed examples illustrate some general aspects and strategies for the incooperation of N_2 into organic molecules. Cleavage of the strong N≡N bond is often accompanied by the formation of strong M≡N-bonds, which require strong electrophiles to be functionalized. This drawback can be overcome with different strategies, like for example the formation of strong N≡C-bonds, like in nitriles, which counterbalance the high energy demand for N_2-cleavage.[146,175–177] Alternatively, N_2-splitting into less stabilized nitrides, like in Scheme 45, allows the usage of weaker electrophiles. The reduced thermodynamic driving force typically leads to higher kinetik barriers for N_2-cleavage, which may be overcome by photolysis.[71] Re-reduction the metal-center should ideally proceed without an additional reagent or electrochemically.[179]

1.3.3 Generation of cyanate from N_2-derived nitrides

Sodium and potassium cyanate salts are used in a variety of applications, like steel hardening, in agrochemical processes or also for the synthesis of fine chemicals or pharmaceuticals. The worldwide yearly demand ranges around 8 to 10 Mt, which are industrially produced upon reacting sodium or potassium carbonate with urea at temperatures above 400 °C to give sodium or potassium cyanate, respectively.[180]

$$2\ H_2N(CO)NH_2 + M_2CO_3 \xrightarrow[400°C]{} 2\ MOCN + (NH_4)_2CO_3 \qquad (1.2)$$

Taking into account that urea itself is produced from carbondioxide and ammonia at high pressures (eqn. 1.3), the overall atom-efficiency for the production of cyanates is relatively low.[181]

$$2\ H_3N + CO_2 \longrightarrow H_2N(CO)NH_2 + H_2O \qquad (1.3)$$

In an alternative approach, cyanates can be generated directly from a metal-nitride and CO. Reformation of the nitride and eviction of the cyanate ligand requires in principle only the addition of one electron and N_2 (Scheme 46). Besides that no other reagents are required, which marks this reaction as potentially very atom efficient. The reduction can be driven electrochemically or *via* addition of a suitable reductant, in case of potassium the reaction is enthalpically favored by -73.4 kcal·mol^{-1}.[179,182,183]

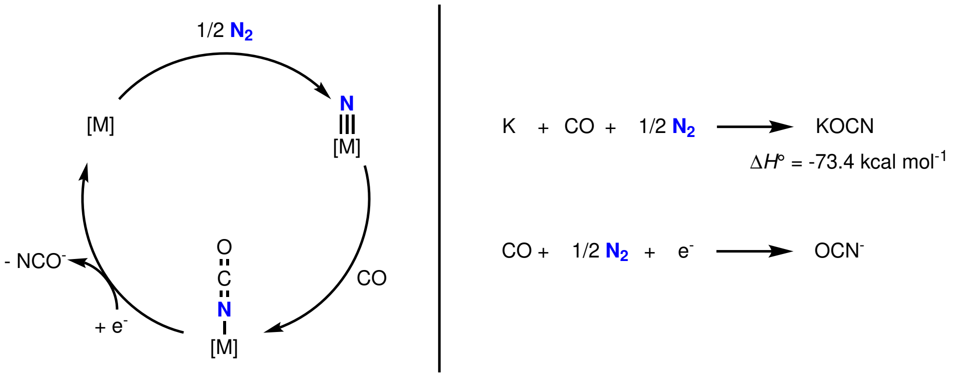

Scheme 46: *left:* An idealized cycle for the formation of cyanate from N_2 and CO. *right:* Overall equations for the formation of potassium cyanate and cyanate.[179,182,183]

Coupling of terminal nitrides with CO has been reported for several, non-N_2-derived nitrides,[184–189] also the CO-mediated cleavage of N_2 under the formation of cyanate has also been reported (see for example Scheme 13).[18,107,108,110] In contrast, coupling of terminal N_2-derived nitrides with CO is surprisingly scarce and has, so far, only been reported once.[179,190]

Cummins presented the coupling of CO with non-N_2-derived Na[V(N)(N(^{t}Bu)Ar)$_3$] (**LXXXIX**), which is the vanadium analogue to N_2-derived **XXXI** (Scheme 47, *top*). Addition of CO to **LXXXIX** results in liberation of NaOCN and formation of [V(N(^{t}Bu)Ar)$_3$] (**XC**), which is not capable for N_2-binding and/or -splitting.[186]
In constrast, no reaction with CO was observed for the Nb-analogue, Na[Nb(N)(N(^{t}Bu)Ar)$_3$] (**XCI**). Instead, reduction of independently prepared [Nb(NCO)(N(^{t}Bu)Ar)$_3$] (**XCII**) results in the reverse: breakage of the C-N-bond, liberation of CO and formation of nitride **XCI** (Scheme 47, *bottom*).[191]
However, neither for the N_2-derived Mo(VI)-nitride **XXXI** nor for the N_2-derived Nb(V)-nitrides [Nb(N)(N(R)Ar)$_3$]$^-$ (**LXXVIII**, R = ^{i}Pr, Np) CN-coupling with CO was reported. Decarbonylation of the independently prepared cyanate complex, [Mo(NCO)(N(^{t}Bu)Ar)$_3$] (**XCIII**), was also not feasable.[179]

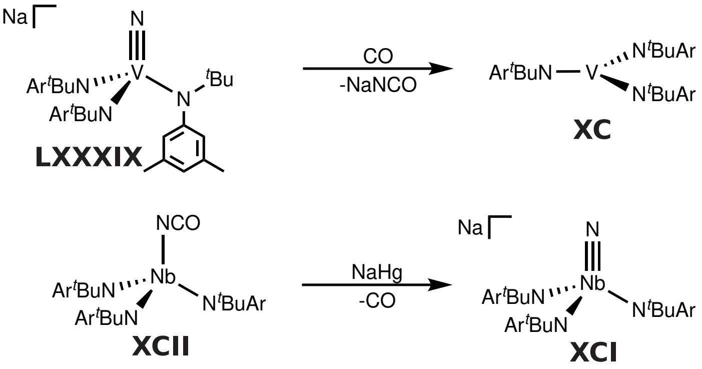

Scheme 47: *Top:* Coupling of a non-N_2-derived V(V)-nitride **LXXXIX** with CO results in formation of NaOCN. *Bottom:* Reduction of the Nb(IV)-cyanate **XCII** results in decarbonylation and formation of the Nb(V)-nitride **XCI**.[186,191]

Cummins proposed the CN-bond formation in **LXXXIX** to occur *via* nucleophilic attack of the nitride on the incoming carbonyl, although initial coordination of the CO-ligand to the metal-center could not be fully excluded.
Such an alternative mechanism was proposed, supported by DFT-calculations, by the group of *Liddle* for non-N_2-derived Tren^{TIPS}-supported uranium nitrides (Tren^{TIPS} = N(CH$_2$CH$_2$NSi^{i}Pr$_3$)$_3$).[188] Carbonylation of [U(N)(Tren^{TIPS})]^n (n = 0 **XCIVa**; n = 1- **XCIVb**) results in formation of the respective cyanate complexes [U(NCO)(Tren^{TIPS})]^n (n = 0 **XCVa**; n = 1- **XCVb**) (Scheme 48). Notably, the reaction proceeds on very different time-scales depending on the oxidation state. While the carbonylation of the U(VI)-nitride **XCIVa** is slow (≈16 h), the anionic U(V)-congener reacts instantaneously with CO even at -78 °C.[188] Computational examination of the reaction revealed a transition state with a η^2_{CN}-bound cyanate-ligand indicating precoordination of the carbonyl-ligand (Scheme 48; *right*). The smaller size of U(VI) compared to U(V) makes such a precoordination more energetically costly, which is expressed in the higher barrier for CN-coupling for the U(VI)-nitride compared to its U(V)-congener.[188]

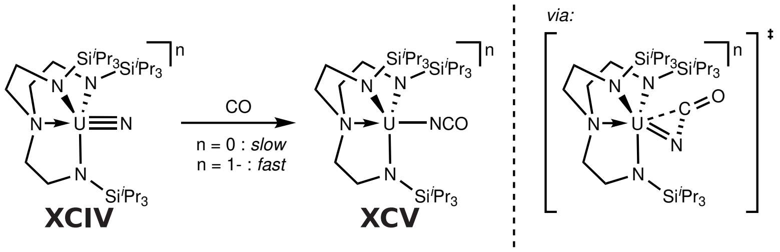

Scheme 48: *left:* Carbonylation of **XCIV** results in CN-coupling to give **XCV** on different time-scales depending on the oxidation state. *right:* The proposed transition state of CN-coupling.[188]

Similar observations were made by the group of *Agapie* using a *para*-terphenyl-diphosphine supported Mo-nitride (**XCVIIa**; Scheme 49). Carbonylation of the formal Mo(IV)-nitride, **XCVIIa**, results in coordination of CO to the metal center and formation of six-coordinate **XCVIIb**, whose further reduction leads to CO loss and reformation of **XCVIIa** accompanied by other decomposition products.[189]
In contrast, two electron-reduction of **XCVIIa** yields formal Mo(II)-nitride **XCVIIc**, which readily reacts with CO to give NaOCN together with the mono- and tris-carbonyl complexes, **XCVIId** and **XCVIIe**, respectively. Although the mechanism of CN-coupling remains elusive, the different reactivity of **XCVIIc** compared to **XCVIIa** was accounted to its coordinative unsaturation and its lower valency.[189]

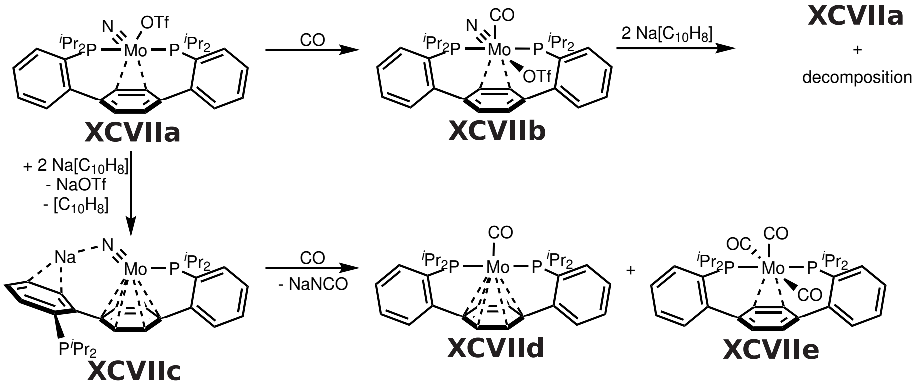

Scheme 49: Carbonylation of *Agapie's* Mo(IV)-nitride **XCVIIa** results in CO coordination, while carbonylation of the corresponinding Mo(II)-nitride **XCVIIa** gives NaOCN.[189]

By now, the only example for a full synthetic cycle for the transformation of N_2 and CO into cyanate has been reported by *Kawaguchi* (Scheme 50).[190] Reduction of [V(thf)(ONO)] (**XCVIIIa**, $[ONO]^{3-} = 2,6\text{-}(3\text{-}^t\text{Bu-5-Me-2-OC}_6H_2CH_2)\text{-4-}^t\text{Bu-}$ (*p*-tolyl)NC_6H_4) with two equiv. potassium hydride results in formation of the bis-nitride bridged dinuclear $[\{K(dme)\}_2\{(\mu\text{ -N})V(ONO)\}]_2$ (**XCVIIIb**). Oxidation of **XCVIIIb** with benzoquinone results in breakage of the nitride-bridges and formation of the terminal V(V)-nitride $[V(N)(ONO)]^-$ (**XCVIIIc**).

Notably, re-reduction of **XCVIIIc** with either KH or KC_8 to give **XCVIIIb** was unsuccessful, indicating that **XCVIIIc** is no intermediate in the N_2-splitting process from **XCVIIIa** to **XCVIIIb**.[190]

Again different selectivity, depending on the oxidation state, was observed. While carbonylation of V(IV)-nitride **XCVIIIb** forms a mixture of $[V(NCO)(ONO)]^-$ (**XCVIIId**) and other unidentified products, reaction of V(V)-nitride **XCVIIIc** with CO (22 bar) results in quantitative formation of **XCVIIId** after two days. Liberation of the formed cyanate ligand as KNCO was achieved upon addition of 2-butyne in toluene in quantitative yield. The so formed $[V(\eta^2\text{-MeCCMe})(ONO)]$ (**XCVIIIe**) can be dissolved in THF to give starting compound **XCVIIIa**, closing the synthetic cycle.[190]

XCVIIIc was also functionalized with isocyanides. Addition of excess CN-Xyl (Xyl = 2,6-$Me_2C_6H_3$) followed by addition of a cryptand forms the corresponding carbodiimide complex **XCVIIIf**. Without additional cryptand the potassium ion is bound to the ONO-ligand and the vanadium-ion is pentacoordinated carrying an additional CN-Xyl ligand, which is released upon addition of cryptand. However, addition of alkynes to **XCVIIIf** results not in liberation of K(NCN-Xyl).[190]

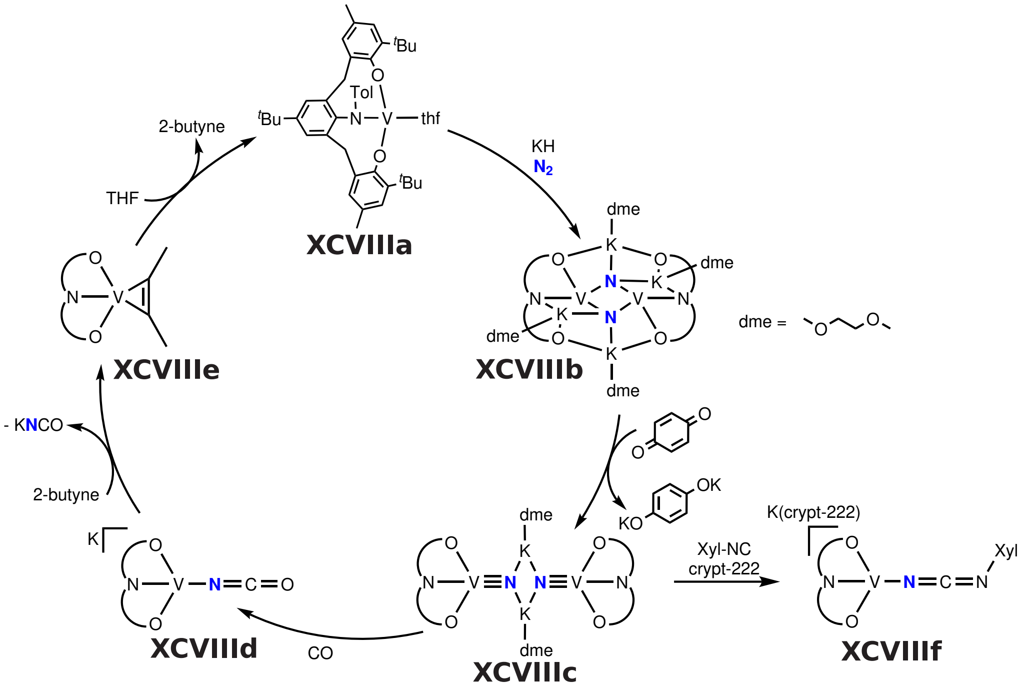

tBu
O
Tol
tBu
N
V
thf
O
tBu
XCVIIIa
KH
N2
2-butyne
THF
dme
K
O
O
dme
N
K
N
V
V
N
K
N
dme
O
O
K
dme
XCVIIIb
dme =
O
O
XCVIIIe
O
N
V
O
- KNCO
2-butyne
O
O
KO
OK
K
O
N
V
N=C=O
O
XCVIIId
CO
dme
K
O
O
N
V≡N
N≡V
N
O
O
K
dme
XCVIIIc
Xyl-NC
crypt-222
K(crypt-222)
O
N
V
N=C=N
Xyl
O
XCVIIIf

Scheme 50: Synthetic cycle for the transformation of N_2 and CO into cyante mediated by a V(ONO)-platform.[190]

This example showcases that the formation of cyante from N_2 and CO, following an N_2-splitting route (Scheme 46), is feasable. However, catalytic turnover is prevented by the requirement of reductant for N_2-cleavage and an oxidant to form **XCVIIIc**. Another drawback is the need for elevated CO-pressures and the addition of an external reagent, 2-butyne, to release the formed cyanate.[190]

1.4 Scope of this work

While there are many examples for N_2-cleavage using Mo-complexes, tungsten mediated N_2-splitting is surprisingly rare and has so far only been reported once.
Taking the established $[(N_2)\{MoCl(PNP)\}_2]$ (**XI**)[70] as inspiration, the tungsten analogue, $[(N_2)\{WCl(PNP)\}_2]$ (**1**), was synthesized and characterized in order to rationalize the influence of the metal center on the structural and spectroscopic properties of such N_2-bridged dinuclear compounds. To further corroborate the proposed bonding-picture (Scheme 8), the oxidation of **1** and its influence on the degree of N_2-activation was analyzed.

Previous studies showed, that the selectivity between competing N_2-reduction and H^+-reduction relies on many different factors, such as the reduction potential, the acid strength and also the acid counterion (see chapter 1.2.1). Therefore, the reactivity of $[(N_2)\{WCl(PNP)\}_2]$ (**1**) with respect to proton-induced N_2-cleavage shall be examined and compared with the Mo-analogue **XI** to show the impact of the metal-ion changing from Mo to W. Furthermore, the influence of the acid and reaction temperature was deeply examined in order to provide guidelines how to suppress competing proton-reduction.

In comparison to $[(N_2)\{ReCl(PNP)\}_2]$ (**XII**), both group 6 congeners, $[(N_2)\{MCl(PNP)\}_2]$ ($M = Mo$ **XI**, W **1**), lack two electrons for direct cleavage of the N_2-bridge.[15,36,70] Therefore, the reduction of **1** is attempted and both chloro-ligands are exchanged *versus* suitable neutral ligands. The targeted $\{\pi^{10}\delta^4\}$-compound shall be characterized in terms of its electronic structure to further support the bonding-picture shown in Scheme 8. Due to its π-electron-count, this $\{\pi^{10}\delta^4\}$-compound should be capable of N_2-cleavage, either thermally or photolytically, which will be explored and analyzed.

The obtained nitrides are functionalized *via* CN-coupling reactions aiming the formation of heterocummulenes, whose strong CN-bonds provide some driving force to overcome the cleavage of the strong W≡N-bond.[192] In an ideal case, the formed heterocummulene is liberated under reformation of a suitable precursor for N_2-binding and/or -cleavage, which would allow the formation of the respective heterocummulene in a synthetic cycle providing guidelines towards a catalytic approach.

2 Results and Discussion

2.1 Synthesis and Characterization of N_2-bridged Ditungsten-PNP-Complexes

2.1.1 Redox-series $[(N_2)\{WCl(PNP)\}_2]^{n+}$ (n = 0-2)[a]

Complexation of commercially available WCl_4 with ^{H}PNP ($^{H}\mathrm{PNP} = \mathrm{HN(CH_2CH_2P^tBu_2)_2}$) in the presence of NEt_3 as base gives [WCl_3(PNP)] (**5**) in yields up to 60%. The ^{1}H NMR spectrum features three sharp, but paramagnetically shifted signals ($\delta_H = 9.13$ (CH_2), 0.82 (^{t}Bu), -139.5 ppm (CH_2)), while no signal could be detected in the $^{31}P\{^1H\}$ NMR spectrum. The magnetic moment in solution ($\mu_{eff} = 2.8 \pm 0.1 \mu_B$) derived by *Evans'* method is in agreement with the formation of a d^2 high spin complex. The molecular structure obtained by X-ray diffraction (Figure 11) shows a tungsten ion in an octahedral coordination sphere and closely reassembles the molecular structures of the already reported Re- and Mo- analogues [MCl_3(PNP)] (M = Re (**LXXXVI**), Mo (**XCIX**)).[70,146]

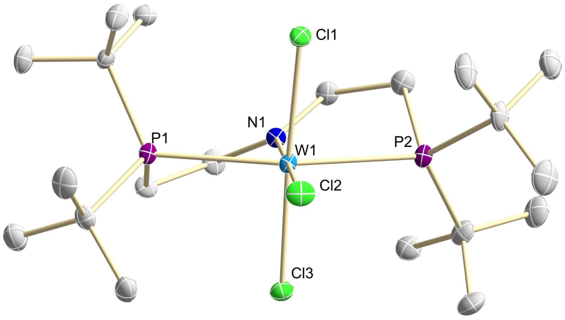

Figure 11: Molecular structure of **5** in the crystal obtained by single crystal X-ray diffraction. Hydrogen atoms were omitted for clarity. Selected bond lengths [Å] and angles [°]: W1-Cl1 2.4020(9), W1-Cl2 2.4137(9), W1-Cl3 2.3811(9), W1-N1 1.938(3), W1-P1 2.5683(9), W1-P2 2.5873(9); Cl1-W1-Cl3 175.71(3), N1-W1-Cl1 91.76(9), N1-W1-Cl2 178.56(9), N1-W1-Cl3 91.91(9), P1-W1-P2 157.28(3).

With successful synthesis of **5** in hand, its N_2-activation capability was examined. Reduction of **5** with 2 equiv. of NaHg under N_2-atmosphere in THF yields in the formation of green, N_2-bridged [$(N_2)\{WCl(PNP)\}_2$] (**1**) in isolated yields up to 66% (Scheme 51). The molecular structure in the solid state features an μ^2:η^1:η^1-N_2 ligand bridging the apical coordination sites of two W ions in distorted square-pyramidal geometry ($\tau_5 = 0.35$, Figure 12).[193] Both {WCl(PNP)}-fragments are twisted with respect to another leading to an idealized C_2-symmetry (Cl1-W1-W1#-Cl1#: 89.59°/ 92.27°). This twist of the {WCl(PNP)}-units is attributed to the large steric bulk of the ^{t}Bu-substituents and was also observed for the Re- (**XII**) and Mo-analogues (**XI**).[36,70]

---

[a] Parts of this work have been published in: "Selectivity of tungsten mediated dinitrogen splitting *vs.* proton reduction", B. Schluschaß, J. Abbenseth, S. Demeshko, M. Finger, A. Franke, C. Herwig, C. Würtele, I. Ivanovic-Burmazovic, C. Limberg, J. Telser, S. Schneider, *Chemical Science*, **2019**, *10*, 10275-10282.

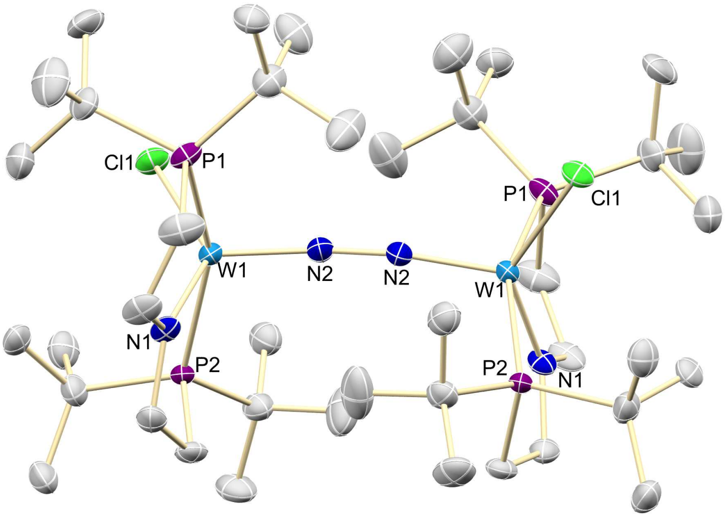

Figure 12: Molecular structure of **1** in the crystal obtained by single crystal X-ray diffraction. Hydrogen atoms were omitted for clarity. Furthermore only one of the two independent molecules in the asymmetric unit is shown. Selected bond lengths [Å] and angles [°]: N2-N2# 1.33(4)/1.27(8), W1-Cl1 2.5082(16)/2.576(4), W1-N1 1.938(6)/1.893(11), W1-N2 1.78(2)/1.82(4), W1-P1 2.444(4)/2.468(4), W1-P2 2.483(4)/2.417(8); Cl1-W1-N1 135.67(16)/135.7(4), Cl1-W1-N2 109.4(3)/106.2(7), N1-W1-N2 135.67(16)/135.7(4), N2-N2#-W1 163.8(18)/160(4), P1-W1-P2 156.91(12)/156.8(3).

The C_2-symmetry persists in solution, as indicated by the presence of two doublets (δ_P = 92.9, 87.8 ppm) with large *trans*-coupling ($^2J_{PP}$ = 147 Hz) in the $^{31}P\{^1H\}$ NMR spectrum. Upon reduction of **5** under $^{15}N_2$-atmosphere one singlet at 31.1 ppm was observed in the $^{15}N\{^1H\}$ NMR spectrum, confirming the synthesis of ^{15}N-**1** and atmospheric N_2-uptake. Comparison of the Raman spectra of ^{14}N-**1** and ^{15}N-**1** give rise to the N-N stretching frequency ($\tilde{\nu}_{NN}$(^{14}N-**1**) = 1392 cm^{-1}, $\tilde{\nu}_{NN}$(^{15}N-**1**) = 1347 cm^{-1}, λ_{exc} = 457 nm, THF solution), which is in between the values for free hydrazine ($\tilde{\nu}_{NN}$ = 1076 cm^{-1}) and *trans*-diazene ($\tilde{\nu}_{NN}$ = 1529 cm^{-1}) (Table 1).[22] These values imply a relatively high degree of N_2-activation, which is further supported by the short W-N_2 (d_{WN_2} = 1.78(2)/1.82(4) Å) and the long N-N distances (d_{NN} = 1.33(4)/1.27(8) Å).

Next the redox chemistry of **1** was examined using cyclic voltammetry (CV, Figure 13). Besides two reversible oxidation waves at low potentials (E_1 = -1.39 V and E_2 = -0.91 V, vs. Fc^+/Fc in THF) no further redox events could be detected in the range of -2.9 to 0.6 V. Compared to the Mo-analogue (**XI**), which also shows two reservible oxidation events (E_1 = -1.14 V and E_2 = -0.64 V, vs. Fc^+/Fc in THF), the observed oxidation potentials are cathodically shifted, implying the nature of these oxidations being metal centered.

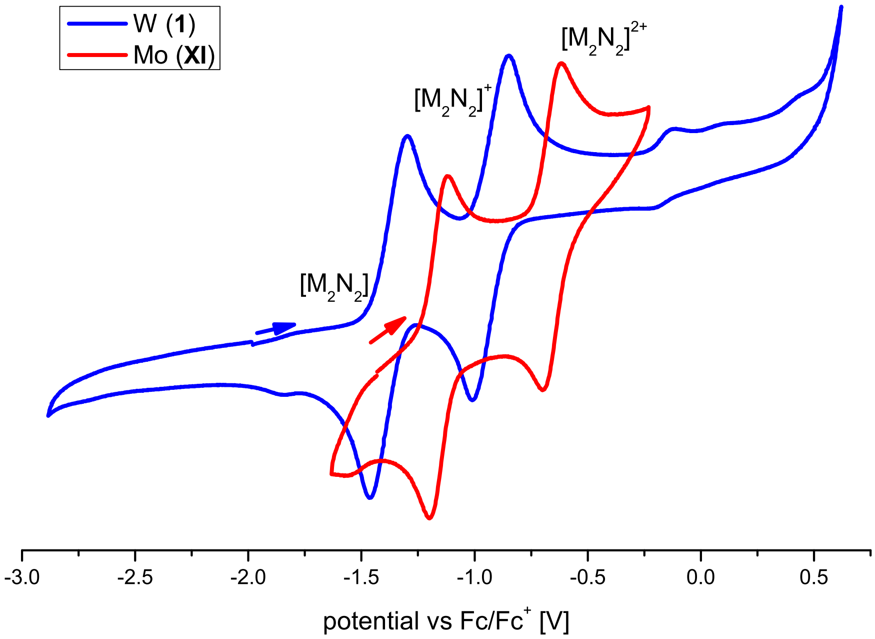

Figure 13: Comparison of the cyclic voltammograms of **1** (blue) and **XI** (red) (both 100 mV/s, THF, Ar).[70]

Chemical oxidation of **1** with either one or two equivalents of silver-salts, results in formation of monocationic $[(N_2)\{WCl(PNP)\}_2]^+$ (**2**) or dicationic $[(N_2)\{WCl(PNP)\}_2]^{2+}$ (**3**), respectively (Scheme 51). Stabilization of **3** requires usage of weakly coordinating anions such as $[BPh_4]^-$ or $[Al(OC(CF_3)_3)_4]^-$.

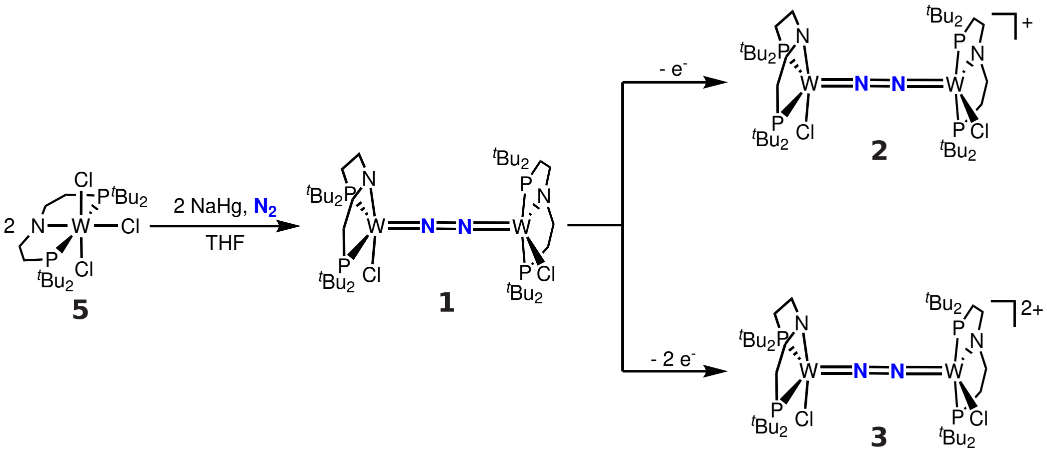

Scheme 51: Synthesis of **1** and its further one or two electron oxidation to **2** and **3**, respectively.

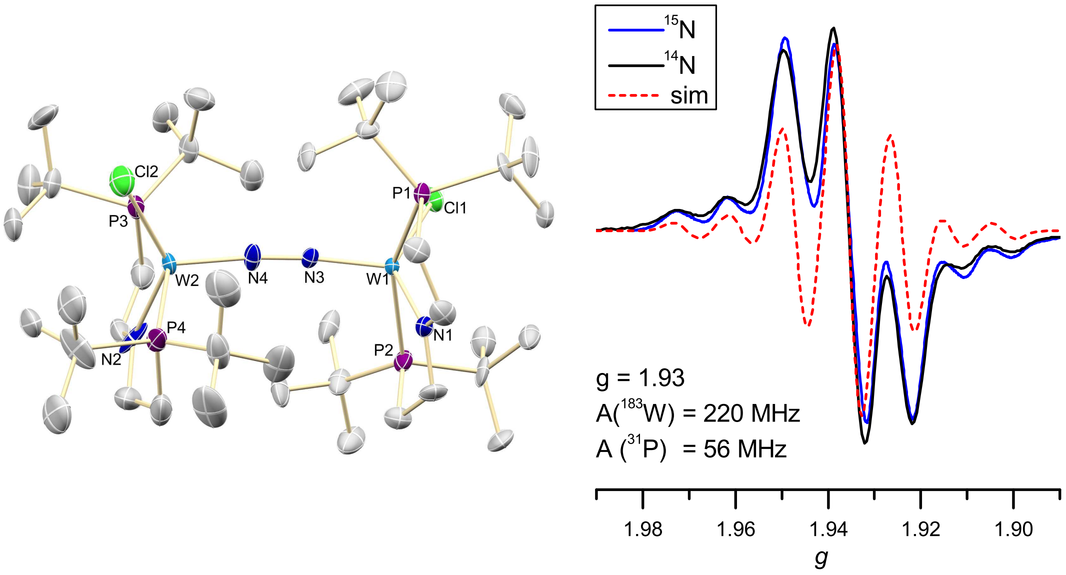

Figure 14: *left*: Molecular structure of **2** in the crystal obtained by single crystal X-ray diffraction. Hydrogen atoms, the triflate anion and co-crystalized solvent molecules were omitted for clarity. Selected bond lengths [Å] and angles [°]: N3-N4 1.266(12), W1-Cl1 2.366(3), W2-Cl2 2.446(3), W1-N1 1.993(10), W2-N2 2.093(13), W1-N3 1.781(9), W2-N4 1.813(10), W1-P1 2.524(3), W1-P2 2.522(3), W2-P3 2.504(4), W2-P4 2.471(3); Cl1-W1-N1 136.0(3), Cl2-W2-N2 133.7(3), W1-N3-N4 169.7(8), W2-N3-N4 172.3(10), N1-W1-N3 114.2(4), N2-W2-N4 113.0(5), P1-W1-P2 154.94(10), P3-W2-P4 154.55(12). *right*: EPR-spectrum of **2** (X-band, THF, r.t.).

The molecular structure of monocationic **2** (Figure 14, *left*) shows distinct differences compared to the one of **1**. Although the N-N distance is nearly unchanged ($d_{NN} = 1.277(5)$ Å), the bond lengths around each tungsten ion in **2** are slightly different, indicating valence localization due to metal centered oxidation, which is in agreement with the large comproportionation constant ($K_c \approx 10^8$) derived from both oxidation potentials.

The EPR spectrum (X-band, r.t.) of **2** shows an isotopic signal ($g_{av} = 1.93$) with hyperfine interaction (HFI) with only one tungsten ($A(^{183}W) = 220$ MHz) and two phosphorous atoms ($A(^{31}P) = 56$ MHz). HFI with the bridging N_2-ligand was not found, as the ^{14}N- and ^{15}N-isotopologues give identical spectra further supporting metal centered oxidation (Figure 14, *right*).

Nevertheless, **2** appears C_2-symmetric on the slow NMR time scale, as its ^{1}H NMR spectrum features four intense, but broad and paramagnetically shifted signals ($\delta_H = 3.13$, 2.99, 2.51 and 2.38 ppm), which could be assigned to the ^{t}Bu-groups, and seven of the expected eight resonances for the ligand backbone.

The N-N stretching frequency ($\tilde{\nu}_{NN}(^{14}$N-**2**$) = 1414$ cm^{-1}, $\tilde{\nu}_{NN}(^{15}$N-**2**$) = 1360$ cm^{-1}, $\lambda_{exc} = 457$ nm, THF solution) is nearly unimpaired compared to **1**.

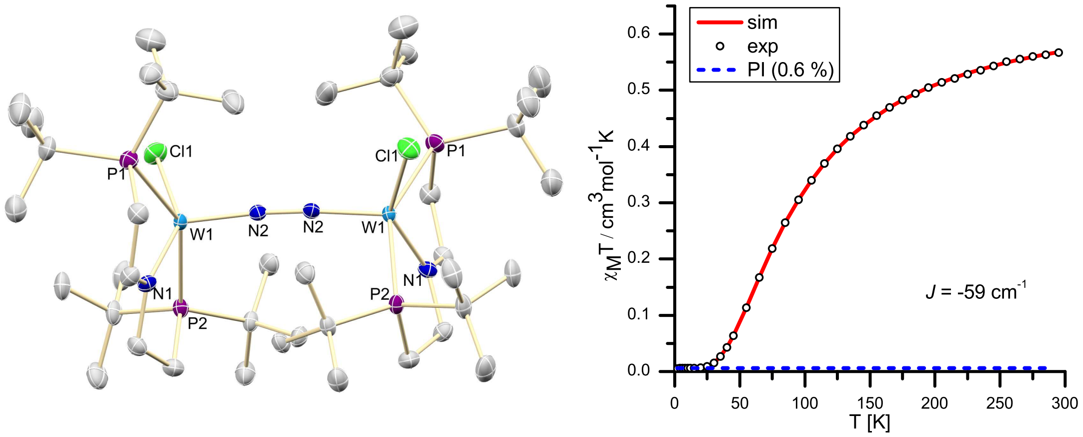

Figure 15: *left*: Molecular structure of **3** in the crystal obtained by single crystal X-ray diffraction. Hydrogen atoms, the tetraphenylborate-anion and co-crystalized solvent molecules were omitted for clarity. Selected bond lengths [Å] and angles [°]: N2-N2# 1.277(5), W1-Cl1 2.3507(8), W1-N1 1.983(3), W1-N2 1.785(2), W1-P1 2.5535(8), W1-P2 2.5269(8); Cl1-W1-N1 105.53(8), Cl1-W1-N2 142.77(7), N1-W1-N2 111.71(10), N2-N2#-W1 169.7(3), P1-W1-P2 150.21(3). *right*: χ_MT vs. T plot for **2**-$[Al(OC(CF_3)_3)_4]_2$. The open circles are the observed susceptibility, the red solid line corresponds to the best fit with the parameters g = 1.90, $J = -59$ cm^{-1}, TIP = $230 \cdot 10^{-6}$ cm^{3}mol^{-1} and PI = 0.6% ($S = 1$, the blue broken line, PI: paramagnetic impurity).

Two electron oxidation of **1** gives dicationic **3**, whose ^{1}H NMR spectrum features four intense but paramagnetically shifted signals for the ^{t}Bu-groups (δ_H = 4.32, 4.19, 3.78 and 3.49 ppm) and eight signals for the ligand backbone, as expected for such a dinuclear C_2-symmetric molecule. No signal could be detected in the ^{31}P{^{1}H} NMR spectrum. Magnetic characterization of dicationic **3** derived by SQUID magnetometry reveals a $\chi_M T$ product of 0.6 cm^{3}mol^{-1}K^{-1} at r.t., which gradually drops to 0 at about 20 K. The data was fitted to a model with two weakly antiferromagnetically coupled (J = -59 cm^{-1}) low spin (S = 1/2) ions, indicating that the second oxidation is also metal centered (Figure 15, *right*).

In the solid state dicationic **3** appears C_2-symmetric with identical bond lengths around each tungsten center (Figure 15, *left*). The NN bond distance (d_{NN} = 1.266(12) Å) as well as the N-N stretching frequency ($\tilde{\nu}_{NN}$(^{14}N-**3**) = 1400 cm^{-1}, $\tilde{\nu}_{NN}$(^{15}N-**3**) = 1356 cm^{-1}, λ_{exc} = 514.5 nm, THF solution) are both nearly unchanged compared to **1** or **2**.

Table 6: Comparison of the structural and spectroscopic features of the bridging N_2 ligand in **1**, **2** and **3** with the Mo-congener **XI** and *Cummins'* dicationic **III**.[61,70]

	1	**2**	**3**	**XI**	**III**
d_{NN} [Å]	1.33(4)/1.27(8)	1.277(5)	1.266(12)	1.258(9)	1.265(5)
$\tilde{\nu}$ ($^{14}N_2$) [cm^{-1}]	1392	1414	1400	1343	1349
$\tilde{\nu}$ ($^{15}N_2$) [cm^{-1}]	1347	1360	1356	-	-

Overall, the structural and spectroscopic features of **1**, **2** and **3** exhibit a unimpaired degree of activation of the bridging N_2-ligand upon oxidation (Table 6). Following the simple bonding model expressed by the MO-scheme for such N_2-bridged dinuclear compounds neutral **1** features $\{\pi^8\delta^4\}$-configuration (Scheme 52, *left*). The eight π-electrons within the {MNNM}-manifold lead to a relatively high degree of N_2-activation, similar to the Mo-analogue **XI** or *Cummins'* dicationic **III** (Table 6).[61,70] The small differences are attributed to slightly reduced backbonding of the 5d-metal. The four additional electrons, compared to **III**, are populating metal centered δ-orbitals with non-bonding character with respect to the bridging N_2ligand (Scheme 52).

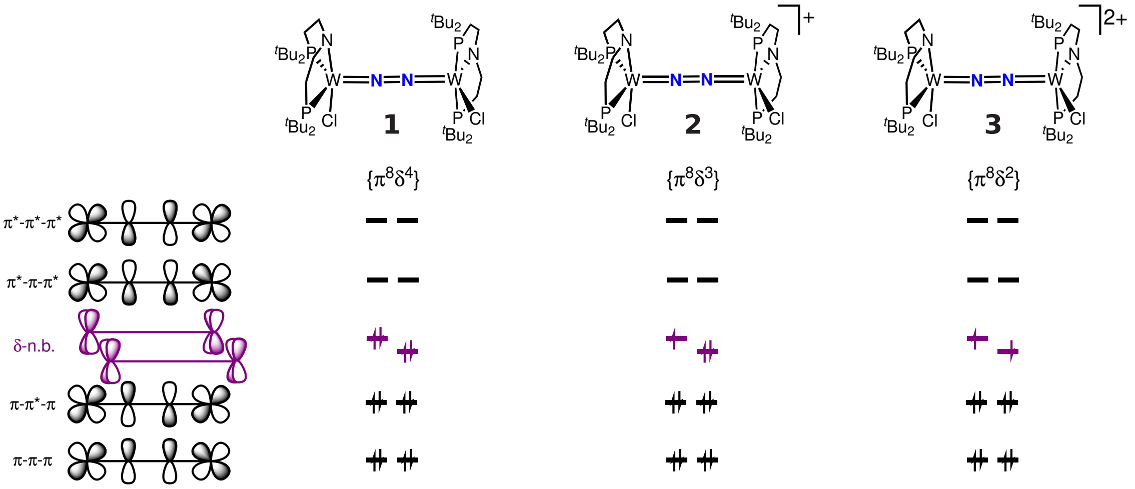

Scheme 52: Qualitative molecular orbital scheme of **1** (*left*), **2** (*middle*) and **3** (*right*)

One electron oxidation of **1** removes one electron from the δ-orbitals to give $\{\pi^8\delta^3\}$-configured **2** (Scheme 52, *middle*). Due to the NN-non-bonding character of these orbitals the bridging N_2 ligand remains unaffected, while one of the two tungsten ions gets oxidized, which results in loss of the C_2-symmetry and a SOMO, which is located on only one metal center. The second oxidation is located on the second tungsten ion and removes another electron from the δ-orbitals. Accordingly, both {WCl(PNP)}-fragments become identical and host both one unpaired electron. The orthogonality of the δ-orbitals to the {WNNW}-core leads to only weak mutual coupling (J(**3**) = -59 cm^{-1}) of both tungsten ions *via* the N_2-bridge.

These interpretations are further verified by DFT-calculations.[b] Monocationic **2** was predicted as a doublet with a $\{\pi^8\delta_1^2\delta_2^1\}$-configuration (Figure 16, *left*), while dicationic **3** was calculated as an open shell singlet with a $\{\pi^8\delta_1^1\delta_2^1\}$-configuration and a low lying triplet state due to weak antiferromagnetic coupling of the two metal-centered spins (J_{DFT}(**3**) = -184 cm^{-1}, Figure 16, *right*).

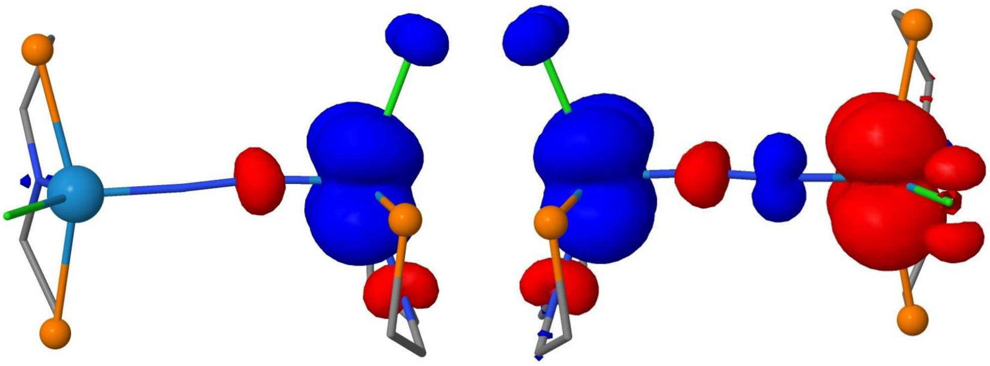

2 **3**

Figure 16: Spin-density-plots for **2** (*left*) and **3** (*right*).

---

[b] DFT-calculations were performed by **Dr. Markus Finger** using: M06/def2-TZVPP (SMD: THF) // D3BJ-RIJCOSX-PBE0/def2-SVP.

2.1.2 Synthesis and characterization of $[(N_2)\{W(CO)(PNP)\}_2]$ (4)[c]

Just as its Mo-congener **XI** or *Cummins'* dicationic **III**, $[(N_2)\{WCl(PNP)\}_2]$(**1**) is not capable for cleavage of the N_2-bridge neither thermally (T = 80 °C) nor photolytically ($\lambda > 305$ nm), which can be rationalized by the lack of two electrons within the {WNNW}-π-manifold.[22,61,70] As indicated by electrochemical studies (Figure 13), reduction of **1** requires very harsh reductants. Besides protonation, which will be discussed in the next chapter, other attempts were sought to shift the reduction potential to a more suitable range. One strategy for that is the coordination of strong π-acceptor ligands, such as carbonyl or isonitrile, to the vacant coordination site at the metals in order to reduce the electron density at the tungsten-ions. Furthermore, these ligands, especially CO, can be used as spectroscopic probes to quantify the electron density at a metal.[194] In this way the actual amount of electron transfer to the bridging N_2 ligand upon splitting can be estimated, which remains surprisingly ill-defined, due to the high covalency in N_2 bridged dinuclear compounds and in the formed nitride-products.

Addition of two equivalents of CN-^{t}Bu to **1** leads to the formation of two products, without full conversion of the starting material, as indicated by $^{31}P\{^1H\}$ NMR spectroscopy (Figure 17, *top*).

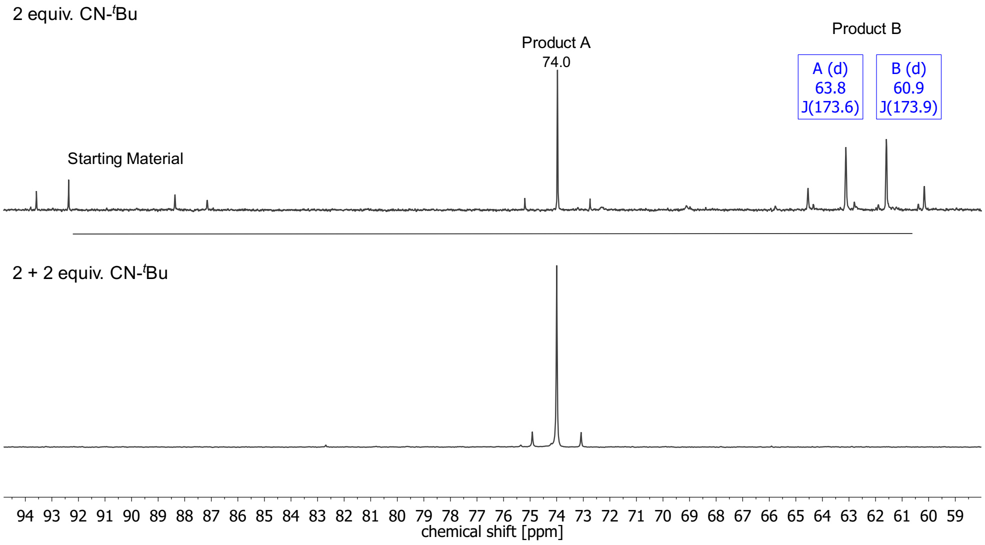

Figure 17: $^{31}P\{^1H\}$ NMR spectrum of the reaction of **1** with 2 equiv. CN-^{t}Bu (*top*) and additional 2 equiv. CN-^{t}Bu (*bottom*) in C_6D_6 at r.t.

---

[c] Parts of this work have been published in:
- N.A. Maciulis "Exploring redox properties of bis(tetrazinyl)pyridine (btzp) complexes of group VI metals, tetrazine and phosphine assisted reduction of H_2O, and dinitrogen cleavage and functionalization" *Ph.D. Thesis*, Indiana University Bloomington, **2019**.
- P.-M. Padonou "Reaktivität dimerer N_2-verbrückter Wolfram-PNP-Pinzetten Komplexe" *Bachelor Thesis*, Georg-August-Universität Göttingen, **2018**.

Upon addition of two further equivalents of CN-^{t}Bu all remaining **1** is consumed (Figure 17, *bottom*). Additionally one of the products (Product B) is transformed into the other product (Product A), which was identified as [WCl(CN^{t}Bu)$_2$(PNP)] (**6**), that could also be synthesized *via* reduction of [WCl$_3$(PNP)] (**5**) with two equivalents of NaHg in the presence of CN-^{t}Bu(Scheme 53. *left*).

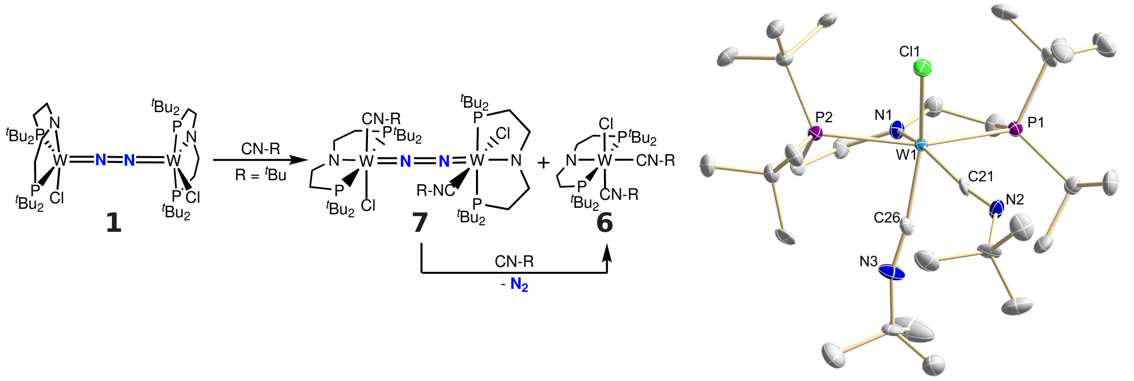

Scheme 53: *left*: Reaction of **1** with CN-^{t}Bu leads to partial loss of the bridging N_2-ligand and formation of **6**. *right*: Molecular structure of **6** in the crystal obtained by single crystal X-ray diffraction. Hydrogen-atoms are omitted for clarity. Furthermore only one of the two independent molecules in the asymmetric unit is shown. Selected bond lengths [Å] and angles [°]: W1-C21 2.034(7), W1-C26 1.996(8), W1-Cl1 2.4830(19), W1-N1 2.018(6), W1-P1 2.465(2), W1-P2 2.507(2); C21-W1-C26 78.7(3), C21-W1-N1 154.4(3), C26-W1-N1 83.0(3), C26-W1-Cl1 149.8(2), P1-W1-P2 154.00(6).

The ^{31}P{^{1}H} NMR spectrum of **6** features one singlet flanked by tungsten satellites at 74.0 ppm. The presence of two signals for the ^{t}Bu-groups of the CN-^{t}Bu and two signals for the ^{t}Bu-groups of the PNP-ligand in the ^{1}H NMR spectrum indicate C_s-symmetry, due to *cis*-coordination of both isonitrile-ligands, which was confirmed by X-ray diffraction (Scheme 53, *right*).
The formation of **6** is consistent with the need of four equivalents CN-^{t}Bu and leads to undesired loss of the bridging N_2 ligand. Due to the characteristic ^{31}P{^{1}H} NMR signature, showing two doublets ($\delta_P = 63.8$, 60.9 ppm) with large *trans*-coupling ($^2J_{PP} = 174$ Hz), product B was assumed to be dinuclear [(N_2){W(CN^{t}Bu)(PNP)}$_2$] (**7**, Scheme 53). Unfortunately, suppression of N_2-loss *via* usage of another iso-cyanide and/or changing the reaction conditions was unsuccessful. Furthermore, all attempts to isolate and characterize **7** failed due to similar solubility properties compared to **1** and **6**.

In contrast to the reaction with isonitriles, short (<20 min) exposure of **1** to CO (1 atm) results in quantitative formation of one product, which was identified as $[(N_2)\{WCl(CO)(PNP)\}_2]$ (**8**) (Scheme 54). Longer reaction times lead to the formation of undesired side-products, including $[W(CO)_3(^{H}PNP)]$ (**9**) and $[WCl(CO)_2(PNP)]$ (**10**) (*vide infra*).

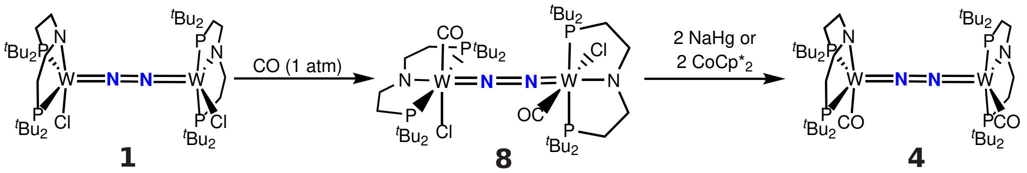

1 **8** **4**

d_{NN} = 1.27(8) / 1.33(4) Å
ν_{NN} = 1392 cm^{-1}

d_{NN} = 1.223(4) Å
ν_{NN} = 1437 cm^{-1}
ν_{CO} = 1883, 1867 cm^{-1}

d_{NN} = 1.207(14) Å
ν_{NN} = 1589 cm^{-1}
ν_{CO} = 1785, 1741 cm^{-1}

Scheme 54: Reaction of **1** with CO yields **8**, which can be further reduced to give **4**.

The molecular structure of **8** derived by X-ray diffraction (Figure 18, *left*) shows a C_2-symmetric, dinuclear species with two tungsten ions in an octahedral coordination sphere, the carbonyl-ligand *trans* to the chloro-ligand and the bridging N_2-ligand *trans* to the pincer-amide-nitrogen.

Compared to **1** the NN-bond length is shorter ($d_{NN} = 1.223(4)$ Å), which, together with the slightly hypsochromically shifted NN stretching frequency ($\tilde{\nu}_{NN}(^{14}N\text{-}\mathbf{8}) = 1437$ cm^{-1}, $\tilde{\nu}_{NN}(^{15}N\text{-}\mathbf{8}) = 1394$ cm^{-1}, $\lambda_{exc} = 457$ nm, THF solution) indicates a slightly weaker degree of activation for the bridging N_2 ligand, which can be attributed to competing backbonding of the CO and N_2 ligands.

In line with the observed C_2-symmetry in the solid state, the ^{1}H NMR spectrum features four resonances assigned to the ^{t}Bu-groups and four resonances for the ligand-backbone. The bridging N_2 ligand of ^{15}N-**8** was found at -0.7 ppm in the $^{15}N\{^{1}H\}$ NMR spectrum. The $^{31}P\{^{1}H\}$ NMR spectrum exhibits one singlet ($\delta_P = 65.9$ ppm), which shows cross-peaks to all four ^{t}Bu-signals in the ^{1}H-^{31}P-HMBC NMR spectrum, indicating incidental coincide of both phosphorus sets. The IR spectrum of solid **8** displays two sharp intense bands assigned to the carbonyl-stretching modes at 1883 and 1867 cm^{-1}. Both carbonyl-stretches of ^{15}N-**8** appear at the same energy, indicating no coupling of the CO- and NN-stretches.

Contrary to the CV of **1**, which shows no reductive features up to -2.9 V, the CV of **8** reveals one irreversible reductive feature ($E_p \approx -2.05$ V, Figure 18, *right*), which was now chemically attempted.

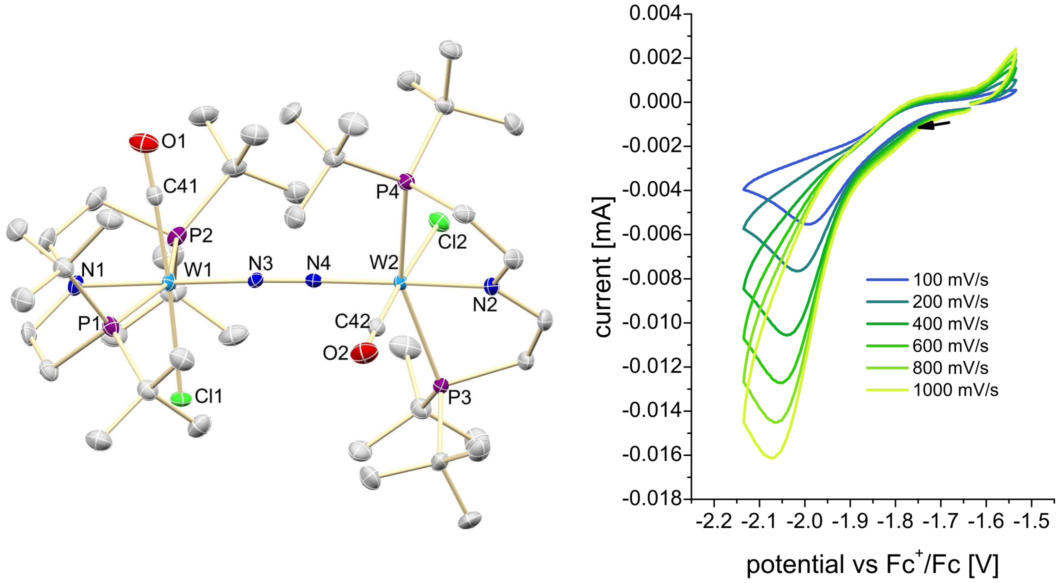

Figure 18: *left*: Molecular structure of **8** in the crystal obtained by single crystal X-ray diffraction. Hydrogen-atoms are omitted for clarity. Selected bond lengths [Å] and angles [°]: N3-N4 1.223(4), W1-N1 2.032(3), W1-N3 1.870(3), W2-N2 2.023(3) W2-N4 1.872(3); W1-N3-N4 174.2(3), W2-N4-N3 174.2(3), N1-W1-N3 177.38(13), N2-W2-N4 174.40(13), P1-W1-P2 155.22(3), P3-W2-P4 157.19(3), C41-W1-Cl1 176.5(2), C42-W2-Cl2 176.09(15). *right*: cyclic voltammogram (THF, Ar) at different scan-rates of the reduction of reduction of **8**.

Chemical reduction of **8** with one equivalent of NaHg or $Co(Cp^{*})_2$ is incomplete, while usage of two equivalents of reductant results in the formation of deep red $[(N_2)\{W(CO)(PNP)\}_2]$ (**4**) (Scheme 54) in isolated yields up to 57%.

In the solid state (Figure 19, *left*), both tungsten ions are in distorted square pyramidal geometry ($\tau_5 = 0.23$)[193] with a bridging μ^2:η^1:η^1-N_2 ligand, due to the loss of the chloro-ligands. Similar to **1** both {W(CO)(PNP)}-fragments are twisted with respect to each other, which is again attributed to the steric bulk of the ^{t}Bu-substituents (C21-W1-W1#-C21#: 87.8°/ 86.6°). Compared to **1** the W-N_2 bond lengths are longer ($d_{WN_2} = 1.869(7)$ Å) and the NN bond lengths ($d_{NN} = 1.207(14)$ Å) are shorter, hinting to a weaker degree of N_2-activation, which is supported by the hypsochromically shifted NN-stretching frequency ($\tilde{\nu}_{NN}(^{14}N\text{-}\mathbf{4}) = 1589$ cm^{-1}, $\tilde{\nu}_{NN}(^{15}N\text{-}\mathbf{4}) = 1540$ cm^{-1}, $\lambda_{exc} = 633$ nm, THF solution) compared to **1** or **8**. In contrast, the CO-stretching frequencies of solid **4** ($\tilde{\nu}_{CO} = 1785, 1741$ cm^{-1}, both ^{14}N-**4** and ^{15}N-**4** identical) are, compared to **8**, bathochromically shifted, implying stronger back-donation of the metal-ions.

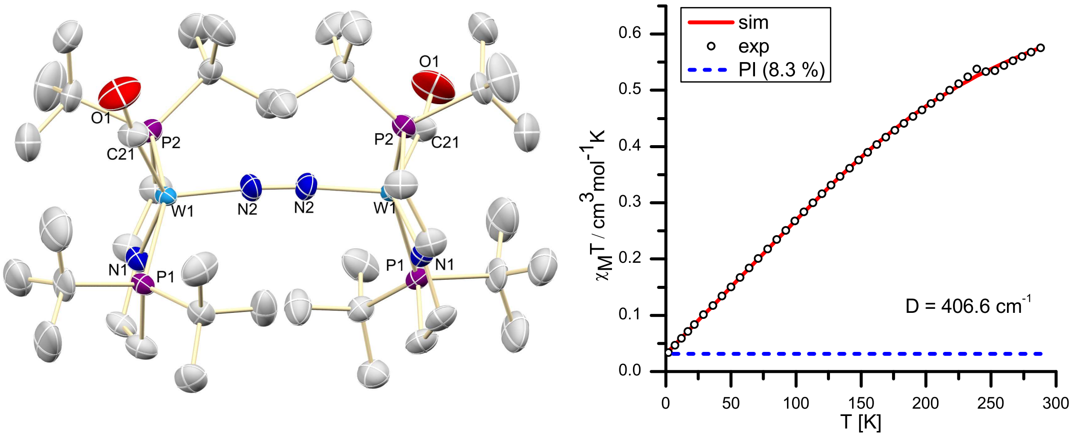

Figure 19: *left*: Molecular structure of **4** in the crystal obtained by single crystal X-ray diffraction. Hydrogen-atoms are omitted for clarity. Selected bond lengths [Å] and angles [°]: N2-N2# 1.207(14), W1-C21 1.956(14)/1.97(2), W1-N1 2.043(10)/2.04(2), W1-N2 1.869(7), W1-P1 2.485(3)/2.398(14), W1-P2 2.435(4)/2.517(17); C21-W1-N1 140.9(9)/156(4), P1-W1-P2 154.79(13)/151.7(6), W1-N2-N2# 173.7(7). *right*: χ_MT vs. T plot for **4**. The open circles are the observed susceptibility, the red solid line corresponds to the best fit with the parameters g_{av} = 1.74 and axial zero-field splitting (D = 406 cm^{-1}) and PI = 8.3% (S = 1/2, the blue broken line, PI: paramagnetic impurity).

The ^{1}H NMR of **4** reveals four sharp and paramagnetically shifted signals assigned to the ^{t}Bu groups and eight signals for the ligand backbone, in line with dinuclear C_2-symmetry in solution. In contrast, no signal could be found in the ^{31}P{^{1}H} NMR spectrum indicating an open-shell ground state at r.t., which is supported by the magnetic moment in solution ($\mu_{eff} = 2.3 \pm 0.1 \mu_B$) derived by *Evans'* method.

The $\chi_M T$ vs. T curve of a powdered sample of **4**, obtained *via* SQUID magnetometry (Figure 19, *right*), exhibits temperature-independent susceptibility below 150 K and could be fitted to a spin Hamiltonian with $S = 1$; $g_{av} = 1.74$ and large axial zero-field splitting (D = 406 cm^{-1}).

Similar magnetic behavior has also been observed for a series of 3rd row complexes with octahedral d^4 (Re^{III} or Os^{IV})[36,71,195,196] or square pyramidal d^6 (Os^{II} or Ir^{III})[197–199] configurations. The temperature independent paramagnetism was rationalized by an electronic triplet state that is strongly split by spin-orbit coupling, which results in an energetically well separated (>> $k_B T$) ground state (J = 0) that experiences only second order paramagnetism through mixing with excited states.[195,200] In contrast to **4** the ^{1}H NMR spectra of most of these compounds reveal sharp signals with resolved J-coupling as well as sharp, but paramagnetically shifted resonances in the ^{31}P{^{1}H} or ^{15}N{^{1}H} NMR spectra, respectively (for example $[(N_2)\{ReCl_2(^{H}PNP^{iPr})\}_2]$ (**XIII**): $\delta_P = -370.6$ (d, $^2J_{PP} = 236.9$ Hz) and -380.4 (d, $^2J_{PP} = 237.2$ Hz); $\delta_N = -1113$ ppm).[71]

These differences are in line with the non-linear behavior of the $\chi_M T$ vs. T curve above 150 K, which implies thermal population of the excited state. The weaker stabilization of the $J = 0$ ground state in **4**, compared to Re or Os, suggests a smaller effective spin-orbit coupling parameter ζ_{eff} most likely due to a high degree of covalency.[196,201]

Overall, these observations support the simple bonding model expressed by the MO-scheme for such N_2-bridged dinuclear compounds described earlier (Figure 20, *left*). Compared to **1**, **4** features two additional electrons within the {WNNW}-core, which are occupying the π^*-π-π^*-orbitals, whose NN-bonding character leads to a weaker degree of N_2-activation. The degree of activation compares well with other π^{10}-configurated N_2-bridged dinuclear compounds, such as *Schneider's* ReCl-congener (**XII**) and *Cummins'* neutral **I** (Figure 20, *right*).[36,60] However, the bathochromic shift of the carbonyl-stretching frequencies, compared to **8**, as well as the magnetic properties of **4**, indicate a high degree of covalency within the {WNNW}-π-core.
These observations are further supported by computational analysis,[d] which found a thermodynamic preference of a triplet-ground state over a closed-shell singlet-ground-state by 1.2 kcal·mol^{-1}, while no clear open-shell-singlet structure could be identified.

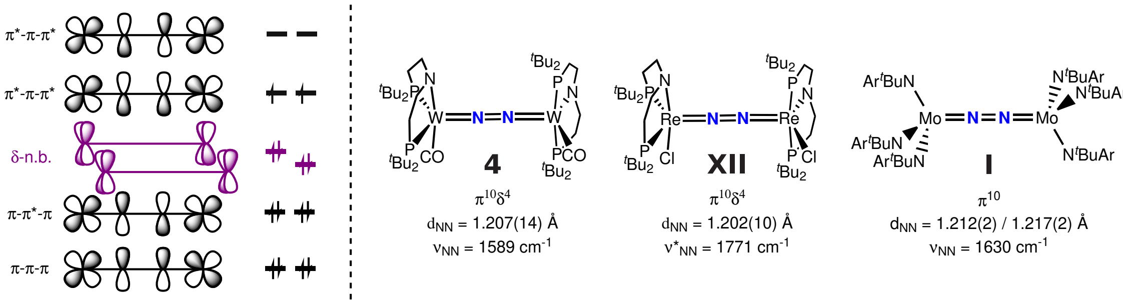

Figure 20: *left*: qualitative MO-scheme for end-on N_2-bridged compound with idealized fourfold symmetry. *right:* Comparison of the structural and spectroscopic features of **4**, *Schneider's* ReCl-congener **XII** and *Cummins'* neutral **I**.[36,60] (* computed value)

In summary, the initial approach of enabling reduction of **1** *via* addition of π-acceptor ligand was successful. The electronic structure of so-obtained **4** was deeply examined and supports the qualitative MO-scheme for such end-on N_2-bridged dinuclear compounds with idealized fourfold symmetry. The presence of ten electrons within the π-manifold is predestined for breakage of the NN-bond, which will be examined and discussed in chapter 2.3.

---

[d] DFT-calculations were performed by **Prof. Dr. Vera Krewald** and **M.Sc. Severine Rupp** using: PBE/def2-TZVP,def2-SVP.

2.2 Proton induced N_2-cleavage *versus* proton reduction[e]

As already discussed, $[(N_2)\{WCl(PNP)\}_2]$ (**1**) is, just as its Mo-analogue **XI**, not capable for N_2-cleavage neither thermally (T = 80 °C) nor photolytically ($\lambda > 305$ nm). However, cleavage of the NN bond in **XI** can be induced upon pincer protonation (Scheme 26), which was now attempted with **1** to investigate if and how the cathodically shifted oxidation potentials of **1** compared to **XI** (Figure 13) influence the reactivity.[70]

Protonation of **1** with two equiv. of triflic acid at -78 °C and gradual warming to r.t. leads to formation of the corresponding W(V)-nitride, $[\mathrm{W(N)Cl(^{\mathit{H}}PNP)}]^+$ (**11**). In the solid state, **11** features a square pyramidally coordinated tungsten ion with the nitride ligand on the apical site (Figure 21, *left*). The triflate anion is hydrogen bonding to the amine proton of the ligand backbone, as indicated by the short NH···O-distance (2.03(3) Å). The W≡N-bond length ($d_{\mathrm{WN}} = 1.679(2)$ Å) as well as the W≡N stretching frequency detected in the IR of solid **11** ($\tilde{\nu}_{\mathrm{WN}}(^{14}\mathrm{N}$-**11**$) = 1058\,\mathrm{cm}^{-1}$, $\tilde{\nu}_{\mathrm{WN}}(^{15}\mathrm{N}$-**11**$) = 1029\,\mathrm{cm}^{-1}$) are in the typical range found for other tungsten-nitrides.[202–205] Due to paramagnetism **11** is NMR silent, but features an isotropic signal ($g_{\mathrm{av}} = 1.93$) in the X-band EPR spectrum (THF, r.t.) with hyperfine interactions (HFI) to the two phosphorous ($A(^{31}\mathrm{P}) = 56$ MHz) and the tungsten nuclei ($A(^{183}\mathrm{W}) = 220$ MHz) (Figure 21, *right*).

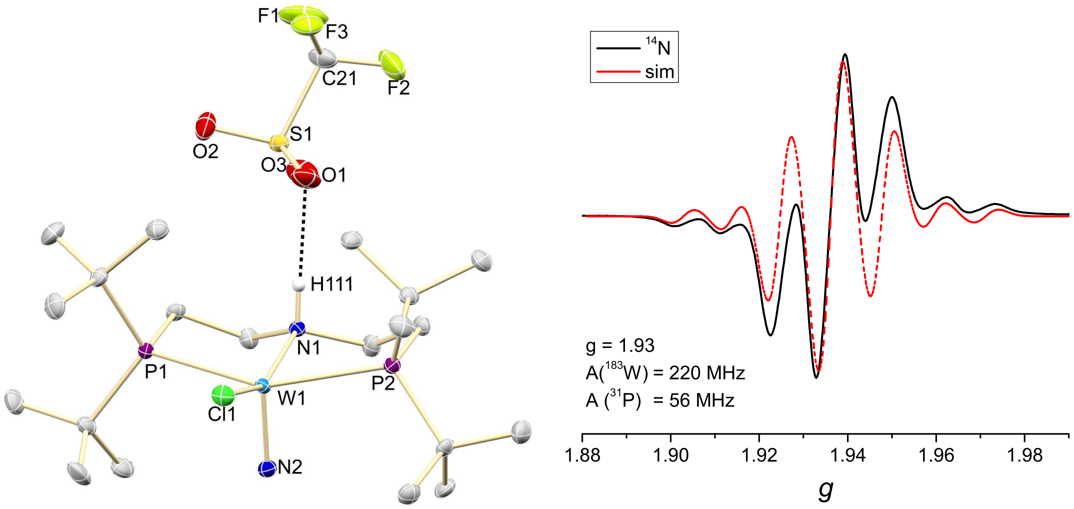

Figure 21: *left:* Molecular structure of **11** in the crystal obtained by single crystal X-ray diffraction. Hydrogen-atoms, with exception of H111, and co-crystalized solvent molecules are omitted for clarity. Selected bond lengths [Å] and angles [°]: W1-Cl1 2.3657(7), W1-N1 2.202(2) W1-N2 1.679(2), W1-P1 2.5308(7), W1-P2 2.5352(7); N1-W1-Cl1 154.83(6), N1-W1-N2 99.26(10), P1-W1-P2 152.54(2). *right*: EPR-Spectrum (X-band, THF, r.t.) of **11**.

---

[e] Parts of this work have been published in: "Selectivity of tungsten mediated dinitrogen splitting *vs.* proton reduction", B. Schluschaß, J. Abbenseth, S. Demeshko, M. Finger, A. Franke, C. Herwig, C. Würtele, I. Ivanovic-Burmazovic, C. Limberg, J. Telser, S. Schneider, *Chemical Science*, **2019**, *10*, 10275-10282.

In contrast to the Mo-analogue (**XI**), the selectivity of protonation induced N_2-cleavage in case of **1** strongly relies on the reaction conditions. For instance, the addition of two equivalents of triflic acid to **1** at r.t. leads to low splitting yields and substantial amounts of the oxidation products **2** and **3**.
The selectivity was further tuned upon usage of two equivalents of a strong acid with a non-coordinating anion, like $[H(OEt_2)_2][Al(OC(CF_3)_3)_4]$ or $[H(OEt_2)_2][BAr^F_{24}]$. In both cases, the addition to **1** lead, independent of the reaction temperature, exclusively to the formation of dicationic **3** and H_2, which was detected in the head-space of the reaction *via* gas chromatography (Scheme 55).

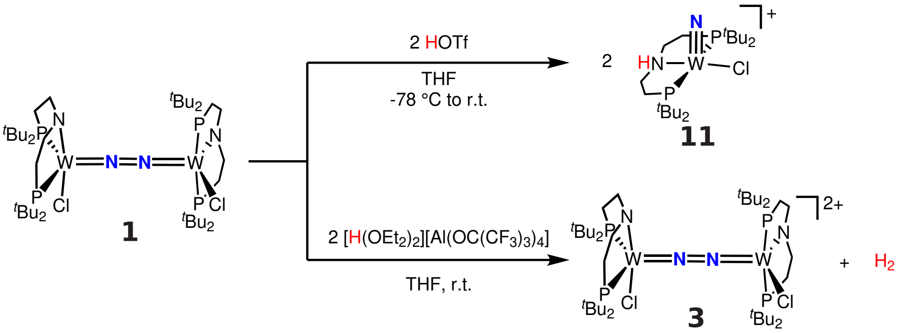

Scheme 55: Protonation of **1** leads either to N_2-cleavage and formation of **11** or to proton-reduction and formation of **3**.

The influence of the acid counteranion was further probed by usage of triethylammonium salts. Protonation of **1** with two equiv. of $[HNEt_3][BAr^F_{24}]$ proceeds slowly and leads to selective formation of monocationic **2** as indicated by *in situ* HR-ESI-MS, EPR and NMR. The slower reaction as well as the not observed second oxidation is explained by the higher pK_a of $[HNEt_3^+]$ compared to $[H(OEt_2)_2][BAr^F_{24}]$ or triflic acid.[206] However, the yield in **2** decreases down to only 30%, if two equiv. of $[HNEt_3]OTf$ are used. As indicated by *in situ* HR-ESI-MS, the only other product formed is splitting product **11**, which showcases that the selectivity of the reaction heavily relies on the acid counteranion (Scheme 56), as it has also been reported by *Nishibayashi* for catalytic nitrogen fixation (see chapter 1.2.1, Table 4).[9] Hence, **1** was also reacted with two equiv. of $[HNEt_3]Cl$, which lead to sluggish mixtures with substantial amounts of trichloride **5** and was therefore not further examined.

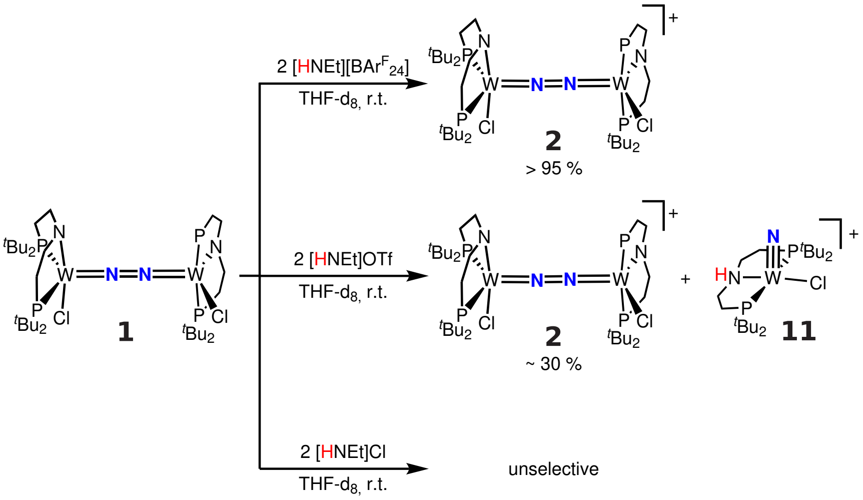

Scheme 56: Anion dependence upon protonation of **1** with different $[HNEt_3^+]X$ salts.

In order to rationalize the origin of this anion dependent selectivity, **1** was also protonated with one equiv. of different Brønsted acids. At r.t. all used acids (HOTf, $[H(OEt_2)_2][BAr^F_{24}]$, $[H(OEt_2)_2][Al(OC(CF_3)_3)_4]$, $[LutH]^+$ or $[HNEt_3]^+$) lead to exclusive formation of monocationic **2** and H_2, which was again detected *via* gas chromatography in the head-space of the reaction.

Significant differences between $[H(OEt_2)_2][BAr^F_{24}]$ and HOTf were observed, when the reaction was carried out at low temperatures. Protonation of **1** with one equiv. triflic acid leads to immediate disappearance of all NMR-signals belonging to **1** and appearance of a new diamagnetic intermediate. The presence of four doublets in the $^{31}P\{^1H\}$ NMR spectrum (Figure 22, *left*) with identical integrals indicate the loss of the C_2-axis and formation of a C_1-symmetric dinuclear complex. If the same reaction is carried out with the ^{15}N-isotopologue, ^{15}N-**1**, the $^{15}N\{^1H\}$ NMR spectrum (Figure 22, *right*) shows two doublets ($\delta_N = 27$ and 24 ppm; $^1J_{NN} = 10$ Hz) close to the resonance found for ^{15}N-**1**, which corroborates the formation of a C_1-symmetric complex and excludes protonation of the bridging N_2 ligand. Ligand protonation within $[(^{H}PNP)ClW\text{-}(N_2)\text{-}WCl(PNP)]^+$ (**12**) could be confirmed by a ^1H NMR signal at 5.41 ppm with typical N-H broadened triplet fine-structure, which shows a cross-peak with the pincer-nitrogen in the ^1H-^{15}N HSQC NMR spectrum and coupling to the ligand backbone signals in the ^1H COSY NMR spectrum.

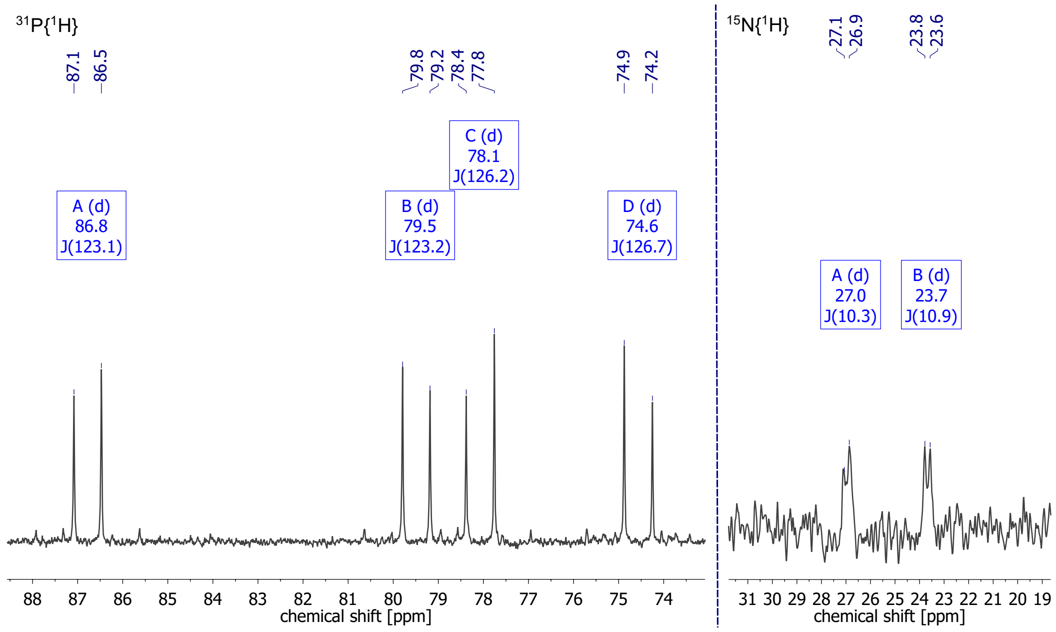

Figure 22: $^{31}P\{^1H\}$ (*left*) and $^{15}N\{^1H\}$ NMR spectra (*right*) of **12** in THF—d_8 at -35 °C.

In contrast to triflic acid, usage of one equiv. $[H(OEt_2)_2][BAr^F_{24}]$ instantaneously gives monocationic **2** even at temperatures down to -75 °C (Scheme 57), which implies stabilization of **12** by the triflate anion. Contact-ion pair formation of the triflate anion with **12** could be confirmed *via* ^{19}F and ^1H DOSY NMR at -35 °C. The diffusion coefficient of the triflate anion in **12**-OTf ($D = 2.29{\cdot}10^{-6}$ cm^{2}s^{-1}) is significantly shifted compared to free triflic acid ($D = 5.11{\cdot}10^{-6}$ cm^{2}s^{-1}) and very close to the diffusion coefficient found for the cation ($D = 2.18\text{-}2.14{\cdot}10^{-6}$ cm^{2}s^{-1}). This interaction is attributed to hydrogen-bonding of the triflate anion with the pincer N-H proton as found in the solid state of **11**-OTf.

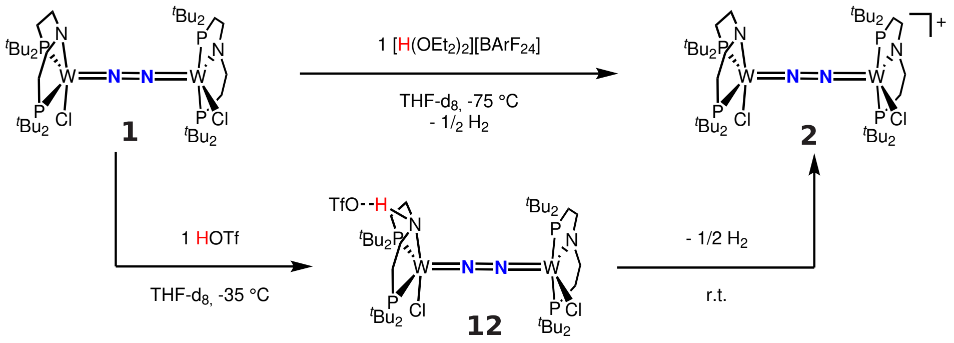

Scheme 57: Protonation of **1** with one equiv. $[H(OEt_2)_2][BAr^F_{24}]$ or HOTf at low temperatures.

Addition of two equiv. triflic acid to **1** at -60 °C leads to a color change from green to yellow, disappearance of all signals in the $^{31}P\{^{1}H\}$ NMR spectrum and new broad, paramagnetically shifted resonances in the ^{1}H NMR spectrum. In analogy to the Mo-congener **XI**, it was assumed, that the second protonation occurs on the second pincer unit to give $[(N_2)\{WCl(^{H}PNP)\}_2]^{2+}$ (**13**). The magnetic moment in solution was determined *via Evans*' method to $\mu_{eff} = 4.7 \pm 0.1$ μ_B, close to the spin-only value for a quintet ground state ($\mu_{eff} = 4.9$ μ_B). Upon raising the temperature to r.t. the yellow color fades and all signals in the ^{1}H NMR spectrum disappear in line with formation of pale NMR-silent **11**.

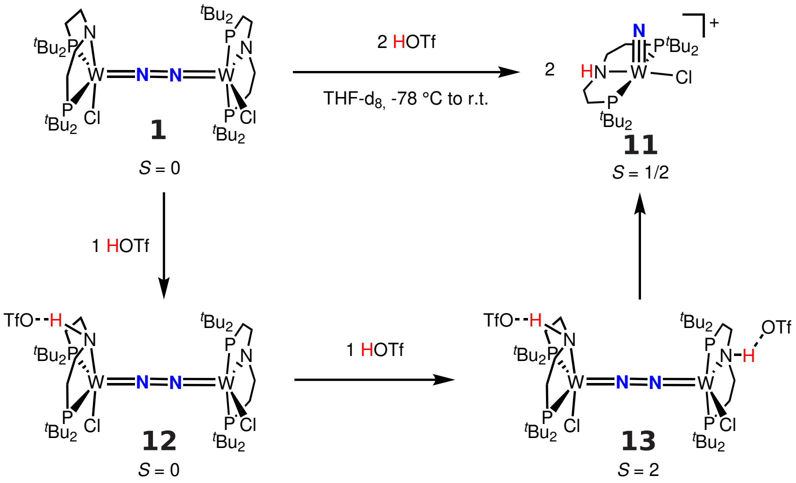

Scheme 58: Proposed mechanism of tungsten mediated proton induced N_2-splitting.

Overall it is proposed, that N_2-cleavage of **1** to give **11** arises from protonation of both pincer units, which changes the electronic configuration from a $\{\pi^8\delta^4\}$-configuration within the {WNNW}-manifold to a $\{\pi^{10}\delta^2\}$ configuration as is was already described for the Mo-analogue **XI** (Scheme 58).[70] However, this mechanism does not explain, how proton reduction to give H_2 and **2** or **3** occurs. Therefore, the kinetics of proton reduction were studied *via* UVvis spectroscopy using $[HNEt_3][BAr^F_{24}]$ as acid, which gives monocationic **2** selectively within a convenient timescale even under pseudo first-order conditions.
Addition of $[HNEt_3][BAr^F_{24}]$ to a THF solution of **1** leads to an immediate drop of the absorbance without any change in the absorption maxima, implying only small changes in the electronic structure (Figure 23, *left*). From the acid concentration dependency of this drop, the equilibrium constant ($K_1 = 1592 \pm 578$ $L \cdot mol^{-1}$) and the forward rate ($k_1 = 163 \pm 47$ $L \cdot mol^{-1} \cdot s^{-1}$) of the first protonation step could be derived (Figure 23, *right*).

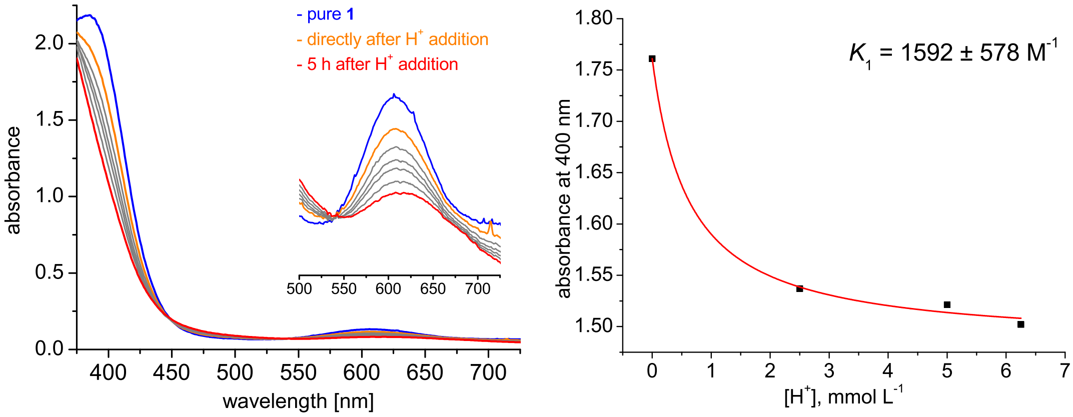

Figure 23: *left*: Examplary UVvis spectrum of the protonation of **1** with $[HNEt_3][BAr^F_{24}]$. The blue trace represents the UVvis spectrum of pure **1**, the orange one directly after the addition of acid and the red one after 5 h of reaction time. *right*: plot of the absorbance at 400 nm directly after the addition of acid *vs* acid-concentration with fitting curve to determine K_1 (R^2=0.998).

Under pseudo first order conditions ($c_0([HNEt_3]^+)/c_0(\mathbf{1}) = 10\text{-}25$) this first fast step is followed by another significantly slower, mono-exponential decay, which was monitored over 5 h (Figure 24, *left*). Thereby, the derived rate constant, $k_{obs(2)}$, shows a linear dependency in acid concentration (Figure 24, *right*), which points to a slow, irreversible second protonation step after the initial, fast pre-equilibrium K_1.

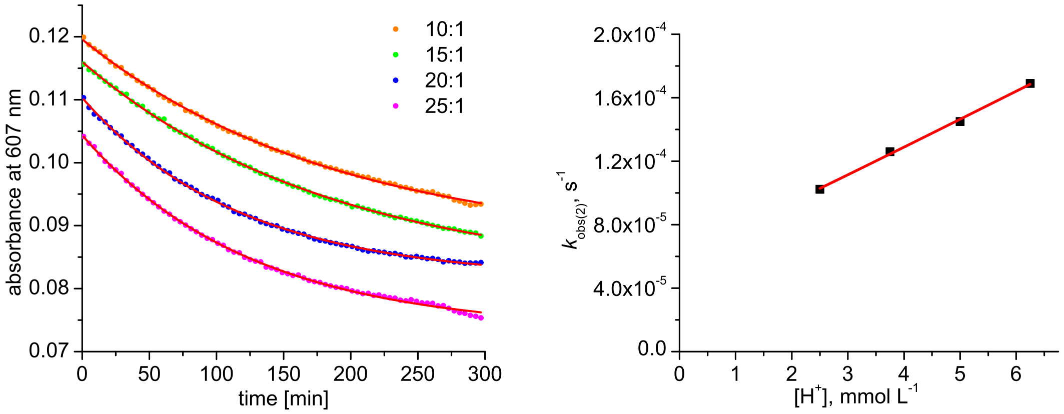

Figure 24: *left*: absorbance (at 607 nm) vs. time plot for different acid concentrations. The red lines represent the fitting curves, while the dots show the measured absorbance. *right:* plot of the determined $k_{obs(2)}$ *vs* acid concentration, showing linear dependence as indicated by the red line.

Nevertheless, the non-zero intercept implies the presence of at least one competitive pathway at low concentrations of acid. Therefore, the rate constant $k_{obs(2)}$ was expressed by eqn. 2.4 as a result of the minimum kinetic model outlined in Scheme 59:

$$k_{obs(2)} = \frac{k_2 K_1 [H^+]^2}{1 + K_1 [H^+]} + k_{3,obs} \tag{2.4}$$

The first term represents a pathway in which **1** is initially protonated to give **12**. Second protonation of **12** results in irreversible H_2 loss and formation of dicationic **3**, which rapidly comproportionates with neutral **1** to give two equiv. of monocationic **2**, in line with the large comproportionation constant ($K_c \approx 10^8$) derived from electrochemical studies (Scheme 59, Path A). The second term in eqn. 2.4 accounts for a bimolecular decay of **12** as an alternative pathway at low concentrations of acid (Scheme 59, Path B).

Under pseudo first-order conditions in acid (10-25 equiv.) the experimental data could be fitted to eqn. 2.4 upon preservation of K_1 to give the rate constant $k_2 = 0.0018 \pm 0.001$ L·mol^{-1}·s^{-1}. The rate constant k_3, assigned to a bimolecular reaction of **12** at low acid concentrations, was derived from the initial rate of the reaction of **1** with one equiv. of $[HNEt_3]^+$ ($k_3 = 0.4$ L·mol^{-1}·s^{-1}). The alternative pathway, that follows the reduction of **12** by **1** was excluded due to the considerably smaller derived rate constant ($k'_3 = 0.12$ L·mol^{-1}·s^{-1}).

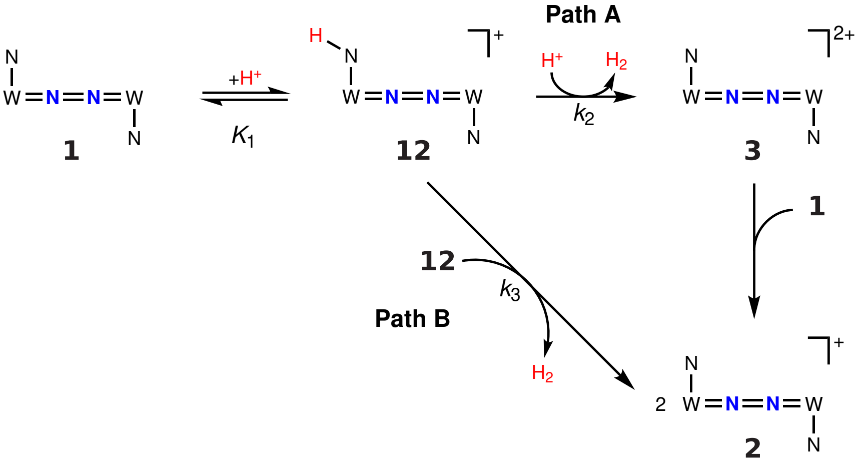

Scheme 59: Proposed mechanistic pathways for proton reduction at high (Path A) and low (Path B) concentrations of acid.

From the kinetic analysis two pathways can be proposed, both proceeding through the spectroscopically characterized intermediate **12**. At low acid concentrations, proton reduction occurs from a bimolecular reaction of **12** (Scheme 59, Path B), which explains its decay even in the absence of acid and the selective formation of monocationic **2** and H_2 upon usage of one equiv. of acid. Similar observations have been

made by *Peters* for his [(Fe(TBP)]$^+$-system (**XXVI**, Figure 8).[126] In case of excess acid, the second pathway (Scheme 59, Path A) becomes predominant. This pathway explains the formation of dicationic **3** upon protonation of **1** with two equiv. of $[H(OEt_2)_2][Al(OC(CF_3)_3)_4]$ or $[H(OEt_2)_2][BAr^F_{24}]$.
Besides these two pathways, the N_2-splitting product **11** is also (at r.t.) or exclusively (at low T) obtained in the presence of triflate as anion. To rationalize the influence of the counteranion the protonation of **1** was studied computationally, using truncated $[HNMe_3]^+$ as model acid (Scheme 60).[f]

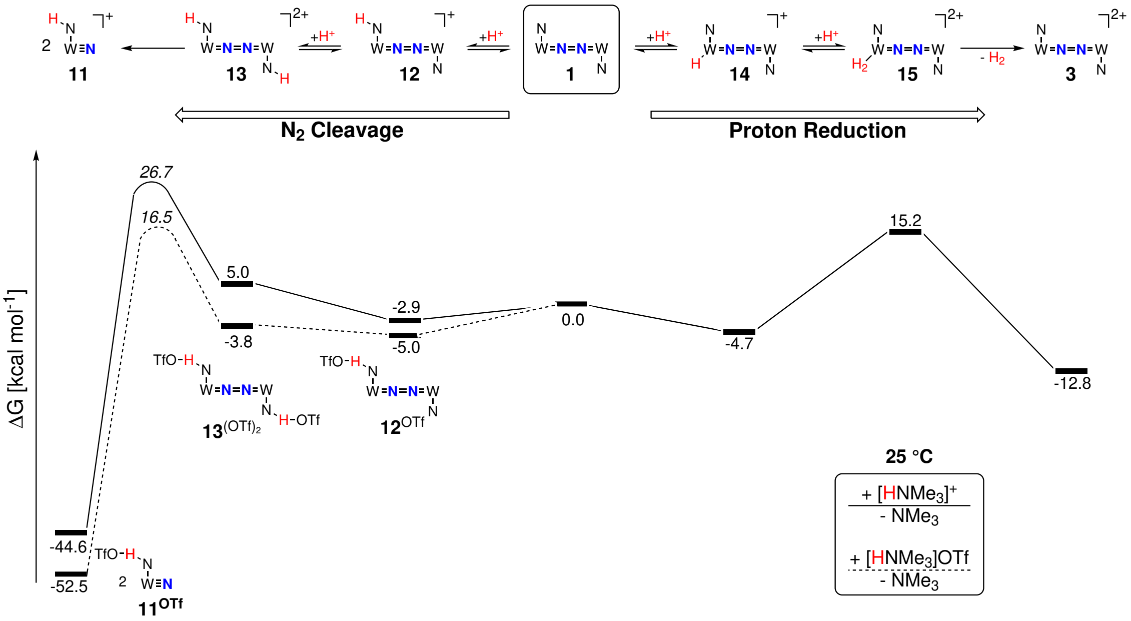

Scheme 60: Computed energy profile for proton induced N_2-cleavage (*left branch*) and proton reduction (*right branch*) both *via* double protonation of **1** at 25 °C in the absence (solid line) and in the presence (dashed line) of triflate as counteranion. The italic energies represent the calculated barriers for N_2-splitting from **13** and **13**^{OTf_2} to give **11** and **11**^{OTf}, respectively.

For the first step two different protonation sites, a tungsten ion and a pincer nitrogen, have been considered. Protonation of one tungsten ion and formation of a hydride product $[(PNP)W(H)Cl\text{-}(N_2)\text{-}WCl(PNP)]^+$ (**14**) with a diamagnetic ground state was calculated to be the global minimum ($\Delta G^\circ_{298\,K} = -4.7$ kcal·mol^{-1}) in excellent agreement with the experimentally derived equilibrium constant K_1. Similiar to the protonation of a PCP-Mo(IV)-nitride with $[HNEt_3][BAr^F_{24}]$ reported by *Schrock*,[14] the structure of **14** features a hydride bridging one pincer phosphorous atom and the tungsten center. Unfortunately, all attempts to experimentally verify the formation of a hydride were unsuccessful. Protonation of the pincer nitrogen to give **12** was calculated to be slightly less exergonic ($\Delta G^\circ_{298\,K} = -2.9$ kcal·mol^{-1}).

---

[f] DFT-calculations were performed by **Dr. Markus Finger** using: M06/def2-TZVPP (SMD: THF) // D3BJ-RIJCOSX-PBE0/def2-SVP.

However, the situation changes in the presence of a triflate anion. Upon usage of $[HNMe_3]OTf$ protonation of the pincer backbone becomes more favorable due to stabilization of the pincer amine moiety *via* hydrogen bonding of the triflate anion ($\Delta G^\circ_{298\,K} = -5.0$ kcal·mol^{-1}). Since hydride **14** is not involved in hydrogen bonding, pincer protonated **12**^{OTf} is the global minimum in presence of a triflate counteranion. Nevertheless, both protonation products should be in rapid equilibrium, which is slightly shifted towards hydride **14** in the absence and slightly shifted towards pincer protonated **12**-OTf in the presence of a triflate counteranion. In all cases hydrogen bonding towards NMe_3 was not observed, most likely due to steric reasons.

The second protonation leads either to H_2-evolution or N_2-cleavage. The formation of H_2 and dicationic **3** was calculated to be exergonic ($\Delta G^\circ_{298\,K} = -12.8$ kcal·mol^{-1}, with respect to **1**; Scheme 60, *right branch*). As most reasonable pathway, the protonation of hydride **14** was considered. As a result a dihydrogen intermediate $[(PNP)W(H_2)Cl\text{-}(N_2)\text{-}WCl(PNP)]^{2+}$ (**15**) is formed, which is unstable and releases H_2 without barrier. Therefore, the free energy of **15** ($\Delta G^\circ_{298\,K} = 15.2$ kcal·mol^{-1}) was used to estimate the kinetic barrier for the protonation of hydride **14**. The so obtained value ($\Delta\Delta G^\circ_{298\,K} = 19.7$ kcal·mol^{-1} with respect to **14**) is in very good agreement with the experimentally derived barrier for Path A ($\Delta G^\ddagger_{eff} = 19$ kcal·mol^{-1}).

Cleavage of the bridging N_2-unit and formation of nitride **11**, was calculated to proceed *via* protonation of the second pincer unit, similar to the Mo-analogue **XI** (Scheme 60, *left branch*).[70] The doubly pincer protonated $[(N_2)\{WCl(^{H}PNP)\}_2]^{2+}$ (**13**) was calculated to adopt a quintet ground-state ($S = 2$), in agreement with the experimentally derived magnetic moment for **13**^{OTf_2} ($\mu_{eff} = 4.7 \pm 0.1\ \mu_B$). In the absence of a triflate anion diprotonated **13** was located at $\Delta G^\circ_{298\,K} = 5.0$ kcal·mol^{-1}(with respect to **1**). N_2-cleavage into nitride **11** is strongly exergonic ($\Delta G^\circ_{298\,K} = -49.7$ kcal·mol^{-1}) with a kinetic barrier of $\Delta G^\ddagger_{298\,K} = 21.7$ kcal·mol^{-1}, in a comparable range to the experimentally derived values for the Re- (**XII**) and Mo-analogues (**XI**).[36,70]

Starting from the most stable monoprotonation product in the absence of triflate, hydride **14**, the effective barrier for N_2-cleavage ($\Delta G^\ddagger_{eff} = 31.4$ kcal·mol^{-1}) is considerably higher than the estimated barrier for H_2-evolution ($\Delta G^\ddagger_{eff} = 19.9$ kcal·mol^{-1}), which explains the observed selective formation of H_2 upon usage of $[HNEt_3][BAr^F_{24}]$.

In the presence of triflate the relative energetics of these two pathways change. As already described, the global minimum of the first protonation in the presence of triflate is **12**^{OTf}. Accordingly, the effective barrier for H_2-evolution is slightly increased by +0.3 kcal·mol^{-1}. Similar to the stabilization of monoprotonation product **12**^{OTf}, doubly pincer protonated **13**^{OTf_2} gets stabilized by hydrogen bonding of the pincer amine moieties with the triflate counteranions by -8.8 kcal·mol^{-1}, which decreases the effective barrier for N_2-cleavage. As a consequence both reaction pathways feature almost isoenergetic effective barriers (Proton reduction: $\Delta G^\ddagger_{eff} = 20.2$ kcal·mol^{-1}; N_2-cleavage: $\Delta G^\ddagger_{eff} = 21.5$ kcal·mol^{-1}; both vs. **12**^{OTf}), in full agreement with the experimental findings upon protonation with $[HNEt_3]OTf$.

Overall, the selectivity upon protonation with $[HNEt_3]^+$-salts follows the *Curtin-Hammett-principle*.[207] The pre-equilibrium is modulated by N-H hydrogen bonding to the counteranion, while the selectivity is only depending on the effective barrier for H_2-evolution and N_2-cleavage, which is strongly influenced by hydrogen bonding of the two N-H moieties with the triflate counteranions.

This picture changes if triflic acid is used instead of $[HNMe_3]^+$, due to the lower pK_a (p$K_a^{THF}([HNMe_3]^+)$-pK_a^{THF}(HOTf) = 4.7) (Scheme 61, black).[206] The pre-equilibrium between hydride **14** ($\Delta G^\circ_{298\ K} = -13.5$ kcal·mol^{-1}) and ligand protonated **12**^{OTf} ($\Delta G^\circ_{298\ K} = -13.9$ kcal·mol^{-1}) is slightly shifted towards the latter, due to its stabilization *via* hydrogen bonding. Furthermore, the effective barriers for N_2-cleavage and H_2-evolution become close in energy (Proton reduction: $\Delta G^\ddagger_{eff} = 11.5$ kcal·mol^{-1}; N_2-cleavage: $\Delta G^\ddagger_{eff} = 12.8$ kcal·mol^{-1}; both vs. **12**^{OTf}). In contrast to protonation with $[HNMe_3]^+$, these barriers are both below the energy of starting compound **1**, which makes the *Curtin-Hammett-principle* not applicable and explains the low selectivity upon protonation of **1** with triflic acid at r.t.

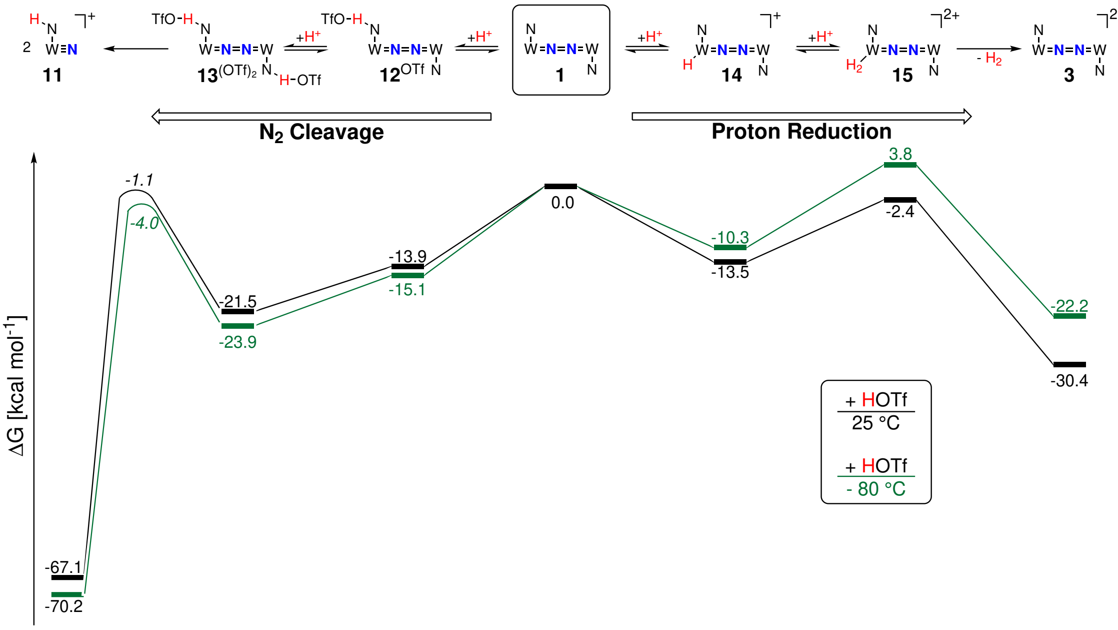

Scheme 61: Computed energy profile for proton induced N_2-cleavage (*left branch*) and proton reduction (*right branch*) both *via* double protonation of **1** with triflic acid at 25 °C (black) and -80 °C (green). The italic energies represent the calculated barriers for N_2-splitting from **13**^{OTf_2} to give **11**^{OTf}.

Lowering the temperature of protonation with HOTf to -80 °C pertubes this picture even further (Scheme 61, green). Compared to r.t. the preference of ligand protonated **12**^{OTf} ($\Delta G^\circ_{193\ K} = -15.1$ kcal·mol^{-1}) over hydride **14** ($\Delta G^\circ_{193\ K} = -10.3$ kcal·mol^{-1}) is increased, due to both, stabilization of **12**^{OTf} and destabilization of **14**, in line with the exclusive experimental observation of **12**^{OTf} and **13**^{OTf_2} upon single and double protonation of **1** with HOTf at low temperatures. The free energy of doubly pincer protonated $\mathbf{13}^{\mathrm{OTf}_2}$ ($\Delta G^\circ_{193\ \mathrm{K}} = -23.9$ kcal·mol^{-1} vs. **1**) is much lower than the one of dihydrogen-complex **15** ($\Delta G^\circ_{193\ \mathrm{K}} = 3.8$ kcal·mol^{-1} vs. **1**), which is even higher than the calculated barrier for N_2-cleavage ($\Delta G^\ddagger_{\mathrm{eff}} = -4.0$ kcal·mol^{-1} vs. **1**). This results in selective N_2-cleavage and formation of $\mathbf{11}^{\mathrm{OTf}}$ as it was experimentally observed.

Overall, these studies provide guidelines how the selectivity between competing proton- and nitrogen-reduction can be tuned. Both reactions proceed through different pathways, either *via* protonation of hydride-isomer (**14**), resulting in proton-reduction, or *via* (double) pincer-protonation, giving nitride **11**. The equilibrium between hydride **14** and pincer-protonated **12** can be shifted to the latter upon usage of hydrogen-bonding anions and low temperatures, overall favoring nitrogen-reduction. Furthermore, the pK_a of the acid can have a kinetic effect on the selectivity. While upon usage of weak acids the selectivity is *Curtin-Hammett*-controlled, this control can be overcome upon usage of strong acids, which can result in different reaction outcomes.

2.3 N_2-cleavage of $[(N_2)\{W(CO)(PNP)\}_2]$ (4)

In contrast to $[(N_2)\{WCl(PNP)\}_2]$ (**1**), its carbonyl-analogue $[(N_2)\{W(CO)(PNP)\}_2]$ (**4**) features two additional electrons within the {WNNW}-π-manifold. As already described in chapter 2.1.2, this leads to a $\{\pi^{10}\delta^4\}$-configuration, which not only changes the degree of N_2-activation, but also the reactivity of **4** with respect to N_2-splitting. While **1** is thermally stable, **4** cleaves the NN-bond upon heating or irradition to give the corresponding W(IV)-nitride, [W(N)(CO)(PNP)] (**16**) (Scheme 62). Both pathways have been examined in detail, which is described in the next two chapters.

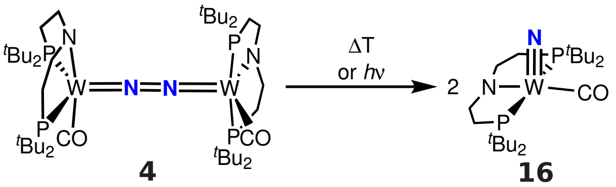

4

ν_{CO} = 1785, 1741 cm^{-1}

16

ν_{CO} = 1883 cm^{-1}

Scheme 62: Thermal and photolytical N_2-cleavage of **4** to give **16**.

The nitride product **16** is light-blue, diamagnetic and gives one singlet resonance flanked by tungsten satellites in the $^{31}P\{^1H\}$ NMR spectrum ($\delta_P = 104.5$ ppm). Starting from ^{15}N-labeled ^{15}N-**4** gives rise to ^{15}N-**16**, whose $^{15}N\{^1H\}$ NMR spectrum reveals one singlet, flanked by tungsten satellites ($\delta_N = 447.0$ ppm). The W≡N stretch of solid **16** ($\tilde{\nu}_{WN}(^{14}N$-**16**$) = 998$ cm^{-1}, $\tilde{\nu}_{WN}(^{15}N$-**16**$) = 973$ cm^{-1}) was found in a similar range compared to the one of $[W(N)Cl(^{H}PNP)]^+$ (**11**) and other related tungsten-nitrides.[202–205]

The carbonyl-stretching frequency of solid **16** as well as of its ^{15}N-labeled isotopomer ^{15}N-**16** was found at 1883 cm^{-1} in the IR-spectrum, strongly shifted compared to dinuclear **4** ($\tilde{\nu}_{CO}$(**4**) = 1785, 1741 cm^{-1}). This hypsochromic shift is attributed to weaker back-donation from the tungsten ions as a result of charge transfer from the metal to the N_2-bridge upon cleavage, which shows, even though both the {WNNW}-core of **4** and the W≡N-bond in **16** are highly covalent, a significant electron transfer to the N_2-bridge upon cleavage.

Due to the good solubility in all tried solvents, no crystals suitable for X-ray diffraction could be obtained.

2.3.1 Thermal N_2-cleavage

The thermal decay of **4** into **16** was monitored by ^1H NMR at different temperatures (75-105 °C). The concentration of **4** was determined using an internal standard and plotted *versus* time (Figure 25, triangles). Notably, the reaction terminates prior to full conversion, which implies an equilibrium between dinuclear **4** and nitride **16**, which is shifted to **16** at higher temperatures.

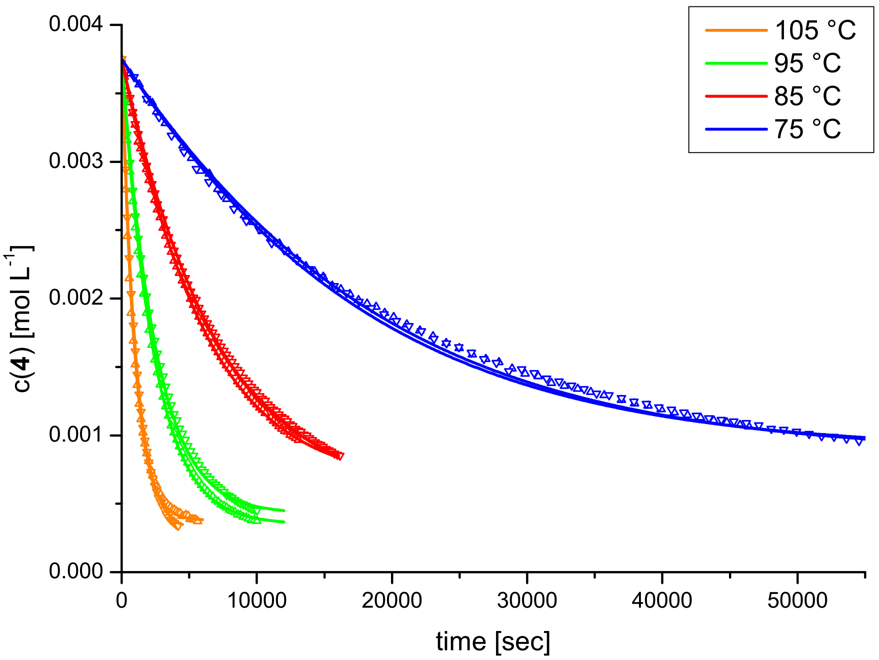

Figure 25: Plot of the concentration of **4** *vs.* time at different temperatures. The triangles represent the measured concentrations, while the blank lines represent the fitted curves.

The obtained kinetic data was fitted to a model with a first order splitting reaction (k_1) and a reverse second order nitride coupling reaction (k_2) according to the rate law shown in Scheme 63 (Figure 25, blank lines).

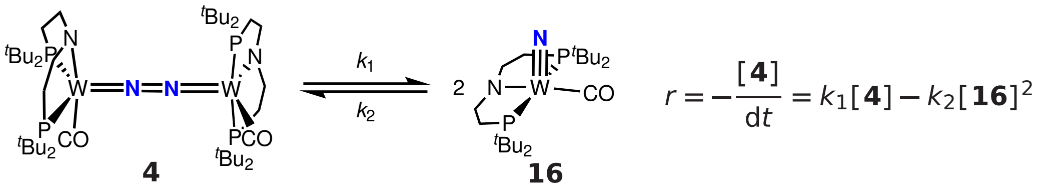

$$r = -\frac{[\mathbf{4}]}{dt} = k_1[\mathbf{4}] - k_2[\mathbf{16}]^2$$

Scheme 63: The equilibrium of **4** and **16** and the resulting rate law for the decay of **4** used to fit the kinetic curves.

The rate constants k_1 and k_2 determine the equilibrium constant K, which was additionally determined by measuring the equilibrium concentrations of **4** and **16** after elongated heating of **4** to 75, 85 and 95 °C, respectively (Figure 26, *right*, blue squares). *Van't Hoff*-analysis (Figure 26, *left*) with the so-obtained values gave rise to the thermodynamic parameters of the reaction, which show that N_2-cleavage is endothermic ($\Delta H^{\circ}_{exp} = 10.9\pm0.7$ kcal·mol^{-1}), but entropically driven at high temperatures ($\Delta S^{\circ}_{exp} = 24.8\pm1.8$ cal·mol^{-1}·K^{-1}).[208]

Eyring-analysis (Figure 26, *right*) of the rate constant k_1 offered the activation parameters for N_2-cleavage ($\Delta H^{\ddagger}_{exp} = 30.1\pm0.9$ kcal·mol^{-1}, $\Delta S^{\ddagger}_{exp} = 2.3\pm0.4$ cal·mol^{-1}·K^{-1}). The high barrier is in line with the stability of **4** at r.t. and also inhibits reverse nitride-coupling at low temperatures. Accordingly, to overcome the kinetic barrier high temperatures are required, which also shift the equilibrium towards entropically favored **16**. This system represents the first example of a reversible N_2-splitting/ nitride-coupling reaction. This holds the promise that the formed nitride species is less "overstabilized" and more reactive towards reagents that are more compatible with reductive conditions. The functionalization of **16** will be discussed in chapter 2.4.

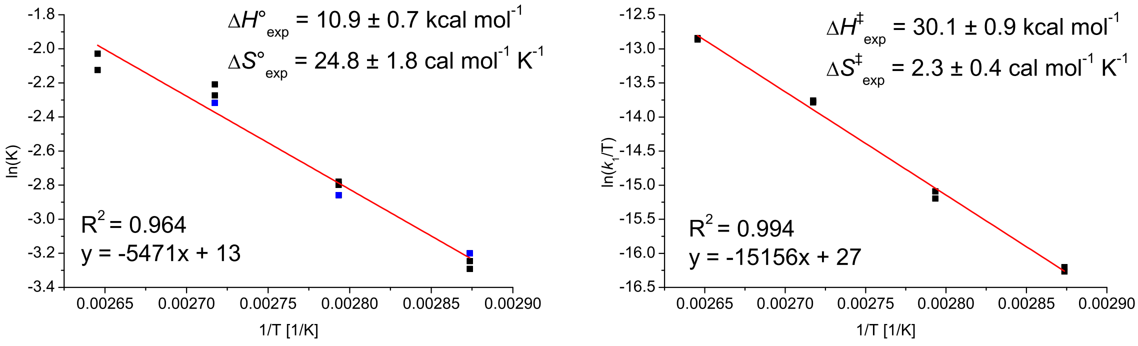

(a) *Van't Hoff*-plot

(b) *Eyring*-plot

Figure 26: *left:* ln(K) *vs.* 1/T -plot for the conversion of **4** into **16**. The black dots represent the K-values obtained by kinetic modeling, while the blue dots are the directly determined K-values. *right:* ln(k_1/T) *vs.* 1/T -plot for the conversion of **4** into **16**.

The experimental results are supported by computational investigations.[g] As already mentioned, the triplet ground state (**^{T}4**) is favored over the closed-shell-singlet ground state (**^{S}4**) by 1.2 kcal·mol^{-1}, while no open-shell-singlet could be found. Additionally, two different isomers of nitride **16**, which differ with respect to the conformation of the ligand backbone, could be identified (Figure 27). The conformation of the ligand-backbone within **16a** is similar to dinuclear **4**, while the backbone of **16b** is flipped (Figure 27, *right*). Both isomers are separated by $\Delta G^{\circ}_{298\,K} = 6.0$ kcal·mol^{-1}, with **16b** being the favored.

---

[g] DFT-calculations were performed by **Prof. Dr. Vera Krewald** and **M.Sc. Severine Rupp** using: PBE/def2-TZVP,def2-SVP.

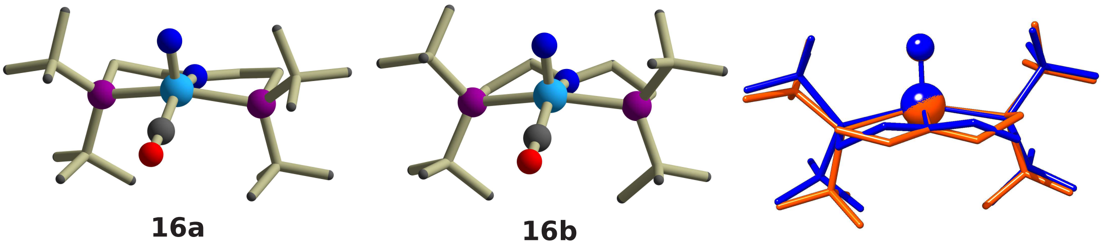
16a **16b**

Figure 27: *left*: Computed structures of **16a**. *middle*: Computed structures of **16b**. *right*: Overall of the computed structures of **16a** (orange) and **16b** (blue). For clarity all hydrogen-atoms were omitted.

Starting from $^{\mathbf{T}}\mathbf{4}$, N_2-cleavage into directly dissociated **16a** was calculated to be slightly endergonic ($\Delta G^{\circ}_{298\,K}$= 5.3 kcal·mol^{-1}). Additional driving force (6.0 kcal·mol^{-1}) is added by isomerization of **16a** into **16b** after cleavage. Overall, the computed value for cleavage of **4** into **16b** ($\Delta G^{\circ}_{298\,K}$= -0.7 kcal·mol^{-1}.) compares well to the experimentally derived value (ΔG°_{exp} = 3.5±0.9 kcal·mol^{-1}, Scheme 64, *left*). The small difference may arise from additional stabilization of $^{\mathbf{T}}\mathbf{4}$ by spin-orbit coupling, which is not sufficiently expressed by the DFT computations.

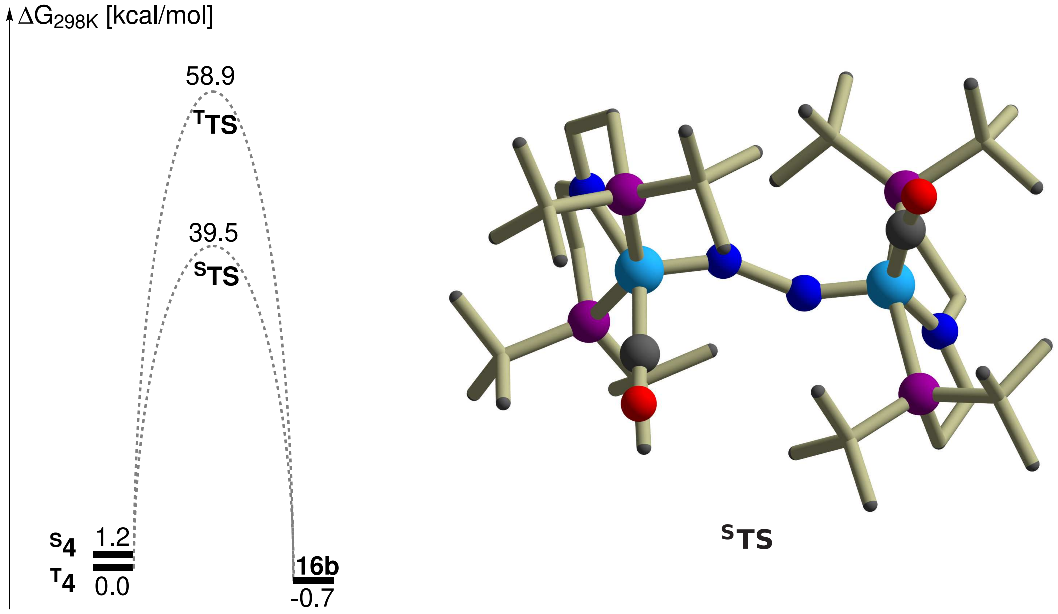

Scheme 64: *left*: Energy-profile for the N_2-splitting of **4** to give **16** including the experimental and computed values. *right*: Structure of the calculated singlet-transition-state, $^{\mathbf{S}}\mathbf{TS}$.

The lowest transition-state for N_2-cleavage without isomerization of the ligand backbone ($^{\mathbf{S}}$**TS**) features a closed-shell singlet-configuration and was localized 39.5 kcal·mol^{-1} above $^{\mathbf{T}}$**4** (Scheme 64, *right*), which is significantly higher than the experimentally derived value ($\Delta G^{\ddagger}_{exp}$ = 29.4±0.1 kcal·mol^{-1}). The transition-state on the triplet-surface ($^{\mathbf{T}}$**TS**) is 19.4 kcal·mol^{-1} above $^{\mathbf{S}}$**TS**.

Preliminary computational results indicate that conformational changes of the ligand backbone prior to N_2-cleavage decrease the kinetic barrier for NN-bond scission and bring the energies of the respective transition states closer to the experimentally derived value. The lowest transition state including these conformational changes of the ligand backbone is calculated to be singlet-configured, which can be accounted to bending of the {WNNW}-core (Scheme 65). Due to the lower symmetry of this *zig-zag*-conformation, the degeneracy of the π^*-π-π^*-orbitals is lifted. As a result spin-pairing to a singlet-conformation becomes favorable, as already described for analogous systems.[15,60,70]

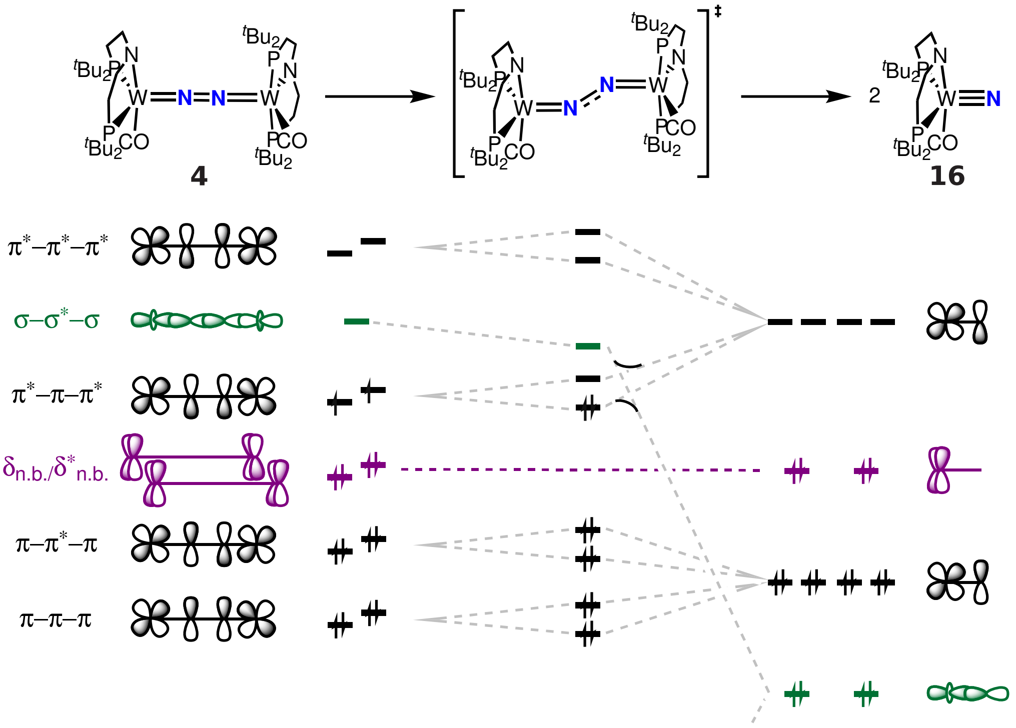

Scheme 65: Qualitative molecular orbital diagram for the splitting of **4** into **16** *via* a *zig-zag*-transition state.

Compared to the isostructural and isoelectronic ReCl-congener **XII** ($\Delta G^{\ddagger}_{exp} = 19.8 \pm 1.3$ kcal·mol^{-1}; $\Delta G^{\circ}_{calc} = -40.3$ kcal·mol^{-1}),[36] splitting of **4** into **16** is both kinetically and thermodynamically less favored, which can be attributed to the strong π-acceptor properties of the carbonyl-ligand. As already described in the introduction (chapter 1.2.2), N_2-cleavage proceeds *via* electron transfer from the π^*-π-π^* into the former σ-σ^*-σ-orbital, which drops in energy and forms the M-N σ-orbital within the generated nitride-species (Scheme 65). Accordingly, the relative energies of these orbitals should correlate to the thermodynamic and kinetic parameters of the reaction.

The presence of a strong π-accepting ligand, such as CO, should lead to stabilization of the π^*-π-π^*-orbitals and a larger energy gap to the σ-σ^*-σ-orbital. Hence, mixing of these orbitals reduced, which results in a higher kinetic barrier for N_2-cleavage for **4** compared to **XII**.

Furthermore, breakage of the NN-bond in **4** is accompanied by a significant amount of charge transfer from the {MNNM}-π-manifold to the N_2-ligand, as indicated by a strong hypsochromic shift of the carbonyl-stretching frequencies ($\Delta\tilde{\nu}_{CO}$(**4**→**16**) = 120 cm^{-1},[h] Scheme 62) upon cleavage. Compared to **XII** the electron density within the {MNNM}-π-core of **4** is decreased by back-bonding to the carbonyl-ligands. Transfer of electron density from the π-manifold to the nitrogen should therefore be thermodynamically less favorable, in line with the different thermodynamic driving forces for **4** and **XII**.[36]

---

[h] The average of both CO-stretching frequencies in **4** was used.

2.3.2 Photolytic N_2-cleavage

Besides the described thermal pathway, **16** can also be obtained *via* photolysis. Irradiation of **4** in benzene at 427 nm (LED, $\Delta\lambda$= 10 nm) for 8 h gives **16** quantitatively with a quantum yield of $\phi_{427\ nm}$ = 0.37±0.03%. The UVvis spectrum of **4** is depicted in Figure 28 and features two intense bands at 343 ($\epsilon = 27000$ L·mol^{-1}·cm^{-1}) and 395 nm ($\epsilon = 28000$ L·mol^{-1}·cm^{-1}) and another intense isolated band at 511 nm ($\epsilon = 21200$ L·mol^{-1}·cm^{-1}). Upon wavelength selective photolysis of **4**, using a Xe-arc lamp with cut-off filters, the selective region for photolytical N_2-cleavage was determined to 395-590 nm. Usage of longer wavelengths showed no reaction, while usage of shorter wavelengths lead to substantial amounts of unidentified side-products, which were tentatively attributed to W-N_2 bond cleavage as reported for related systems.[61,133,136]

However, photolysis of **4** at $\lambda > 305$ nm under $^{15}N_2$-atmosphere does not lead to ^{15}N incorporation into the nitride photoproduct **16**, indicating that the W–N bond might be photostable. Instead, photolysis of **16** at $\lambda > 305$ nm resulted in formation of undefined products, which can be associated to CO-loss of the nitride product under these conditions.

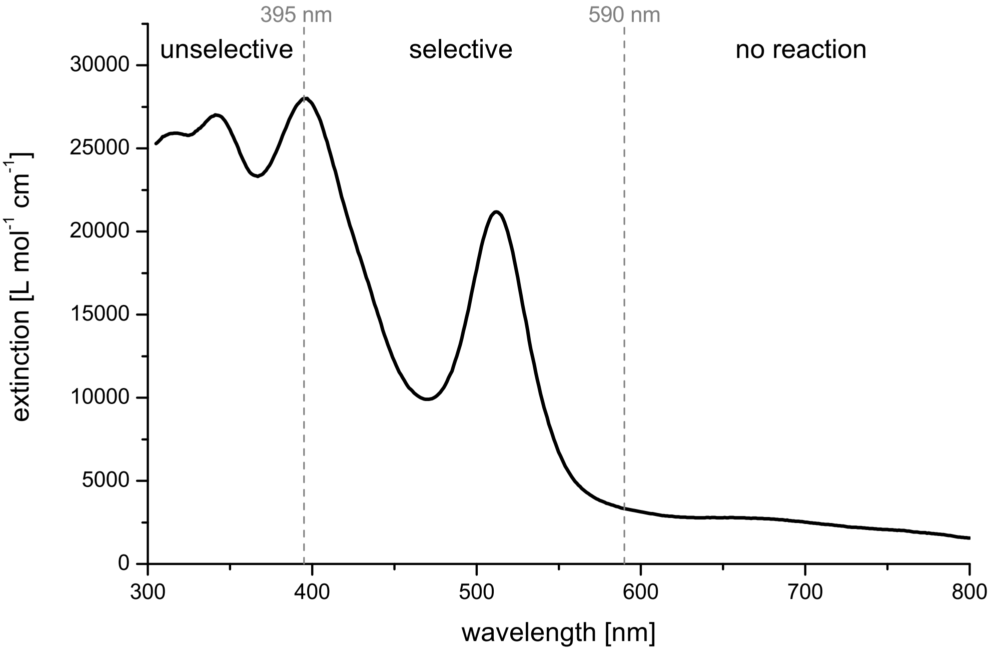

Figure 28: Experimental UVvis spectrum of **4** in THF.

For further inside, the photochemical and photophysical properties of **4** were examined *via* UVvis/UVvis pump-probe transient absorption spectroscopy.[i] For all used pump wavelengths within the the productive window (440, 475, 511, 530 nm) no features of an electronically excited state could be detected. Instead all transient difference spectra directly after excitation show bleaching in the band centers and enhanced absorption at the low energy sides of the ground state absorption spectrum (Figure 29, *left*), which is a typical signature of a vibrationally hot electronic ground state formed within the temporal resolution of the experiment ($\tau_{exc} \approx 70\pm20$ fs). Thermal cooling occurs within 60 ps and results in almost full relaxation, in line with the low quantum yield for N_2-cleavage.
Usage of shorter pump wavelengths (330 and 380 nm) lead to slow decomposition into undefined products, in agreement with steady state photolysis.

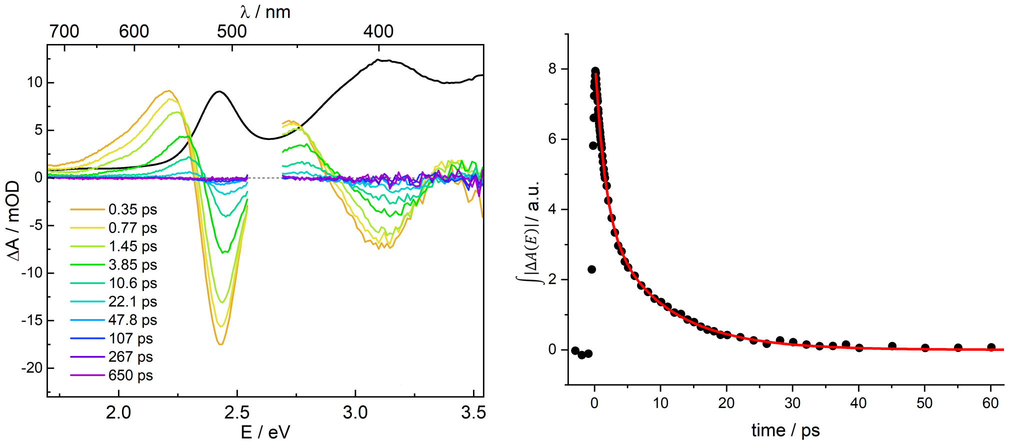

Figure 29: *left:* Transient UVvis difference spectra of **4** in THF at selected pump-probe delays (pump wavelength: 475 nm). The black line shows the scaled linear absorption spectrum. *right:* Time-dependence of the integrated absolute absorption changes (red line is a bi-exponential fit with $\tau_1 = 1.5\pm0.2$ ps and $\tau_2 = 9.2\pm0.5$ ps).

By analysing the integral over the absolute value of the difference spectra ($|\Delta A(E)|$) integrated over the whole measured spectral range the relaxation dynamics of the ground state were quantified (Figure 29, *right*). Using a bi-exponential decay the time dependence could be fitted, which gave rise to two time constants (relative amplitudes) of $\tau_1 = 1.5\pm0.2$ ps (54%) and $\tau_2 = 9.2\pm0.5$ ps (46%).
While the slower component (τ_2) is a typical value for vibrational energy transfer of a vibrationally highly excited molecule to a solvent, the faster component (τ_1) can be attributed to intramolecular vibrational redistribution (IVR), which implies a non-statistical energy distribution directly after relaxation from the exited state created by preferential population of those vibrational modes which couple to the electronic transition. Within the timescale of $\tau_1 = 1.5$ ps the energy is redistributed over the whole molecule to establish a quasi-equilibrium of the internal energy.

---

[i] The pump-probe experiments were run and analyzed by **Prof. Dr. Dirk Schwarzer** and **M.Sc. Jan-Hendrik Borter**.

Since the carbonyl stretching vibrations represent excellent IR-probes, the photochemistry of **4** was also examined by UVvis/IR pump-probe transient absorption spectroscopy (Figure 30, 400 nm pump pulse). As for the UVvis/UVvis pump-probe transient absorption measurements no features of an electronically excited state could be detected, which is in line with the poorer time resolution of the UVvis/IR pump-probe transient absorption measurements. The transient difference spectra directly after excitation (Figure 30) show bleaching in the band centers and an increased absorption at the high energy sides of the ground state absorption spectrum, which is again a typical signature of a vibrationally hot electronic ground state and supports the observations made in the UVvis/UVvis pump-probe transient absorption measurements.

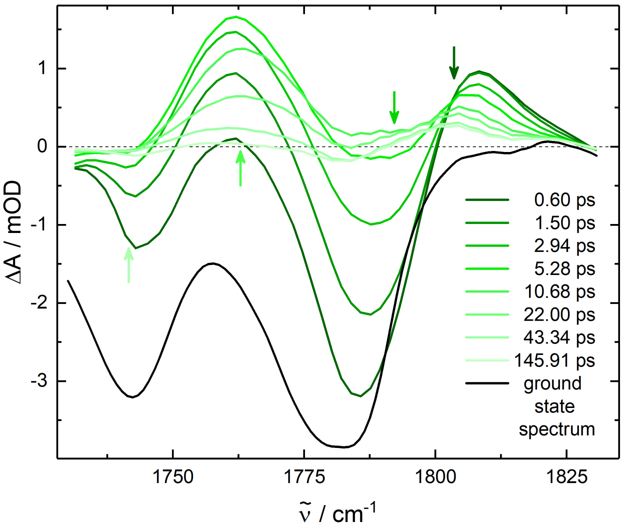

Figure 30: Transient IR difference spectra of **4** in THF at selected pump-probe delays (pump wavelength: 400 nm).

Overall, these observations indicate three characteristics of this system. First, the lifetime of the excited state is shorter than the time-resolution of the experiment (70±20 fs). Second, the energy directly after relaxation to the electronic ground state is non-statistically distributed and requires another 1.5 ps to reach quasi-equilibrium. Finally, all photoreactivity has to occur within a timescale of 60 ps, since afterwards the molecule has completely relaxed.

Taking these considerations into account, two scenarios are envisioned, a diabatic pathway (Figure 31, *left*) and a hot-ground-state pathway (Figure 31, *right*). An adiabatic pathway, where the reaction proceeds on the energy-surface of the exited state, would require longer lifetimes of the excited state and can therefore be excluded.[209,210]

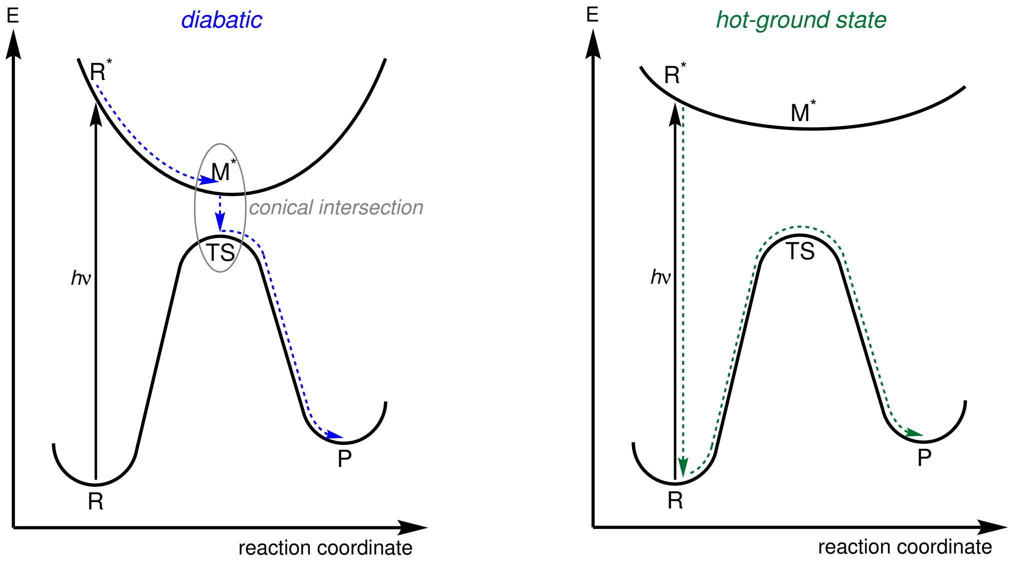

Figure 31: Simplified energy surfaces for a diabatic photoreaction (*left*) and a reaction proceeding *via* a hot-ground state (*right*) with R = reactant, TS = transition state, P = product, M* = minimum of the energy surface of the excited state.[209,210]

In case of a diabatic photoreaction, strong coupling of the ground- and excited-state energy surfaces is required. At a certain geometry along the reaction coordiniate between the reactant (R) and the product (P) both energy-surfaces converge, which allows energetically favorable irradiationless "jumps" from the excited-state to the ground-state surface. In a simplified picture (Figure 31, *left*), following a representative point, irradiation leads to vertical excitation of the reactand from the ground- into the excited state surface ($R \xrightarrow{h\nu} R^*$), followed by relaxation towards the energetic minimum of the excited state ($R^* \rightarrow M^*$). At a certain geometry, it is possible for the representative point to fall back to the ground-state energy-surface. If this jump proceeds prior to the transition state (TS) the molecule relaxes back into R, without any product formation. Crossing beyond the transition state results in relaxation to the minimum of product P.[209,210]

In case of a hot-ground-state reaction (Figure 31, *right*), the molecule relaxes directly after excitation back to the ground-state surface. The energy of the absorbed photon is distributed over the molecule by population of higher vibrational states. If the absorbed energy is large enough, dissociative modes can also be populated, which can induce bond-breakage and product formation.[209,210]
To estimate if such a hot-ground-state pathway is possible, the internal energy of the molecule after excitation and IVR was calculated and compared with the derived kinetic barrier for N_2-cleavage. The DFT-calculated vibrational frequencies of **4** were used to determine its internal vibrational energy at r.t. ($E_{\mathrm{r.t.}} = 15700\ \mathrm{cm}^{-1}$). Addition of a 400 nm photon leads to an internal vibrational energy of $E_{\mathrm{exc}} = 40700\ \mathrm{cm}^{-1}$, which corresponds to an internal vibrational temperature of $T \approx 500$ K.

According to eqn. 2.5, this value, together with the experimentally derived activation parameters ($\Delta H^{\ddagger}_{exp} = 30.1 \pm 0.9$ kcal·mol^{-1}, $\Delta S^{\ddagger}_{exp} = 2.3 \pm 0.4$ cal·mol^{-1}·K^{-1}), gives rise to the rate constant k_{splitt} for unimolecular splitting, which is too small to compete with rapid cooling ($\tau_2 = 9.2 \pm 0.5$ ps).[211]

$$k_{splitt} = \frac{k_b \cdot T}{h} \cdot \exp\left(-\frac{\Delta H^{\ddagger} - T \cdot \Delta S^{\ddagger}}{R \cdot T}\right) = 2.3\ s^{-1} \qquad (2.5)$$

In consequence, N_2-splitting from a hot-ground state after statistical energy-distribution is not feasible. However, the smaller time constant ($\tau_1 = 1.5$ ps) indicates a non-statistical energy distribution directly after relaxation to the hot-ground-state. Vibronic coupling of the electronically exited state with, for example, bending-modes of the {MNNM}-core *en route* to a *zig-zag*-transition state, might decrease the kinetic barrier for NN-bond scission. Such vibronic coupling has been observed by *Cummins* and *Blank* for $[(N_2)\{Mo(N(^tBu)Ar)_3\}_2]$ (**I**; Ar = 3,5-$C_6H_3Me_2$) as an underdamped oscillation in the pump-probe decay, which was assigned to vibronic coupling of a bending mode of the {MoNNMo}-core.[136]
By now, no direct indication for coupling of a productive vibrational mode to the electronic excitation could be found for **4**, which might indicate that N_2-cleavage proceeds *via* direct population or rapid internal conversion into an N–N dissociative state.

For further insides into the nature of the excited state, the photochemistry of **4** was examined computationally using TD-DFT.[j] The experimentally obtained UVvis spectrum of **4** is well reproduced by TD-DFT calculations for both electronic configurations, triplet (**^{T}4**) and closed-shell singlet (**^{S}4**), but with a blue-shift of 0.38 eV in both cases (Figure 32).

---

[j] TD-DFT calculations were performed by **Prof. Dr. Vera Krewald** and **M.Sc. Severine Rupp** using: PBE0(THF).

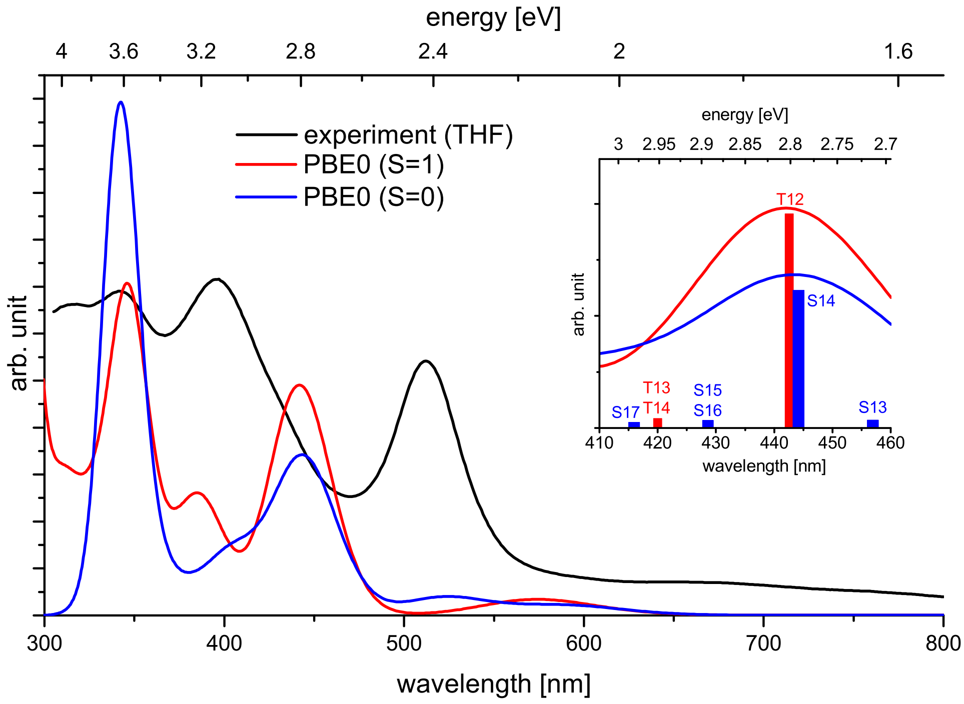

Figure 32: Comparison of the experimental (black) and TD-DFT computed (blue: $S = 0$; red: $S = 1$) electronic absorption spectra of **4**. The inset shows the potentially active transitions.

To distinguish which of the calculated transitions within the photolytical active window (395-590 nm) are the actually productive ones for N_2-cleavage, **4** was photolyzed with wavelengths longer than 530 nm. Although, some conversion could be observed, the rate was significantly slower compared to irradiation with shorter wavelengths, which indicates that the productive transition is energetically slightly above 530 nm (or 2.72 eV/456 nm in the calculated spectrum). Therefore, T13/T14 (both 2.89 eV/429 nm (calc.)) or S15/S16 (both 2.51 eV/494 nm (calc.)) are assumed as the productive transitions for photolytic N_2-cleavage in **4**.

The difference density plots of all these four transitions reveal {W-CO} → N_2-character (Figure 33, *left*), which can be rationalized as an metal-to-ligand charge transfer (MLCT) from the metal-carbonyl centered δ/δ^*-orbitals to the π^*-π^*-π^*-orbitals within the {WNNW}-core (Figure 33, *right*). Due to its all anti-bonding character population of this orbital should decrease the bond-orders within the {M-N-N-M}-core and therefore increase its flexibility. In this way, bending to a *zig-zag*-conformation might be induced, which finally leads to cleavage of the NN-bond.

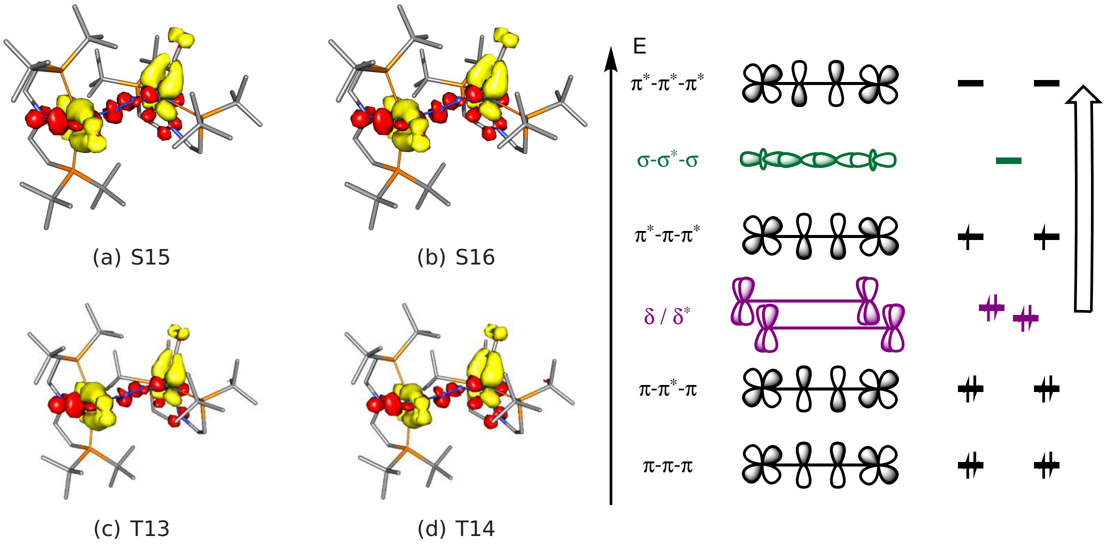
(a) S15 (b) S16

(c) T13 (d) T14

Figure 33: *left*: Difference density plots (loss in yellow,gain in red) for the transitions S15, S16, T13 and T14 calculated for **4**. *right*: Simplified MO-scheme for **4** with the electronic excitation assigned to productive in photolytic N_2-cleavage.

Overall, the TD-DFT calculations imply a photochemical pathway in which N_2-cleavage proceeds *via* direct population or rapid internal conversion into an N–N dissociative state. Population of the π^*-π^*-π^*-orbitals leads to bending of the {W-N-N-W}-core, which should lower the σ-σ^*-σ-orbital in energy. In consequence, mixing between the π^*-π-π^*- and σ-σ^*-σ-orbitals is enabled, which finally leads to cleavage of the NN-bond. Nevertheless, a final assignment is currently prevented by the rapid timescales and low quantum yields.

However, a $\delta/\delta^* \rightarrow \pi^*$-$\pi^*$-$\pi^*$-excitation with MLCT-character was also found to be productive for N_2-cleavage within **XIII** and might therefore hint to a general feature for photolytic N_2-cleavage from an idealized fourfold symmetry.[71] In contrast, the active transition within *Cummins'* **I** was assigned to a π-π^*-$\pi \rightarrow \pi^*$-π-π^*-transition, which should strengthen the NN-bond and might explain the different photochemistry of **I** compared to **4**.[136]

2.4 Functionalization of tungsten-nitrido-complexes

As described in the previous chapters, two different tungsten-nitrido-complexes, [W(N)Cl(^{H}PNP)]$^{+}$ (**11**) and [W(N)CO(PNP)] (**16**), could be obtained *via* N_2-cleavage from **1** and **4**, respectively. However, comparison of their thermodynamic driving forces for N_2-cleavage shows, that splitting of **17** into **11** upon protonation is strongly downhill. Accordingly, **11** should be largely overstabilized and more difficult to functionalize. In contrast, splitting of **4** into **16** is almost thermoneutral, rendering the nitride product more reactive based on thermodynamic arguments. Additionally, synthetic access to **16** *via* photolysis is much more convenient and does not compete with any other side reaction. Therefore, further functionalization attempts focused on **16**.

2.4.1 Alternative synthesis of [W(N)(CO)(PNP)] (16) *via* an azide route[k]

Since the synthesis of [W(N)(CO)(PNP)] (**16**) *via* the N_2-splitting route requires several reaction steps with moderate overall yields, alternative synthetic pathways to generate **16** have been developed in cooperation with the group of *Caulton*, which will be described in this chapter (Scheme 66).

Refluxing a mixture of [W(CO)$_6$] with ^{H}PNP in toluene or acetonitrile gives [W(CO)$_3$(^{H}PNP)] (**9**) in good yields. The diamagnetic compound shows a singlet signal in the ^{31}P{^{1}H} NMR spectrum at 89.5 ppm flanked by tungsten satellites. The ^{1}H NMR spectrum shows two resonances for the ^{t}Bu-groups and four signals for the ligand CH-protons, indicating C_s-symmetry, due to the presence of the NH-proton, which was assigned to a signal at 2.53 ppm based on a cross-peak in the ^{1}H -^{15}N HSQC NMR spectrum. The IR spectrum of solid **9** shows a band at 3227 cm^{-1} that was assigned to the N-H-stretch and three intense bands at 1896, 1773 and 1753 cm^{-1} assigned to the three carbonyl-ligands, similar to other W(0)-triscarbonyl-complexes.[212] The molecular structure obtained by X-ray diffraction shows that the ^{H}PNP-ligand is coordinated in a meridional fashion, most likely due to the steric bulk of the ^{t}Bu-substituents (Figure 34, *left*).

---

[k] Parts of this work have been published in:
- N.A. Maciulis "Exploring redox properties of bis(tetrazinyl)pyridine (btzp) complexes of group VI metals, tetrazine and phosphine assisted reduction of H_2O, and dinitrogen cleavage and functionalization" *Ph.D. Thesis*, Indiana University Bloomington, **2019**.
- J. Schneider "Synthese und Funktionalisierung von Wolfram-PNP-Nitrid Komplexen" *Bachelor Thesis*, Georg-August Universität Göttingen, **2019**.

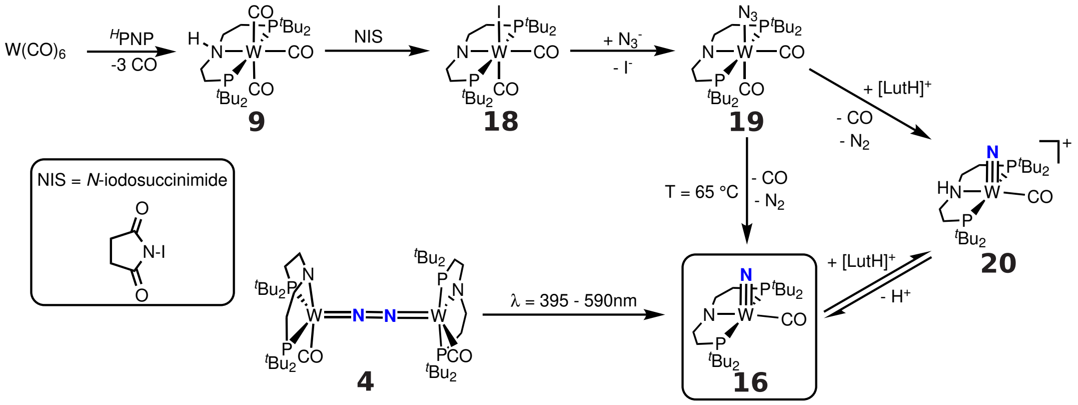
W(CO)6
HPNP
-3 CO
9
NIS
18
+ N3-
- I-
19
+ [LutH]+
- CO
- N2
20
T = 65 °C
- CO
- N2
NIS = N-iodosuccinimide
N-I
4
λ = 395 - 590nm
16
+ [LutH]+
- H+

Scheme 66: The two possible synthetic pathways for the synthesis of **16**.

9 can be oxidized and deprotonated in one step using *N*-iodosuccinimide to give deep purple [WI(CO)$_2$(PNP)] (**18**) in almost quantitative yield. Notably, the *N*-halosuccinimides can also be used to generate the corresponding chloro- and bromo-analogues of **18**. However, only the iodo-complex **18** was feasible for anion exchange reactions, most likely due to the better leaving group character of iodide compared to chloride and bromide.

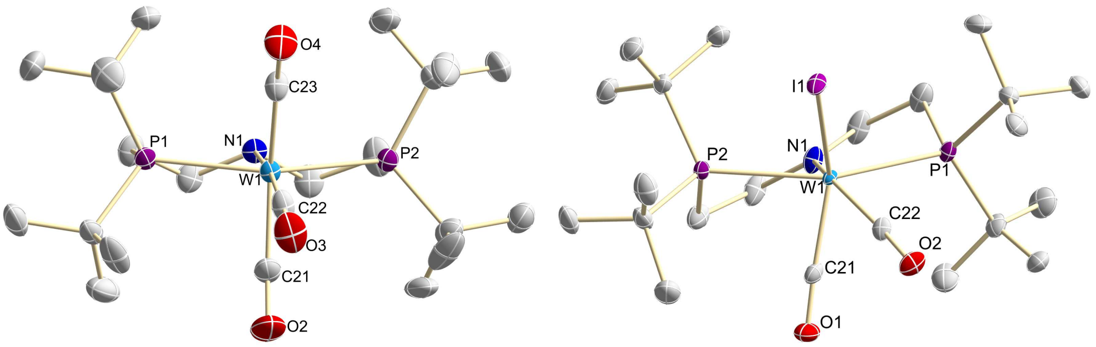
O4
C23
P1
N1
W1
P2
C22
O3
C21
O2
I1
P2
N1
W1
P1
C22
O2
C21
O1

9 **18**

Figure 34: Molecular structures of **9** (*left*) and **18** (*right*) in the crystal obtained by single crystal X-ray diffraction. Hydrogen-atoms are omitted for clarity. Selected bond lengths [Å] and angles [°] for **9**: W1-C21 1.990(3), W1-C22 1.928(3), W1-C23 1.999(3), W1-N1 2.344(2), W1-P1 2.5058(7), W1-P2 2.4944(7); C21-W1-C23 154.79(13), N1-W1-C22 169.19(11), P1-W1-P2 154.04(2). Selected bond lengths [Å] and angles [°] for **18**: W1-C21 1.920(4)/1.973(15), W1-C22 2.000(4)/1.971(16), W1-I1 2.8256(4)/2.831(6), W1-N1 2.008(3)/2.062(4), W1-P1 2.5246(9)/2.564(3), W1-P2 2.5307(8)/2.522(3); C21-W1-I1 134.87(11)/141.9(13), C22-W1-N1 148.05(14)/160.2(17), P1-W1-P2 150.91(3)/148.34(15).

In the $^{31}P\{^{1}H\}$ NMR spectrum of **18** a singlet resonance flanked by tungsten-satellites was found at 67.6 ppm. The ^{1}H NMR spectrum features two signals corresponding to the ^{t}Bu-groups and four signals for the ligand backbone, indicating C_s-symmetry with the iodo substituent *trans* to one carbonyl-ligand, which was confirmed by the molecular structure obtained by X-ray diffraction (Figure 34, *right*). In the IR spectrum of solid **18** two carbonyl stretching vibrations at 1907 and 1799 cm^{-1} could be observed. The absence of an N-H stretch in the IR as well as of an NH-proton in the ^{1}H NMR together with the planarity of the PNP-nitrogen evidences the deprotonation of the PNP-ligand. As an effect of stronger σ- and π-donation of the amide compared to the amine ligand the W-N distance decreases from 2.344(2) Å (in **9**) to 2.008(3) Å (in **18**).

Salt metathesis of **18** with $[nBu_4N]N_3$ gives $[W(N_3)(CO)_2(PNP)]$ (**19**) in almost quantitative yield. The NMR spectroscopic features are similar to the ones for **18** and show a singlet flanked by tungsten satellites in the $^{31}P\{^{1}H\}$ NMR spectrum at 77.7 ppm, two signals for the ^{t}Bu-groups and four signals for the ligand backbone in the ^{1}H NMR spectrum. The IR spectrum of solid **19** features two nearly unchanged carbonyl stretching vibrations at 1907 and 1828 cm^{-1}, while the band for the azide stretching vibration was found at 2072 cm^{-1}. The molecular structure of **19** derived by X-ray diffraction also closely reassembles the structure of **18**. **19** is thermally unstable and releases N_2 and CO upon heating to 65 °C to give nitride **16**. However, the reaction is not quantitative due to the formation of one major side product, which was identified as $[W(NCO)(CO)_2(PNP)]$ (**21**). The selective synthesis of **21** will be described later in this chapter.

Therefore, alternative ways to trigger N_2-loss from **19** were investigated. Mild acids, such as lutidinium-salts, lead to clean formation of ligand protonated, cationic $[W(N)(CO)(^{H}PNP)]^{+}$ (**20**) in good yields (Scheme 67).

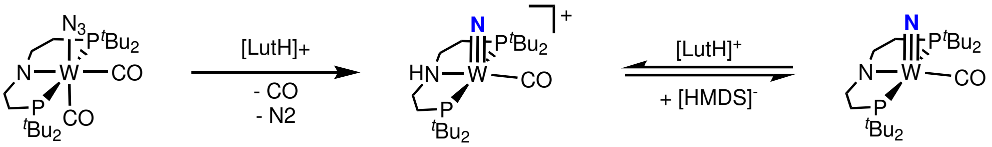

19 **20** **16**

Scheme 67: Protonation of **19** liberates CO and N_2 and gives **20**.

The ^{1}H NMR spectrum of **20** displays two signals for the ^{t}Bu-groups, four multiplets for the ligand backbone and one signal at 5.93 ppm attributed the NH-proton. In the $^{31}P\{^{1}H\}$ NMR spectrum one singlet at 93.1 ppm was detected. Alternatively, **20** can also be synthesized upon protonation of **16** with lutidinium-salts, giving identical NMR signature. An ^{15}N-labeled sample (^{15}N-**16**) derived *via* the N_2-splitting route, gave rise to a resonance in the $^{15}N\{^{1}H\}$ NMR spectrum at 445.7 ppm. The IR spectrum of solid

20 shows a sharp, intense band for the carbonyl ligand at 1928 cm^{-1}. Compared to neutral **16**, this band is shifted at about 45 cm^{-1} to higher wavenumbers, which can be attributed to the reduced donor properties of the amine ligand. The W≡N-stretch was found at 1048 cm^{-1} ($\tilde{\nu}_{WN}$ (^{15}N-**20**) = 1014 cm^{-1}) close to the W≡N-stretch of **11** ($\tilde{\nu}_{WN}$ (^{14}N-**11**) = 1058 cm^{-1}) and other, related tungsten-nitrides.[202–205] The N-H-stretching vibration was detected at 3118 cm^{-1}.

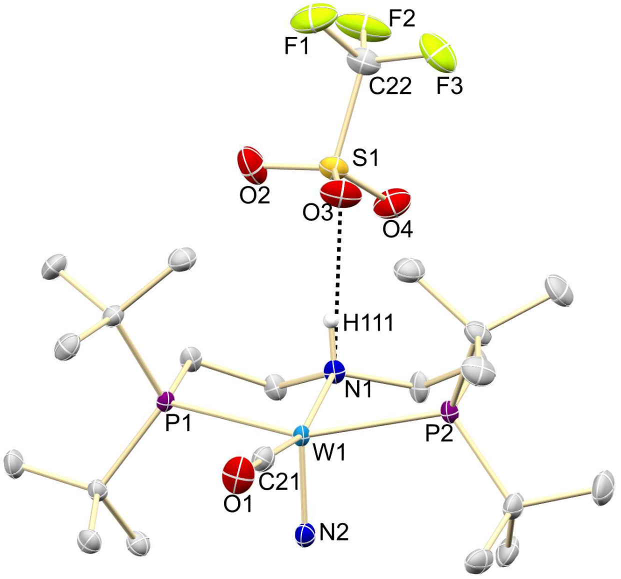

Figure 35: Molecular structure of **20** in the crystal obtained by single crystal X-ray diffraction. Hydrogen-atoms, with exception of H111, and co-crystalized solvent molecules are omitted for clarity. Selected bond lengths [Å] and angles [°]: W1-C21 2.005(2), W1-N1 2.2402(17), W1-N2 1.6861(18), W1-P1 2.4886(5), W1-P2 2.5006(5); C21-W1-N1 162.75(8), N1-W1-N2 103.59(8), P1-W1-P2 153.504(18).

In the solid state **20** is isostructural with the previously described **11** (Figure 35) and features a square pyramidally coordinated tungsten atom (τ=0.15)[193] with the nitride ligand in the apical position and a short W≡N-distance (1.6861(18) Å). The triflate anion is hydrogen bonded to the NH-proton of the ligand backbone, which was found in the residual density map and isotropically refined. Due to the lack of π backdonation of the amine ligand, the distance between the tungsten ion and the PNP-ligand-nitrogen is relatively long (2.2402(17) Å).

Finally, **20** can be deprotonated with weakly coordinating bases like, NaHMDS or KHMDS, to give quantitatively the splitting product **16**, which was then used for further functionalization.

2.4.2 Functionalization of [W(N)(CO)(PNP)] (16) using π-acceptor ligands

As already mentioned, the thermal transformation of [W(N_3)$(CO)_2$(PNP)] (**19**) into [W(N)(CO)(PNP)] (**16**) is not quantitative due to the formation of one side-product. Within this reaction besides one equivalent of N_2 one equivalent of CO is liberated, which is known to couple with nitride-moieties to cyanate in some cases (see chapter 1.3.3). Therefore the reactivity of **16** with CO was examined.

Addition of CO to **16** results in the almost quantitative formation of deep purple [(PNP)W(NCO)$(CO)_2$] (**21**) (Scheme 68). Alternatively, **21** was also synthesized *via* salt-metathesis of **18** with [nBu$_4$N][OCN] in isolated yields up to 80%. The NMR signature of **21** is similar to those of **18** or **19**, respectively, and features one singlet in the ^{31}P{^{1}H} NMR spectrum at 76.7 ppm, two signals for the ^{t}Bu-groups and four signals for the ligand backbone in the ^{1}H NMR spectrum.

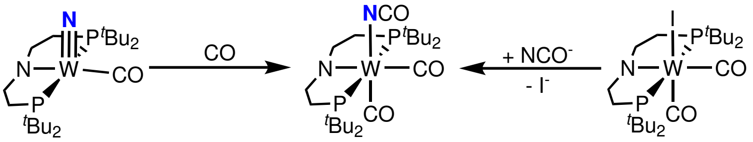

16 **21** **18**

Scheme 68: Carbonylation of **16** leads to formation of **21**.

Carbonylation of a ^{15}N-labeled sample of **16** gives rise to ^{15}N-**21**, whose ^{15}N{^{1}H} NMR spectrum features a triplet ($^2J_{NP} = 2.6$ Hz) at -347 ppm, flanked by tungsten-satellites indicating *N*-coordination of the NCO-ligand. Accordingly, the ^{31}P{^{1}H} NMR spectrum of ^{15}N-**21** shows a doublet. Furthermore, the broad signal at 145 ppm in the ^{13}C{^{1}H} NMR of unlabeled **21** assigned to the NCO-ligand sharpens upon ^{15}N-labeling to a doublet ($^1J_{CN} = 33.8$ Hz) (Figure 36).

In the IR spectrum of solid **21**, the carbonyl-stretching vibrations appear at 1910 and 1831 cm^{-1}. The intense sharp band at 2203 cm^{-1} is assigned to the NCO-ligand and shifts upon ^{15}N-labeling ($\tilde{\nu}_{NCO}$(^{15}N-**21**) = 2197 cm^{-1}) . In the solid state (Figure 37), the molecular structure of **21** derived by X-ray diffraction closely reassembles the structures of **18** and **19**.

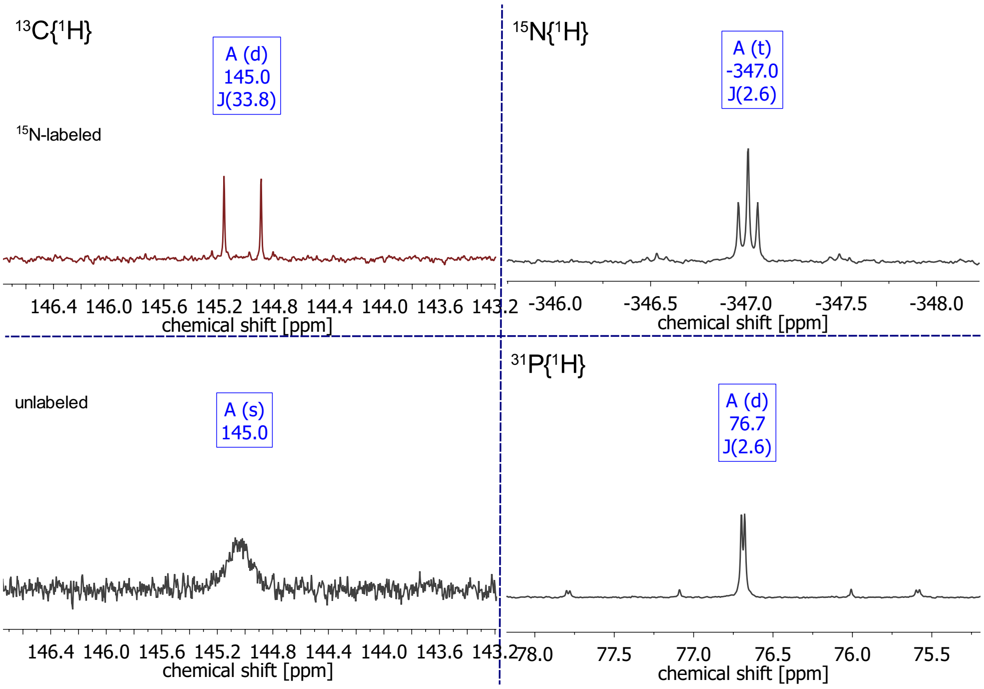

Figure 36: NMR signature of ^{15}N-**21**. *left:* ^{13}C{^{1}H} NMR signal of the ^{15}NCO- and ^{14}NCO-ligand. *right:* ^{15}N{^{1}H} and ^{31}P{^{1}H} NMR signals of ^{15}N-**21**.

Importantly, the described spectroscopic features of **21** are the same as for the observed side-product in the formation of **16** upon heating of **19**. Therefore, the formation of the side product from reaction of **19** to **16** can be explained by the liberation of CO, which readily reacts with **16**.

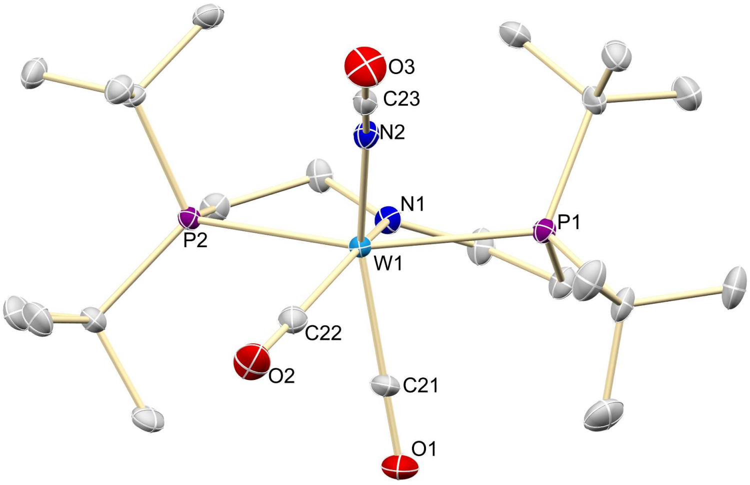

Figure 37: Molecular structure of **21** in the crystal obtained by single crystal X-ray diffraction. Hydrogen atoms were omitted for clarity. Selected bond lengths [Å] and angles [°]: W1-C21 1.964(4), W1-C22 2.028(4), W1-N1 2.011(3), W1-N2 2.116(3), W1-P1 2.5030(10), W1-P2 2.5077(10); C21-W1-C22 77.03(16), C21-W1-N1 85.54(15), C22-W1-N1 153.31(14), N1-W1-N2 122.56(13), P1-W1-P2 155.09(3).

2.4.3 Mechanistic investigations on CN-bond coupling[I]

To elucidate whether the CN-bond formation occurs *intramolecularly via* insertion of the nitride-nitrogen into the W-CO bond or *intermolecularly via* nucleophilic attack of the nitride on the incoming carbonyl-ligand, **16** was carbonylated with ^{13}CO. Depending on the mechanism, this should result in the formation of different products (Scheme 69), either showing an uneffected NCO- and two ^{13}CO-ligands (*intramolecular*, **21a**) or one N^{13}CO-ligand with one ^{12}CO- and one ^{13}CO-ligand (*intermolecular*, **21b**).

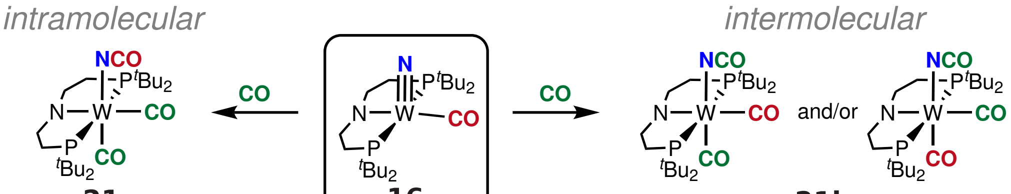

21a **16** **21b**

Scheme 69: Possible pathways for the formation of **21** *via* carbonylation of **16**, either following an intramolecular (*left*) or an intermolecular (*right*) pathway for C-N coupling to give **21a** or **21b**, respectively.

The ^{13}C{^{1}H} NMR spectrum of the obtained ^{13}CO-labeled product clearly displays an increased intensity of the resonances assigned to the two carbonyl-ligands at 266 and 262 ppm, while the intensity of the NCO-ligand at 145 ppm is uneffected compared to unlabeled **21** (Figure 38), indicating the incooperation of two ^{13}CO ligands into the formed complex, which was further supported LIFDI-MS. Both carbonyl-resonances give multiplets due to coupling with the two P-atoms of the PNP-ligand as well as coupling with each other. The signal in the ^{31}P{^{1}H} NMR spectrum gives a doublet of doublets ($^2J_{CP} = 8.4, 4.3$ Hz), also implying coordination of two ^{13}CO-ligands to the tungsten center (Figure 38). Consequently, in the IR spectrum the NCO-stretch is unaffected, while both carbonyl-stretches are bathochromically shifted ($\tilde{\nu}_{CO}$(^{13}CO-**21**) = 1860, 1762 cm^{-1}). These findings proof the formation of **21a** *via* an intramolecular pathway, similar to the one proposed by *Liddle* (Scheme 48).[188]

[I] Parts of this work have been published in: J. Schneider "Synthese und Funktionalisierung von Wolfram-PNP-Nitrid Komplexen" *Bachelor Thesis*, Georg-August Universität Göttingen, **2019**.

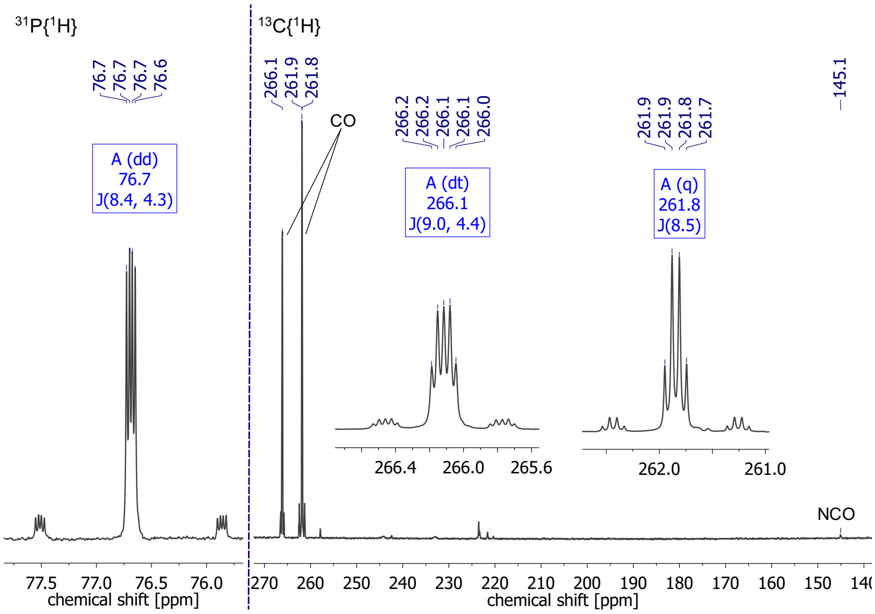

Figure 38: NMR signature of ^{13}CO-**21**. *left:* $^{31}P\{^1H\}$ NMR spectrum. *right:* $^{13}C\{^1H\}$ NMR spectrum, the inlays show a zoom into the signals of the two carbonyl ligands.

Since such a reactivity does not necessarily require the addition of CO, **16** was also functionalized using other ligands. Addition of two equivalents of isocyanide (CN-R, R = ^{t}Bu ,C_6H_4OMe) to **16** yields in the formation of [W(NCO)(CN-R)$_2$(PNP)] (R = ^{t}Bu (**22**), C_6H_4OMe (**23**)), in line with an intramolecular CN coupling reaction (Scheme 70). Other potential ligands, such as pyridine or trimethylphosphine, showed no reaction with **16**, which might be due to their slightly higher steric encumbrance.

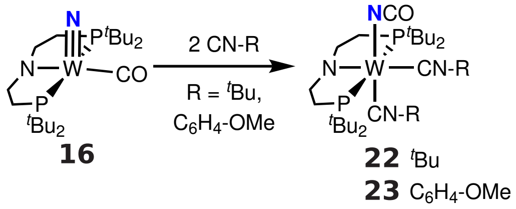

Scheme 70: Functionalization of **16** using isocyanides.

The formation of NCO$^-$ in **22** and **23** was proven *via* $^{13}C\{^1H\}$ NMR, which features in both cases a broad signal at 143 ppm very close to the signal assigned to the NCO-ligand in **21**. Furthermore, the IR spectra of solid **22** and **23** both show a intense sharp band at 2203 cm^{-1} identical with the NCO-stretch observed in **21**. Finally, the formation of a cyanate ligand could be confirmed by X-ray diffraction (Figure 39).

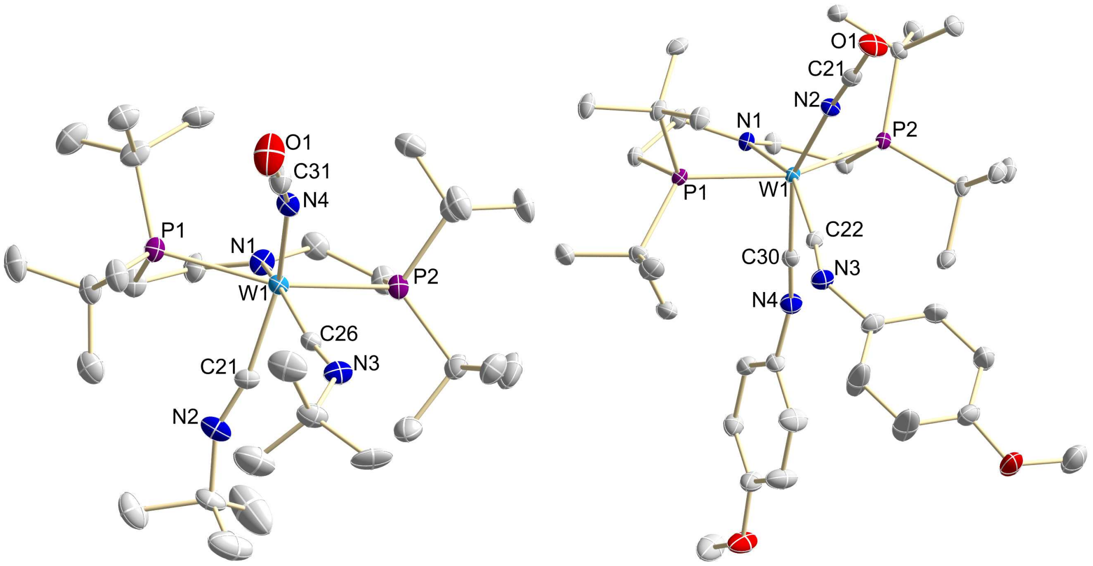

22 **23**

Figure 39: Molecular structures of **22** (*left*) and **23** (*right*) in the crystal obtained by single crystal X-ray diffraction. Hydrogen atoms and cocrystalized solvent molecules were omitted for clarity. Selected bond lengths [Å] and angles [°] for **22**: W1-C21 2.014(8), W1-C26 2.035(8), W1-N1 2.028(11), W1-N4 2.102(13), W1-P1 2.4906(18), W1-P2 2.4533(19); C21-W1-N4 153.4(4), C26-W1-N1 156.6(4), P1-W1-P2 155.23(7). Selected bond lengths [Å] and angles [°] for **23**: W1-C22 2.020(2), W1-C30 2.000(2), W1-N1 2.020(2), W1-N2 2.118(2), W1-P1 2.4735(6), W1-P2 2.4960(6); C22-W1-N1 155.95(9), C30-W1-N1 155.48(9), P1-W1-P2 155.36(2).

These intramolecular CN-coupling reactions contrast with the nucleophilic attack of the nitride to CO, which was proposed by *Cummins* for $Na[V(N)(N(^tBu)Ar)_3]$ (**LXXXIX**) (Scheme 47).[186] The differences might account from the different d-electron counts of both compounds. *Cummins'* vanadium(V)-nitride exhibits a d^0-configuration, which might, together with the steric encumbrance of the supporting ligands, circumvent binding of a carbonyl-ligand to the metal. In case of **16**, the tungsten ion is d^2-configurated and the carbonyl-ligand is already coordinated, which might explain the different mechanism. Nevertheless, the formation of **21** represents, after *Kawaguchi's* N_2-derived V(V)-nitride $[V(N)(ONO)]^-$ (**XCVIIIc**), the second example for CN-coupling of an N_2-derived nitride with CO.[190]

2.4.4 Liberation of cyanate and closure of the synthetic cycle

In the previous chapters the cleavage of N_2 and the formation of cyanate *via* C-N-coupling with CO to give $[W(NCO)(CO)_2(PNP)]$ (**21**) has been discussed. This chapter will focus on the release of the formed cyanate and closure of the synthetic cycle.

First, abstraction of the formed NCO^- *via* reduction, attempting direct reformation of N_2-bridged **4** was probed. For this purpose the redox chemistry of **21** was studied *via* cyclic voltammetry (CV). The cyclic voltammogram shows an irreversible reduction event at a potential of -2.0 V (vs. Fc^+/Fc in THF). The reduction product shows an irreversible oxidative wave at -1.55 V (vs. Fc^+/Fc in THF), which was not observed without prior reduction of **21** (Figure 40).

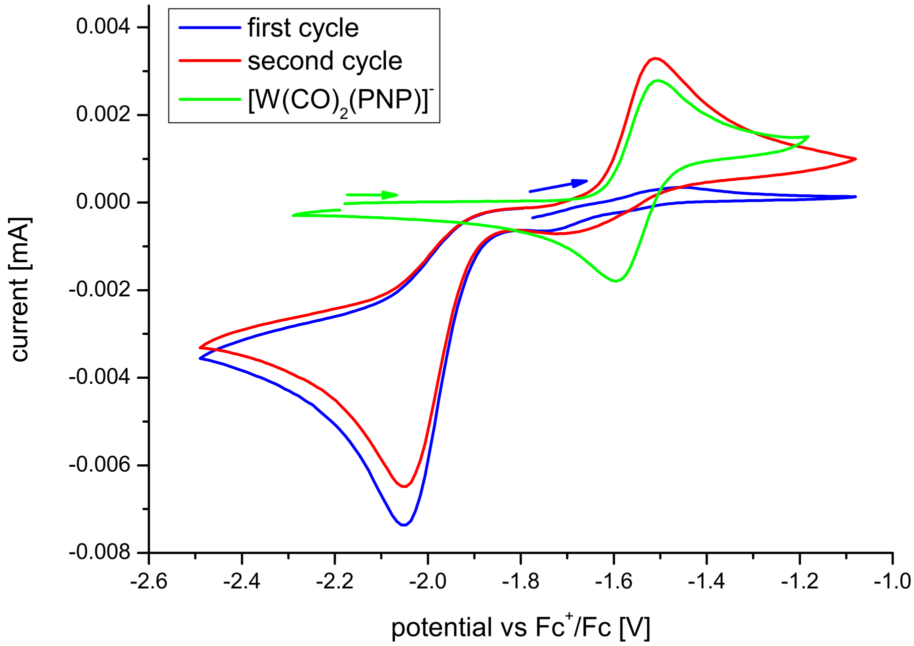

Figure 40: Cyclic voltammogram (100 mV/s, THF, Ar) of the reduction of **21**, showing the first cycle in blue and the second cycle in red. The green trace shows the oxidation of **24** measured independently.

Chemical reduction of **21** with one equiv. NaHg results in incomplete conversion of the starting material and formation of one new diamagnetic species. Usage of two equivalents of reductant gives rise to full conversion to this diamagnetic species, which was identified as anionic $[W(CO)_2(PNP)]^-$ (**24**) both under Ar or N_2. In a similar way, bright orange **24** can also be synthesized *via* reduction of **18** with 2 equiv. of NaHg or upon deprotonation of **9** with strong bases such as NaHMDS (Scheme 71).

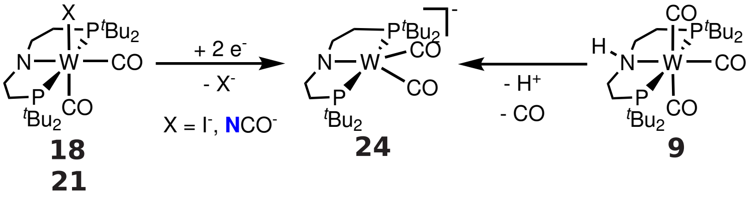

Scheme 71: Formation of **24** *via* reduction of **18** or **21** or *via* deprotonation of **9**.

In the solid state, **24** features a square pyramidally coordinated tungsten ion with one carbonyl ligand in the apical site ($\tau_5 = 0.15$, Figure 41).[193] However, in solution on the NMR timescale **24** appears C_{2v}-symmetric as indicated by only one signal for two carbonyl ligands in the $^{13}C\{^1H\}$ NMR spectrum as well as the presence of only one resonance for the ^{t}Bu-groups and two signals for the methylene protons of the ligand backbone in the ^{1}H NMR spectrum.

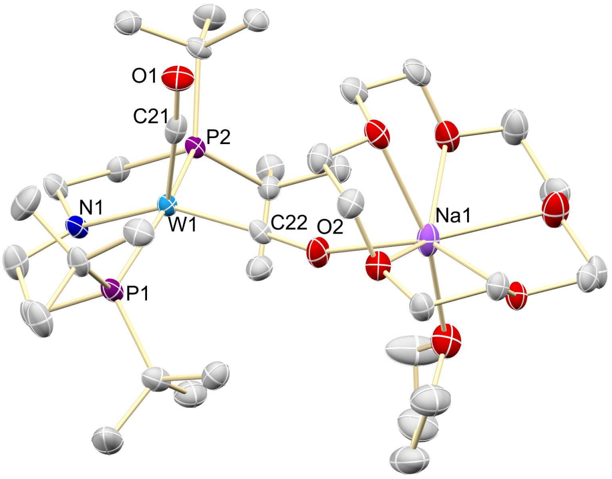

Figure 41: Molecular structure of **24** in the crystal obtained by single crystal X-ray diffraction. Selected bond lengths [Å] and angles [°]: W1-C21 1.902(9), W1-C22 1.911(8), W1-N1 2.088(6), W1-P1 2.426(2), W1-P2 2.4484(19); C21-W1-C22 87.7(3), C21-W1-N1 124.3(3), C22-W1-N1 148.0(3), P1-W1-P2 156.74(6).

Both carbonyl ligands are strongly activated as indicated by the long CO- and the short WC-distances as well as the very low CO-stretching frequencies found in the IR-spectrum of solid **24**. This higher degree of activation of the carbonyl ligands is attributed to the lower oxidation-state of the tungsten ion compared to the other discussed biscarbonyl complexes (Table 7).

Table 7: Comparison of the spectroscopic and structural parameters of the synthesized tungsten(II)-biscarbonyl-complexes ([WX(CO)$_2$(PNP)]) with the tungsten(0)-biscarbonyl-complex (**24**).

X =	**18** I^-	**10** Cl^-	**19** N_3^-	**21** NCO^-	**24** -
Oxidation-State	+II	+II	+II	+II	0
$d_{W\text{-}CO}$ [Å]	1.920(4) 2.000(4)	1.939(8) 2.013(6)	1.943(4) 2.001(4)	1.964(4) 2.028(4)	1.902(9) 1.911(8)
$d_{C\text{-}O}$ [Å]	1.169(4) 1.158(5)	1.104(9) 1.159(10)	1.169(4) 1.167(5)	1.153(5) 1.151(5)	1.206(10) 1.205(9)
$\tilde{\nu}_{CO}$ [cm^{-1}]	1907 1799	1914 1815	1907 1828	1909 1831	1677 1604

The cyclic voltammogram of **24** shows a reversible oxidation wave at -1.55 V (vs. Fc$^+$/Fc in THF), which is identical to the new formed oxidation wave monitored in the CV of **21** indicating that the reduction of **21** results in the formation of **24** also on the CV-timescale (Figure 40, *green*). Nevertheless, it remains unclear, why the observed oxidative wave in case of **21** appears irreversible even at higher scan-rates (1000 mV/s). One explanation could be a decreased stability of the oxidation product in the presence of NCO$^-$, which could be proven by CV-measurements of **24** in the presence of a suitable NCO$^-$-source.
Overall, reductive abstraction of the cyanate-ligand does not lead to N$_2$-binding and/or reformation of **4**, therefore other strategies for cyanate-abstraction and closure of the synthetic cycle have been probed.

Addition of TMS-Cl to **21** yields TMS-NCO and [WCl(CO)$_2$(PNP)] (**10**, Scheme 72), both in quantitative yield. Similar to its iodo-congener **18**, **10** can also be synthesized upon oxidation of **9** with NCS (NCS = *N*-chlorosuccinimide). The structural and spectroscopic features of **10** are very similar to the other tungsten(II)-biscarbonyl-species (**18**, **19**, **21**) described earlier (Figure 42). Notably, no reaction was observed upon addition of [PPN]Cl or benzyl chloride to **21** even at elevated temperatures.

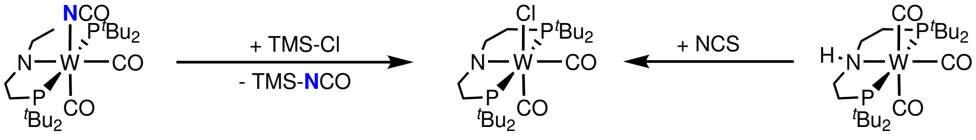

Scheme 72: Liberation of NCO from **21** *via* salt-metathesis with TMS-Cl giving **10** and TMS-NCO in quantitative yields.

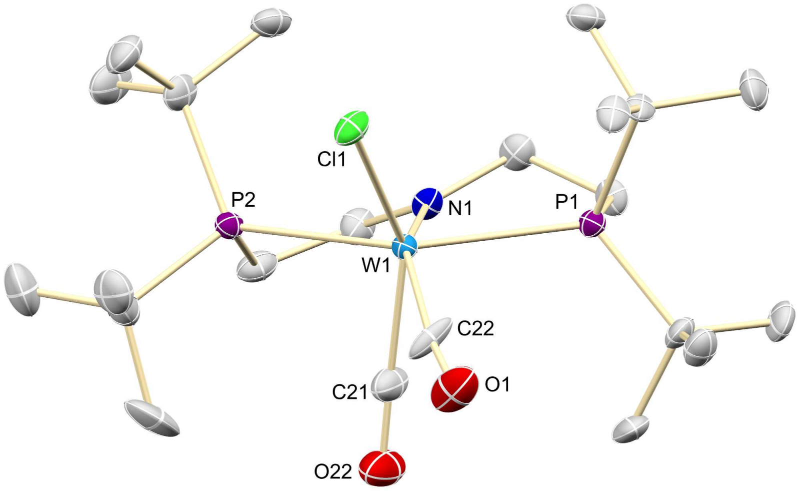

Figure 42: Molecular structure of **10** in the crystal obtained by single crystal X-ray diffraction. Selected bond lengths [Å] and angles [°]: W1-C21 1.939(8), W1-C22 2.056(8), W1-N1 2.013(6), W1-Cl1 2.4682(19), W1-P1 2.5175(19), W1-P2 2.516(2); C21-W1-C22 73.0(3), C21-W1-N1 89.2(3), C22-W1-N1 152.9(3), N1-W1-Cl1 122.32(18), P1-W1-P2 155.24(6).

The formation of TMS-NCO was confirmed upon comparision of the NMR-features with an original sample. Additionally, the $^{15}N\{^1H\}$ NMR signal of TMS-^{15}NCO, which was synthesized from ^{15}N-**21**, was detected at -346 ppm. The $^{29}Si\{^1H\}$ NMR of the formed TMS-NCO features a singlet at 4.5 ppm, which becomes a doublet ($^1J_{SiN} = 14.2$ Hz) upon ^{15}N-labeling, proving Si-N-bond formation.

The formation of **10** holds the promise of reforming either $[(N_2)\{WCl(PNP)\}_2]$ (**1**) or $[(N_2)\{WCl(CO)(PNP)\}_2]$ (**8**), upon abstraction of at least one carbonyl ligand per tungsten and binding of N_2. Release of a carbonyl-ligand using a CO-abstracting agent, such as Me_3N-O or C_5H_5N-O, was unsuccessful and showed no reaction, even under N_2-atmosphere, elevated temperatures and/or photolysis (λ>305 nm). Therefore the oxidation of **10** was performed with *N*-chlorosuccinimide (NCS) as both oxidant and chloride donor in order to reform $[WCl_3(PNP)]$ (**5**), which can finally be reduced to give N_2-bridged **1**.

While there was no reaction of **10** with two equiv. of NCS at r.t., heating of the reaction mixture lead to decomposition to unidentified, insoluable products and only traces (<5%) of **5**. However, upon photolysis of **10** with NCS at r.t. the yield in **5** could be increased to 30% (Scheme 73). In this way a synthetic cycle for the formation of NCO^- from N_2 and CO could be closed (Scheme 74). Similar to *Kawaguchi's* **XCVIII**, the only other system capable for this transformation, the requirement of both reductant (NaHg) and oxidant (NCS) prevents catalytic turnover under a chemical redox regime.[190]

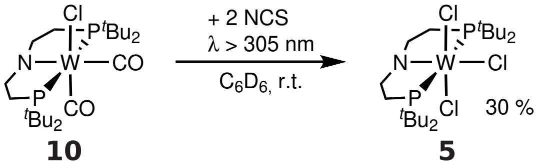

Scheme 73: Oxidation of **10** under photolytic conditions with NCS (*N*-chloro-succinimide) reforms **5**.

In summary, carbonylation of N_2-derived **16** results in formation of **21** in nearly quantitative yield. ^{13}CO-labeling revealed a intramolecular CN-bond formation *via* formal insertion of the nitride-nitrogen into the W-CO bond. The formed cyanate-ligand can be abstracted either *via* reduction or quantitatively *via* salt-metathesis using TMS-Cl (Scheme 74).

Abstraction of the carbonyl ligands requires the addition of a strong oxidant and UV-light and gives only moderate yields, which also prevents catalytic reactivity. Nevertheless, this system represents the second example for the transformation of N_2 and CO into cyanate using a terminal nitrido-complex.

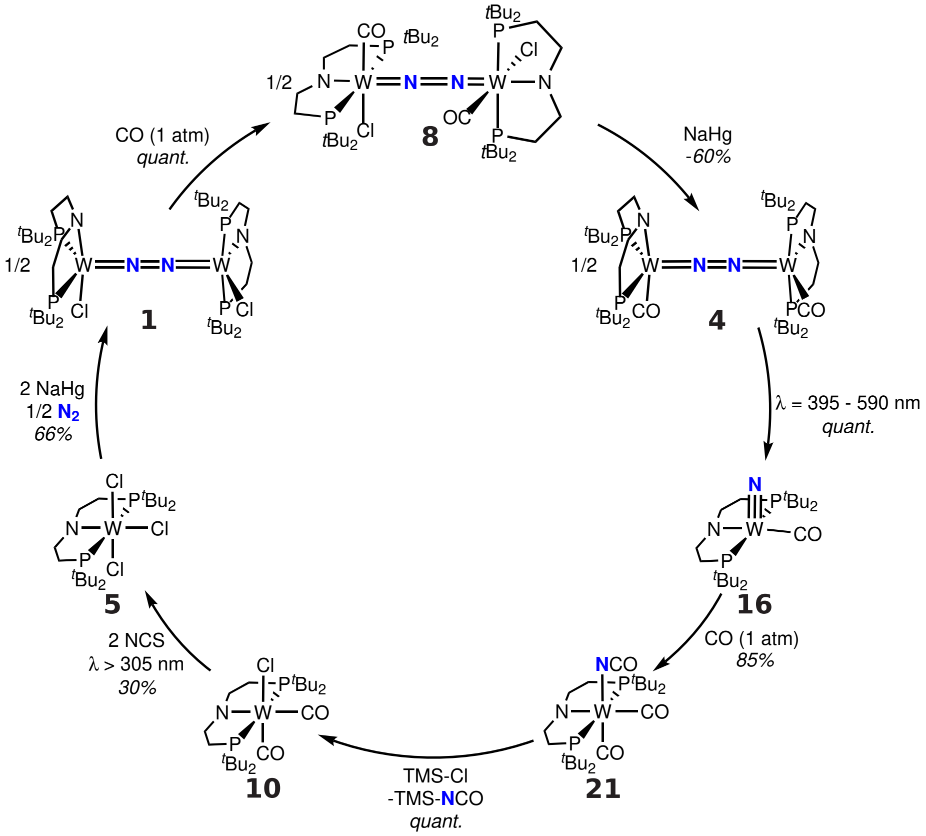

Scheme 74: Synthetic cycle for the formation of TMS-NCO from N_2 and CO using a W(PNP)-platform.

2.5 Summary and Outlook[m]

In summary, a series of four isostructural N_2-bridged ditungsten compounds was successfully synthesized and characterized. The derived structural and spectroscopic parameters fully corroborate the proposed bonding-scheme for such idealized D_{4h}-symmetric molecules (Scheme 75). Accordingly, oxidation of $\{\pi^8\delta^4\}$-configurated $[(N_2)\{WCl(PNP)\}_2]$ (**1**) is metal centered without any significant impact on the degree of N_2-activation. A significantly smaller degree of N_2-activation was observed for **4**, which can be rationalized by two additional electrons within the {WNNM}-core populating the π^*-π-π^*-orbitals.

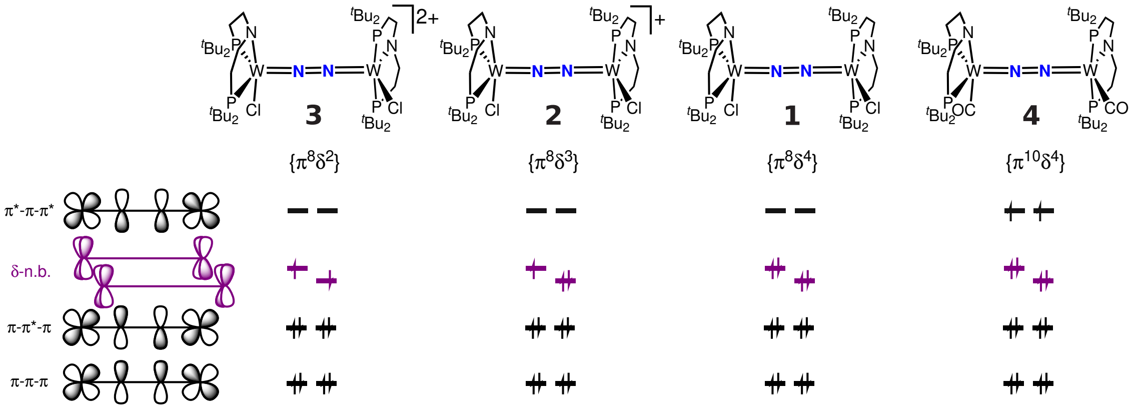

Scheme 75: Comparison of the electronic structures of **3**, **2**, **1** and **4**.

The comparison of **1** with its Mo-analogue **XI** reveals a slightly weaker activated bridging N_2 ligand for the 5d-metal-complex, which was rationalized by weaker backbonding. Nevertheless, both compounds are stable with respect to N_2-cleavage, underlining the requirement of ten π-electrons within the {MNNM}-core. Compared to **XI**, the oxidation potentials of **1** are cathodically shifted, marking it as the better reductant, which effects the reactivity upon protonation.[70]

---

[m] Parts of this work have been published in:
-"Selectivity of tungsten mediated dinitrogen splitting *vs.* proton reduction", B. Schluschaß, J. Abbenseth, S. Demeshko, M. Finger, A. Franke, C. Herwig, C. Würtele, I. Ivanovic-Burmazovic, C. Limberg, J. Telser, S. Schneider, *Chemical Science*, **2019**, *10*, 10275-10282.
-N.A. Maciulis "Exploring redox properties of bis(tetrazinyl)pyridine (btzp) complexes of group VI metals, tetrazine and phosphine assisted reduction of H_2O, and dinitrogen cleavage and functionalization" *Ph.D. Thesis*, Indiana University Bloomington, **2019**.

While protonation of **XI** leads, independent of acid and temperature, to N_2-cleavage,[70] protonation of **1** can also result in proton-reduction and oxidation of **1** (Scheme 76), which was rationalized by an equilibrium between ligand-protonated **12** and hydride **14**. Similar to **XI**, protonation of both PNP-pincer units in **1** results in N_2-cleavage and formation of nitride **11**. In contrast, protonation of the hydride-isomer **14** results in H_2-evolution and oxidation of the tungsten-ions. The equilibrium between **12** and **14** can be modulated by the choice of acid and temperature, with strong, hydrogen-bonding acids and low temperatures favoring ligand-protonation and therefore N_2-cleavage.

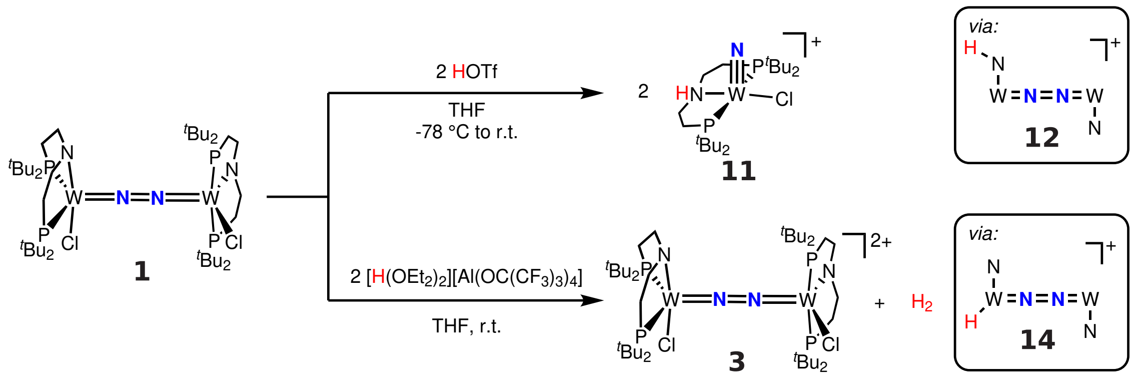

Scheme 76: Protonation of **1** leads either to N_2-cleavage and formation of **11** or to proton-reduction and formation of **3**.

In contrast to its isoelectronic ReCl-congener **XII**, **4** is stable at r.t., which was attributed to the π-accepting properties of the carbonyl-ligands, which stabilize the π^*-π-π^*-orbitals in energy and thereby increase the kinetic barrier for N_2-cleavage (Scheme 77). Furthermore, due to mixing of the CO-ligand with the {WNNW}-π-manifold electron transfer from the π-system to the bridging N_2-ligand upon cleavage becomes less favorable, which leads to a slightly endergonic splitting reaction and represents the first example for an equilibrium between N_2-cleavage and reverse nitride-coupling.

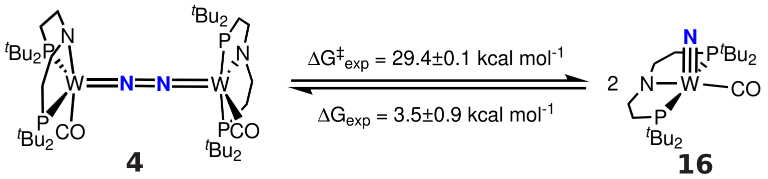

Scheme 77: The experimentally derived kinetic and thermodynamic parameters for N_2-cleavage in **4** yielding **16**.

Quantitative N_2-splitting can be acchieved *via* photolysis (λ = 395-590 nm). The productive transitions feature $\delta/\delta^* \rightarrow \pi^*\text{-}\pi^*\text{-}\pi^*$-character, similar to **XIII**.[71] Population of this all-antibonding orbital within the {W-N-N-W}-core might increase the flexibility and induce bending to a *zig-zag*-conformation, which finally leads to N_2-cleavage. Examination of the photochemical and photophysical properties of **4** *via* UVvis/UVvis and UVvis/IR transient spectroscopies revealed that the lifetime of the excited state is shorter than the temporal resolution of the experiment ($\tau_{exc} \approx 70\pm20$ fs). Directly after relaxation to the electronic ground state, the energy is non-statistically distributed, which might facilitate N_2-cleavage. However, vibronic coupling of the electronically excited state with bending-modes of the {WNNW}-core, as observed by *Cummins* and *Blank* for **I** as an underdamped oscillation in the pump-probe decay,[136] could not be detected. Once the pump-energy is statistically distributed ($\tau_1 = 1.5\pm0.2$ ps) the internal temperature of **4** is too low to show thermal reactivity. Due to the very fast timescales and the poor quantum yields a final assignment, whether N_2-cleavage follows a diabatic pathway or proceeds from an vibrationally hot-ground-state with a non-statistical energy distribution, cannot be made yet and relies on further examinations.

The obtained splitting product **16** was successfully functionalized with CO to give cyanate-complex **21** in nearly quantitative yield. ^{13}CO-labeling studies revealed an intramolecular pathway, in which the CN-bond is formed *via* insertion of the nitride-nitrogen into the tungsten-carbonyl-bond. Even though such a mechanism has already been suggested,[188] these current studies reveal the first direct experimental evidence for such a pathway.
Full *N*-atom-transfer can be achieved upon either reduction of **21** to give **24** or upon salt-metathesis using TMS-Cl, which forms TMS-NCO and **10** in quantitative yield. The latter can be oxidized with NCS, which also serves as a chloride-source, under photolytic conditions to give **5** and closes the synthetic cycle (Scheme 78). Besides *Kawaguchi's* {V(ONO)}-platform (**XCVIII**, Scheme 50), the presented {W(PNP)}-system represents the second example for N_2-derived nitride-CO-coupling and full *N*-atom-transfer.[190]

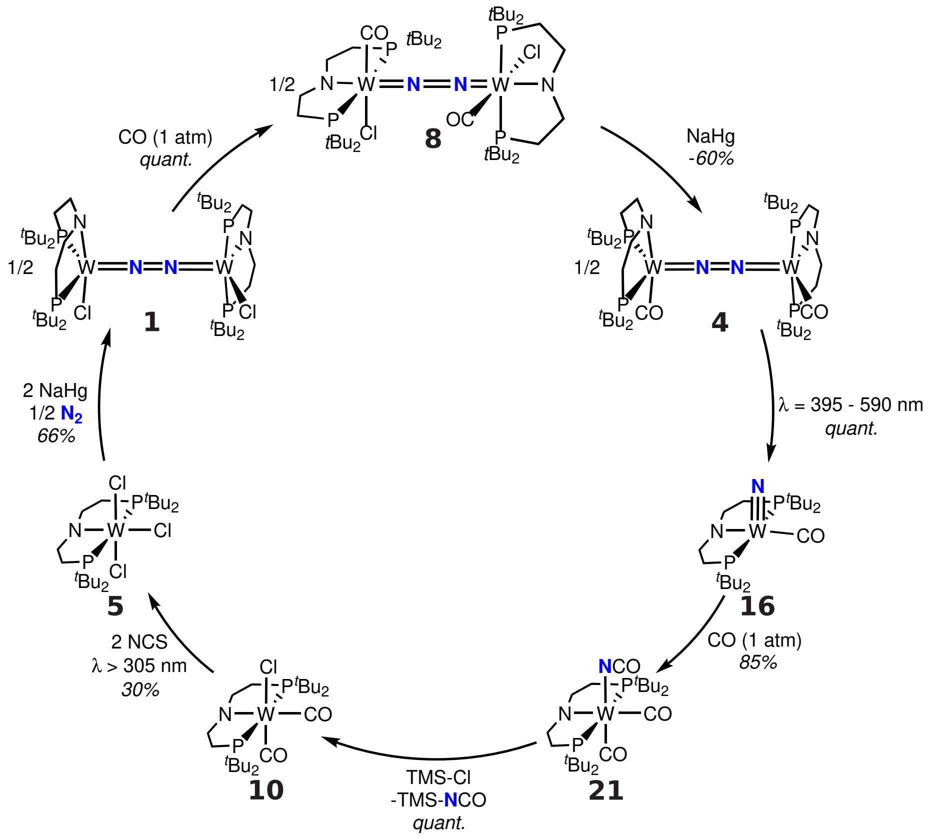
1/2
8
1
4
CO (1 atm)
quant.
NaHg
-60%
λ = 395 - 590 nm
quant.
16
CO (1 atm)
85%
21
TMS-Cl
-TMS-NCO
quant.
10
2 NCS
λ > 305 nm
30%
5
2 NaHg
1/2 N2
66%

Scheme 78: Synthetic cycle for the formation of TMS-NCO from N_2 and CO using a W(PNP)-platform.

The established {W(PNP)}-platform can be used for further investigations. So far, the reactivity of dinuclear **1**, with respect to N_2-cleavage, has only been examined with Brønsted acids. An intriguing question would be the use of Lewis-acids in order to cancel out the interaction of the pincer-amide-p-orbitals with the {WNNW}-π-manifold, which should lead to N_2-cleavage and (depending on the Lewis-acid) direct formation of the respective tungten(V)-nitride, [W(N)Cl(PNP)] (**25**), without the drawback of competing proton-reduction.

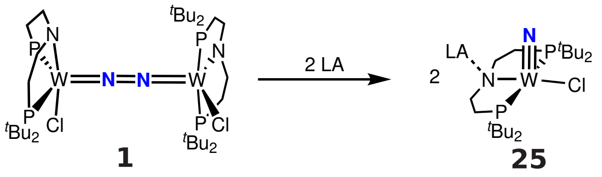

Scheme 79: Proposed Lewis-acid induced N_2-cleavage of **1**.

Although a series of four isostructural N_2-bridged ditungsten compounds was successfully synthesized and characterized, a compound with a $\{\pi^9\delta^4\}$-configuration is not included. Such a compound would fill the gap between $\{\pi^8\delta^4\}$-configurated **1** and $\{\pi^{10}\delta^4\}$-configurated **4** and would, due to its $S = 1/2$ magnetic ground state, allow deeper investigations of the electronic structure. Preliminary electrochemical studies of **4** indicated that such a species might be accessible by oxidation of **4**.
In that respect, the replacement of the carbonyl-ligands in **4** by other neutral ligands might give insights into the influence of the auxiliary ligands on the degree of N_2-activation and stability with respect to N_2-cleavage. Furthermore, the photolytic active transition for N_2-cleavage in **4** was identified as a {M-CO}→ N_2-transition, which will shift upon replacement of the CO-ligand. This shift could be correlated to the ligand-strength and provide some guidelines for the design of future systems capable for photolytic N_2-cleavage.

Regarding N_2-functionalization, the access *via* photolytic N_2-cleavage, using visibile light, makes **16** an attractive platform. Besides the already mentioned reagents (CO and CN-R), there are still potential candidates for nitride-functionalization, including benzoyl- and alkyl-halides or O-atom transfer agents, such as mCBPA (mCBPA = 3-chloroperbenzoic acid) or *N*-oxides.
The electrophilicity of the nitride-moiety could be increased upon oxidation of **16**. Preliminary attempts were always accompanied by the formation of substantial amounts of ligand-protonated $[W(N)(CO)(^{H}PNP)]^+$ (**20**), whose presence complicated the isolation and characterization of other potential products, but also revealed an increased reactivity of the potentially formed W(V)-product, which might be useful for further functionalization attempts.

3 Experimental

3.1 General Working Techniques

All experiments were carried out under inert atmosphere (Ar or N_2, both 5.0, Linde gas) using standard Schlenk and glove-box techniques, unless otherwise noted. Purification of CO gas (Air Liquide, 99.997%) was obtained by passing the gas through a steel coil cooled to -78 °C. ^{13}CO (Eurisotop GmbH, 99.30% ^{13}C) and $^{15}N_2$ (Sigma Aldrich, 98% ^{15}N) were used as purchased without further purification.
All glassware was cleaned in KOH/*iso*-propanol baths, neutralized in HCl baths, washed with deionized water and dried at 120 °C. Prior to use, all vessels were evacuated at a Schlenk line with periodically applied heating. Small scale reactions ($\leq$ 10 mg) were typically performed in J-Young NMR tubes.

Unless otherwise noted all solvents were purchased in HPLC quality (Merck) and used as obtained from an MBraun Solvent Purification System. THF and toluene were further purified by stirring over Na/K-alloy for several days, PhCl was dried over CaH_2. Deuterated solvents were obtained from Eurisotop GmbH and dried by stirring over Na/K-alloy (THF—d_8, C_6D_6, Tol—d_8) or CaH_2 (CD_2Cl_2, CD_3CN). NEt_3 was dried over KOH and CaH_2, whereas $W(CO)_6$, *N*-chlorosuccinimide and Fc were sublimed prior usage. TMS-Cl and TMS-NCO were distilled and degased. Celite and Silica gel 60 silanized were heated over 150 °C under vacuum for several days prior usage. All other chemicals were used as purchased without further purification.

^{H}PNP,[213] $[H(OEt_2)_2][BAr^F_{24}]$,[214] $[H(OEt_2)_2][Al(OC(CF_3)_3)_4]$,[215] $Ag[BPh_4]$,[216] FcOTf,[217] [LutH]OTf,[217] $[PPN]N_3$[218,219] and [PPN][NCO][218,219] were synthesized according to literature procedures.

3.2 Analytical Methods

3.2.1 Crystallographic details

Suitable single crystals for X-ray structure determination were selected from the mother liquor under an inert gas atmosphere and transferred in protective perfluoro polyether oil on a microscope slide. The selected and mounted crystals were transferred to the cold gas stream on the diffractometer. The diffraction data were obtained at 100 K on a Bruker D8 three-circle diffractometer, equipped with a Photon 100 CMOS detector and an Incoatec microfocus source with Quazar mirror optics (Mo-Kα radiation, $\lambda = 0.71073$ Å). The data obtained were integrated with SAINT and a semi-empirical absorption correction from equivalents with SADABS was applied. The structures were solved and refined using the Bruker SHELX 2014 software package.[220–223] All non-hydrogen atoms were refined with anisotropic displacement parameters. All C-H hydrogen atoms were refined isotropically on calculated positions by using a riding model with their U_{iso} values constrained to 1.5 U_{eq} of their pivot atoms for terminal sp^3 carbon atoms and 1.2 times for all other atoms.

3.2.2 Cyclic voltammetry

All electrochemical data were recorded on a Metrohm PGSTAT101 using the Nova 2.0 software. The cyclic voltammetry (CV) data were recorded either in a UVvis cell or a three neck cell equipped with a glassy carbon (Ø = 1.6 mm) working electrode (WE), a Pt-wire counter electrode (CE) and a Ag wire pseudo-reference electrode (RE). Referencing was performed against the Fc / Fc^+ couple. All experiments were performed under Ar in 0.1 m $[^nBu_4N][PF_6]$ in THF.
During the second half of this thesis, CV data were compensated for internal resistance (iR). In these cases, the scan rate dependence of the peak currents i_p was analyzed according to the *Randles-Sevcik* equation:

$$i_p = 0.446nFAC^0\left(\frac{nFvD_0}{RT}\right)^{1/2} \tag{3.6}$$

where n is the number of transferred electrons, F is the *Faraday's* constant, A is the electrode surface in cm^2, C^0 is the bulk concentration of the analyte in $mol{\cdot}cm^3$, v is the scan rate in $V{\cdot}s^{-1}$ and D_0 is the diffusion coefficient of the oxidized species in $cm^2{\cdot}s^{-1}$.[224] This equation is valid for freely diffusing, non absorbed analyte in solution which undergoes fast, electrochemically reversible electron transfer. Thus deviations from linearity of a plot of i_p vs. $v^{1/2}$ can indicate quasi-reversible electron transfer (accompanied by a scan rate dependent peak-to-peak separation) or absorption of the analyte on the electrode surface (which should have a constant peak-to-peak separation).

3.2.3 Electron Paramagnetic Resonance

Experimental X-band EPR spectra were recorded on a Bruker ELEXSYS-II E500 CW-EPR. Simulations were carried out using the program QPOW, as modified by *J. Telser*.[225]

3.2.4 Elemental Analysis

Elemental analysis were obtained from the Analytical Laboratories at the Georg-August-University Göttingen using an Elementar Vario EL 3 analyzer.

3.2.5 Head Space Analysis

The H_2 was detected by a Shimadzu GC-2014 gas chromatograph equipped with a TCD detector and a ShinCarbon ST 80/100 Silco column.

3.2.6 Irradition

All photolysis experiments were performed using either a Kessil PR160-427 LED (427 nm) or a 150 W Hg(Xe) arc lamp with lamp housing and arc lamp power supply from LOT-Quantum Design GmbH. For the latter, IR radiation was eliminated by use of a water filter and photolyzed samples were kept at r.t. by a water bath.

3.2.7 Magnetic measurements

Magnetic moments were determined by Evans' method as modified by Sur and corrected for diamagnetic contributions.[226]
Magnetic susceptibility measurements were performed with a Quantum Design MPMS-XL-5 SQUID magnetometer in the temperature range from 295 to 2 K at 0.5 T applied field. The powdered sample was contained in a Teflon bucket and fixed in a non-magnetic sample holder. Each raw data point for the measured magnetic moment of the sample was corrected for the diamagnetic contribution by subtraction of the experimentally determined magnetic measurement of the Teflon bucket. The molar susceptibility data were corrected for the diamagnetic contribution using the Pascal constants and the increment method according to Haberditzel.[227,228] Experimental data were modelled with the julX program.[229]

3.2.8 Mass spectrometry

HR-ESI-MS (Bruker maXis QTOF) and LIFDI-MS (JEOL AccuTOF JMS-T100GCV) spectra were measured by the Zentrale Massenabteilung, Fakultät für Chemie, Georg-August-Universität Göttingen.

3.2.9 Nuclear magnetic resonance

NMR spectra were recorded on Bruker Avance III 300 or Avance III 400 spectrometers or an Avance 500 spectrometer with a Prodigy broadband cryoprobe, respectively, and calibrated to the residual solvent signals (C_6D_6: $\delta_H = 7.16$ ppm, $\delta_C = 128.4$ ppm; THF—d_8: $\delta_H = 3.58$ ppm, $\delta_C = 67.6$ ppm).[230] ^{31}P, ^{29}Si and ^{15}N NMR chemical shifts are reported relative to external phosphoric acid, tetramethyl silan and nitromethane ($\delta = 0.0$ ppm), respectively. Signal multiplicities are abbreviated as: s (singlet), d (doublet), triplet (t), m (multiplet), br (broad).

3.2.10 Quantum yield determination

The quantum yield for the photochemical splitting reaction of **4** into **16** was determined for photolysis with a 427 nm LED lamp. The lamps photon flux was determined prior to the experiment using a Thorlabs S120VC, 200-1100 nm photodiode, which was placed in 20 cm distance to the lamp and photolyzed with 25% power output to:

$$I = 6.5977 \cdot 10^{-7} \pm 1.3 \cdot 10^{-12}\ \text{mol cm}^{-2}\text{min}^{-1} \tag{3.7}$$

For the quantum yield determination, a solution of complex **4** in THF (2 mL, $5.1{\cdot}10^{-5}$ mol·L^{-1}) was irradiated with the same setup (same distance and output power from the LED lamp) for a total of 30 min. After every 2 min, the irradiation was stopped and the concentration of **4** was determined by monitoring of the absorbance at $\lambda = 512$ nm. The quantum yield was determined by:

$$\phi = \frac{\Delta n_{t_x - t_{(x-1)}}}{n_{\text{Photons, 2 min}} \cdot (1 - 10^{-A_{427\ \text{nm}}})} \tag{3.8}$$

Where $\Delta n_{t_x - t_{(x-1)}}$ is the amount of **4** decomposed between two measurements, i.e. by irradiating for 2 min, $n_{\text{Photons, 2 min}}$ is the amount of photons reaching the sample during 2 minutes ($2.6391{\cdot}10^{-6}$ mol in the above described set-up, calculated by $n = I \cdot t \cdot a$) and $A_{427\ \text{nm}}$ is the absorbance of the solution at 427 nm at the beginning of each photolysis step. This results in a quantum yield of 0.37±0.03%.

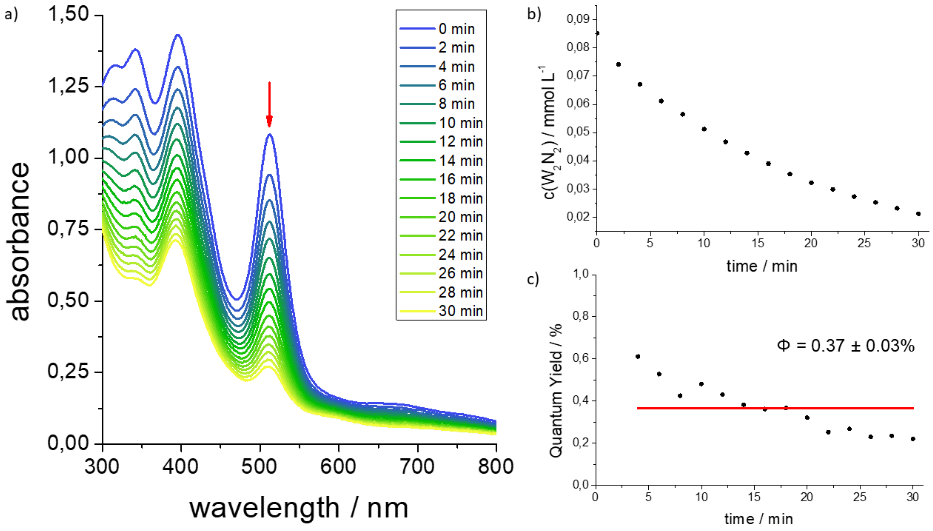

Figure 43: Quantum yield determination of the photosplitting of **4** by 427 nm LED lamp. a) Decay of **4** during photolysis. b) Concentration profile of **4** during the reaction. c) Quantum yields between each irradiation interval.

3.2.11 Transient UVvis spectra

The transient UVvis-pump-probe setup described in ref[231] was updated with a new laser system (Solstice Ace, spectra physics) It includes a regenerative amplifier seeded by a diode pumped Ti:Sapphire seed laser (Mai Tai SP, spectra physics) and pumped by a diode pumped Nd:YLF-laser (Ascend 40, spectra physics). The significantly shorter 35 fs pulses at 800 nm central wavelength produce a mean output power of ~5 W at a repetition rate of 1 kHz.

A small percentage (about 3 μJ) was passing a translational stage (M-415.DG, Physik Instrumente) of 16.5 cm delay path for up to ~1.1 ns pump-probe-delay after transmitting a high reflective mirror ($R \approx 99.9\%$) and focused on a 4 mm CaF_2 crystal generating a white light continuum as probe beam. A semi-transparent mirror split the beam into reference and probe which were focused onto their individual 256-element linear diode array mounted on a spectrograph (spectral window: 350-730 nm). The latter was passing a far UV quartz cuvette (Starna, optical path: 2 mm, transmission: 170-2700 nm) containing the sample (0.12-0.17 mM in THF) stirred by a magnet in order to refresh it between pulses.

The pump beam containing the residual output can now be prepared for wavelengths 240 nm − 2.6 μm using an automated optical parametric amplifier (TOPAS Prime+, light conversion, spectra physics) and subsequent frequency mixer (NirUVis, light conversion, spectra physics). The resulting beam was attenuated by an iris (0.3-1.0 μJ), passed a perforated rotating wheel cutting every second pulse for subtraction of spectra without pump excitation and rotated in polarization to 54.7° (magic angle) relative to probe for elimination of molecular rotational effects and focused into the sample and spatially overlapping with the probe beam. Both sample in solution and pure solvent transient spectra were measured at pre-programmed pump-probe-delays. Baseline, wavelength dependent temporal shifts due to group velocity dispersion of the probe beam and solvent transient spectra were corrected.

3.2.12 Transient IR spectra

A libra laser system (coherent) is the basis for the transient IR-pump-probe-setup. A Ti:Sapphire oscillator is pumped by a diode-pumped Nd:YAG laser (Evolution 30, coherent) and seeded laser (Vitesse, coherent) consisting of a diode-pumped, frequency doubled $Nd:YVO_4$ laser (Verdi, coherent) pumping a Ti:Sapphire laser head (VPUF e. g. Verdi pumped ultrafast laser head, coherent). A regenerative amplifier with compressor/stretcher unit is included. The output beam pulsing an 800 nm central wavelength at 1 kHz repetition rate possessed a temporal puls width of about 150 fs and a mean energy of 0.7 mJ. A semi-transparent mirror split the power 60:40.

About 60% served as input for an optical parametric amplifier with subsequent difference frequency generation of idler and signal as described in ref[232] producing an IR-probe-spectrum of 50-150 cm^{-1} spectral width depending on the wavelength region. Another semi-transparent mirror was used separating equally into reference and probe. After the probe beam passed a translational stage (M-ILS250CCL, New-

port) both were focused 5 mm apart into the sample (2 mM, solvent: THF) in a stainless steel sample cell with an optical path of 0.8 mm enclosed by two CaF_2 windows (1 mm each, optically polished, Korth Kristalle) and stirred by a rotating magnet bar. A combination of polychromator (Chromex 250is, Bruker Optics) and liquid nitrogen cooled 2x32-element MCT-detector (IR-6416 system MCT-32/2-10, infrared systems development corporation) measured the spectra.
The pump (wavelength: 400 nm) was produced using the spare 40% laser output and a BBO (beta-barium borate) crystal. The beam was passing a perforated rotating plate, its polarization was rotated to 54.7°, it was attenuated to 0.5 μJ and focused into the cell superimposing with the probe beam.
The spectra were measured in regions without strong solvent absorption and corrected in baseline, slope and offset and merged together.

3.2.13 UVvis spectroscopy

UVvis spectra were recorded on an Agilent Cary 60 equipped with an Unisoku Cryostat (CoolSpek) and magnetic stirrer using quartz cuvettes with an attached tube and a screw cap with a septum or a J-Young-cap. All UVvis samples were prepared in a glovebox and transferred out of the glovebox prior to the measurement.

3.2.14 Vibrational spectroscopy

IR spectra were recorded using a Bruker ALPHA FT-IR spectrometer with Platinum ATR module.
All Resonance Raman spectra except for **3** were recorded using a Horiba Scientific LabRAM HR 800 spectrometer with open-electrode CCD detector in combination with a free space optical microscope and a He:Ne-laser (632.8 nm). The Resonance Raman spectra for **3** were recorded using a Triple Raman Spectrometer TR 557 from S& I (Spectroscopy & Imaging GmbH).

3.3 Synthesis[n]

3.3.1 [WCl_3(PNP)] (5)

Complexation of WCl_4

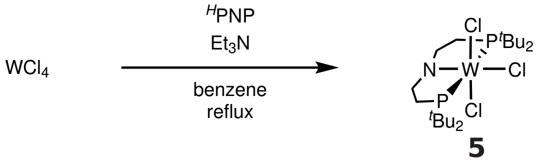

(3.9)

WCl_4 (509 mg, 1.54 mmol, 1.1 equiv.) was added to a mixture of Et_3N (0.4 mL, 288 mg, 2.85 mmol, 2.1 equiv.) and $HN(CH_2CH_2P^tBu_2)_2$ (500 mg, 1.38 mmol, 1.0 equiv.) in benzene (50 mL) and stirred for minimum 5 d at 90 °C. After removal of the solvent *in vacuo*, the crude product was extracted with benzene (4x 15 mL) and dried *in vacuo*.The residue was dissolved in THF (4 mL), layered with pentane (20 mL) and stored at -40 °C to give **5** as dark yellow crystals (540 mg, 60%).

*Oxidation of **10***

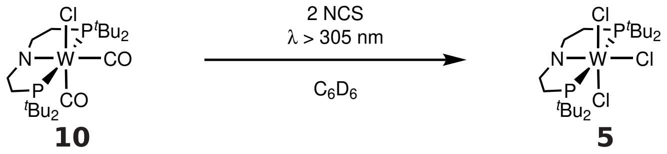

(3.10)

In a J-Young NMR-tube **10** (6.4 mg, 10.1 μmol, 1.0 equiv.) and NCS (3.0 mg, 22.1 μmol, 2.2 equiv.) were dissolved in C_6D_6. The mixture was irradiated with λ>305 nm in a waterbath for three hours showing a color-change from deep purple to yellow-brownish. **5** was obtained in 30% spectroscopic yield.

^{1}H NMR (C_6D_6, 300 MHz, [ppm]): δ = 9.13 (s_{br}, CH_2), 0.82 (s_{br}, CMe_3), -139.5 (s_{br}, CH_2).
Elem. Anal. found (calc) for $C_{20}H_{44}Cl_3NP_2W$: C 36.85 (36.92); H 6.93 (6.82); N 2.16 (2.15).
$\mu_{\mathbf{eff}} = 2.8 \pm 0.1\mu_B$.

---

[n] Parts of this work have been published in:
-"Selectivity of tungsten mediated dinitrogen splitting *vs.* proton reduction", B. Schluschaß, J. Abbenseth, S. Demeshko, M. Finger, A. Franke, C. Herwig, C. Würtele, I. Ivanovic-Burmazovic, C. Limberg, J. Telser, S. Schneider, *Chemical Science*, **2019**, *10*, 10275-10282.
-N.A. Maciulis "Exploring redox properties of bis(tetrazinyl)pyridine (btzp) complexes of group VI metals, tetrazine and phosphine assisted reduction of H_2O, and dinitrogen cleavage and functionalization" *Ph.D. Thesis*, Indiana University Bloomington, **2019**.
-P.-M. Padonou "Reaktivität dimerer N_2-verbrückter Wolfram-PNP-Pinzetten Komplexe" *Bachelor Thesis*, Georg-August-Universität Göttingen, **2018**.
-J. Schneider "Synthese und Funktionalisierung von Wolfram-PNP-Nitrid Komplexen" *Bachelor Thesis*, Georg-August Universität Göttingen, **2019**.

3.3.2 [(N_2){WCl(PNP)}$_2$] (1)

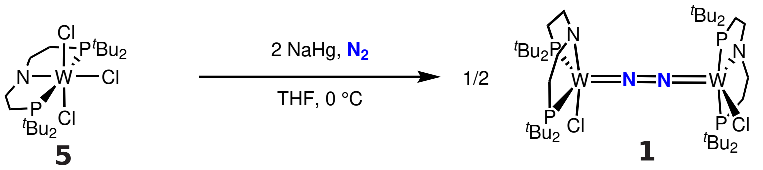

(3.11)

Under an N_2 atmosphere **5** (250 mg, 0.384 mmol, 1.0 equiv.) and NaHg (11.5 g, 0.845 mmol, 2.2 equiv.) were stirred in THF (10 mL) for 3 h at 0 °C to give a color change from yellow to dark green.

After extraction with THF (3x 8 mL) the solvent was removed *in vacuo*. The residue was then washed with pentane (3x 8 mL), extracted with benzene (5x 8 mL) and dried *in vacuo*. After column chromatography over Silica gel 60 silanized using benzene as eluent and lyophilisation out of benzene, **1** was obtained as a green powder (150 mg, 66%).

For $^{15}N_2$ labeling the synthesis was done using an $^{15}N_2$ atmosphere.

^{1}**H NMR** (THF—d_8, 500 MHz, [ppm]): δ = 3.66 (m, 4 H, NCH_2), 3.54 (m, 4 H, NCH_2), 2.39 (m, 2 H, PCH_2), 2.29 (m, 2 H, PCH_2), 1.74 (m, 2 H, PCH_2), 1.55 (d, $^3J_{HP}$=12.8 Hz, 18 H, 2x CMe_3), 1.35 (m, 2 H, PCH_2), 1.16 (d, $^3J_{HP}$=13.9 Hz, 18 H, 2x CMe_3), 1.13 (d, $^3J_{HP}$=12.8 Hz, 36 H, 4x CMe_3).

^{13}**C{^{1}H} NMR** (THF—d_8, 126 MHz, [ppm]): δ = 30.7 (d, $^2J_{CP}$ = 4.3 Hz, 2x CMe_3), 30.7 (d, $^2J_{CP}$ = 5.7 Hz, 2x CMe_3), 30.8 (d, $^2J_{CP}$ = 3.9 Hz, 2x CMe_3), 31.8 (d, $^1J_{CP}$ = 7.62 Hz, 2x PCH$_2$), 31.6 (d, $^1J_{CP}$ = 7.35 Hz, 2x PCH$_2$), 32.0 (d, $^2J_{CP}$ = 4.9 Hz, 2x CMe_3), 38.5-38.9 (m, PCMe$_3$), 78.9 (s, 2x NCH$_2$), 79.4 (s, 2x NCH$_2$).

^{15}**N{^{1}H} NMR** (THF—d_8, 50.7 MHz, [ppm]): δ = 31.1 (s).

^{31}**P{^{1}H} NMR** (THF—d_8, 162 MHz, [ppm]): δ = 92.9 (d, $^2J_{PP}$ = 147.4 Hz), 87.8 (d, $^2J_{PP}$ = 147.4 Hz).

Elem. Anal. found (calc) for $C_{40}H_{88}Cl_2N_4P_4W_2$: C 40.39 (40.45); H 7.27 (7.47); N 2.69 (4.72).

[The lower N content found is attributed to decomposition of highly sensitive **1** during transport/manipulations.]

rRaman (λ_{ex} = 457 nm, frozen THF—d_8, cm^{-1}): $\tilde{\nu}$ = 1392 ($^{14}N_2$); 1347 ($^{15}N_2$).

3.3.3 [(N_2){WCl(PNP)}$_2$]$^+$ (2)

via oxidation

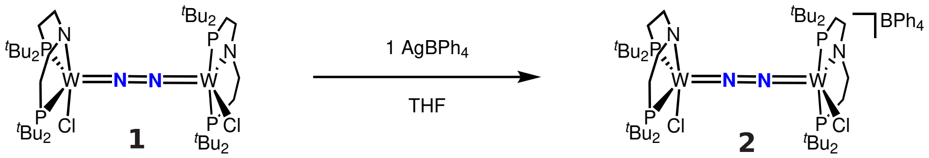

(3.12)

Ag[BPh4] (14.4 mg, 33.7 μmol, 1.0 equiv.) was added to a solution of **1** (40.0 mg, 33.7 μmol, 1.0 equiv.) in THF (5 mL) leading to a direct color change from green to dark brown. After stirring for 1 h the mixture was filtrated over celite, dried *in vacuo*, washed with pentane (3x 4 mL) and extracted with THF (2x 4 mL). After removal of the solvent *in vacuo* **2**-[BPh_4] was obtained as a dark brown solid (43 mg, 85%).

via protonation

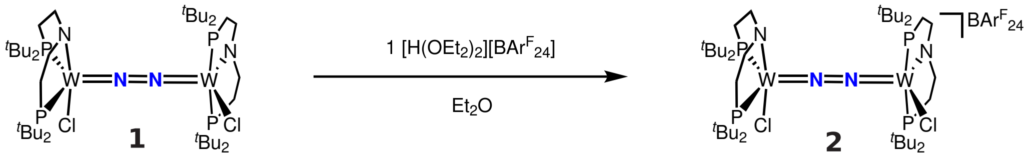

(3.13)

[$H(OEt_2)_2$][BAr^F_{24}] (31 mg, 30.6 μmol, 1.0 equiv.) was added to a solution of **1** (40.0 mg, 33.7 μmol, 1.1 equiv.) in Et_2O (8 mL) leading to a direct color change from green to dark brown. After stirring for 1 h the mixture was filtrated, dried *in vacuo* and washed with pentane (3x 10 mL). The crude product was then extracted over celite with Et_2O and dried *in vacuo* to give **2** as a brown solid (47 mg, 75%).

^{1}H NMR (THF—d_8, 300 MHz, [ppm]): δ = 4.37 (s_{br}, CH*H*), 3.13 (s_{br}, C*Me*$_3$), 2.99 (s_{br}, C*Me*$_3$), 2.51 (s_{br}, C*Me*$_3$), 2.38 (s_{br}, C*Me*$_3$), -5.60 (s_{br}, CH*H*), -14.1 (s_{br}, CH*H*), -22.1 (s_{br}, CH*H*), -25.1 (s_{br}, CH*H*), -27.8 (s_{br}, CH*H*).
Elem. Anal. found (calc) for $C_{64}H_{108}BCl_2N_4P_4W_2$ (**2**-[BPh_4]): C 51.52 (51.01); H 7.17 (7.22); N 3.29 (3.72).
rRaman (λ_{ex} = 457 nm, frozen THF—d_8, cm^{-1}): $\tilde{\nu}$ = 1414 ($^{14}N_2$); 1360 ($^{15}N_2$).
HR-ESI-MS found (calc) for [$C_{40}H_{88}Cl_2N_4P_4W_2$]$^+$: 1186.4347 (1186.4339), 1188.4368 (1188.4380).

3.3.4 [(N_2){WCl(PNP)}$_2$]$^{2+}$ (3)

via oxidation

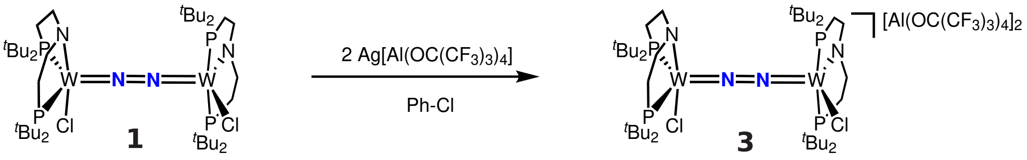

(3.14)

To a solution of **1** (20.0 mg, 16.8 μmol, 1.0 equiv.) in Ph-Cl (8 mL) Ag(Al(OC(CF_3)$_3$)$_4$) (35.3 mg, 32.8 μmol, 2.0 equiv.) was added. The solution was stirred under exclusion of light for 12 h. Afterwards the precipitate was filtered off, washed with benzene (6 ml) and extracted with DCM (16 mL). The solution was concentrated *in vacuo*, layered with pentane and stored at -40 °C for 3 d. The resulting brown precipitate was decanted, washed with pentane (2x 2 mL), extracted with THF and dried *in vacuo* to give **3** as a brown solid (39.3 mg, 75%).

via protonation

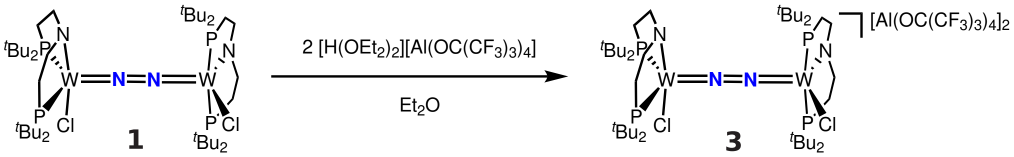

(3.15)

A solution of [H(OEt_2)$_2$][Al(OC(CF_3)$_3$)$_4$] (9.9 mg, 8.84 μmol, 2.1 equiv.) in Et_2O (2 mL) was added dropwise to a suspension of **1** (5.0 mg, 4.21 μmol, 1.0 equiv.) in Et_2O (5 mL). After stirring for 12 h all volatiles were removed *in vacuo* and the remaining yellowish brown residue was taken up in THF—d_8 (90% spectroscopic yield).

^{1}H NMR (THF—d_8, 400 MHz, [ppm]): δ = 4.32 (s_{br}, C*Me*$_3$), 4.19 (s_{br}, C*Me*$_3$), 3.78 (s_{br}, C*Me*$_3$), 3.49 (s_{br}, C*Me*$_3$), -1.56 (s_{br}, CH*H*), -7.03 (s_{br}, CH*H*), -8.81 (s_{br}, CH*H*), -8.99 (s_{br}, CH*H*), -32.1 (s_{br}, CH*H*), -46.9 (s_{br}, CH*H*), -56.6 (s_{br}, CH*H*), -62.0 (s_{br}, CH*H*).
Elem. Anal. found (calc) for $C_{72}H_{88}Al_2Cl_2F_{72}N_4O_8P_4W_2$ (**3**-[Al(OC(CF_3)$_3$)$_4$]): C 29.2 (29.4); H 3.30 (3.01); N 1.66 (1.90).
rRaman (λ_{ex} = 633 nm, -100 °C, THF—d_8, cm^{-1}): $\tilde{\nu}$ = 1400 ($^{14}N_2$); 1356 ($^{15}N_2$).
HR-ESI-MS found (calc) for [$C_{40}H_{88}Cl_2N_4P_4W_2$]$^{2+}$: 593.2181 (593.2166), 594.2182 (594.2177).

3.3.5 [W(N)Cl(^{H}PNP)]$^+$ (11)

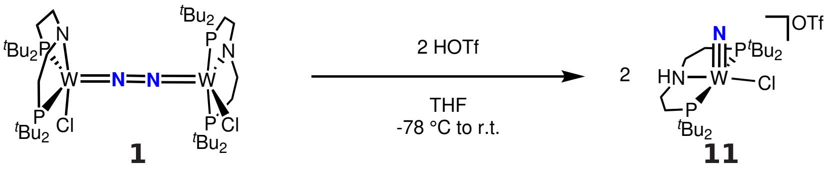

(3.16)

At -78 °C to a solution of **1** (50 mg, 42.1 µmol, 1.0 equiv.) in THF (8 mL) was added a solution of HOTf (7.8 µL, 13.3 mg, 88.4 mmol, 2.1 equiv.) in THF (6 mL) leading to a color change from green to brownish orange. After stirring for 3 h the solution was warmed to r.t. and dried *in vacuo*. The residue was then washed with pentane (4x 5 mL), extracted with benzene (3x 4 mL) and concentrated *in vacuo*. Diffusion of pentane into a saturated benzene solution at r.t. gives **26**-OTf as pale yellow crystals (48 mg, 60%).

Elem. Anal. found (calc) for $C_{21}H_{45}ClF_3N_2O_3P_2SW \cdot 0.8C_6H_6$: C 38.23 (38.34); H 6.21 (6.22); N 3.29 (3.46).
HR-ESI-MS found (calc) for $C_{20}H_{45}ClN_2P_2W^+$: 594.2240 (594.2242), 596.2271 (596.2269).
IR (ATR-IR, cm^{-1}): $\tilde{\nu}$ = 3079 (N-H); 1058 (W≡N).
$\mu_{\mathbf{eff}} = 1.8 \pm 0.1\mu_B$.

3.3.6 *in situ* [(^{H}PNP)ClW-(N$_2$)-WCl(PNP)]$^+$ (12)

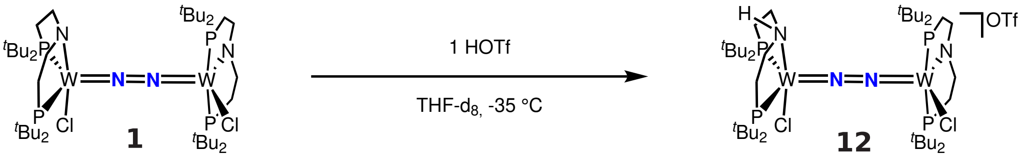

(3.17)

In a J-Young NMR tube HOTf (0.2 µL, 0.34 mg, 2.27 µmol, 1.0 equiv.) was added to a solution of **1** (2.7 mg, 2.27 µmol, 1.0 equiv.) in THF—d$_8$ (0.6 mL) at -35 °C. The reaction mixture was *in situ* characterized by NMR-spectroscopy.

^{1}**H NMR** (THF—d$_8$, 400 MHz, -35 °C, [ppm]): δ = 5.43 (m, 1 H, N-*H*), 1.53 (d, $^3J_{HP}$ = 13.7 Hz, 9 H, C*Me*3), 1.40 (d, $^3J_{HP}$ = 13.1 Hz, 9 H, C*Me*3), 1.39 (d, $^3J_{HP}$ = 11.8 Hz, 9 H, C*Me*3), 1.26 (d, $^3J_{HP}$ = 14.4 Hz, 9 H, C*Me*3), 1.17-1.07 (m, 36 H, 4x C*Me*3).
^{15}**N{^{1}H} NMR** (THF—d$_8$, 50.7 MHz, -35 °C, [ppm]): δ = 27.0 (d, $^1J_{NN}$ = 10.3 Hz), 23.7 (d, $^1J_{NN}$ = 10.9 Hz).
^{31}**P{^{1}H} NMR** (THF—d$_8$, 162 MHz, -35 °C, [ppm]): δ = 86.8 (d, $^2J_{PP}$ = 123.1 Hz), 79.5 (d, $^2J_{PP}$ = 123.2 Hz), 78.1 (d, $^2J_{PP}$ = 126.2 Hz), 74.6 (d, $^2J_{PP}$ = 126.7 Hz).

3.3.7 *in situ* $[\{(^{H}\mathrm{PNP})\mathrm{ClW}\}(\mu\text{–}\mathrm{N_2})]^{2+}$ (13)

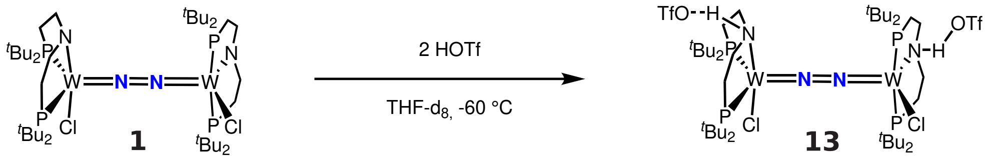

^{t}Bu$_2$P
N
W
N
N
W
^{t}Bu$_2$
P
N
P
^{t}Bu$_2$
Cl
1
P Cl
^{t}Bu$_2$
2 HOTf
THF-d$_8$, -60 °C
TfO--H
N
^{t}Bu$_2$P
W
N
N
W
^{t}Bu$_2$
P
N-H
OTf
P
^{t}Bu$_2$
Cl
13
P Cl
^{t}Bu$_2$

(3.18)

In a J-Young NMR tube HOTf (0.4 μL, 0.68 mg, 4.52 μmol, 2.0 equiv.) was added to a solution of **1** (2.7 mg, 2.27 μmol, 1.0 equiv.) in THF–d$_8$ (0.6 mL) at -60 °C. The reaction mixture was *in situ* characterized by NMR-spectroscopy.

3.3.8 $[(\mathrm{N_2})\{\mathrm{WCl(CO)(PNP)}\}_2]$ (8)

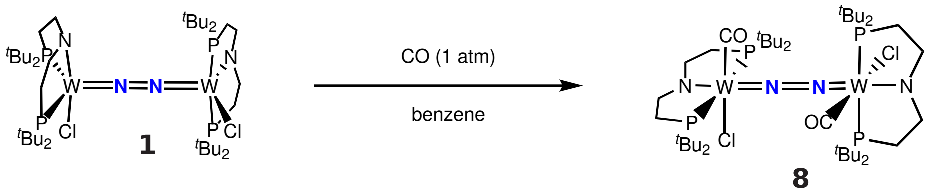

^{t}Bu$_2$P
N
W
N
N
W
^{t}Bu$_2$
P
N
P
^{t}Bu$_2$
Cl
1
P Cl
^{t}Bu$_2$
CO (1 atm)
benzene
CO
P
^{t}Bu$_2$
N
W
N
N
W
N
P
^{t}Bu$_2$
Cl
Cl
OC
P
^{t}Bu$_2$
P
^{t}Bu$_2$
8

(3.19)

A solution of **1** (100 mg, 84 μmol) was dissolved in benzene (10 mL), degassed *via* one *freeze-pump-thaw*-cycle and stirred under CO (1 atm) for 20 min. After removal of the solvent *in vacuo* **8** was obtained as a black-yellow solid (102 mg, 98%).

^{1}H{^{31}P} NMR (C_6D_6, 500 MHz, [ppm]): δ = 3.55 (m, 4 H, NC*H*H), 3.26 (m, 4 H, NC*H*H), 2.42 (m, 4 H, PC*H*H), 1.89 (m, 4 H, PC*H*H), 1.60 (s, 18 H, C*Me*$_3$), 1.53 (s, 18 H, C*Me*$_3$), 1.43 (s, 18 H, C*Me*$_3$), 1.31 (s, 18 H, C*Me*$_3$).
^{13}C{^{1}H} NMR (C_6D_6, 126 MHz, [ppm]): δ = 25.4 (AXY, N = $|^1J_{AX} + ^3J_{AY}|$ = 16.9 Hz, 2x P*C*H$_2$), 25.7 (AXY, N = $|^1J_{AX} + ^3J_{AY}|$ = 17.1 Hz, 2x P*C*H$_2$), 31.0 (m, 2x C*Me*$_3$), 31.1 (m, 2x C*Me*$_3$), 31.3 (m, 2x C*Me*$_3$), 31.4 (m, 2x C*Me*$_3$), 37.2 (AXY, N = $|^1J_{AX} + ^3J_{AY}|$ = 16.0 Hz, 2x P*C*Me$_3$), 37.8 (AXY, N = $|^1J_{AX} + ^3J_{AY}|$ = 16.7 Hz, 2x P*C*Me$_3$), 38.4 (AXY, N = $|^1J_{AX} + ^3J_{AY}|$ = 10.5 Hz, 2x P*C*Me$_3$), 38.8 (AXY, N = $|^1J_{AX} + ^3J_{AY}|$ = 11.5 Hz, 2x P*C*Me$_3$), 59.2 (AXY, N = $|^2J_{AX} + ^4J_{AY}|$ = 9.9 Hz, 2x N*C*H$_2$), 59.4 (AXY, N = $|^2J_{AX} + ^4J_{AY}|$ = 9.6 Hz, 2x N*C*H$_2$), 263 (m, 2x *C*O).

^{15}N{^{1}H} NMR (C_6D_6, 50.7 MHz, [ppm]): δ = -0.69 (s).
^{31}P{^{1}H} NMR (C_6D_6, 121k MHz, [ppm]): δ = 65.9 (s).
Elem. Anal. found (calc) for $C_{42}H_{88}Cl_2N_4O_2P_4W_2$: C 40.63 (40.56); H 6.69 (7.13); N 4.52 (4.51).
IR (ATR-IR, cm^{-1}): $\tilde{\nu}$ = 1883 (C≡O), 1867 (C≡O).
rRaman (λ_{ex} = 457 nm, frozen THF–d$_8$, cm^{-1}): $\tilde{\nu}$ = 1437 ($^{14}N_2$); 1394 ($^{15}N_2$).

3.3.9 [(N$_2$){W(CO)(PNP)}$_2$] (4)

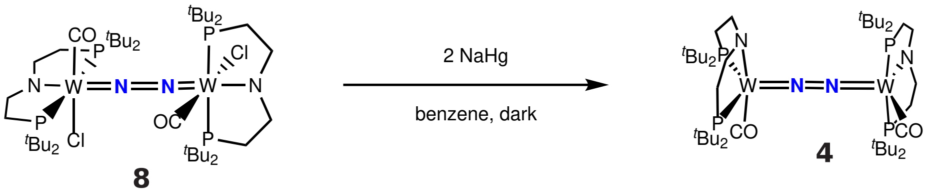

(3.20)

8 (80 mg, 67 µmol, 1.0 equiv.) and NaHg (2.2 g, 162 µmol, 2.4 equiv.) were stirred for 12 h in benzene (20 mL) under the exclusion of light. Afterwards the solvent was removed *in vacuo* and the red-brown residue was extracted with pentane to give **4** as a red-brown solid (45 mg, 57%).

^{1}**H NMR** (C$_6$D$_6$, 300 MHz, [ppm]): δ = 14.6 (s, CH*H*), 13.6 (s, CH*H*), 12.9 (s, CH*H*), 7.79 (s, CH*H*), 7.25 (s, C*Me*$_3$), 6.45 (s, CH*H*), 6.38 (s, C*Me*$_3$), 4.54 (s, C*Me*$_3$), 3.53 (s, C*Me*$_3$), -2.58 (s, CH*H*), -14.4 (s, CH*H*), -16.0 (s, CH*H*).
Elem. Anal. found (calc) for $C_{42}H_{88}N_4O_2P_4W_2$: C 43.17 (43.01), H 7.23 (7.56), N 3.64 (4.78).
[The lower N content found is attributed to decomposition of highly sensitive **4** during transport/manipulations.]
IR (ATR-IR, cm^{-1}): $\tilde{\nu}$ = 1785 (C≡O), 1741 (C≡O).
rRaman (λ_{ex} = 633 nm, frozen THF—d$_8$, cm^{-1}): $\tilde{\nu}$ = 1589 ($^{14}N_2$); 1540 ($^{14}N_2$).
$\mu_{\mathbf{eff}} = 2.3 \pm 0.1\mu_B$.

3.3.10 [W(N)(CO)(PNP)] (16)

thermochemical N_2-splitting

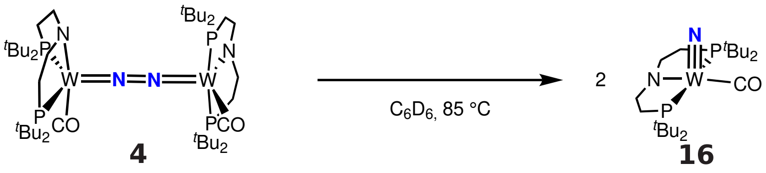
^{t}Bu$_2$P
N
W
N
N
W
P
CO
^{t}Bu$_2$
P
N
PCO
^{t}Bu$_2$
4
C$_6$D$_6$, 85 °C
2
N
P^{t}Bu$_2$
N
W
CO
P
^{t}Bu$_2$
16

(3.21)

A solution of **4** (5.5 mg, 4.69 µmol) in C_6D_6 (0.5 mL) was heated to 85 °C for 12 h, leading to a color change from deep red to pale green.

photochemical N_2-splitting

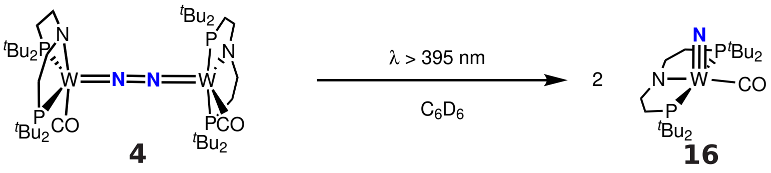
^{t}Bu$_2$P
N
W
N
N
W
P
CO
^{t}Bu$_2$
P
N
PCO
^{t}Bu$_2$
4
λ > 395 nm
C$_6$D$_6$
2
N
P^{t}Bu$_2$
N
W
CO
P
^{t}Bu$_2$
16

(3.22)

A solution of **4** (5.5 mg, 4.69 µmol) in C_6D_6 (0.5 mL) was irradiated with λ>395 nm in a water bath for 12 h.

deprotonation of ***20***

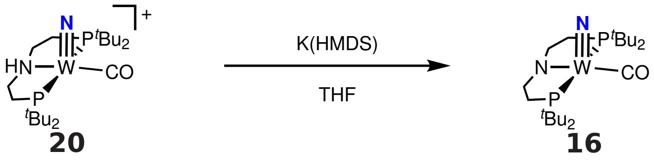
N
P^{t}Bu$_2$
+
HN
W
CO
P
^{t}Bu$_2$
20
K(HMDS)
THF
N
P^{t}Bu$_2$
N
W
CO
P
^{t}Bu$_2$
16

(3.23)

To a solution of **20-OTf** (35 mg; 47.5 µmol, 1.0 equiv.) in benzene (5 mL) was added K(HMDS) (11.4 mg, 57 µmol, 1.2 equiv.). The mixture was stirred for 1 h, pumped to dryness, extracted with pentane over celite and dried *in vacuo* to give **16** as a light blue solid (19.5 mg, 70%).

^{1}H{^{31}P} NMR (C_6D_6, 500 MHz, [ppm]): δ = 3.90 (m, 2 H, NCH*H*), 3.76 (m, 2 H, NCH*H*), 1.79 (m, 2 H, PCH*H*), 1.55 (m, 2 H, PCH*H*), 1.49 (s, 18 H, 2x C*Me*$_3$), 0.89 (s, 18 H, 2x C*Me*$_3$).
^{13}C{^{1}H} NMR (C_6D_6, 126 MHz, [ppm]): δ = 24.5 (AXY, $N = |{}^1J_{AX} + {}^3J_{AY}|$ = 18.5 Hz, 2x P*C*H$_2$), 29.1 (AXY, $N = |{}^2J_{AX} + {}^4J_{AY}|$ = 5.4 Hz, 2x C*Me*$_3$), 29.3 (AXY, $N = |{}^2J_{AX} + {}^4J_{AY}|$ = 5.5 Hz, 2x C*Me*$_3$), 35.0 (AXY, $N = |{}^1J_{AX} + {}^3J_{AY}|$ = 15.5 Hz, 2x P*C*Me$_3$), 35.1 (AXY, $N = |{}^1J_{AX} + {}^3J_{AY}|$ = 20.5 Hz, 2x P*C*Me$_3$), 66.2 (AXY, $N = |{}^2J_{AX} + {}^4J_{AY}|$ = 14.8 Hz, 2x N*C*H$_2$), 283.4 (t, $^2J_{CP}$ = 4.40 Hz, *C*O).
^{15}N{^{1}H} NMR (C_6D_6, 50.7 MHz, [ppm]): δ = 447.0 (s).
^{31}P{^{1}H} NMR (C_6D_6, 203 MHz, [ppm]): δ = 104.4 (s).
Elem. Anal. found (calc) for $C_{21}H_{44}N_2OP_2W$: C 43.04 (43.01); H 7.53 (7.56); N 4.93 (4.78).
IR (ATR-IR, cm^{-1}): $\tilde{\nu}$ = 1883 (C≡O), 998 (W≡N).

3.3.11 [W(CO)$_3$(^{H}PNP)] (9)

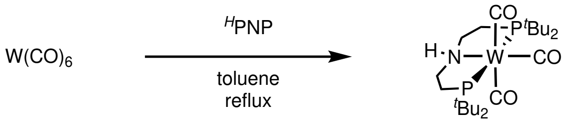

9

(3.24)

$W(CO)_6$ (500 mg, 1.42 mmol, 1.0 equiv.) was refluxed in toluene (50 mL) for 2 d. Afterwards a solution of $HN(CH_2CH_2P^tBu_2)_2$ (565 mg, 1.56 mmol, 1.1 equiv.) in toluene (10 mL) was added. The mixture was refluxed for min. 7 days while a yellow precipitate is forming. After removal of the solvent *in vacuo*, the residue was washed with pentane and dried *in vacuo* to give **9** as a yellow solid (832 mg. 94%).

^{1}H{^{31}P} NMR (CD_2Cl_2, 500 MHz, [ppm]): δ = 3.53 (m, 2 H, 2x NCH*H*), 2.53 (m, 1 H, N*H*), 2.40 (m, 2 H, 2x NCH*H*), 2.15 (m, 2 H, 2x PCH*H*), 1.58-1.51 (m, 2 H, 2x PCH*H*), 1.36 (s, 18 H, 2x C*Me*$_3$), 1.35 (s, 18 H, 2x C*Me*$_3$).
^{13}C{^{1}H} NMR (CCl_2D_2, 126 MHz, [ppm]): δ = 25.4 (AXY, $N = |{}^1J_{AX} + {}^3J_{AY}|$ = 17.5 Hz, 2x P*C*H$_2$), 30.4 (AXY, $N = |{}^2J_{AX} + {}^4J_{AY}|$ = 5.3 Hz, 2x C*Me*$_3$), 30.6 (AXY, $N = |{}^2J_{AX} + {}^4J_{AY}|$ = 5.7 Hz, 2x C*Me*$_3$), 37.3 (AXY, $N = |{}^1J_{AX} + {}^3J_{AY}|$ = 17.2 Hz, 2x P*C*Me$_3$), 38.7 (AXY, $N = |{}^1J_{AX} + {}^3J_{AY}|$ = 12.6 Hz, 2x P*C*Me$_3$), 58.0 (AXY, $N = |{}^2J_{AX} + {}^4J_{AY}|$ = 10.2 Hz, 2x N*C*H$_2$), 224 (m, 2x *C*Oax), 226.4 (t, $^2J_{CP}$ =5.6 Hz, *C*Oeq).
^{31}P{^{1}H} NMR (CCl_2D_2, 203 MHz, [ppm]): δ = 88.5 (s).
Elem. Anal. found (calc) for $C_{23}H_{45}NO_3P_2W$: C 43.73 (43.89); H 6.89 (7.21); N 2.11 (2.23).
IR (ATR-IR, cm^{-1}): $\tilde{\nu}$ = 3227 (N-H), 1896 (C≡O), 1773 (C≡O), 1753 (C≡O).

3.3.12 [WI(CO)$_2$(PNP)] (18)

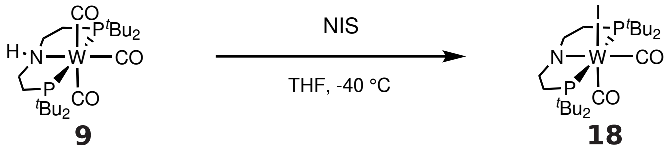

(3.25)

At -40 °C a solution of N-iodosuccinimide (54 mg, 0.238 mmol, 1.0 equiv.) in THF (5 mL) was added to a solution of **9** (150 mg, 0.238 mmol, 1.0 equiv.) in THF (10 mL). The reaction was stirred for 4 h while warming to r.t. and dried *in vacuo*. The resulting brownish-violett residue was extracted with Et_2O (5x 5 mL) at -40 °C. The filtrate was dried *in vacuo*, side products were removed *via* sublimation under vacuum at 85 °C and **18** was obtained as a dark violet powder (160 mg, 92%).

^{1}H{^{31}P} NMR (C_6D_6, 300 MHz, [ppm]): δ = 2.80-2.74 (m, 2 H, 2x NCH*H*), 2.47-2.40 (m, 2 H, 2x NCH*H*), 2.11-2.04 (m, 2 H, 2x PCH*H*), 1.96-1.90 (m, 2 H, 2x PCH*H*), 1.39 (s, 18 H, 2x C*Me*$_3$), 1.13 (s, 18 H, 2x C*Me*$_3$).
^{13}C{^{1}H} NMR (C_6D_6, 126 MHz, [ppm]): δ = 26.7 (AXY, N = $|^1J_{AX} + ^3J_{AY}|$ = 17.5 Hz, 2x P*C*H$_2$), 30.4 (AXY, N = $|^2J_{AX} + ^4J_{AY}|$ = 3.9 Hz, 2x C*Me*$_3$), 31.8 (AXY, N = $|^2J_{AX} + ^4J_{AY}|$ = 3.5 Hz, 2x C*Me*$_3$), 38.7 (AXY, N = $|^1J_{AX} + ^3J_{AY}|$ = 13.6 Hz, 2x P*C*Me$_3$), 39.2 (AXY, N = $|^1J_{AX} + ^3J_{AY}|$ = 15.0 Hz, 2x P*C*Me$_3$), 67.2 (AXY, N = $|^2J_{AX} + ^4J_{AY}|$ = 11.0 Hz, 2x N*C*H$_2$), 248 (t, ^2J = 9.2 Hz, *C*O), 253 (t, ^2J = 6.0 Hz, *C*O).
^{31}P{^{1}H} NMR (C_6D_6, 162 MHz, [ppm]): δ = 67.6 (s).
Elem. Anal. found (calc) for $C_{22}H_{44}ClNO_2P_2W$: C 36.33 (36.33); H 6.16 (6.10); N 2.16 (1.93).
IR (ATR-IR, cm^{-1}): $\tilde{\nu}$ = 1907 (C≡O), 1799 (C≡O).

3.3.13 [WCl(CO)$_2$(PNP)] (10)

*Oxidation of **9***

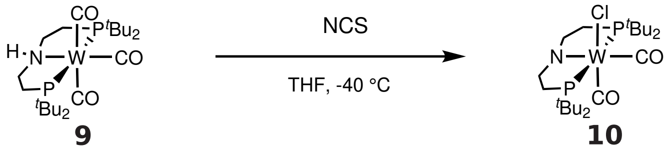

(3.26)

At -40 °C a solution of N-chlorosuccinimide (25.5 mg, 0.19 mmol, 1.2 equiv.) in THF (7 mL) was added to a solution of **9** (100 mg, 0.16 mmol, 1.0 equiv.) in THF (6 mL). The reaction was stirred for 4 h while warming to r.t. and dried *in vacuo*. The resulting brownish-violett residue was extracted with Et$_2$O (5x 5 mL) at -40 °C. The filtrate was dried *in vacuo*, side products were removed *via* sublimation under vacuum at 85 °C and **10** was obtained as a dark violet powder (56 mg, 55%).

*Salt metathesis of **21***

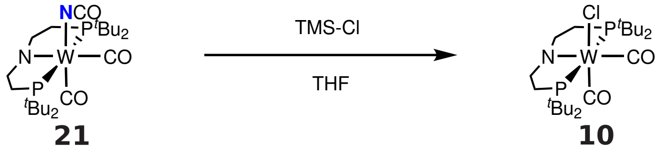

(3.27)

To a solution of **21** (5.0 mg, 7.8 μmol, 1.0 equiv.) in THF—d$_8$ (0.5 ml) was added TMS-Cl (1.0 μL, 0.9 mg, 7.8 μmol, 1.0 equiv.). The solution was stirred over night to give **10** and TMS-NCO (both >99% spectroscopic yield). The formed TMS-NCO could be separated *via* vacuum trap-to-trap transfer.

^{1}H{^{31}P} NMR (C$_6$D$_6$, 300 MHz, [ppm]): δ = 3.13-2.99 (m, 2 H, 2x NCH*H*), 2.70-2.58 (m, 2 H, 2x NCH*H*), 2.05-1.84 (m, 4 H, 4x PCH*H*), 1.34 (s, 18 H, 2x C*Me*$_3$), 1.10 (s, 18 H, 2x C*Me*$_3$).
^{13}C{^{1}H} NMR (C$_6$D$_6$, 126 MHz, [ppm]): δ = 26.9 (AXY, N = $|^1J_{AX} + ^3J_{AY}|$ = 17.1 Hz, 2x PCH$_2$), 30.1 (AXY, N = $|^2J_{AX} + ^4J_{AY}|$ = 4.6 Hz, 2x C*Me*$_3$), 31.0 (AXY, N = $|^2J_{AX} + ^4J_{AY}|$ = 4.0 Hz, 2x C*Me*$_3$), 37.8 (AXY, N = $|^1J_{AX} + ^3J_{AY}|$ = 13.6 Hz, 2x PCMe$_3$), 38.5 (AXY, N = $|^1J_{AX} + ^3J_{AY}|$ = 14.6 Hz, 2x PCMe$_3$), 67.9 (AXY, N = $|^2J_{AX} + ^4J_{AY}|$ = 11.0 Hz, 2x NCH$_2$), 259 (t, ^{2}J = 8.7 Hz, CO), 264 (t, ^{2}J = 4.8 Hz, CO).
^{31}P{^{1}H} NMR (C$_6$D$_6$, 162 MHz, [ppm]): δ = 73.9 (s).
Elem. Anal. found (calc) for C$_{22}$H$_{44}$ClNO$_2$P$_2$W: C 41.35 (41.56); H 7.00 (6.98); N 2.19 (2.20).
IR (ATR-IR, cm^{-1}): $\tilde{\nu}$ = 1914 (C≡O), 1815 (C≡O).

Characterization of TMS-NCO

^{1}**H NMR** (THF—d$_8$, 300 MHz, [ppm]): δ = 0.25 (s, 9 H, Si(*Me*$_3$)).
^{13}**C{^{1}H} NMR** (THF—d$_8$, 126 MHz, [ppm]): δ = 0.78 (s, Si(*Me*$_3$)).
^{29}**Si{^{1}H} NMR** (THF—d$_8$, 90.4 MHz, [ppm]): δ = 4.5 (s, *Si*(Me$_3$)).

Characterization of TMS-^{15}NCO

^{1}**H** (THF—d$_8$, 500 MHz, [ppm]): δ = 0.25 (d, $^3J_{HN}$ = 1.4 Hz, 9 H, Si(*Me*$_3$)).
^{13}**C{^{1}H} NMR** (THF—d$_8$, 126 MHz, [ppm]): δ = 0.79 (d, $^2J_{CN}$ = 2.8 Hz, Si(*Me*$_3$)).
^{15}**N{^{1}H} NMR** (THF—d$_8$, 50.7 MHz, [ppm]): δ = -346 (s).
^{29}**Si{^{1}H} NMR** (THF—d$_8$, 90.4 MHz, [ppm]): δ = 4.5 (d, $^1J_{SiN}$ = 14.2 Hz).

3.3.14 [W(N$_3$)(CO)$_2$(PNP)] (19)

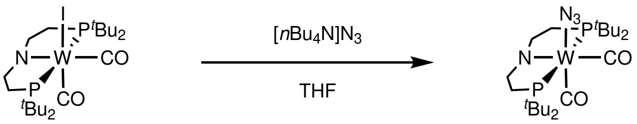

9 **19** (3.28)

18 (20 mg, 27.5 μmol, 1.0 equiv.) and [*n*Bu$_4$N]N$_3$ (9.4 mg, 33 μmol, 1.2 equiv.) were stirred in THF for 30 min. After removal of the solvent *in vacuo* the product was extracted with Et$_2$O over celite. After drying *in vacuo* **19** was obtained as red-purple solid (17 mg, 96%).

^{1}**H{^{31}P} NMR** (C$_6$D$_6$, 300 MHz, [ppm]): δ = 3.01 (m, 2 H, 2x NCH*H*), 2.61 (m, 2 H, 2x NCH*H*), 1.81 (m, 4 H, 4x PCH*H*), 1.20 (s, 18 H, 2x C*Me*$_3$), 1.03 (s, 18 H, 2x C*Me*$_3$).
^{13}**C{^{1}H} NMR** (C$_6$D$_6$, 126 MHz, [ppm]): δ = 26.6 (AXY, N = $|^1J_{AX} + ^3J_{AY}|$ = 17.1 Hz, 2x P*C*H$_2$), 29.8 (m, 2x C*Me*$_3$), 30.2 (m, 2x C*Me*$_3$), 36.9 (AXY, N = $|^1J_{AX} + ^3J_{AY}|$ = 14.3 Hz, 2x P*C*Me$_3$), 37.2 (AXY, N = $|^1J_{AX} + ^3J_{AY}|$ = 14.2 Hz, 2x P*C*Me$_3$), 67.6 (m, 2x N*C*H$_2$), 262 (t, ^2J = 8.5 Hz, *C*O), 264 (t, ^2J = 4.4 Hz, *C*O).
^{31}**P{^{1}H} NMR** (C$_6$D$_6$, 162 MHz, [ppm]): δ = 77.7 (s).
IR (ATR-IR, cm^{-1}): $\tilde{\nu}$ = 2072 (N═N═N), 1907 (C≡O), 1828 (C≡O).

3.3.15 [W(N)(CO)(^{H}PNP)]$^+$ (20)

salt metathesis route

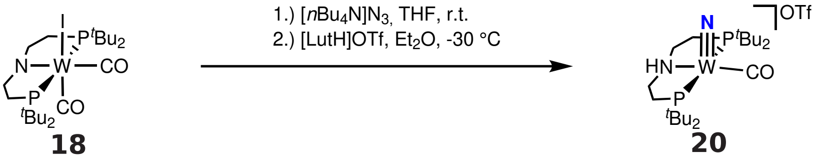
1.) [nBu$_4$N]N$_3$, THF, r.t.
2.) [LutH]OTf, Et$_2$O, -30 °C
18
20
OTf

(3.29)

18 (110 mg, 0.151 mmol, 1.1 equiv.) and [nBu$_4$N]N$_3$ (51 mg, 0,179 mmol, 1.3 equiv.) were dissolved in THF (6 mL) and stirred for 30 min at r.t. After evaporation of the solvent, the residue was extracted with Et$_2$O at -30 °C into a solution of [LutH][OTf] (35.4 mg, 0.138 mmol, 1.0 equiv.) in THF (2 mL). The mixture was stirred for 2 h, warmed to r.t. and dried *in vacuo*. The residue was then washed with pentane (5x 4 mL) and Et$_2$O (2x 2 mL) and extracted with benzene. After evaporation of the solvent **20** was obtained as deep blue powder (55 mg, 55%)

*protonation of **16***

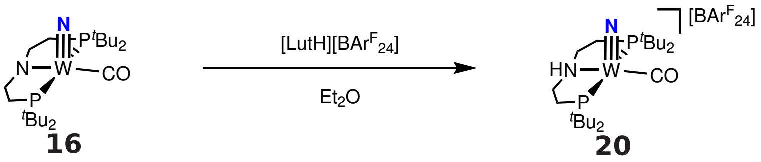

(3.30)

16 (7.2 mg, 12.3 µmol, 1.2 equiv.) and [LutH][BAr$^F_{24}$] were stirred in Et$_2$O (4 mL). After evaporation of the solvent, the residue was washed with pentane (2x 2 mL) and extracted with Et$_2$O. After evaporation of the solvent *in vacuo* **20** was obtained as dark powder (14.7 mg ,89%).

^{1}H{^{31}P} NMR (C$_6$D$_6$, 500 MHz, [ppm]): δ = 5.92 (m, 1 H, N-*H*), 4.03-4.00 (m, 2 H, 2x NC*H*H) 2.58-2.50 (m, 2 H, 2x NC*H*H), 2.31-2.24 (m, 2 H, 2x PC*H*H), 1.62-1.58 (m, 2 H, 2x PC*H*H), 1.15 (s, 18 H, 2x C*Me*$_3$), 0.77 (s, 18 H, 2x C*Me*$_3$).
^{13}C{^{1}H} NMR (C$_6$D$_6$, 126 MHz, [ppm]): δ = 22.9 (AXY, $N = |^{1}J_{AX} + {}^{3}J_{AY}| = 9.1$ Hz, 2x PCH$_2$), 28.0 (AXY, $N = |^{2}J_{AX} + {}^{4}J_{AY}| = 2.0$ Hz, 2x C*Me*$_3$), 28.4 (AXY, $N = |^{2}J_{AX} + {}^{4}J_{AY}| = 2.7$ Hz, 2x C*Me*$_3$), 34.5 (AXY, $N = |^{1}J_{AX} + {}^{3}J_{AY}| = 8.8$ Hz, 2x PCMe$_3$), 35.4 (AXY, $N = |^{1}J_{AX} + {}^{3}J_{AY}| = 10.9$ Hz, 2x PCMe$_3$), 58.4 (AXY, $N = |^{2}J_{AX} + {}^{4}J_{AY}| = 3.8$ Hz, 2x NCH$_2$), 279 (m, *C*O).
^{15}N{^{1}H} NMR (C$_6$D$_6$, 50.7 MHz, [ppm]): δ = 445.7 (s).
^{31}P{^{1}H} NMR (C$_6$D$_6$, 203 MHz, [ppm]): δ = 93.1 (s).
Elem. Anal. found (calc) for $C_{53}H_{57}BF_{24}N_2OP_2W$ (**20**-[BAr$^F_{24}$]): C 44.21 (43.88); H 4.00 (3.96); N 1.72 (1.94).
IR (ATR-IR, cm^{-1}): $\tilde{\nu}$ = 3118 (N—H), 1928 (C≡O), 1048 (W≡N).

3.3.16 [W(NCO)(CO)$_2$(PNP)] (21)

*Carbonylation of [W(N)(CO)(PNP)] (**16**)*

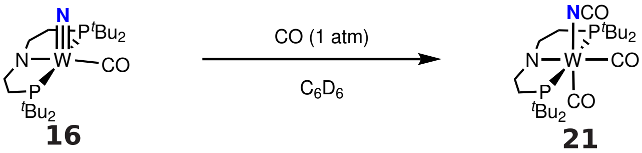

(3.31)

In a J-Young NMR tube **16** (6.0 mg, 10 µmol) was dissolved in C_6D_6. The NMR tube was degassed *via* two *freeze-pump-thaw* cycles and set under CO (1 atm). After stirring for 16 h the solution was degassed again *via* two *freeze-pump-thaw* cycles to give **21** (85% spectroscopic yield).

*Salt-metathesis of [WI(CO)$_2$(PNP)] (**18**)*

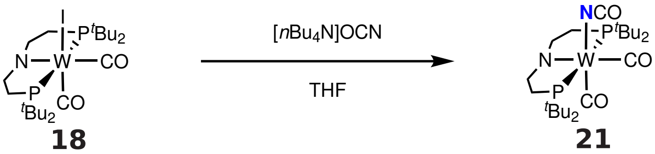

(3.32)

18 (26.0 mg, 35.7 µmol, 1.0 equiv.) and [nBu$_4$N][NCO] (12.2 mg, 42.9 µmol, 1.2 equiv.) were stirred in THF (5 mL) for 1 h at r.t. Afterwards the solvent was removed *in vacuo* and the purple residue extracted with Et_2O over Celite. After removal of the solvent *in vacuo*, column chromatography over silanized silica 60 using benzene as eluent and lyophilization **21** was obtained as a purple powder (18.5 mg, 80%).

^{1}H{^{31}P} NMR (C_6D_6, 500 MHz, [ppm]): δ = 3.01-2.95 (m, 2 H, 2x NC*H*H). 2.56-2.50 (m, 2 H, 2x NC*H*H), 1.88-1.76 (m, 4 H, 2x PC*H*H), 1.21 (s, 18 H, 2x C*Me*$_3$), 1.02 (s, 18 H, 2x C*Me*$_3$).
^{13}C{^{1}H} NMR (C_6D_6, 126 MHz, [ppm]): δ = 26.9 (AXY, N = $|^1J_{AX} + ^3J_{AY}|$ = 17.1 Hz, 2x P*C*H$_2$), 29.8 (AXY, N = $|^2J_{AX} + ^4J_{AY}|$ = 4.5 Hz, 2x C*Me*$_3$), 30.4 (AXY, N = $|^2J_{AX} + ^4J_{AY}|$ = 3.9 Hz, 2x C*Me*$_3$), 37.3 (AXY, N = $|^1J_{AX} + ^3J_{AY}|$ = 14.3 Hz, 2x P*C*Me$_3$), 37.4 (AXY, N = $|^1J_{AX} + ^3J_{AY}|$ = 14.3 Hz, 2x P*C*Me$_3$), 68.2 (AXY, N = $|^2J_{AX} + ^4J_{AY}|$ = 10.8 Hz, 2x N*C*H$_2$), 145 (s$_{br}$, N*C*O), 262 (t, $^2J_{CP}$ = 8.3 Hz, *C*O), 266 (t, $^2J_{CP}$ = 4.4 Hz, *C*O).
^{15}N{^{1}H} NMR (C_6D_6, 50.7 Hz, [ppm]): δ = -347 (t, $^2J_{NP}$ = 2.6 Hz, *N*CO).
^{31}P{^{1}H} NMR (C_6D_6, 162 MHz, [ppm]): δ = 76.6 (s).
Elem. Anal. found (calc) for $C_{23}H_{44}N_2O_3P_2W$: C 42.97 (43.00), H 6.82 (6.90), N 4.37 (4.36).
IR (ATR-IR, cm^{-1}): $\tilde{\nu}$ = 2203(N=C=O), 1909 (C≡O), 1831 (C≡O).

3.3.17 [W(NCO)(CN^{t}Bu)$_2$(PNP)] (22)

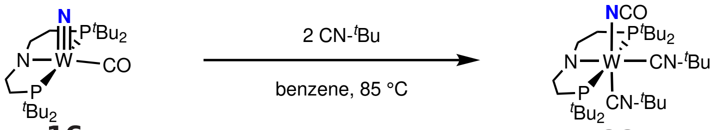

16 **22**

(3.33)

To a solution of **16** (21.3 mg, 36.3 μmol, 1.0 equiv.) in benzene (20 mL) was added CN-^{t}Bu (7.8 μL, 5.7 mg, 69 μmol, 1.9 equiv.). The mixture was heated to 85 °C for 3 h. After removal of the solvent *in vacuo*, the residue was extracted with benzene over silanized Silica 60. After evaporation of the solvent **22** was obtained as a green solid (15.3 mg, 56%).

^{1}H{^{31}P} NMR (C_6D_6, 300 MHz, [ppm]): δ = 3.10 (m, 2 H, NC*H*H), 2.76 (m, 2 H, NC*H*H), 1.99 (m, 2 H, PC*H*H), 1.90 (m, 2 H, PC*H*H), 1.46 (s, 9 H, CN-C*Me*$_3$), 1.39 (s, 18 H, 2x C*Me*$_3$), 1.27 (s, 18 H, 2x C*Me*$_3$), 1.11 (s, 9 H, CN-C*Me*$_3$).
^{13}C{^{1}H} NMR (C_6D_6, 126 MHz, [ppm]): δ = 27.4 (AXY, N = $|^1J_{AX} + ^3J_{AY}|$ = 14.0 Hz, 2x P*C*H$_2$), 30.7 (s, 2x P(C*Me*$_3$)$_2$), 31.0 (s, 2x P(C*Me*$_3$)$_2$), 32.2 (s, CN-C*Me*$_3$), 32.3 (s, CN-C*Me*$_3$), 37.7 (AXY, N = $|^1J_{AX} + ^3J_{AY}|$ = 11.8 Hz, 2x P(*C*Me$_3$)$_2$), 39.0 (AXY, N = $|^1J_{AX} + ^3J_{AY}|$ = 12.6 Hz, 2x P(*C*Me$_3$)$_2$), 58.4 (s, CN-*C*Me$_3$), 63.6 (s, CN-*C*Me$_3$), 69.6 (AXY, N = $|^2J_{AX} + ^4J_{AY}|$ = 12.1 Hz, 2x N*C*H$_2$), 143 (s$_{br}$, N*C*O), 213 (s, *C*N-^{t}Bu), 246 (s, *C*N-^{t}Bu).
^{31}P{^{1}H} NMR (C_6D_6, 121 MHz, [ppm]): δ = 76.6 (s).
Elem. Anal. found (calc) for $C_{37}H_{58}N_4O_3P_2W$: C 49.65 (49.47), H 7.78 (8.30), N 7.00 (7.44).
IR (ATR-IR, cm^{-1}): $\tilde{\nu}$ = 2203 (N=C=O), 1994 (C≡N), 1832 (C≡N).

3.3.18 [W(NCO)(CN-C_6H_4-OMe)$_2$(PNP)] (23)

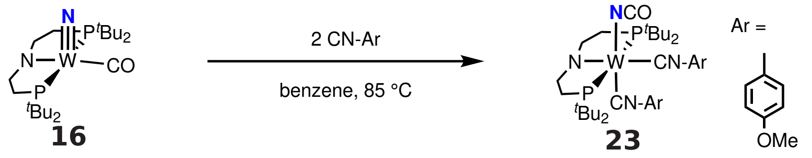

(3.34)

To a solution of **16** (10.0 mg, 17.1 µmol, 1.0 equiv.) in benzene (5 mL) was added CN-C_6H_4-OMe (4.5 mg, 34.1 µmol, 2.0 equiv.). The mixture was heated to 85 °C for 3 h. After removal of the solvent *in vacuo*, the residue was extracted with benzene over silanized Silica 60. After evaporation of the solvent **23** was obtained as a yellow-brownish solid (8.4 mg, 58%).

^{1}H{^{31}P} NMR (C_6D_6, 300 MHz, [ppm]): δ = 7.33 (d, $^3J_{HH}$ = 8.99 Hz, 2 H, Ar-*H*), 6.78 (d, $^3J_{HH}$ = 8.94 Hz, 2 H, Ar-*H*), 6.75 (d, $^3J_{HH}$ = 8.91 Hz, 2 H, Ar-*H*), 6.67 (d, $^3J_{HH}$ = 8.93 Hz, 2 H, Ar-*H*), 3.31 (m, 2 H, NC*H*H), 3.23 (s, 3 H, O*Me*), 3.21 (s, 3 H, O*Me*), 2.84 (m, 2 H, NC*H*H), 2.01 (m, 4 H, PC*H*H), 1.37 (s, 18 H, 2x P(C*Me*$_3$)$_2$), 1.18 (s, 18 H, 2x P(C*Me*$_3$)$_2$).
^{13}C{^{1}H} NMR (C_6D_6, 126 MHz, [ppm]): δ = 27.7 (AXY, N = $|^1J_{AX} + ^3J_{AY}|$ = 15.6 Hz, 2x P*C*H$_2$), 30.5 (AXY, N = $|^2J_{AX} + ^4J_{AY}|$ = 5.21 Hz, 2x P(C*Me*$_3$)$_2$), 30.8 (AXY, N = $|^2J_{AX} + ^4J_{AY}|$ = 4.20 Hz, 2x P(C*Me*$_3$)$_2$), 36.0 (AXY, N = $|^1J_{AX} + ^3J_{AY}|$ = 13.8 Hz, 2x P(*C*Me$_3$)$_2$), 37.8 (AXY, N = $|^1J_{AX} + ^3J_{AY}|$ = 13.2 Hz, 2x P(*C*Me$_3$)$_2$), 55.0 (s, O-*Me*), 69.6 (AXY, N = $|^2J_{AX} + ^4J_{AY}|$ = 11.4 Hz, 2x N*C*H$_2$), 114 (s, 2x ^{Ar}C), 115z (s, 2x ^{Ar}C), 122 (s, 2x ^{Ar}C), 124 (s, 2x ^{Ar}C), 135 (s, $^{Ar}C_q$), 136 (t, $^4J_{CP}$ = 2.47 Hz, $^{Ar}C_q$), 143 (s$_{br}$, N*C*O), 157 (s, $^{Ar}C_q$), 158 (s, $^{Ar}C_q$), 246 (s, *C*N-R), 257 (s, *C*N-R).
^{31}P{^{1}H} NMR (C_6D_6, 121 MHz, [ppm]): δ = 78.7 (s).
Elem. Anal. found (calc) for $C_{31}H_{62}N_4OP_2W$: C 52.37 (52.12), H 6.30 (6.86), N 6.20 (6.57).
IR (ATR-IR, cm^{-1}): $\tilde{\nu}$ = 2205 (N=C=O), 1911 (C≡N), 1757 (C≡N).

3.3.19 [WCl(CN^{t}Bu)$_2$(PNP)] (6)

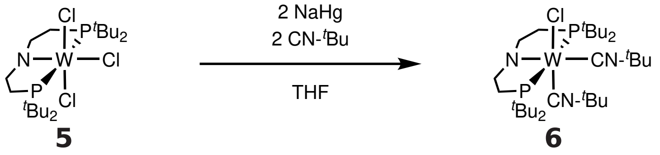

(3.35)

A mixture of **5** (100 mg, 0.154 mmol, 1.0 equiv.), NaHg (4.60 g, 0.338 mmol, 2.2 equiv.) and
CN-^{t}Bu(38.2 μL, 28.1 mg, 0.338 mmol, 2.2 equiv.) was stirred for 4 h at r.t. in THF. After evaporation of the solvent, extraction over silanized Silica 60 with pentane as eluent and lyophilisation out of benzene **6** was obtained as a green solid (35 mg, 30%).

^{1}H{^{31}P} NMR (C_6D_6, 500 MHz, [ppm]): δ = 3.25-3.20 (m, 2 H, NC*H*H), 2.90-2.84 (m, 2 H, NC*H*H), 2.12-2.07 (m, 2 H, PC*H*H), 1.99-1.92 (m, 2 H, PC*H*H), 1.52 (s, 18 H, 2x P(C*Me*$_3$)$_2$), 1.47 (s, 9 H, CN-C*Me*$_3$), 1.34 (s, 18 H, 2x P(C*Me*$_3$)$_2$), 1.14 (s, 9 H, CN-C*Me*$_3$).
^{13}C{^{1}H} NMR (C_6D_6, 126 MHz, [ppm]): δ = 28.3 (AXY, N = $|^1J_{AX} + ^3J_{AY}|$ = 13.8 Hz, 2x P*C*H$_2$), 31.5 (AXY, N = $|^2J_{AX}+^4J_{AY}|$ = 5.2 Hz, 2x P(C*Me*$_3$)$_2$), 31.7 (AXY, N = $|^2J_{AX}+^4J_{AY}|$ = 4.1 Hz, 2x P(C*Me*$_3$)$_2$), 32.2 (s, CN-C*Me*$_3$), 32.6 (s, CN-C*Me*$_3$), 38.0 (AXY, N = $|^1J_{AX} + ^3J_{AY}|$ = 11.5 Hz, 2x P(*C*Me$_3$)$_2$), 40.1 (AXY, N = $|^1J_{AX} + ^3J_{AY}|$ = 12.7 Hz, 2x P(*C*Me$_3$)$_2$), 58.5 (s, CN-*C*Me$_3$), 63.5 (s, CN-*C*Me$_3$), 69.8 (AXY, N = $|^2J_{AX} + ^4J_{AY}|$ = 11.7 Hz, 2x N*C*H$_2$), 213 (s, *C*N-^{t}Bu), 247 (s, *C*N-^{t}Bu).
^{31}P{^{1}H} NMR (C_6D_6, 162 MHz, [ppm]): δ = 73.7 (s).
Elem. Anal. found (calc) for $C_{30}H_{62}ClN_3P_2W$: C 48.27 (48.30), H 8.35 (8.38), N 5.63 (5.59).
IR (ATR-IR, cm^{-1}): $\tilde{\nu}$ = 1964 (C≡N), 1842 (C≡N).

3.3.20 Na[W(CO)$_2$(PNP)] (24)

Deprotonation of ***9***

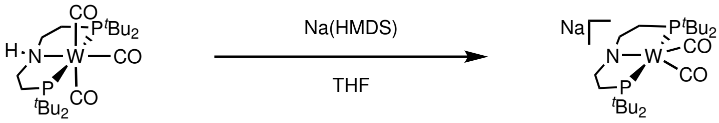

9 **24**

(3.36)

9 (100 mg, 0.159 mmol, 1.0 equiv.) and NaHMDS (32 mg, 0.175 mmol, 1.1 equiv.) were stirred in THF showing a color change from yellow to bright orange. After 30 min the solvent was removed *in vacuo* and the residue was washed with pentane (3x 8 mL). After extraction with THF **24** was obtained as a bright orange solid (59 mg, 60%).

Reduction of ***18***

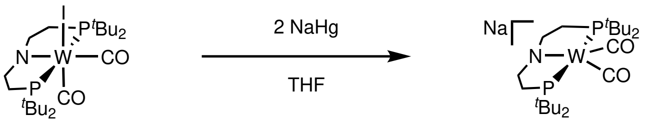

18 **24**

(3.37)

18 (20 mg, 27.5 μmol, 1.0 equiv.) and NaHg (823 mg, 60.5 μmol, 2.2 equiv.) were stirred in THF for 4 h while the color changes from purple to orange. The mixture was dried *in vacuo* and extracted with THF. After evaporation of the solvent **24** was obtained as orange solid (15 mg, 87%).

Addition of 15-cr-5 (1.0 equiv.) makes the compound soluble in benzene. In this way crystals suitable for X-ray diffraction could be obtained by diffusion of pentane into a saturated THF solution of -40 °C.

^{1}**H{^{31}P} NMR** (THF–d$_8$, 500 MHz, [ppm]): δ = 3.22 (t, $^2J_{HH}$ = 6.42 Hz, 4 H, NCH_2), 1.94 (t, $^2J_{HH}$ = 6.39 Hz, 4 H, PCH_2), 1.32 (s, 36 H, 4x P(CMe_3)$_2$).
^{13}**C{^{1}H} NMR** (THF–d$_8$, 126 MHz, [ppm]): δ = 27.4 (AXY, N = $|^1J_{AX} + ^3J_{AY}|$ = 10.8 Hz, 2x PCH$_2$), 30.9 (AXY, N = $|^2J_{AX} + ^4J_{AY}|$ = 6.3 Hz, 4x P(CMe_3)$_2$), 38.5 (AXY, N = $|^1J_{AX} + ^3J_{AY}|$ = 11.5 Hz, 4x P(CMe$_3$)$_2$), 66.4 (AXY, N = $|^2J_{AX} + ^4J_{AY}|$ = 19.7 Hz, 2x NCH$_2$), 240 (t, ^2J = 3.6 Hz, 2x CO).
^{31}**P{^{1}H} NMR** (THF–d$_8$, 162 MHz, [ppm]): δ = 105.4 (s).
Elem. Anal. found (calc) for $C_{22}H_{44}NNaO_2P_2W$: C 42.35 (42.39), H 6.97 (7.11), N 2.21 (2.25).
IR (ATR-IR, cm^{-1}): $\tilde{\nu}$ = 1677 (C≡O), 1604 (C≡O).

3.4 Kinetic Analysis: Protonation of 1 with $[HNEt_3][BAr^F_{24}]$

3.4.1 Exemplary UVvis spectrum

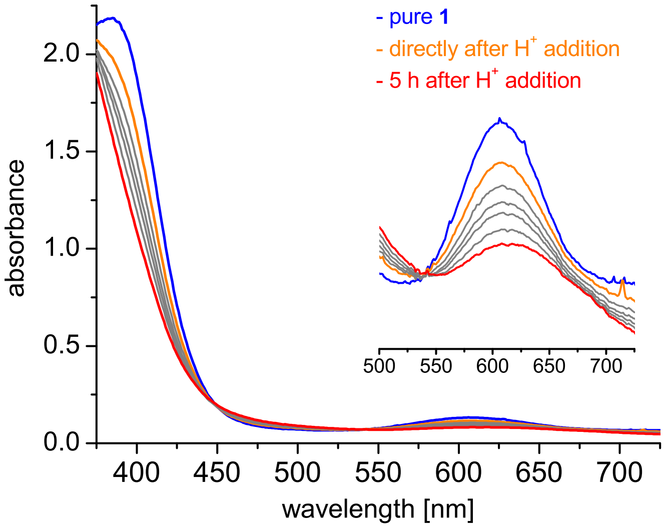

Figure 44: Exemplary UVvis spectrum of the protonation of **1** with $[HNEt_3][BAr^F_{24}]$. The blue trace represents the spectrum of pure **1**, the orange one the spectrum directly after addition of acid and the red one after 5 h reaction time.

3.4.2 Determination of equilibrium constant K_1

A solution of $[HNEt_3][BAr^F_{24}]$ in THF (0.25 mol·L^{-1}; 20, 30, 40, 50 µL, respectively) was added to a stirred solution of **1** in THF (2 mL, 0.25 mmol·L^{-1}) at 25 °C. The reaction was monitored by UVvis spectroscopy, measuring one spectrum every 3 sec.

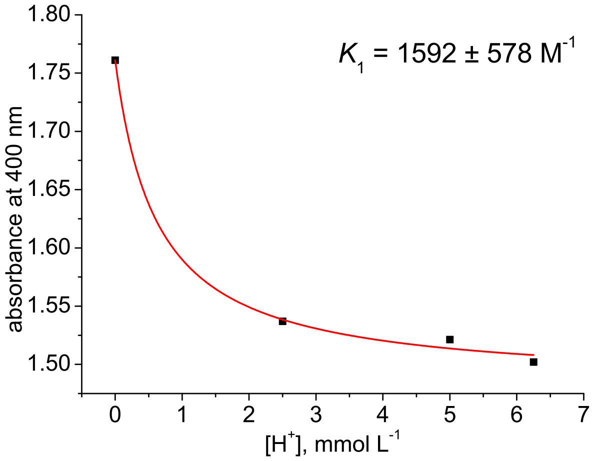

Figure 45: Plot of the absorbance at 400 nm vs. the concentration of $[HNEt_3][BAr^F_{24}]$ giving rise to the equilibrium constant K_1 = 1592±578 mol·L^{-1}.

3.4.3 Determination of rate constants k_2 and k_3

A solution of $[HNEt_3][BAr^F_{24}]$ (0.5, 5, 7.5, 10, 12.5 mmol·L^{-1}) in THF (1 mL) was added to a solution of **1** (0.5 mmol·L^{-1}) in THF (1 mL) at 25 °C. The reaction was stirred and monitored *via* UVvis spectroscopy for 5 h, measuring one spectrum every 4 min.

3.4.4 Determination of rate constant k_3 via initial rate method

The rate constant k_3 was determined *via* the initial rate method using an equimolar mixture of **1** and $[HNEt_3][BAr^F_{24}]$ (both 0.25 mmol·L^{-1}). It is assumed that under such conditions the reaction proceeds mainly *via* Path B (Scheme 59). The initial rate was determined from the spectral changes ascribed to the decrease in the concentration of **12** after the time needed for setting of the first equilibrium and calculated to be $v = 1.35 \cdot 10^{-9}$ mol·L^{-1}·s^{-1}. Taking the previously determined equilibrium constant K_1 into account, the concentration of **12** in the equilibrium was calculated to be $5.84 \cdot 10^{-5}$ mol·L^{-1} (with $K_1 = 1592$ mol·L^{-1} and c(**1**) = 0.25 mmol·L^{-1}). With $v = k_3 \cdot (c(\mathbf{12}))^2$, k_3 was calculated as $k_3 = 0.4$ L·mol^{-1}·s^{-1}.

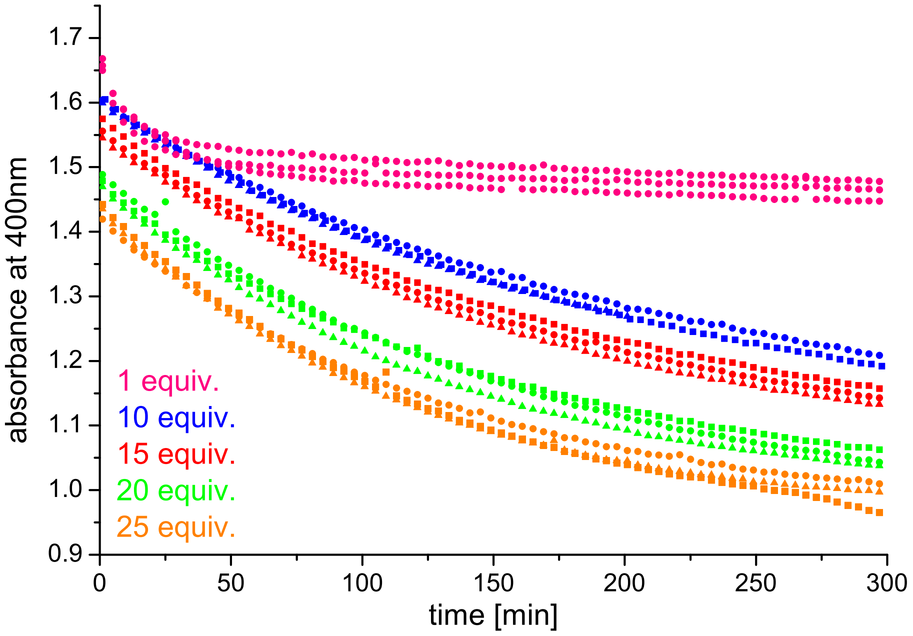

Figure 46: Absorbance at 607 nm vs time plot for different ratios of $[HNEt_3][BAr^F_{24}]$ to **1**.

3.5 Kinetic Analysis: N_2-cleavage of $[(N_2)\{W(CO)(PNP)\}_2]$(4)

3.5.1 Reaction Monitoring

A J-Young NMR tube containing 0.5 mL of a 3.75 mM stock solution of **4** in Tol–d_8 was put into a pre-heated NMR machine. The decay of **4** was monitored *via* ^{1}H NMR at different temperatures. Each temperature was repeated at least twice.

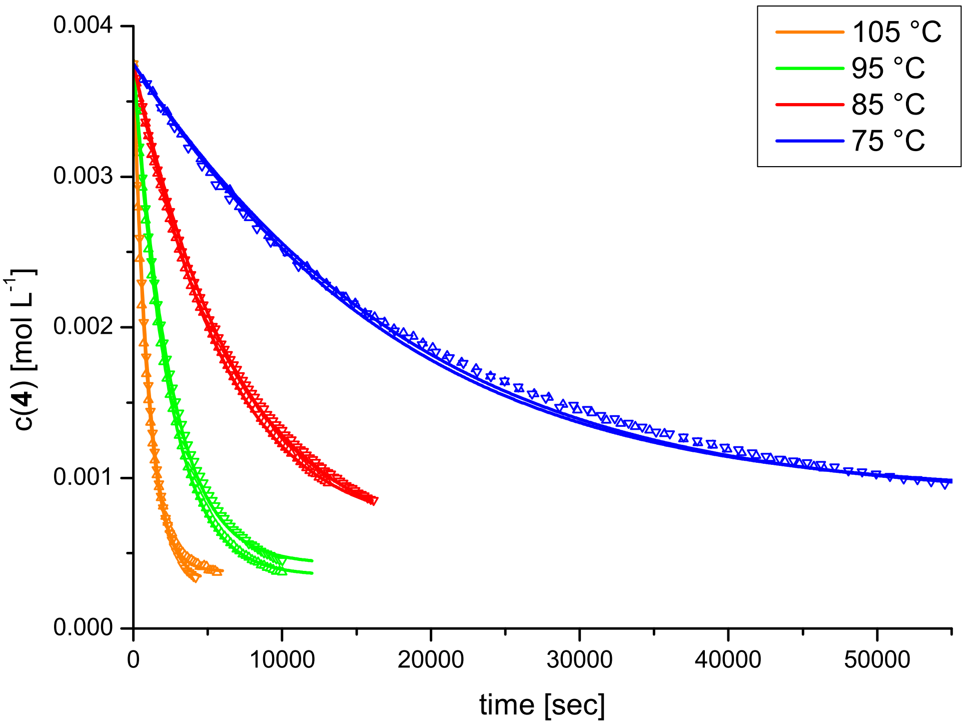

Figure 47: c(**4**) *vs.* time plot at different temperatures. The triangles represent the measured concentrations, while the black lines represent the fitting curve.

3.5.2 Kinetic Modelling

The derived curves were fitted using the COPASI 4.27 (Build 213) software[233] according to the model shown in Scheme 80. The derived rate constants k_1 and k_2 as well as the so obtained equilibrium constants K and free energies ΔG are given in Table 8.

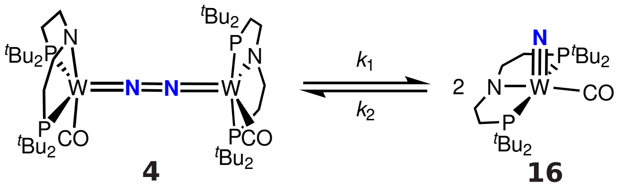

4 **16**

$$r = -\frac{[\mathbf{4}]}{\mathrm{d}t} = k_1[\mathbf{4}] - k_2[\mathbf{16}]^2$$

Scheme 80: The equilibrium of **4** and **16** and the resulting rate law for the decay of **4** used to fit the kinetic curves.

Table 8: The derived rate constants k_1 and k_2 and the so obtained equilibrium constants K and ΔG-values.

T [K]	k_1 [s^{-1}]	k_2 [$L\ mol^{-1}\ s^{-1}$]	K [$mol\ L^{-1}$]
348	$3.0\cdot10^{-5}$	$7.70\cdot10^{-4}$	0.039
	$3.2\cdot10^{-5}$	$8.63\cdot10^{-4}$	0.037
358	$1.0\cdot10^{-4}$	$16.4\cdot10^{-4}$	0.061
	$0.9\cdot10^{-4}$	$14.5\cdot10^{-4}$	0.062
368	$3.9\cdot10^{-4}$	$35.5\cdot10^{-4}$	0.110
	$3.8\cdot10^{-4}$	$36.9\cdot10^{-4}$	0.103
378	$9.8\cdot10^{-4}$	$82.0\cdot10^{-4}$	0.120
	$10.0\cdot10^{-4}$	$76.0\cdot10^{-4}$	0.132

3.5.3 *Eyring* Analysis

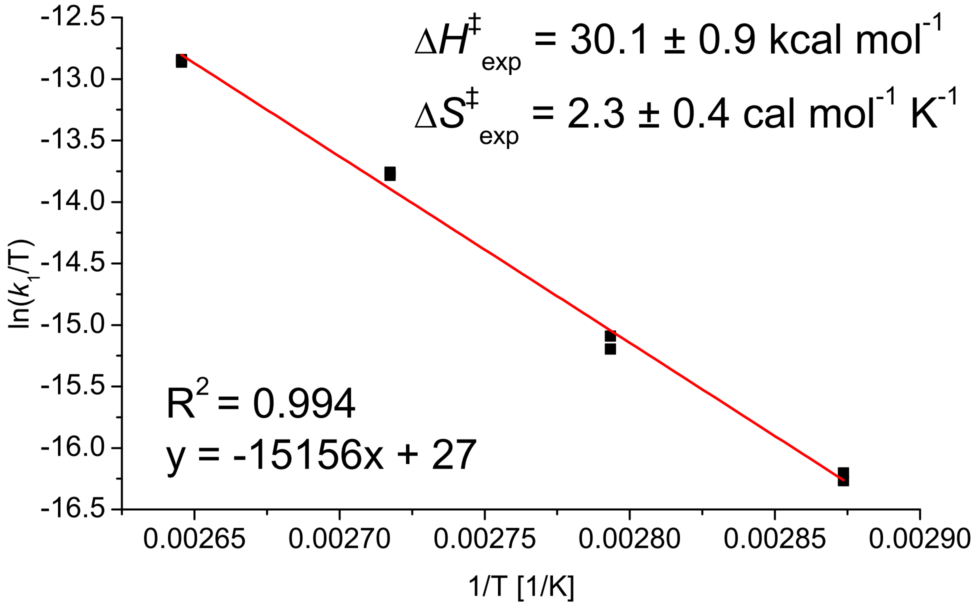

Figure 48: $\ln(k_1/T)$ vs. 1/T plot (*Eyring-plot*) for the thermal splitting of **4** into **16**.

3.5.4 *Van't Hoff* Analysis

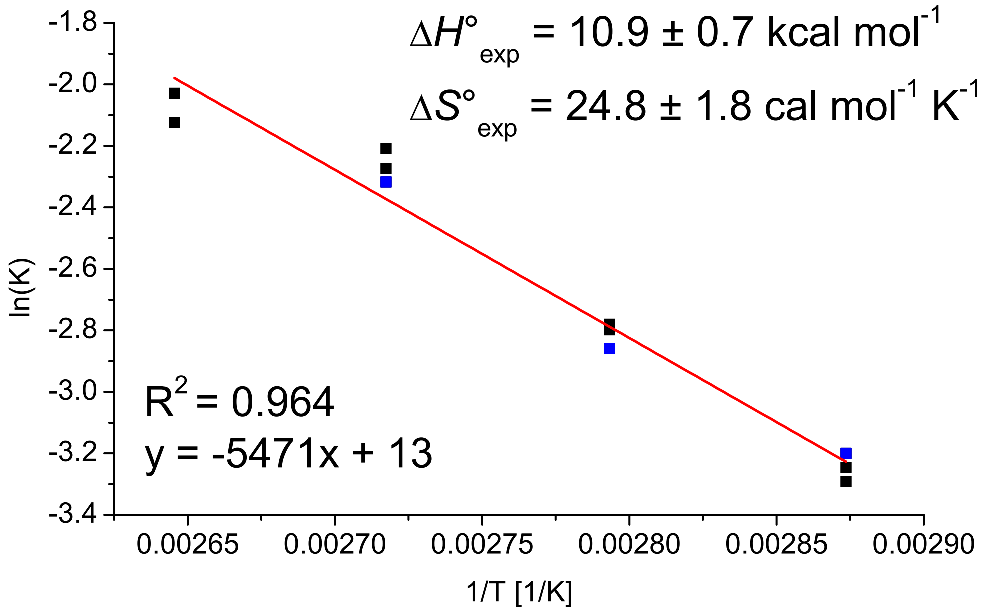

Figure 49: $\ln(K/T)$ vs. 1/T plot (*Van't Hoff-plot*) for the thermal splitting of **4** into **16**.

3.6 Transient spectroscopy

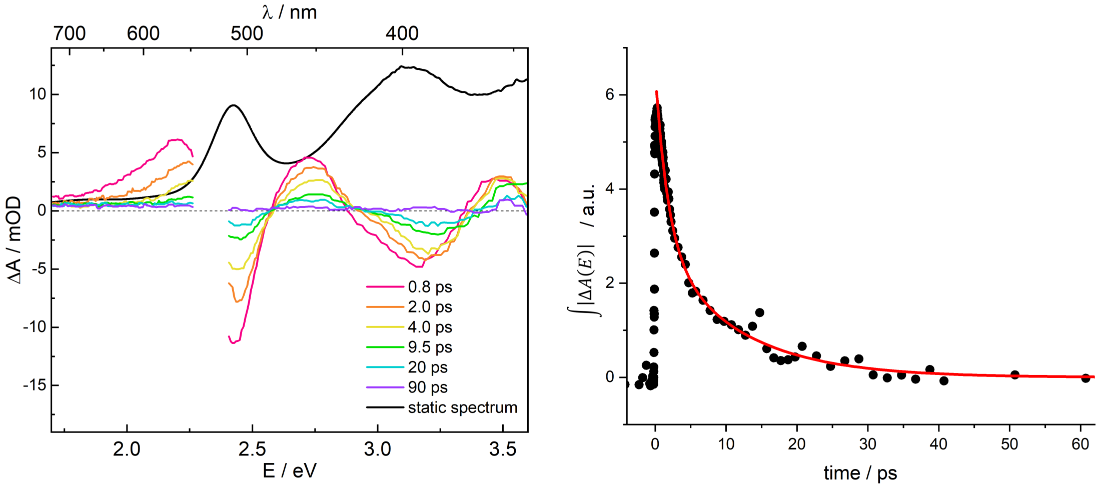

Figure 50: *left:* Transient UVvis difference spectra of **4** in THF at selected pump-probe delays (pump wavelength: 530 nm). The black line shows the scaled linear absorption spectrum. *right:* Time-dependence of the integrated absolute absorption changes (red line is a bi-exponential fit with $\tau_1 = 1.8$ ps and $\tau_2 = 11.1$ ps).

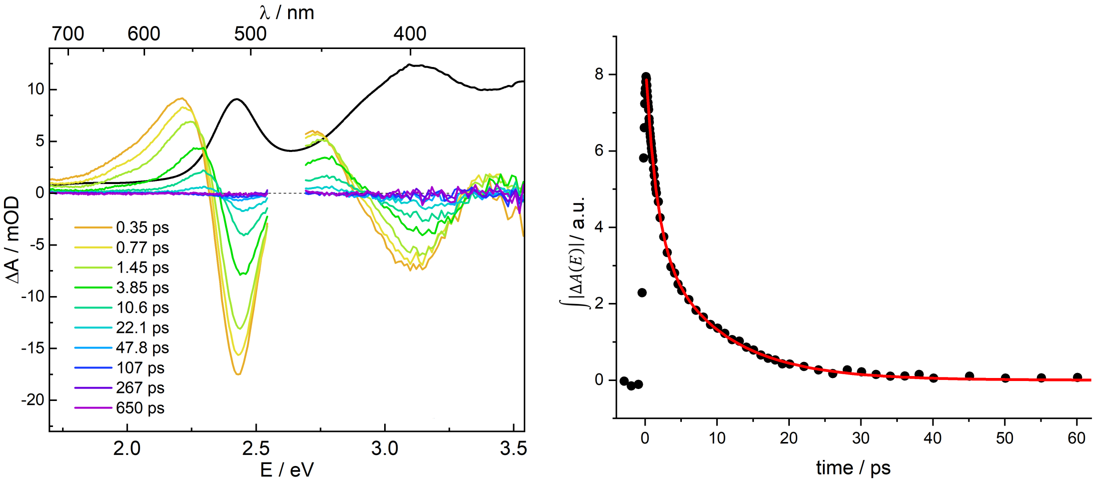

Figure 51: *left:* Transient UVvis difference spectra of **4** in THF at selected pump-probe delays (pump wavelength: 475 nm). The black line shows the scaled linear absorption spectrum. *right:* Time-dependence of the integrated absolute absorption changes (red line is a bi-exponential fit with $\tau_1 = 1.5$ ps and $\tau_2 = 9.2$ ps).

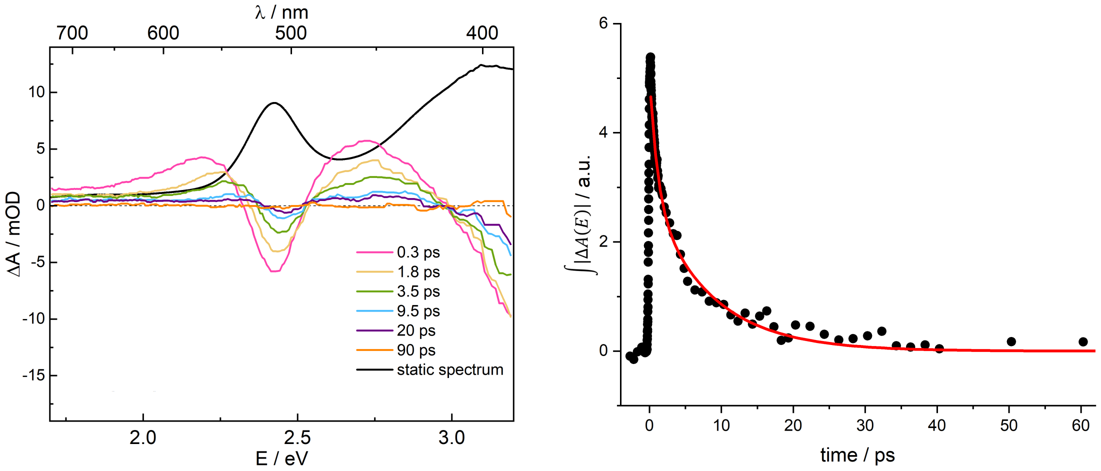

Figure 52: *left:* Transient UVvis difference spectra of **4** in THF at selected pump-probe delays (pump wavelength: 380 nm). The black line shows the scaled linear absorption spectrum. *right:* Time-dependence of the integrated absolute absorption changes (red line is a bi-exponential fit with $\tau_1 = 1.1$ ps and $\tau_2 = 8.3$ ps).

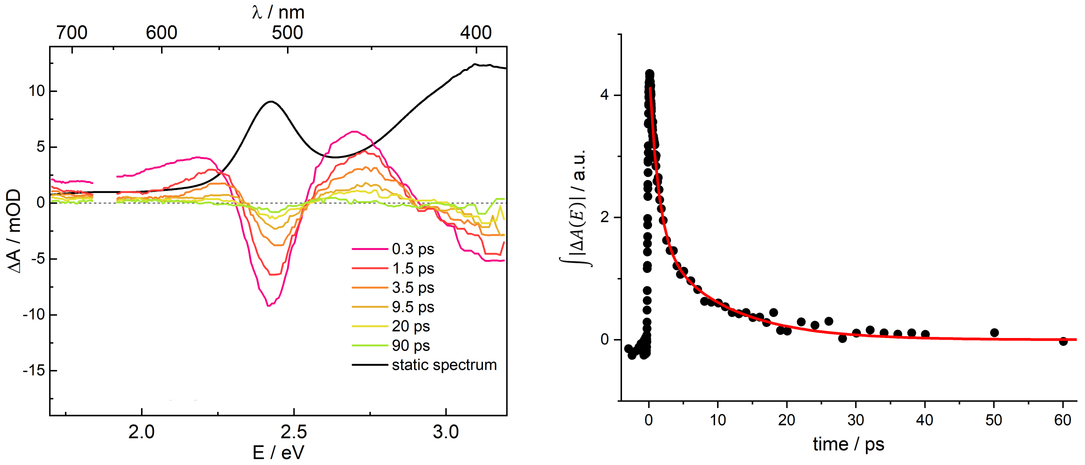

Figure 53: *left:* Transient UVvis difference spectra of **4** in THF at selected pump-probe delays (pump wavelength: 330 nm). The black line shows the scaled linear absorption spectrum. *right:* Time-dependence of the integrated absolute absorption changes (red line is a bi-exponential fit with $\tau_1 = 1.3$ ps and $\tau_2 = 9.9$ ps).

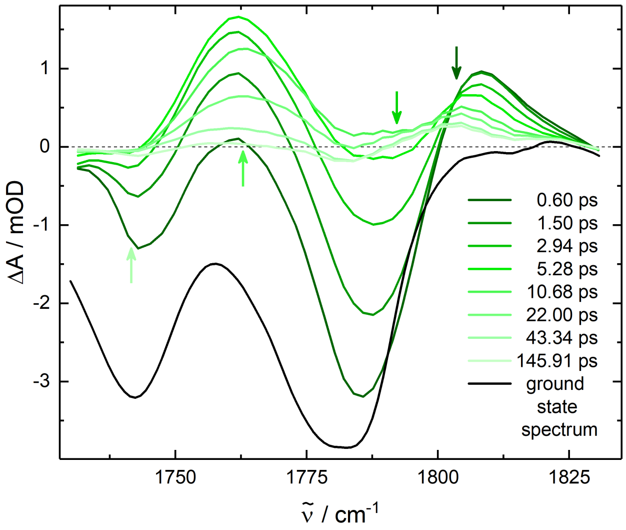

Figure 54: Transient IR difference spectra of **4** in THF at selected pump-probe delays (pump wavelength: 400 nm).

4 List of compounds

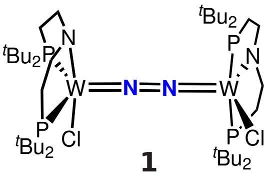

1

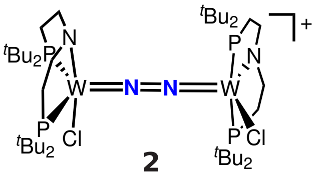

2

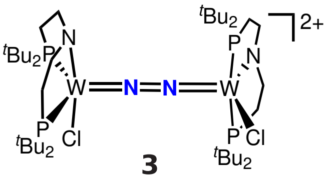

3

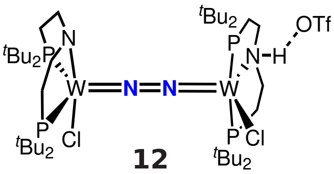

12

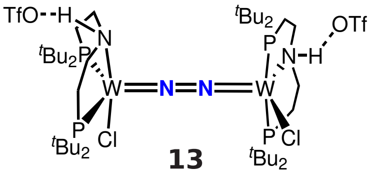

13

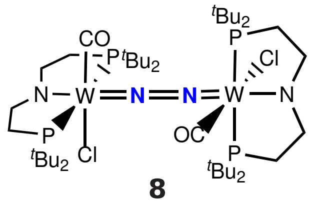

8

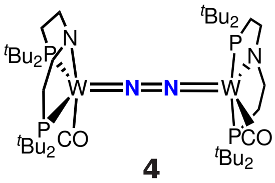

4

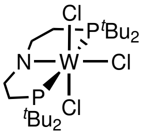

5

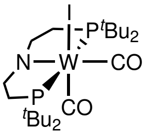

18

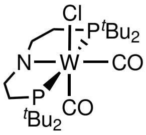

10

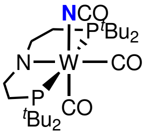

21

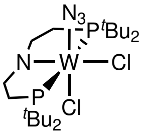

19

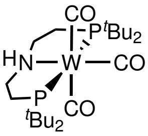

9

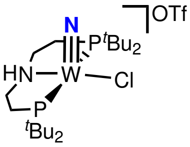

11

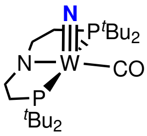

16

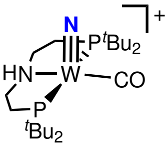

20

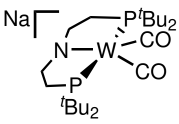

24

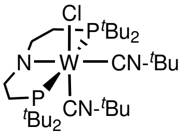

6

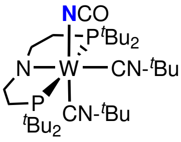

22

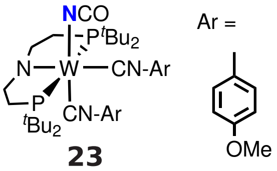

23

5 List of abbreviations

r.t.	Room Temperature
BDE	Bond dissoziation energy
BDFE	Bond dissoziation free energy
equiv.	Equivalents
FMO	Frontier Molecular Orbitals
HER	Hydrogen Evolution Reaction
NRR	Nitrogen Reduction Reaction
HOMO	Highest Occupied Molecule Orbital
LUMO	Lowest Unoccupied Molecule Orbital
MO	Molecular Orbital
PCET	Proton Coupled Electron Transfer
SOMO	Single Occupied Molecule Orbital

15-cr-5	15-crown-5 (1,4,7,10,13-Pentaoxacyclopentadecane)
$[\mathrm{BAr}^{\mathrm{F}}_{24}]^-$	Tetrakis(3,5-bis(trifluoromethyl)phenyl)borate
[Fc]	Ferrocen
*H*PNP	bis(2-(di-*tert*-butylphosphanyl)ethyl)amin, $H\mathrm{N}(\mathrm{CH_2CH_2P}^t\mathrm{Bu_2})_2$
^{i}Pr	*iso*-Propyl
LutH	2.6-lutidinum, $2.6\text{-}\mathrm{Me_2\text{-}C_5H_3NH^+}$
Np	Neopentyl
$[\mathrm{PPN}]^+$	μ-nitrido-bis(triphenylphosphan), $[(\mathrm{Ph_3P})_2\mathrm{N}]^+$
^{t}Bu	*tert*-Butyl
$\mathrm{Tren}^{\mathrm{TIPS}}$	$\mathrm{N(CH_2CH_2NSi^iPr_3)_3}$
NMR	Nuclear Magnetic Resonance
COSY	Correlation Spectroscopy
HMBC	Heteronuclear Multiple Bond Correlation
HSQC	Heteronuclear Single Quantum Coherence
s	Singulett
d	Duplett
t	Triplett
q	Quartett
qu	Quintett
sex	Sextett
hpt	Heptett
m	Multiplett
br	broad

CV	Cyclic Voltammetry
CE	Counter Electrode
RE	Reference Electrode
WE	Working Electrode

EPR	Electron Paramagnetic Resonance
HFI	Hyperfine Interaction
MS	Massenspectrometry
ESI	Electrospray Ionisation
LIFDI	Liquid Field Desorption Ionisation
UVvis	Ultraviolett / visibile
SQUID	Superconducting Quantum Interference Device
TIP	Temperature Independent Paramagnetism
PI	Paramagnetic Impurity

IC	Internal Conversion
ISC	Inter System Crossing
IVR	Intramolecular vibrational redistribution
LMCT	Ligand to Metal Charge Transfer
LLCT	Ligand to Ligand Charge Transfer
MLCT	Metal to Ligand Charge Transfer
MMCT	Metal to Metal Charge Transfer
VC	Vibrational Cooling

6 Appendix°

6.1 Spectroscopic Results

6.1.1 [WCl_3(PNP)] (5)

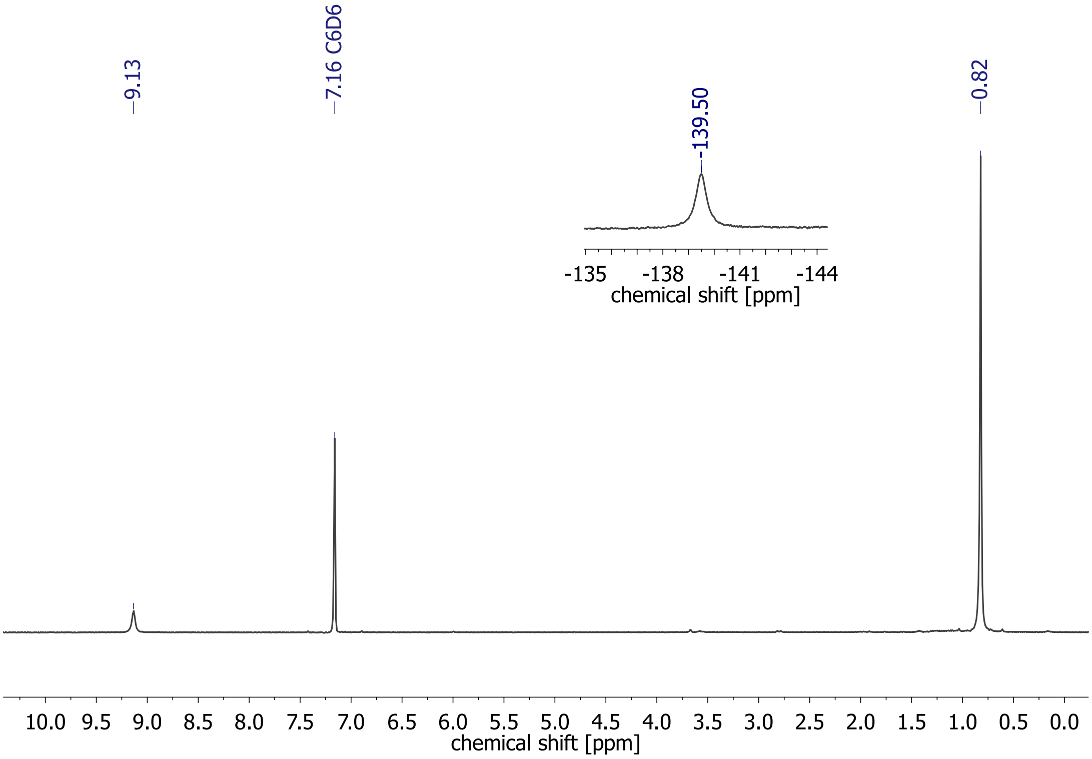

Figure 55: ^1H NMR Spectrum of **5** in C_6D_6 at r.t.

° Parts of this work have been published in:
-"Selectivity of tungsten mediated dinitrogen splitting *vs.* proton reduction", B. Schluschaß, J. Abbenseth, S. Demeshko, M. Finger, A. Franke, C. Herwig, C. Würtele, I. Ivanovic-Burmazovic, C. Limberg, J. Telser, S. Schneider, *Chemical Science*, **2019**, *10*, 10275-10282.
-N.A. Maciulis "Exploring redox properties of bis(tetrazinyl)pyridine (btzp) complexes of group VI metals, tetrazine and phosphine assisted reduction of H_2O, and dinitrogen cleavage and functionalization" *Ph.D. Thesis*, Indiana University Bloomington, **2019**.
-P.-M. Padonou "Reaktivität dimerer N_2-verbrückter Wolfram-PNP-Pinzetten Komplexe" *Bachelor Thesis*, Georg-August-Universität Göttingen, **2018**.
-J. Schneider "Synthese und Funktionalisierung von Wolfram-PNP-Nitrid Komplexen" *Bachelor Thesis*, Georg-August Universität Göttingen, **2019**.

6.1.2 $[(N_2)\{WCl(PNP)\}_2]$(1)

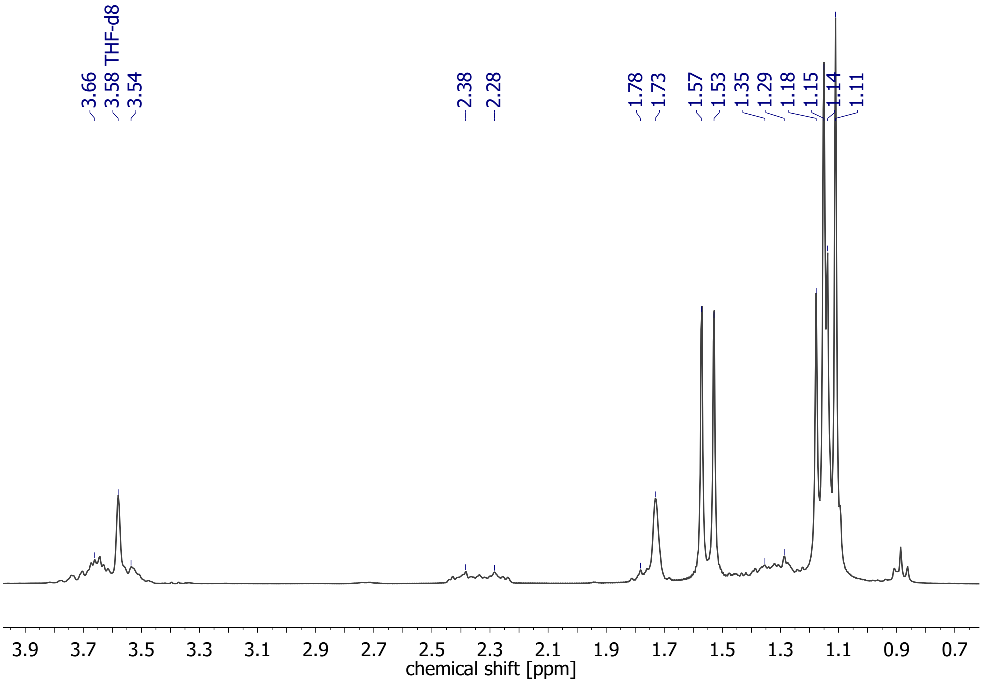

Figure 56: ^{1}H NMR Spectrum of **1** in THF—d_8 at r.t.

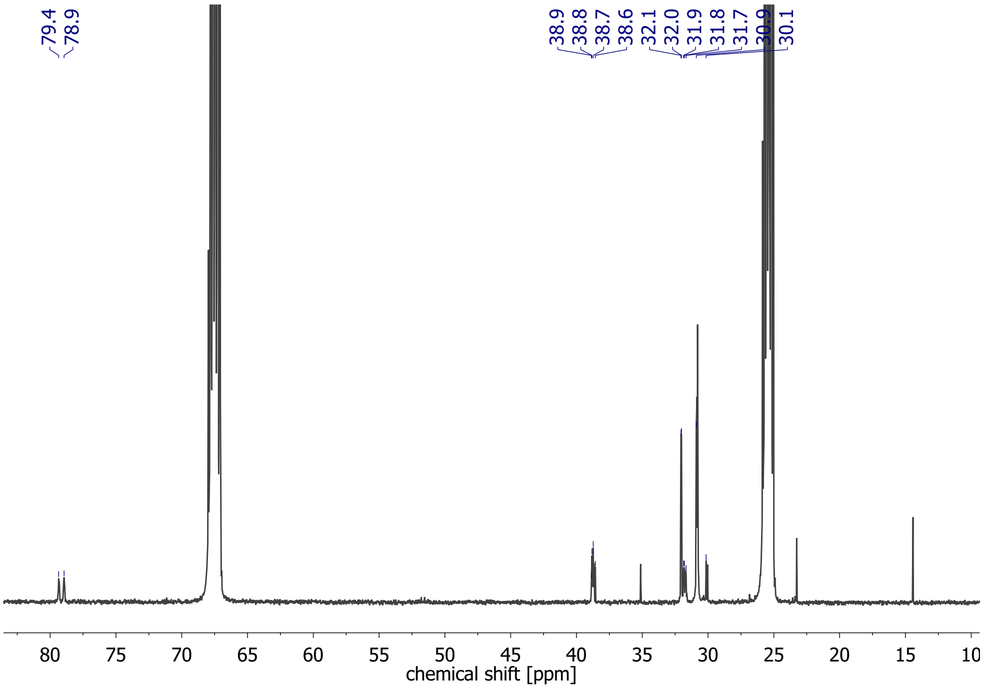

Figure 57: $^{13}C\{^1H\}$ NMR Spectrum of **1** in THF—d_8 at r.t.

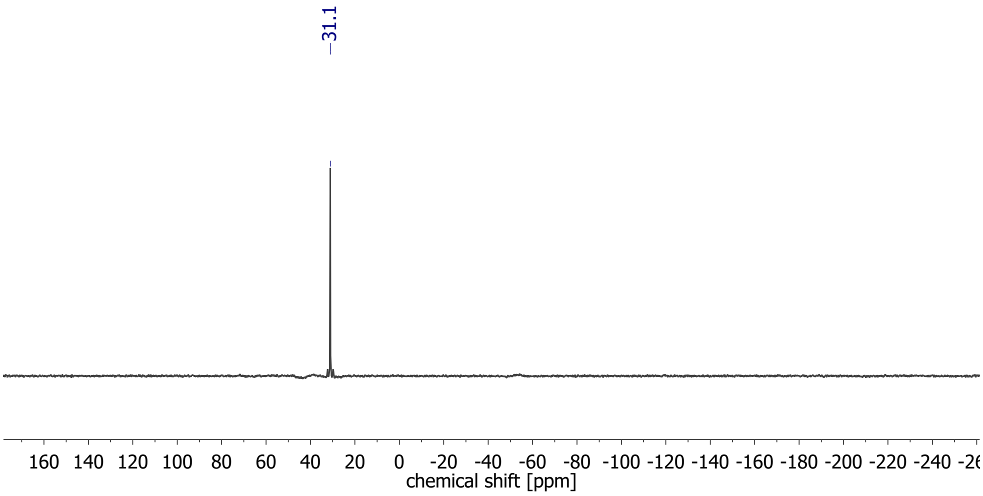

Figure 58: $^{15}N\{^1H\}$ NMR Spectrum of ^{15}N-**1** in THF—d_8 at r.t.

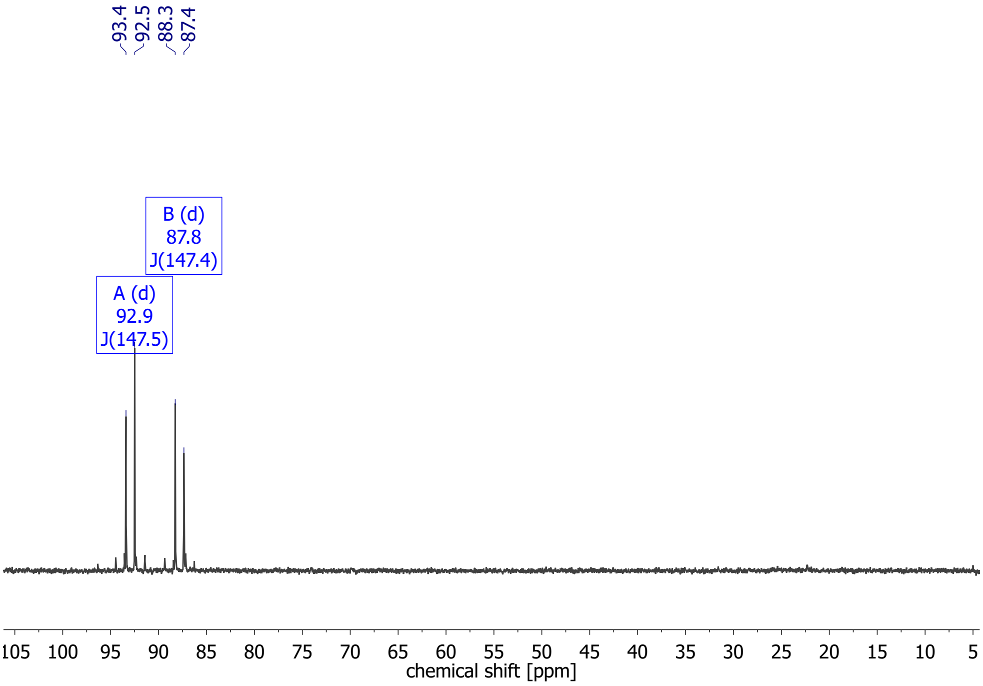

Figure 59: $^{31}P\{^1H\}$ NMR Spectrum of **1** in THF—d_8 at r.t.

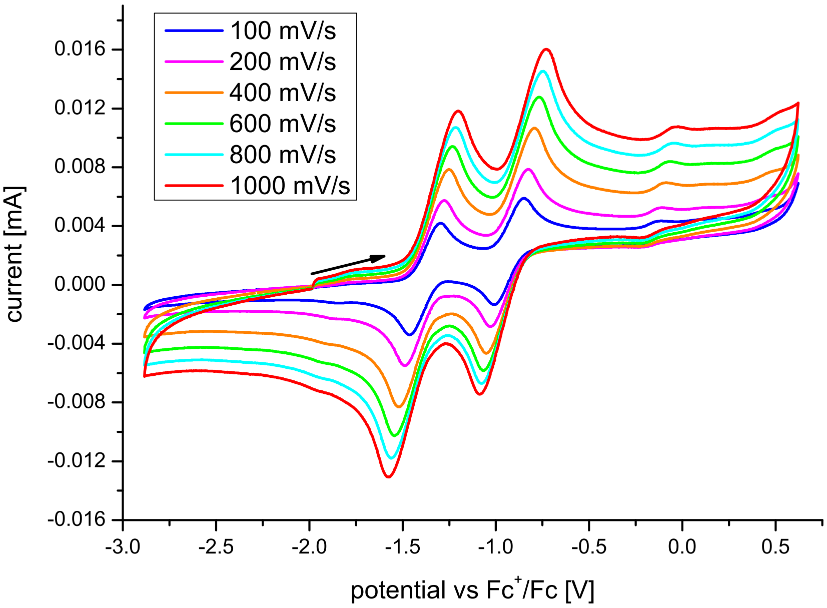

Figure 60: CV of **1** in 0.1 M solution of [^{n}Bu$_4$N][PF$_6$] in THF (WE = GC, RE = Ag/Ag$^+$, CE = Pt) at different scan rates.

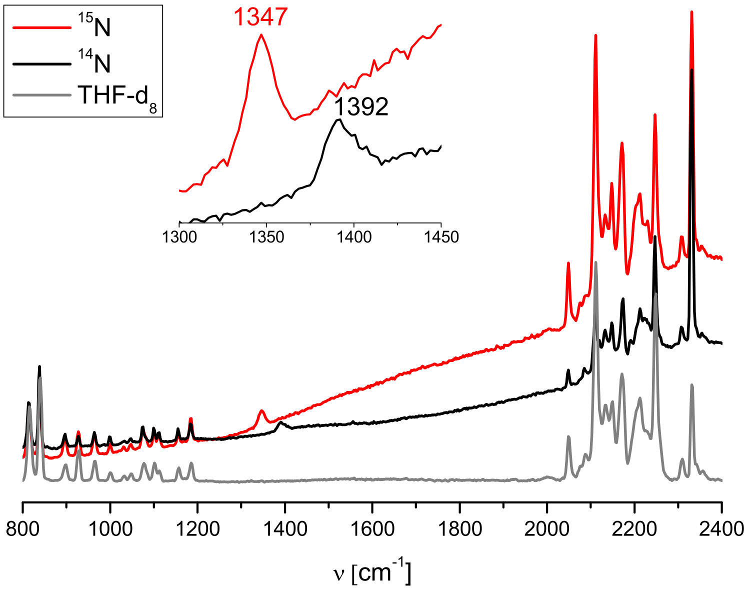

Figure 61: rRaman Spectrum (457 nm) of ^{14}N/^{15}N-**1** in frozen THF—d$_8$.

6.1.3 $[(N_2)\{WCl(PNP)\}_2]^+$(2)

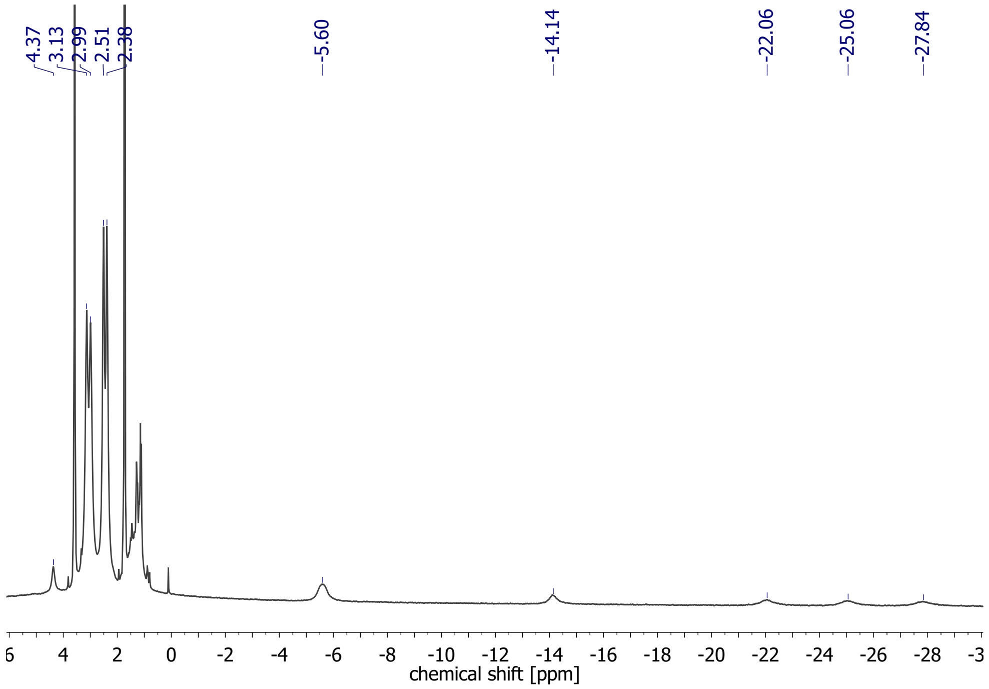

Figure 62: ^{1}H NMR Spectrum of **2**-[BPh$_4$] in THF—d$_8$ at r.t.

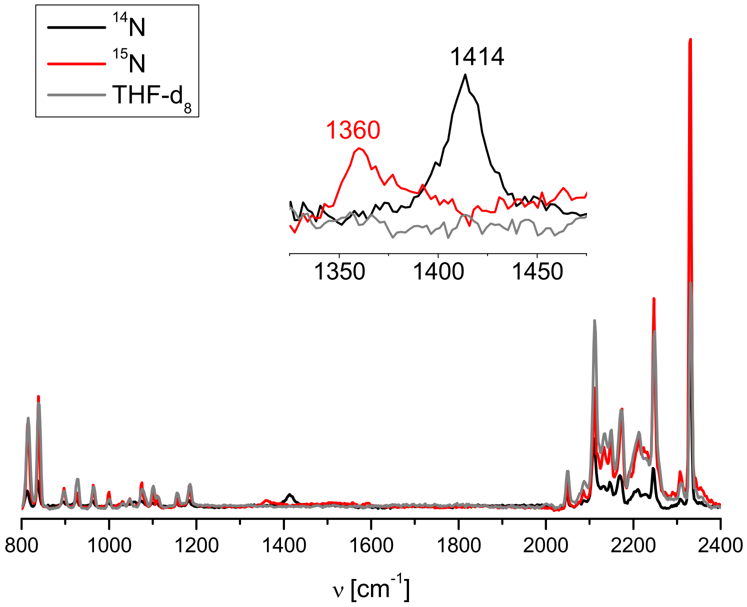

Figure 63: rRaman Spectrum (457 nm) of ^{14}N/^{15}N-**2**-[BPh$_4$] in frozen THF—d$_8$.

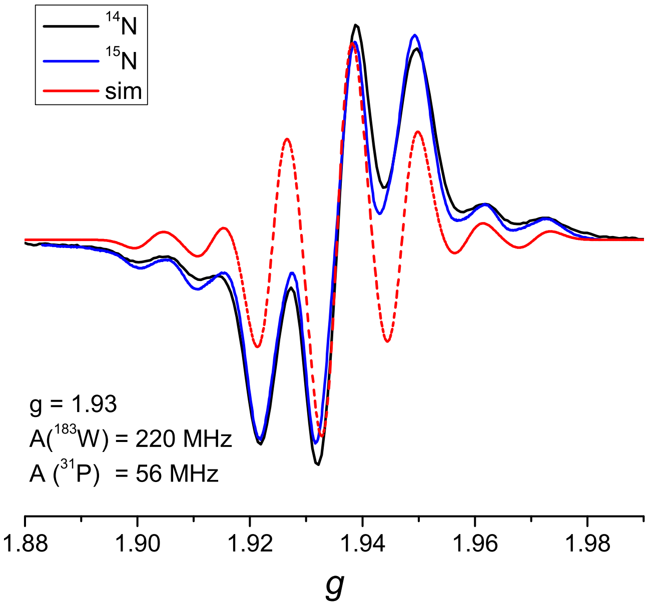

Figure 64: Comparison of the EPR-Spectra of ^{14}N/^{15}N-**2**, both in THF at r.t.

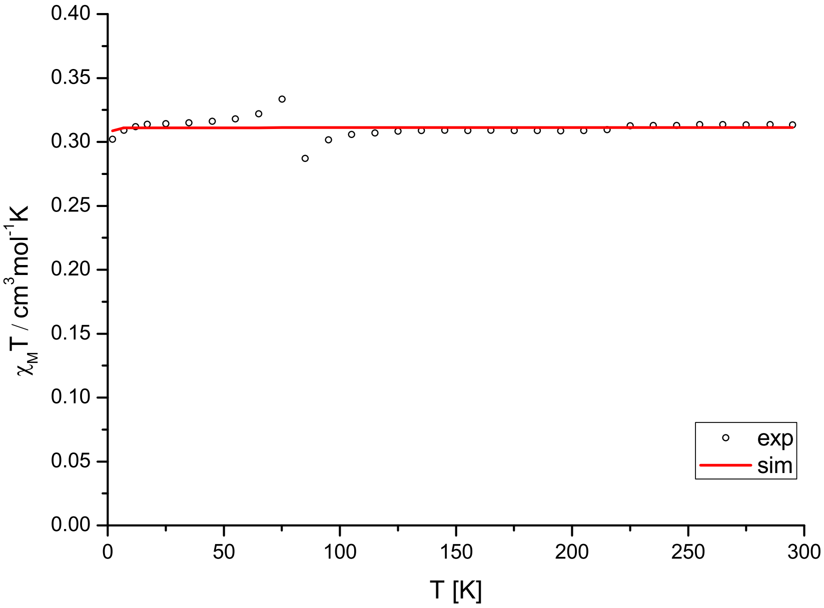

Figure 65: χ_MT vs. T plot for **2**-[BAr$^F_{24}$]. The open circles are the observed susceptibility, the red solid line corresponds to the best fit with the parameters g = 1.82 and TIP = $120 \cdot 10^{-6}$ cm^{3}mol^{-1} (TIP: temperature independent paramagnetism).

6.1.4 [(N$_2$){WCl(PNP)}$_2$]$^{2+}$ (3)

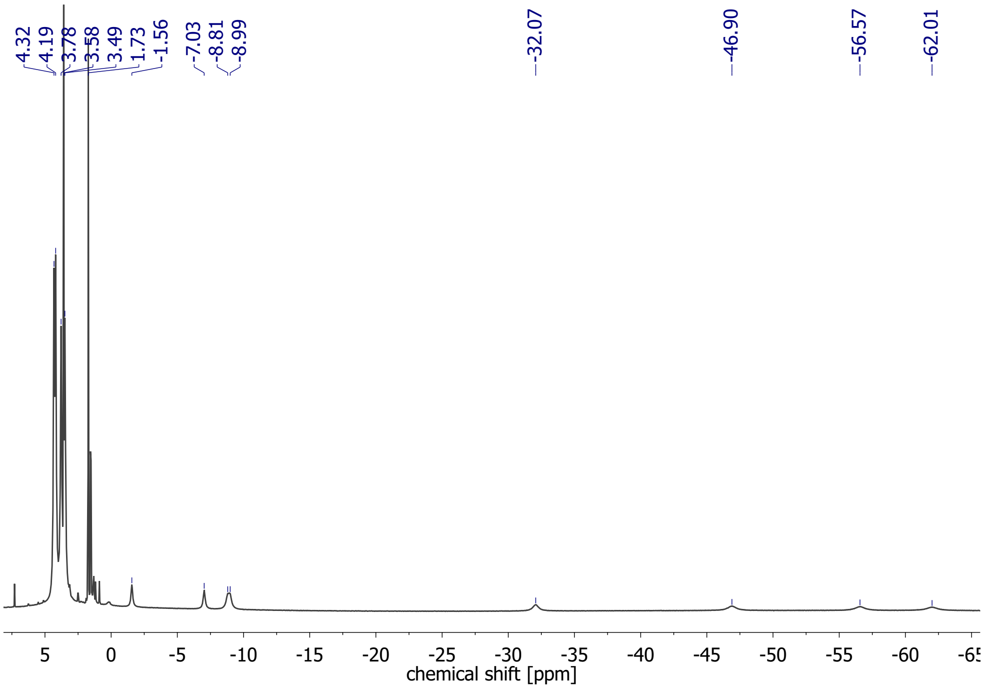

Figure 66: ^{1}H NMR Spectrum of **3**-[Al(OC(CF$_3$)$_3$)$_4$]$_2$ in THF—d$_8$ at r.t.

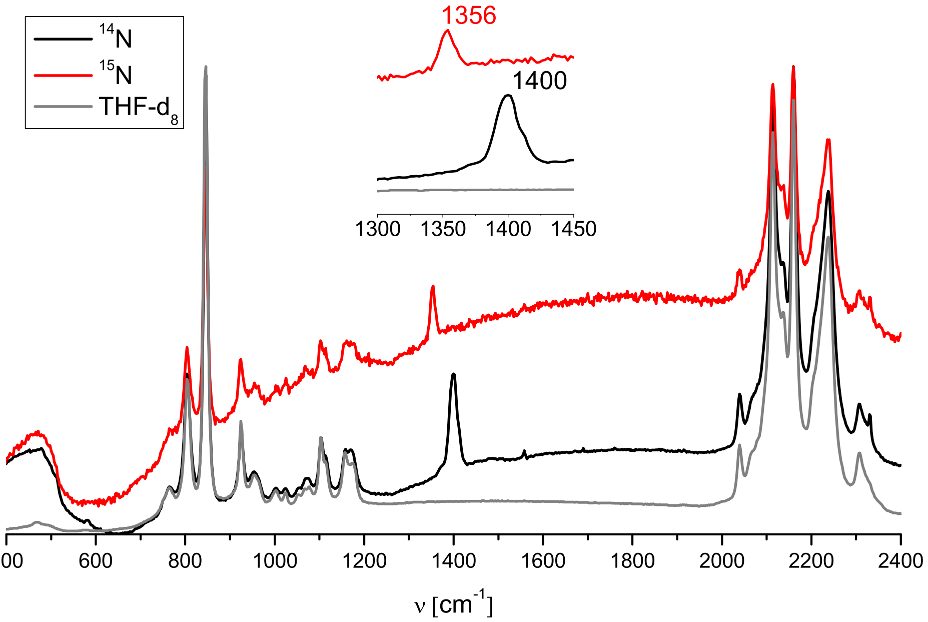

Figure 67: rRaman Spectrum (514.5 nm) of ^{14}N/^{15}N-**3**-[Al(OC(CF$_3$)$_3$)$_4$]$_2$ in THF—d$_8$ at -100 °C.

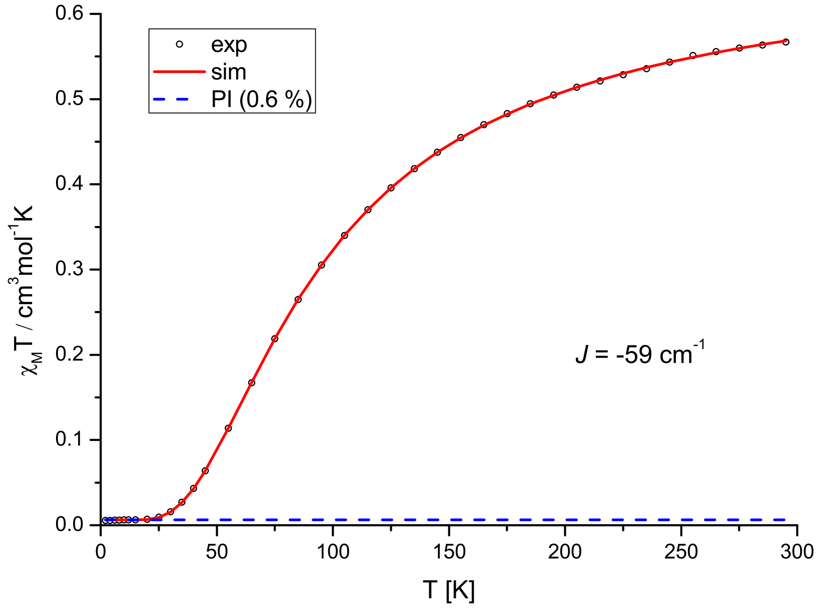

Figure 68: $\chi_M T$ vs. T plot for **2**-[Al(OC(CF_3)$_3$)$_4$]$_2$. The open circles are the observed susceptibility, the red solid line corresponds to the best fit with the parameters $g = 1.90$, $J = -59\ cm^{-1}$, $TIP = 230 \cdot 10^{-6}\ cm^3 mol^{-1}$ and $PI = 0.6\%$ ($S = 1$, the blue broken line, PI: paramagnetic impurity).

6.1.5 [W(N)Cl(^{H}PNP)]$^+$ (11)

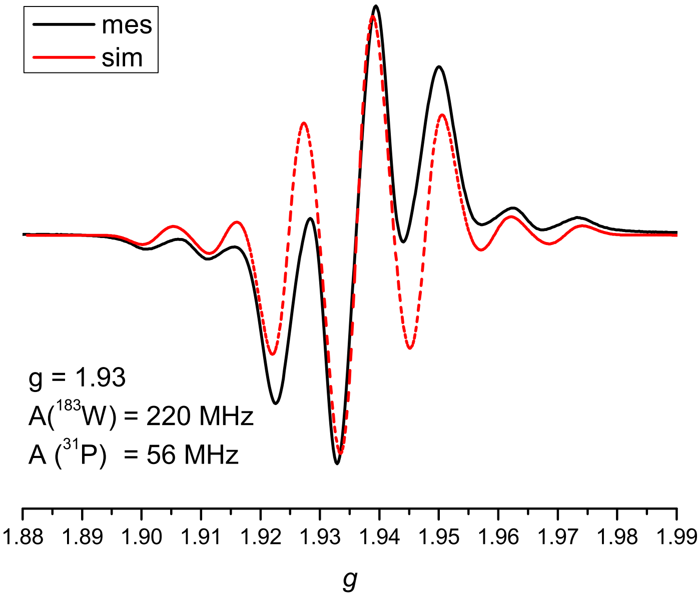

Figure 69: EPR-Spectrum of **11** in THF at r.t.

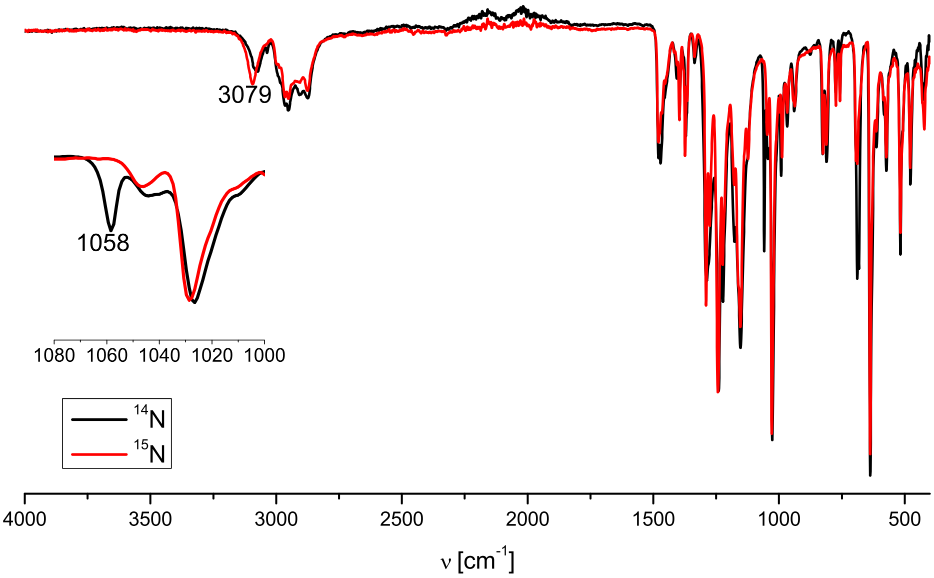

Figure 70: ATR-IR-Spectrum ^{14}N/^{15}N-**11**.

6.1.6 *in situ* [(^{H}PNP)ClW-(N$_2$)-WCl(PNP)]$^+$ (12)

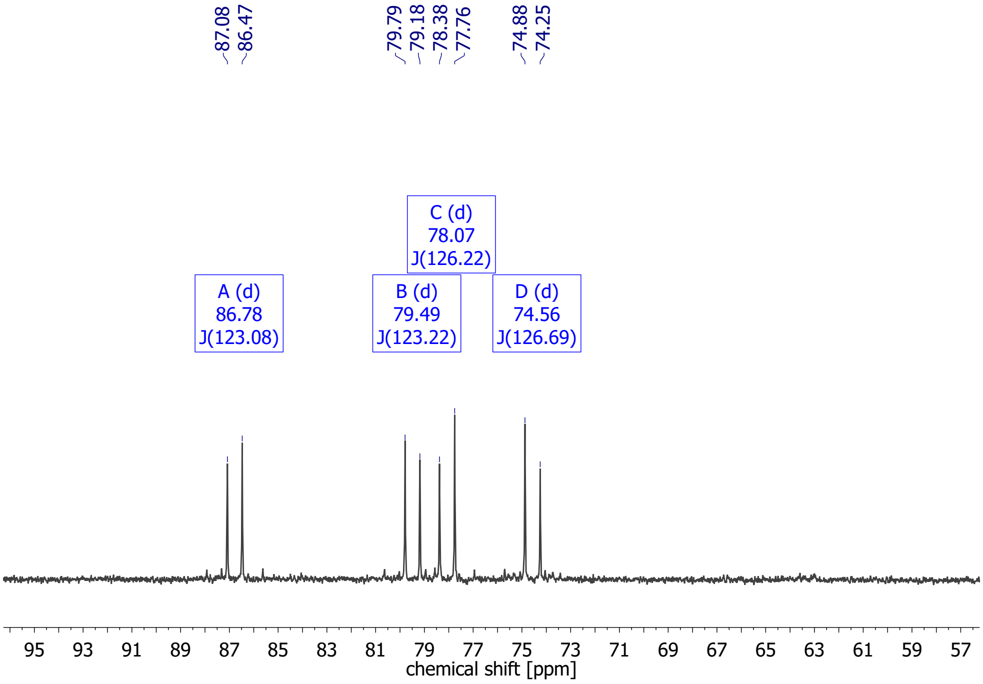

Figure 71: $^{31}P\{^{1}H\}$ NMR Spectrum of **12**-OTf in THF—d$_8$ at -35 °C.

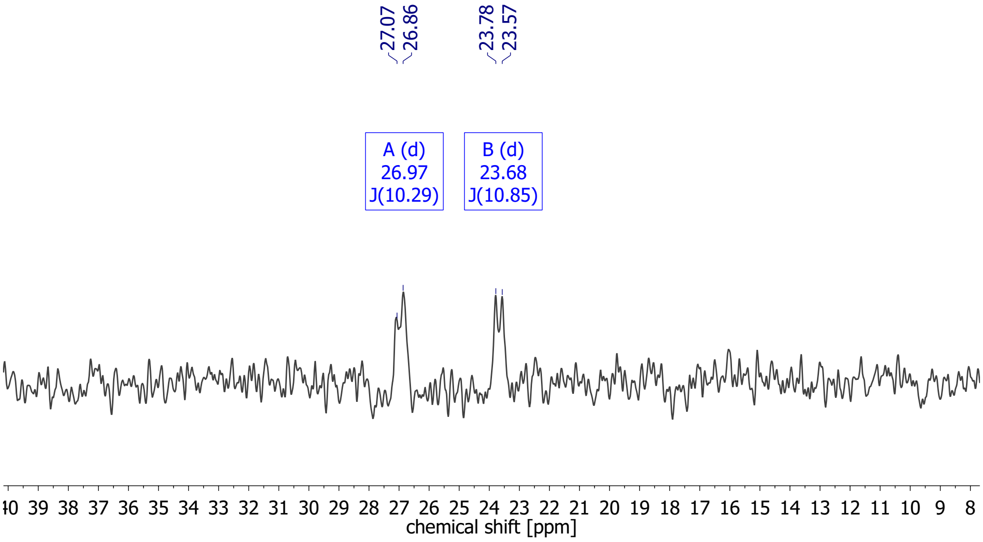

Figure 72: $^{15}N\{^{1}H\}$ NMR Spectrum of ^{15}N-**12**-OTf in THF—d$_8$ at -35 °C.

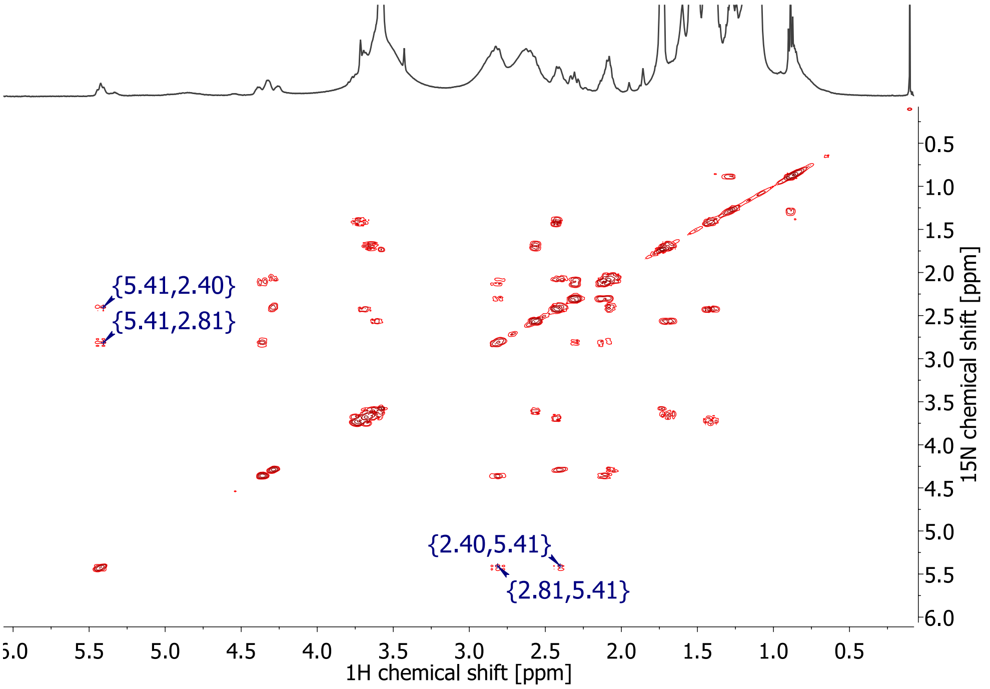

Figure 73: ^{1}H COSY NMR Spectrum of **12**-OTf in THF—d_8 at -35 °C.

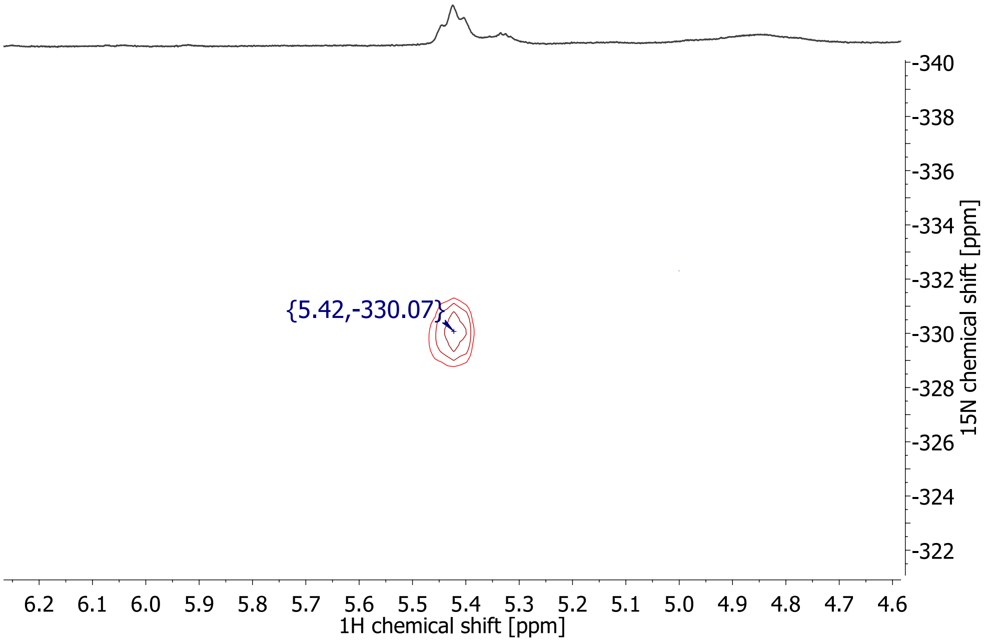

Figure 74: ^{1}H -^{15}N HSQC NMR Spectrum of **12**-OTf in THF—d_8 at -35 °C.

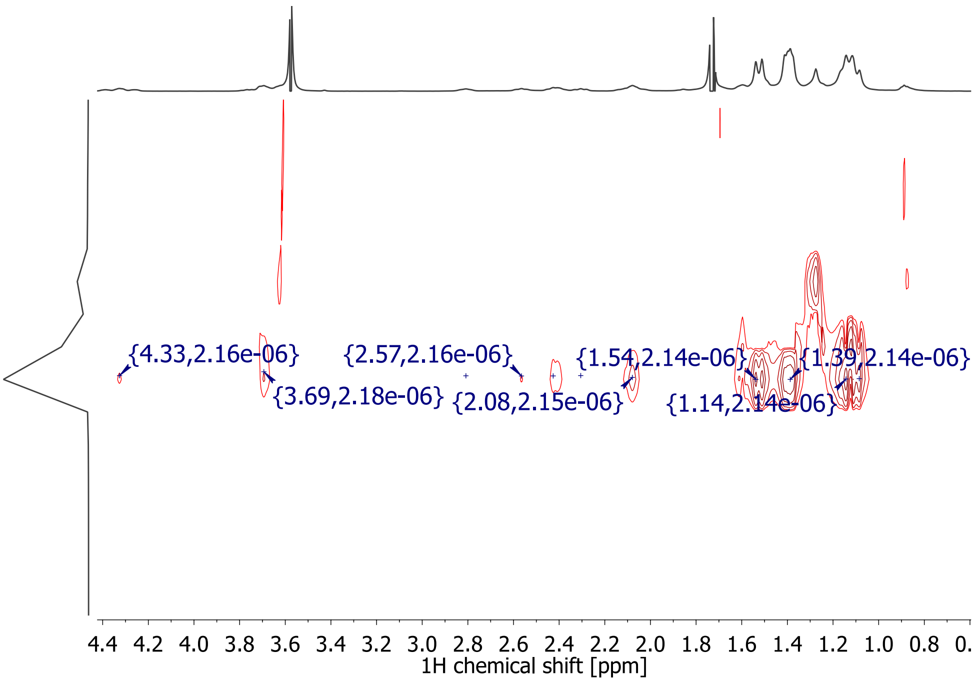

Figure 75: ^{1}H -DOSY NMR Spectrum of **12**-OTf in THF—d_8 at -35 °C.

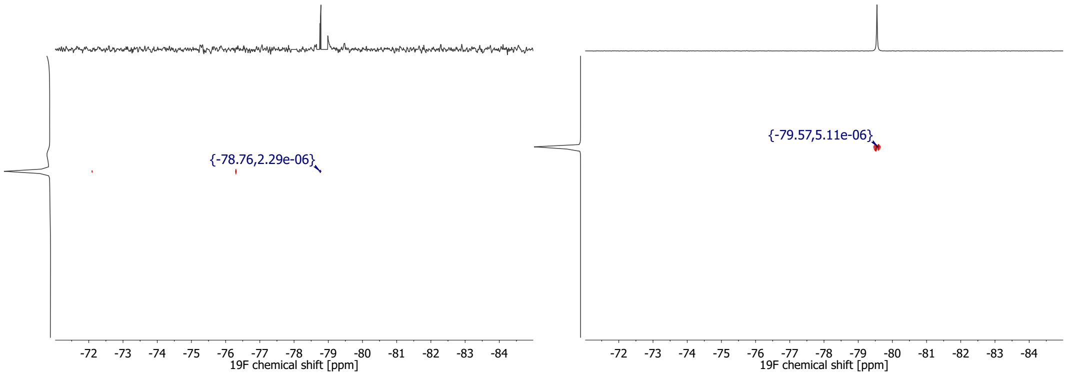

12-OTf

HOTf

Figure 76: *left*: ^{19}F{^{1}H} -DOSY NMR Spectrum of **12**-OTf, *right*: ^{19}F{^{1}H} -DOSY NMR Spectrum of HOTf; both in THF—d_8 at -35 °C.

6.1.7 *in situ* [{(^{H}PNP)ClW}(μ–N$_2$)]$^{2+}$ (13)

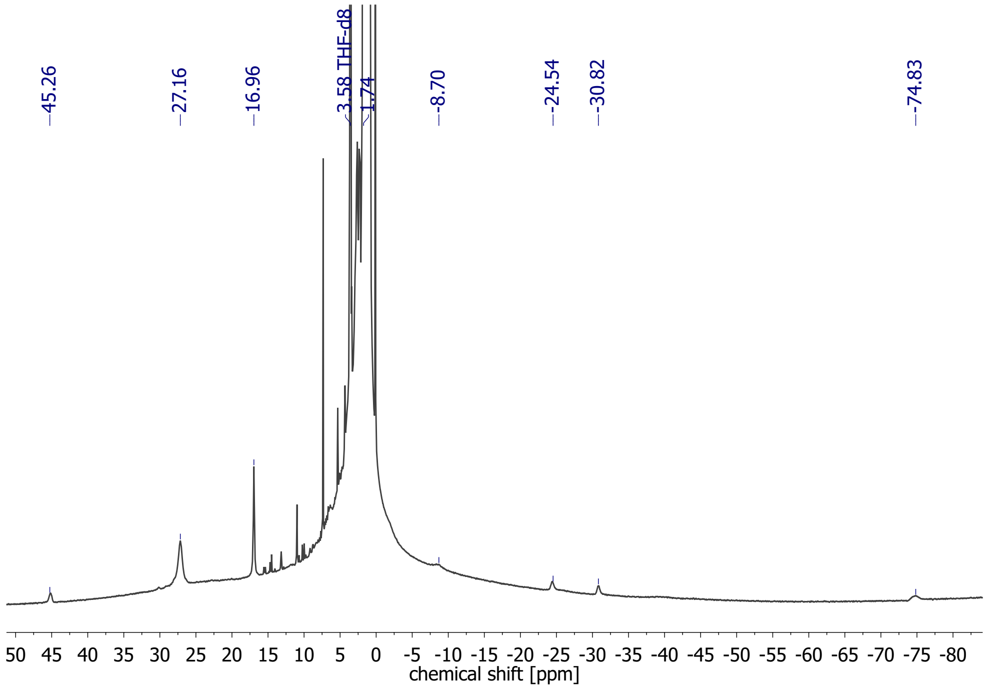

Figure 77: ^{1}H NMR Spectrum of **13**-(OTf)$_2$ in THF–d$_8$ at -65 °C.

6.1.8 [(N_2){WCl(CO)(PNP)}$_2$](8)

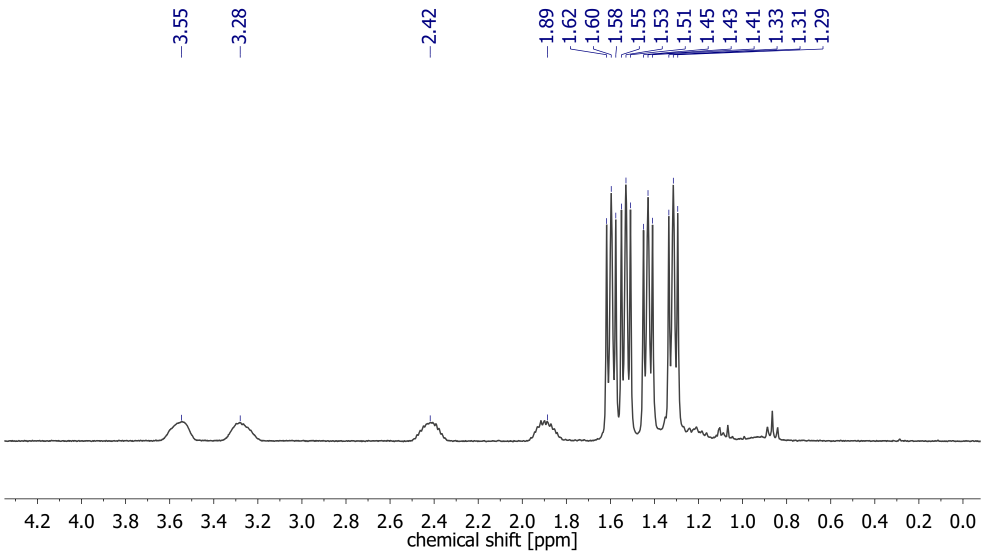

Figure 78: ^{1}H NMR Spectrum of **8** in C_6D_6 at r.t.

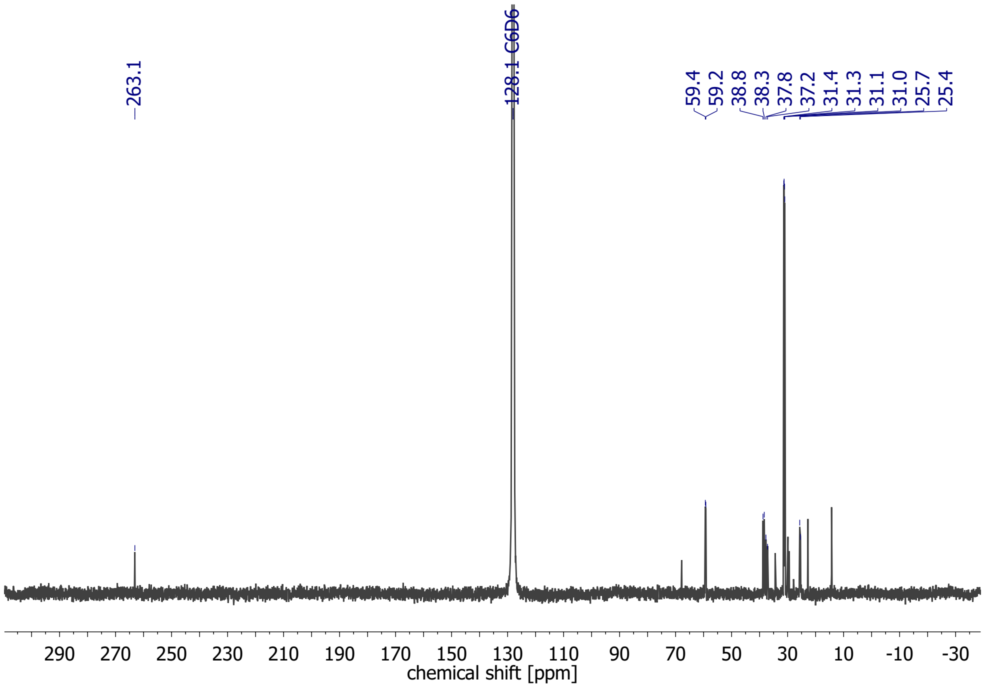

Figure 79: ^{13}C{^{1}H} NMR Spectrum of **8** in C_6D_6 at r.t.

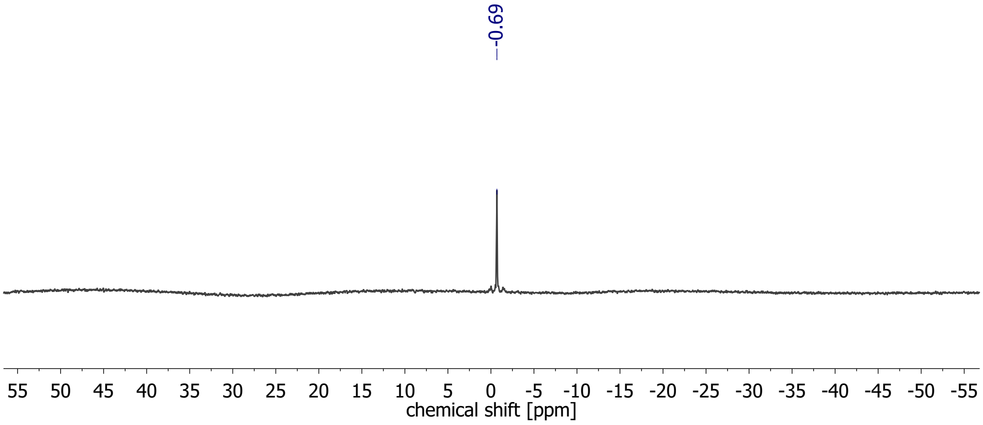

Figure 80: $^{15}N\{^{1}H\}$ NMR Spectrum of **8** in C_6D_6 at r.t.

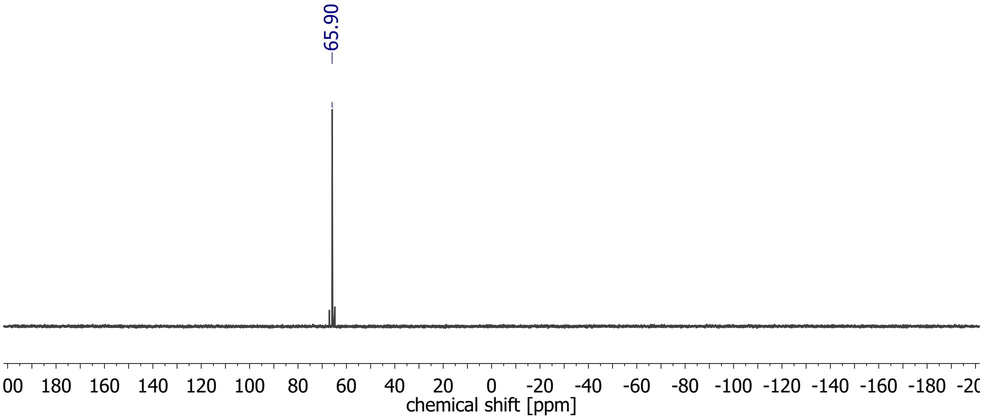

Figure 81: $^{31}P\{^{1}H\}$ NMR Spectrum of **8** in C_6D_6 at r.t.

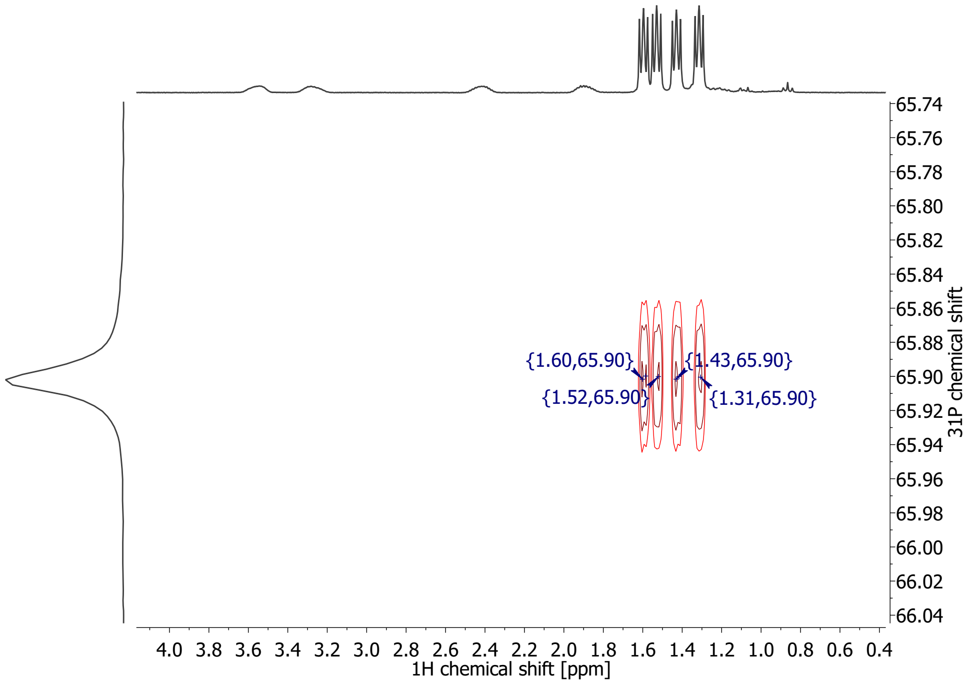

Figure 82: ^{1}H-^{31}P-HMBC NMR Spectrum of **8** in C_6D_6 at r.t. showing a cross-peak for all four ^{t}Bu-groups to only one ^{31}P-signal.

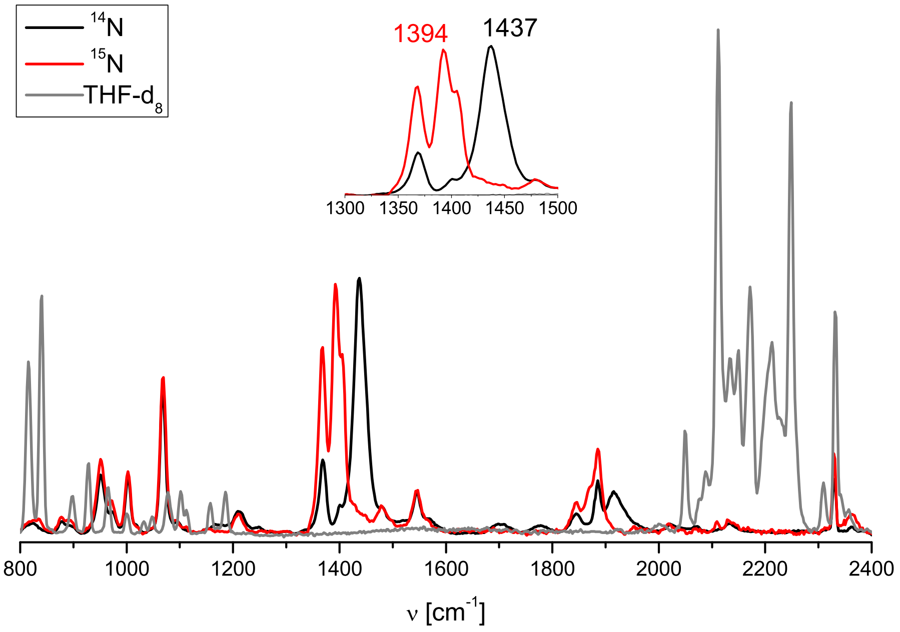

Figure 83: rRaman Spectrum (457 nm) of ^{14}N/^{15}N-**8** in frozen THF—d_8.

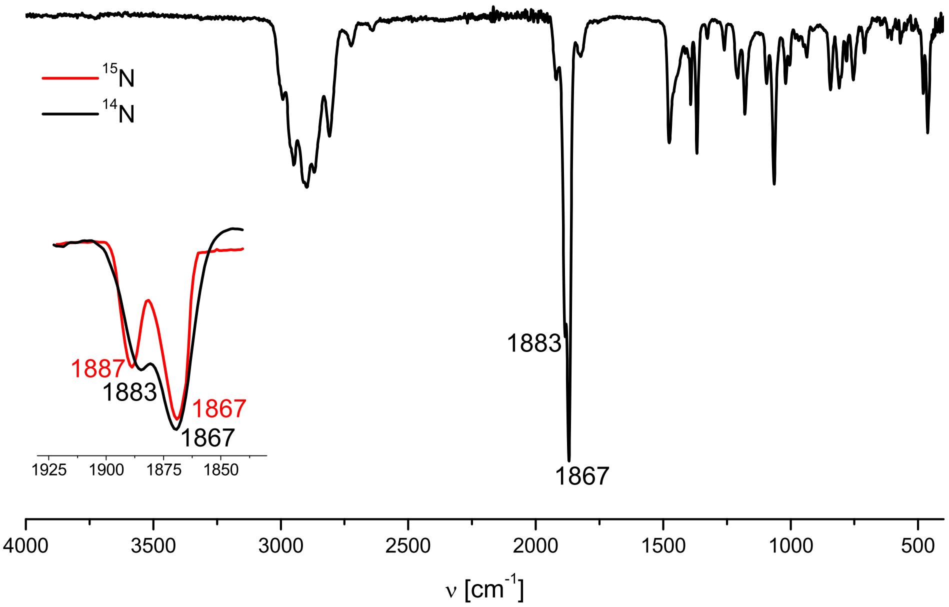

Figure 84: ATR-IR Spectrum of **8**.

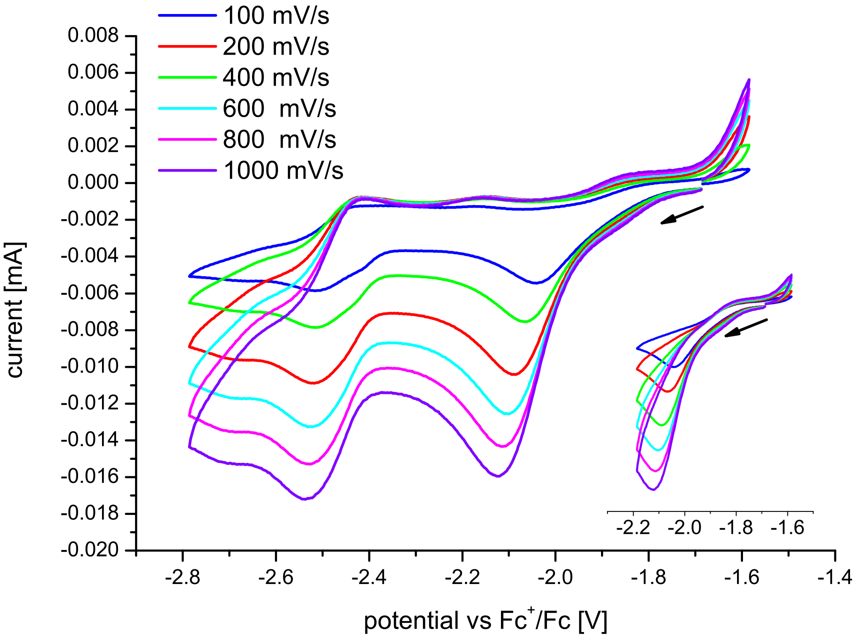

Figure 85: CV of **8** in 0.1 M solution of [^{n}Bu$_4$N][PF$_6$] in THF (WE = GC, RE = Ag/Ag$^+$, CE = Pt) at different scan rates.

6.1.9 [(N_2){W(CO)(PNP)}$_2$](4)

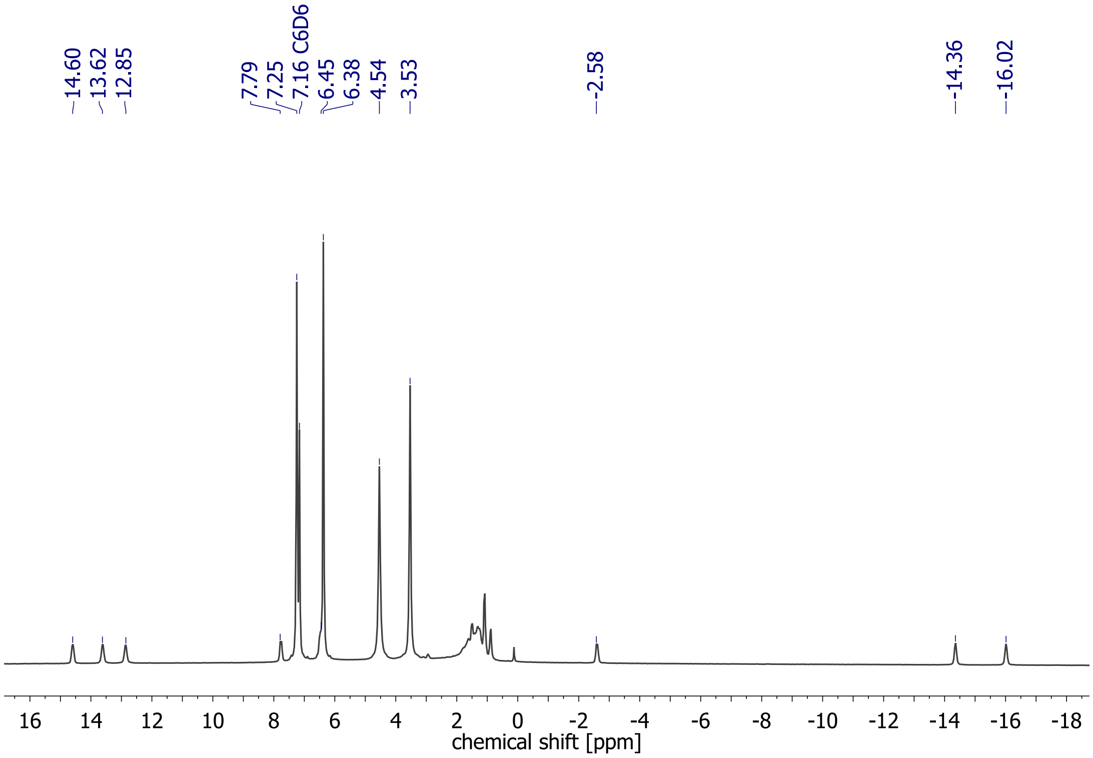

^{1}H NMR Spectrum of **4** in C_6D_6 at r.t.

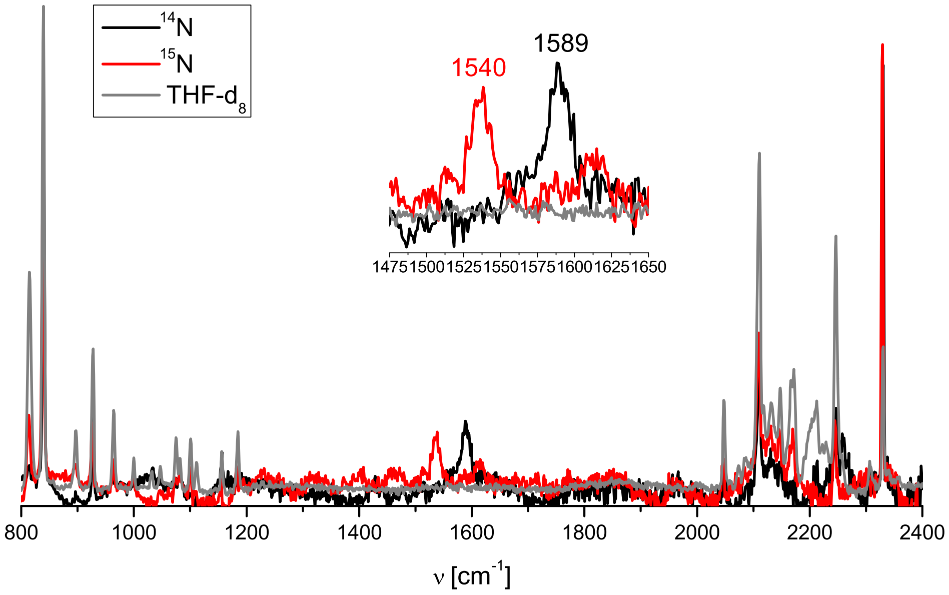

Figure 86: rRaman Spectrum (633 nm) of ^{14}N/^{15}N-**4** in frozen THF—d$_8$.

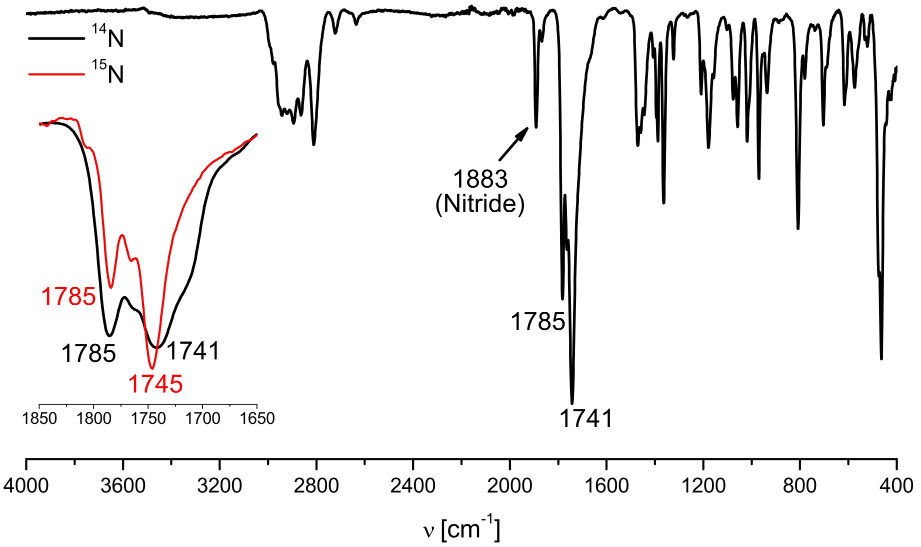

Figure 87: ATR-IR Spectrum **4**.

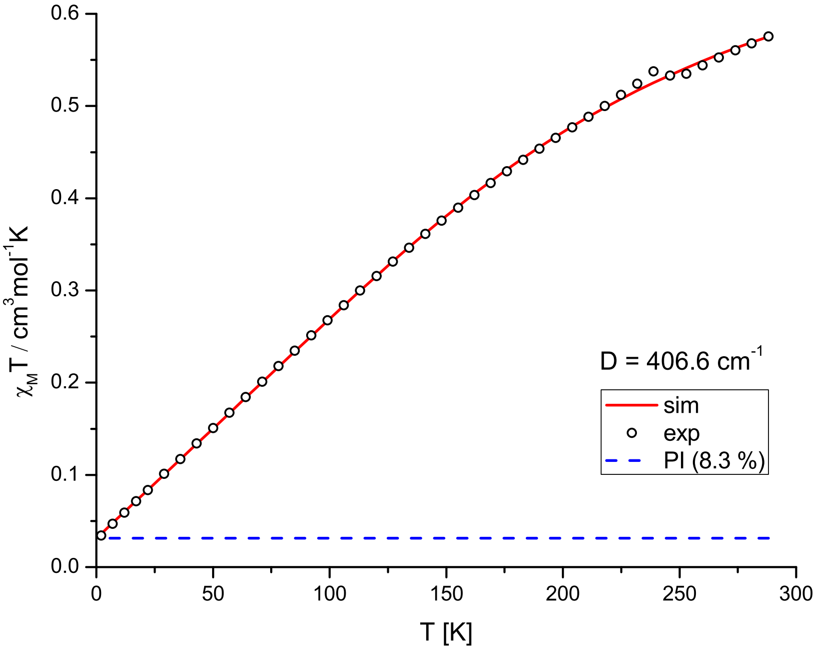

Figure 88: $\chi_M T$ vs. T plot for **4**. The open circles are the observed susceptibility, the red solid line corresponds to the best fit with the parameters $g = 1.74$ and $D = 406.6$ cm^{-1} (TIP: temperature independent paramagnetism).

6.1.10 [W(N)(CO)(PNP)] (16)

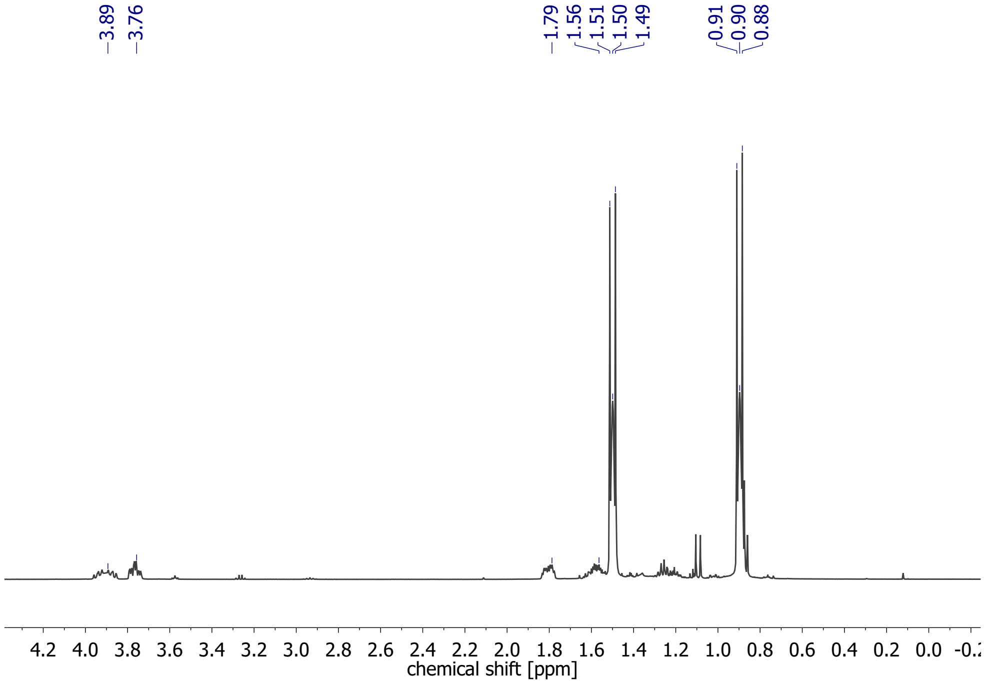

Figure 89: ^{1}H NMR Spectrum of **16** in C_6D_6 at r.t.

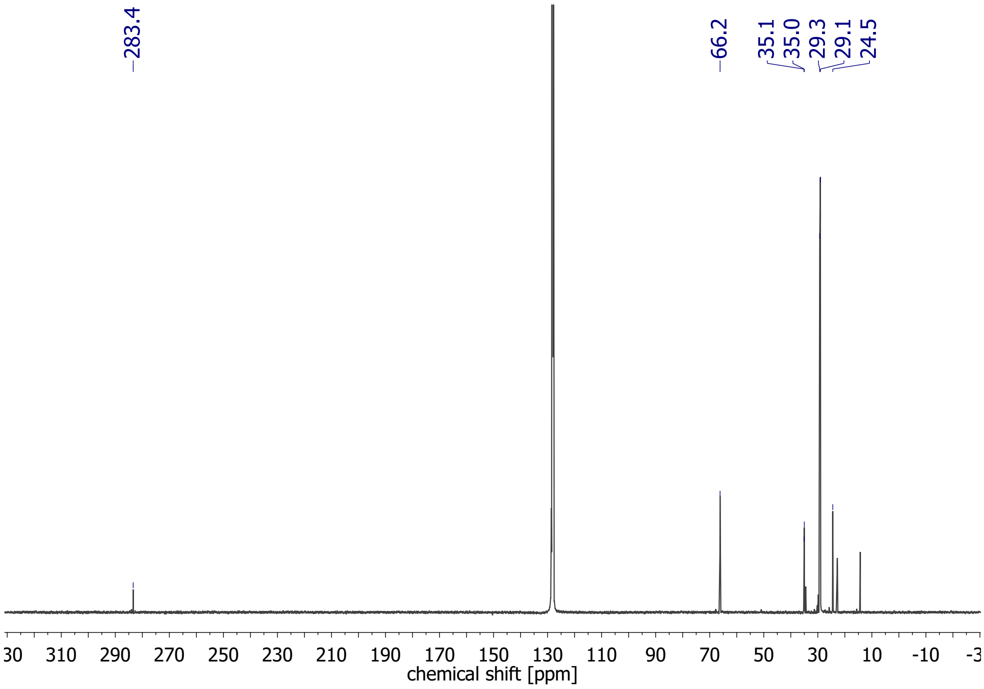

Figure 90: ^{13}C{^{1}H} NMR Spectrum of **16** in C_6D_6 at r.t.

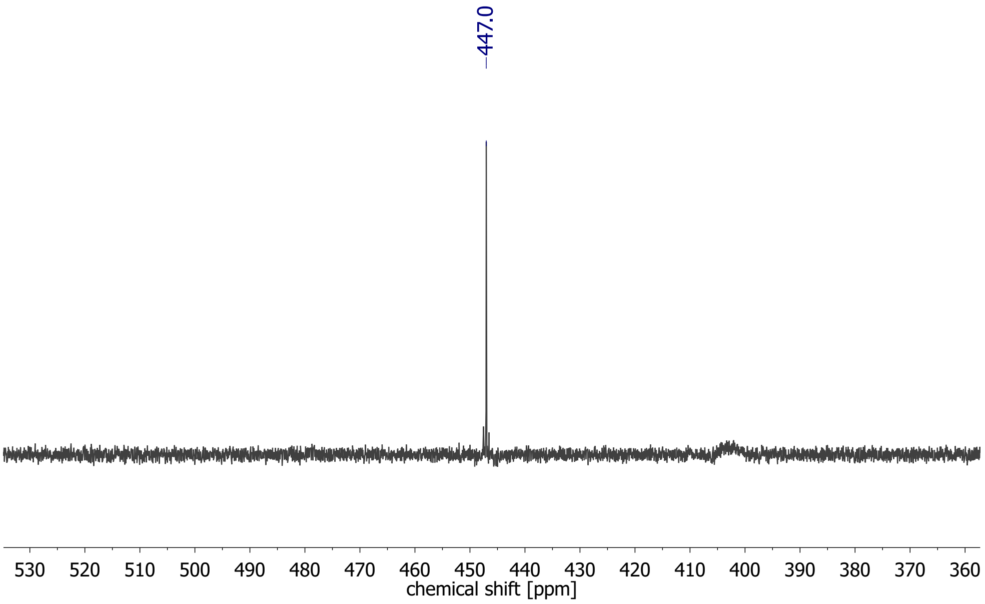

Figure 91: $^{15}N\{^1H\}$ NMR Spectrum of **16** in C_6D_6 at r.t.

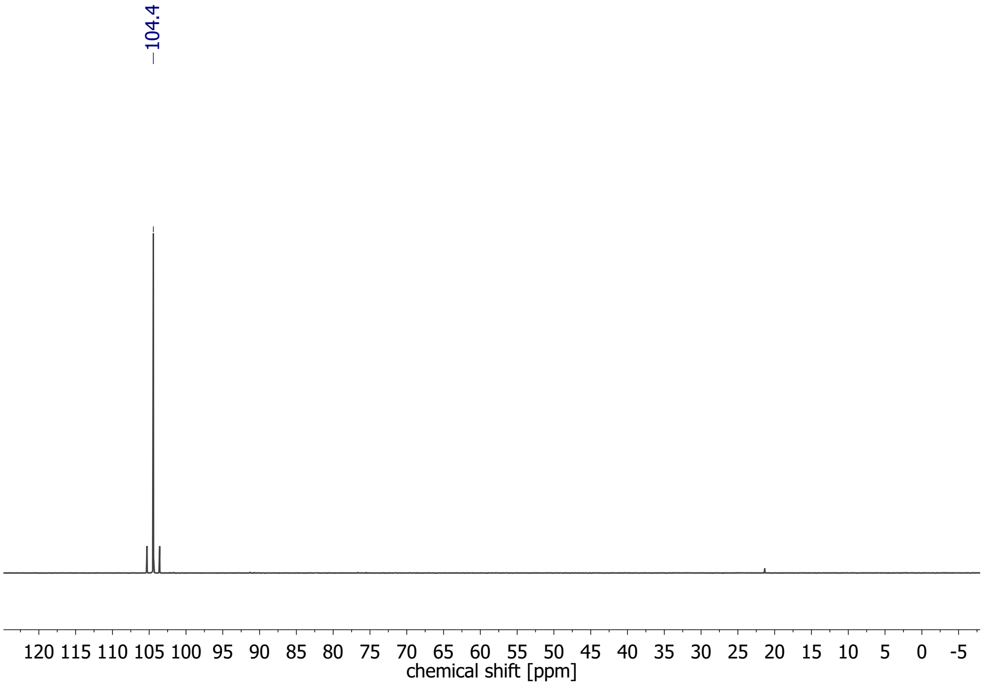

Figure 92: $^{31}P\{^1H\}$ NMR Spectrum of **16** in C_6D_6 at r.t.

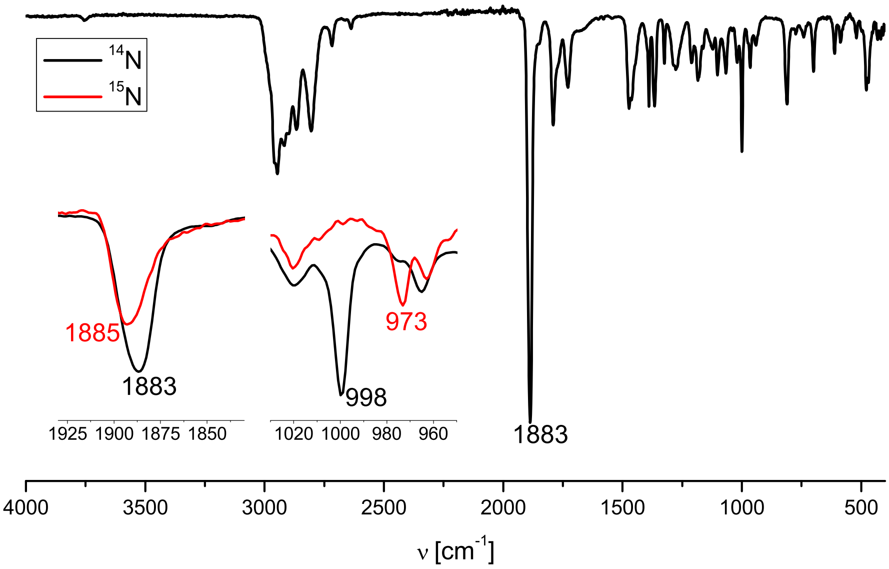

Figure 93: ATR-IR Spectrum of **16**.

6.1.11 [W(N)(CO)(^{H}PNP)]$^{+}$ (20)

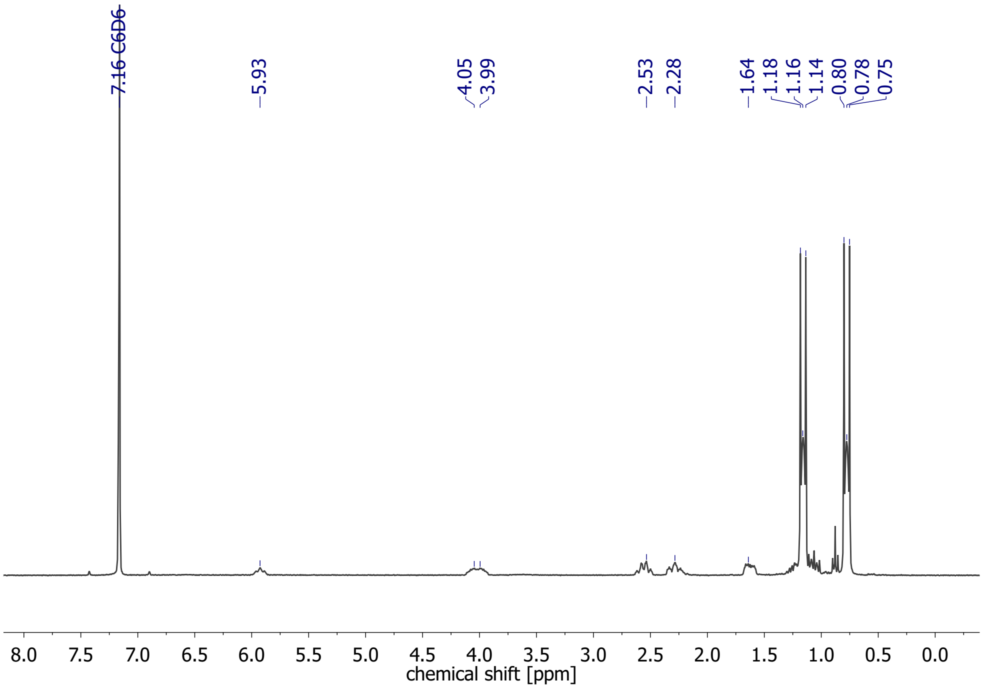

Figure 94: ^{1}H NMR Spectrum of **20** in C_6D_6 at r.t.

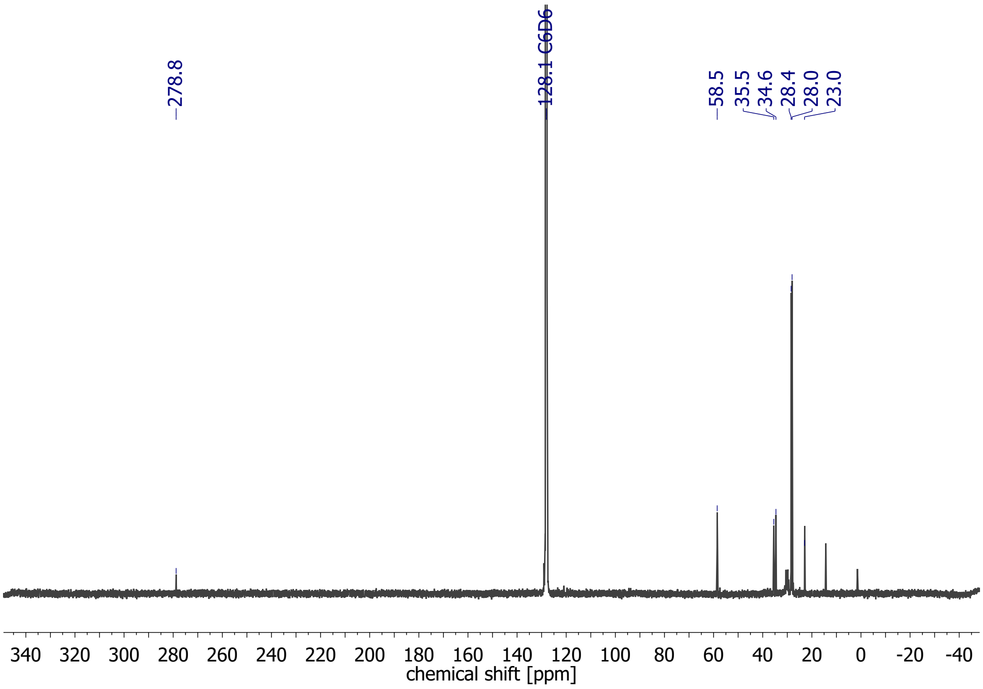

Figure 95: ^{13}C{^{1}H} NMR Spectrum of **20** in C_6D_6 at r.t.

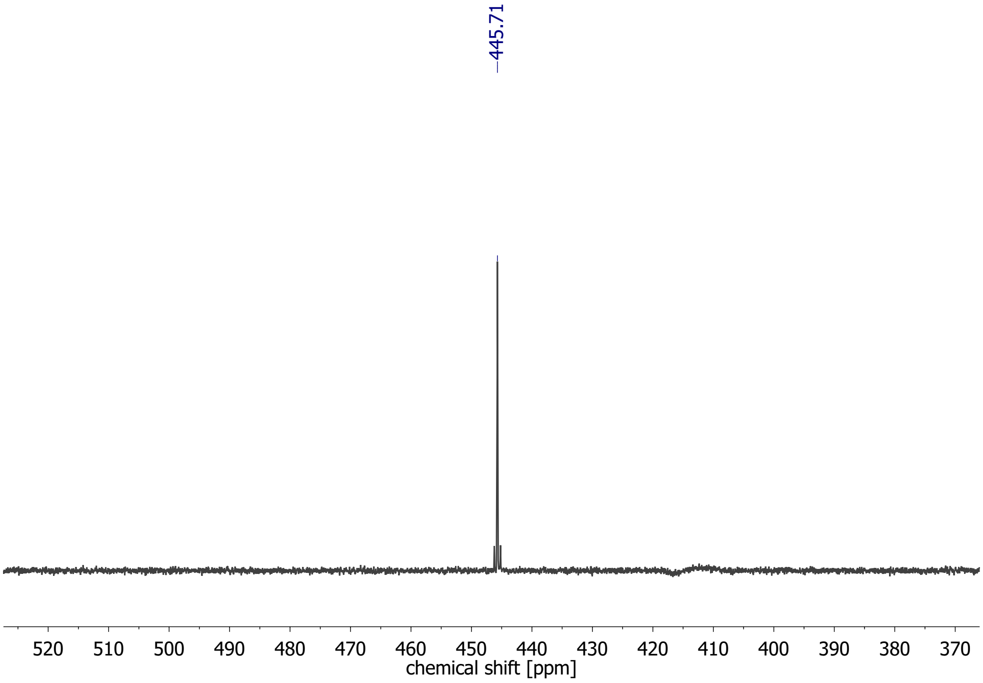

Figure 96: ^{15}N{^{1}H} NMR Spectrum of **20** in C_6D_6 at r.t.

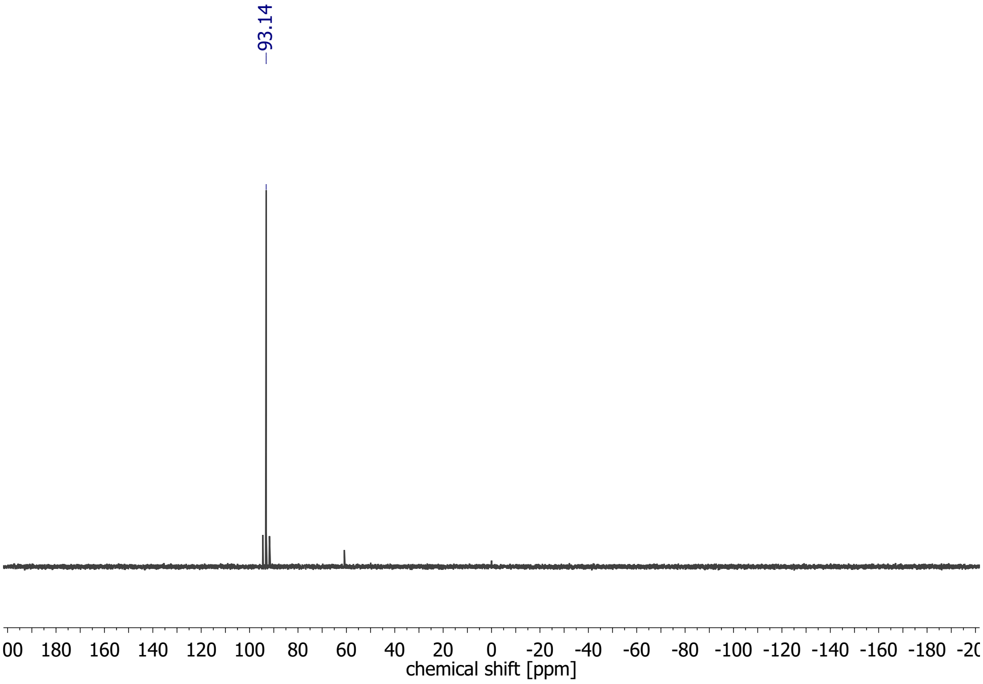

Figure 97: ^{31}P{^{1}H} NMR Spectrum of **20** in C_6D_6 at r.t.

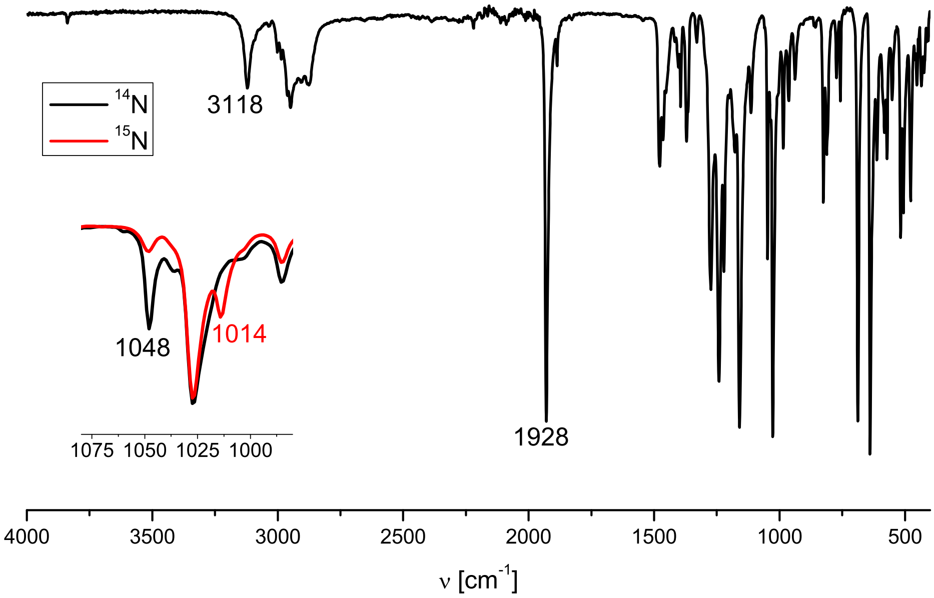

Figure 98: ATR-IR Spectrum of **20**.

6.1.12 [W(CO)$_3$(^{H}PNP)] (9)

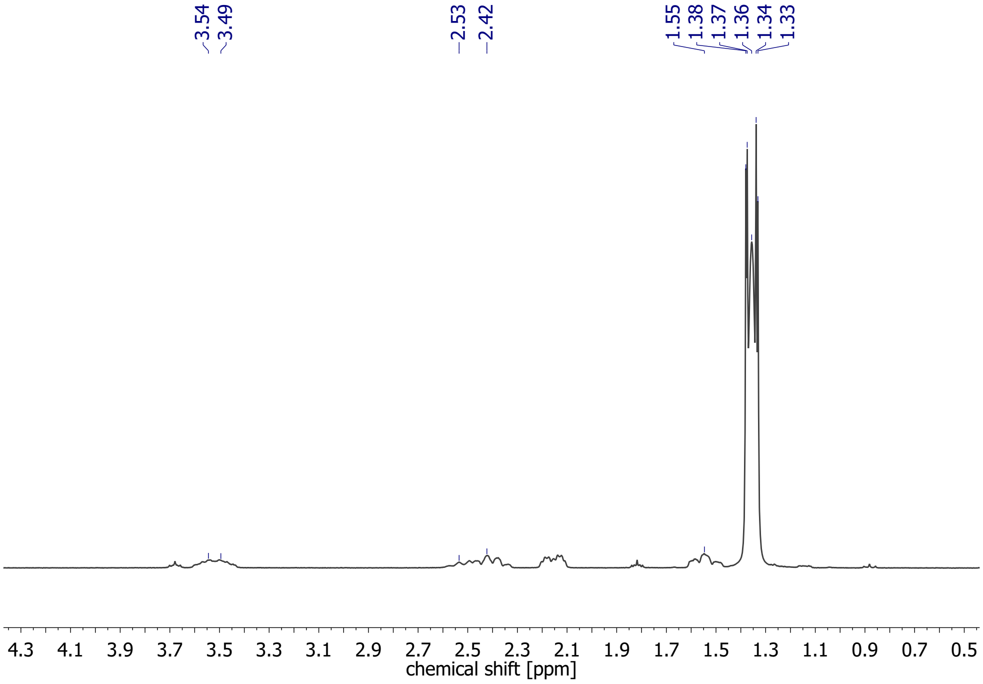

Figure 99: ^{1}H NMR Spectrum of **9** in CD_2Cl_2 at r.t.

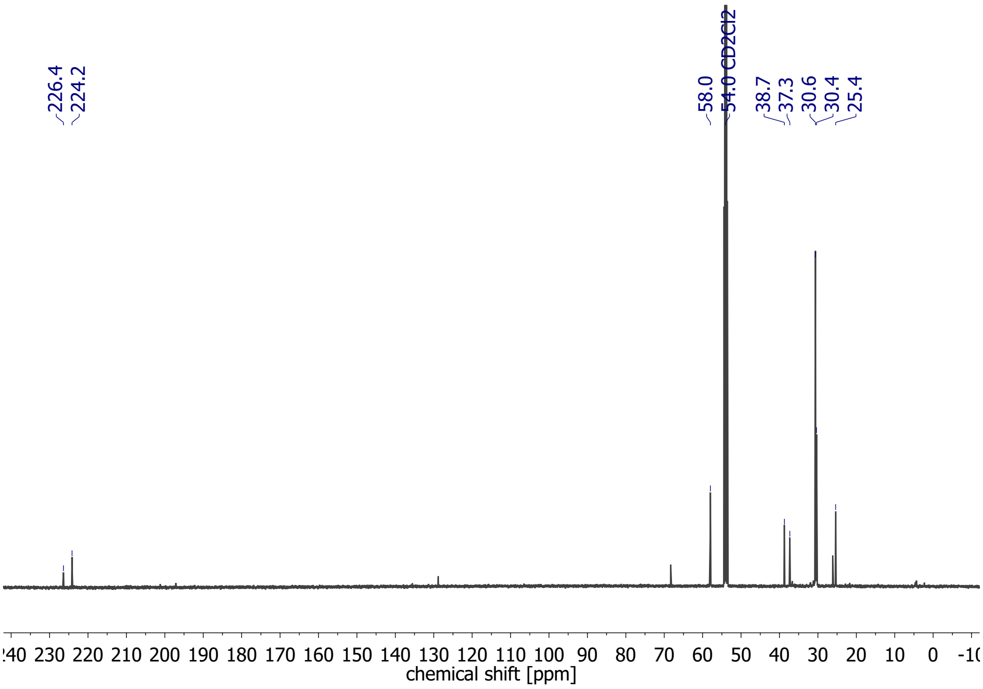

Figure 100: $^{13}C\{^1H\}$ NMR Spectrum of **9** in CD_2Cl_2 at r.t.

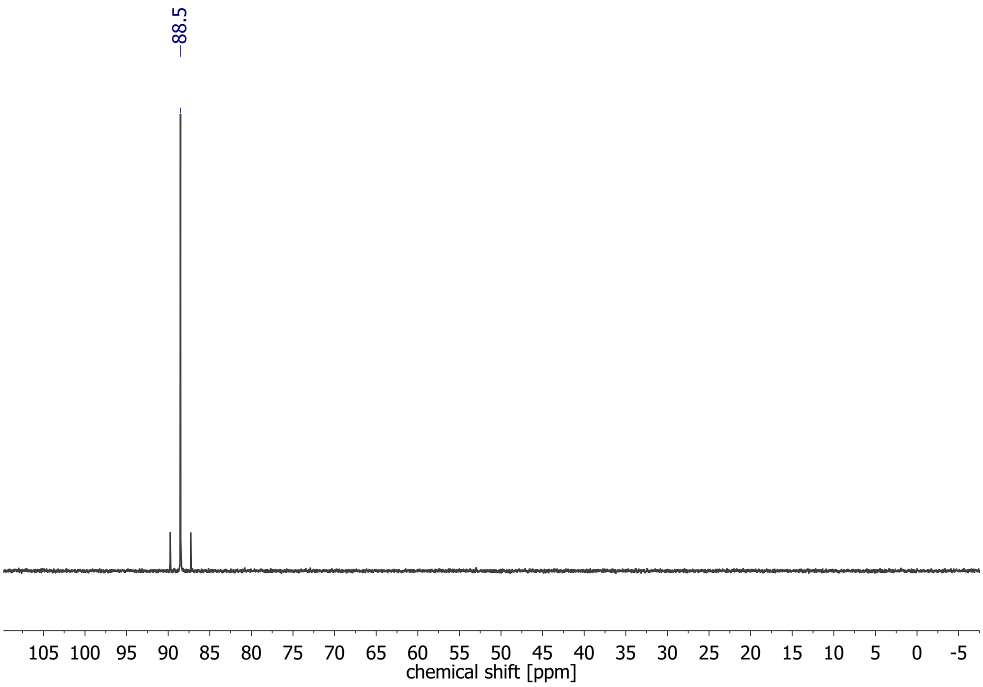

Figure 101: $^{31}P\{^{1}H\}$ NMR Spectrum of **9** in CD_2Cl_2 at r.t.

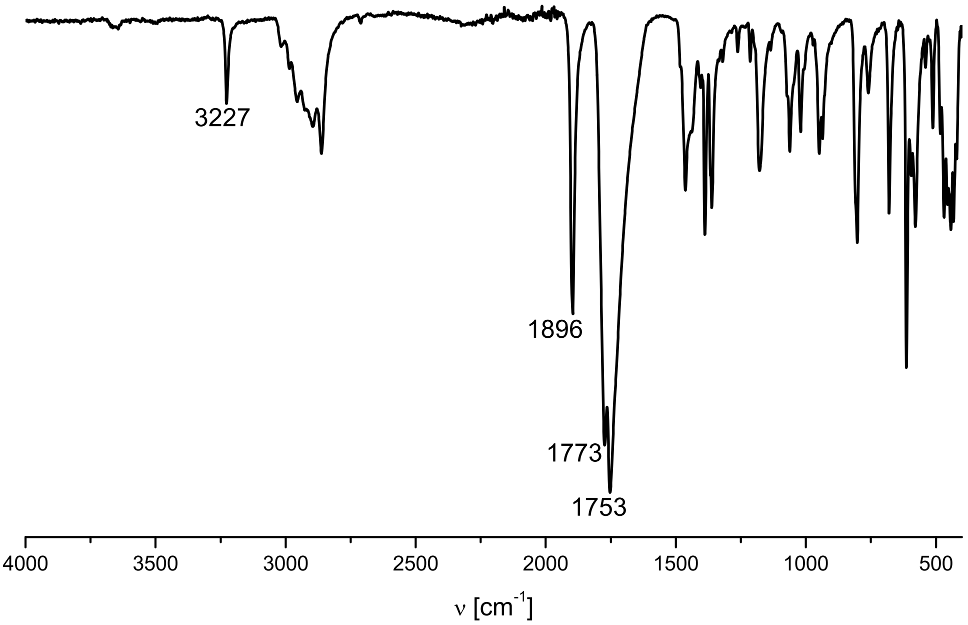

Figure 102: ATR-IR Spectrum of **9**.

6.1.13 [WI(CO)$_2$(PNP)] (18)

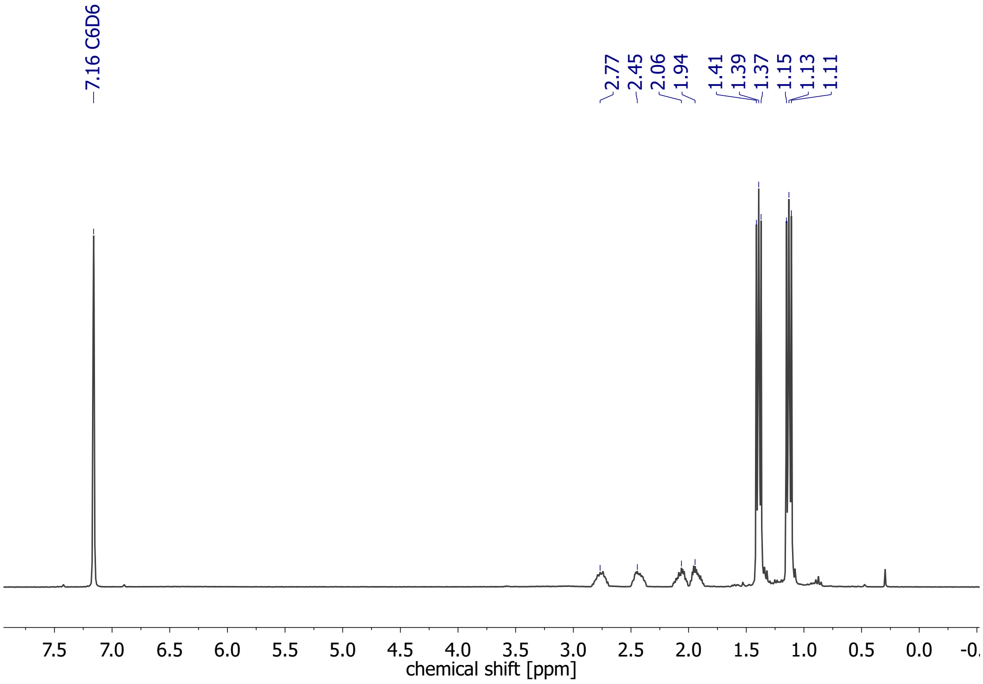

Figure 103: ^{1}H NMR Spectrum of **18** in C_6D_6 at r.t.

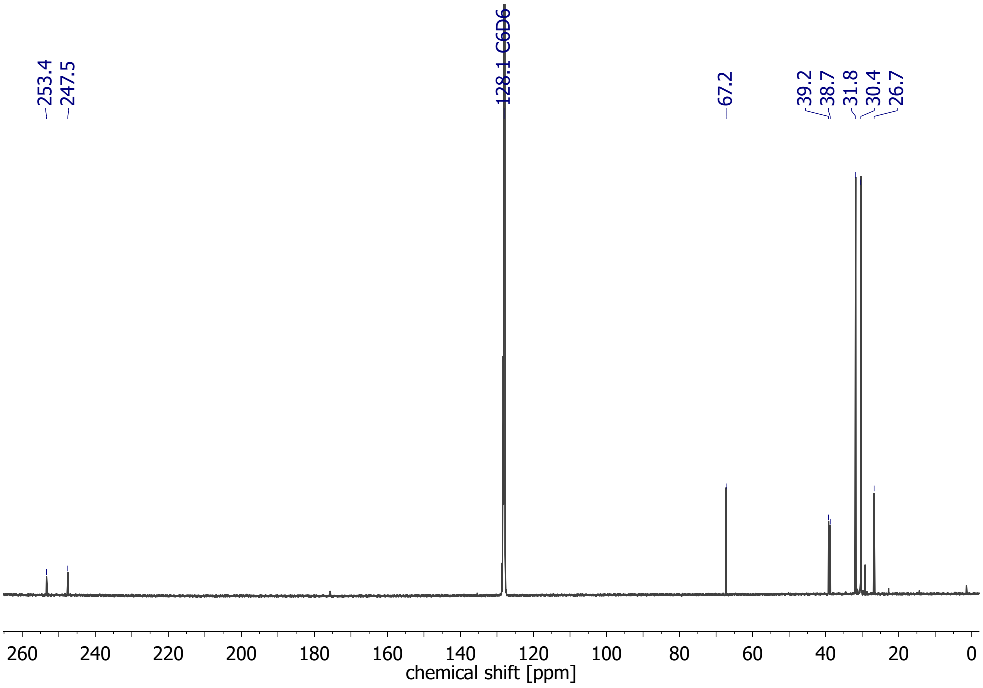

Figure 104: ^{13}C{^{1}H} NMR Spectrum of **18** in C_6D_6 at r.t.

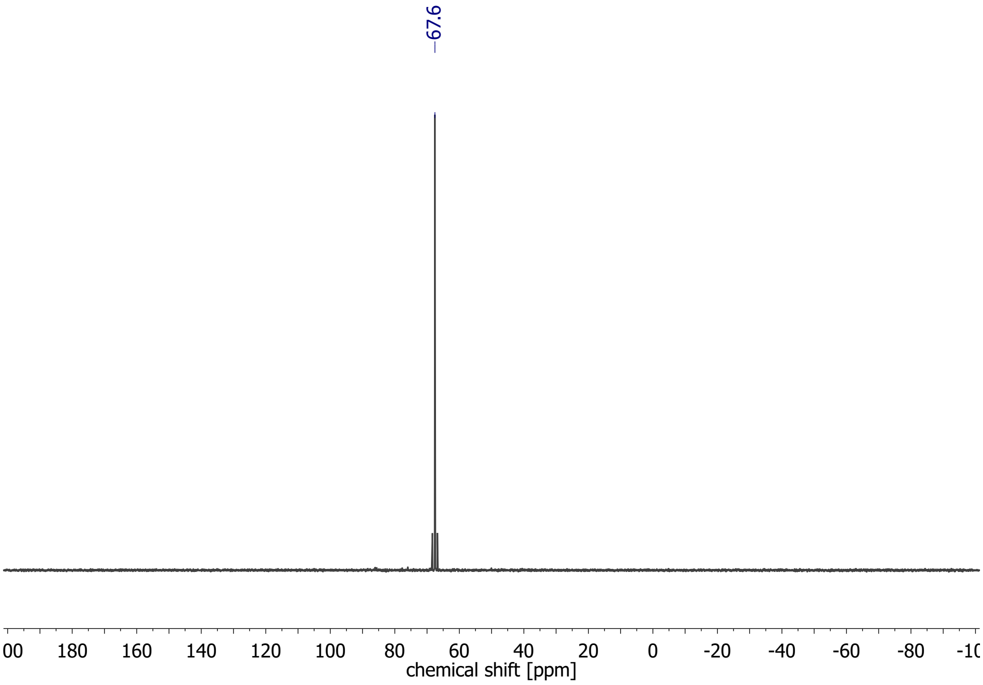

Figure 105: $^{31}P\{^{1}H\}$ NMR Spectrum of **18** in C_6D_6 at r.t.

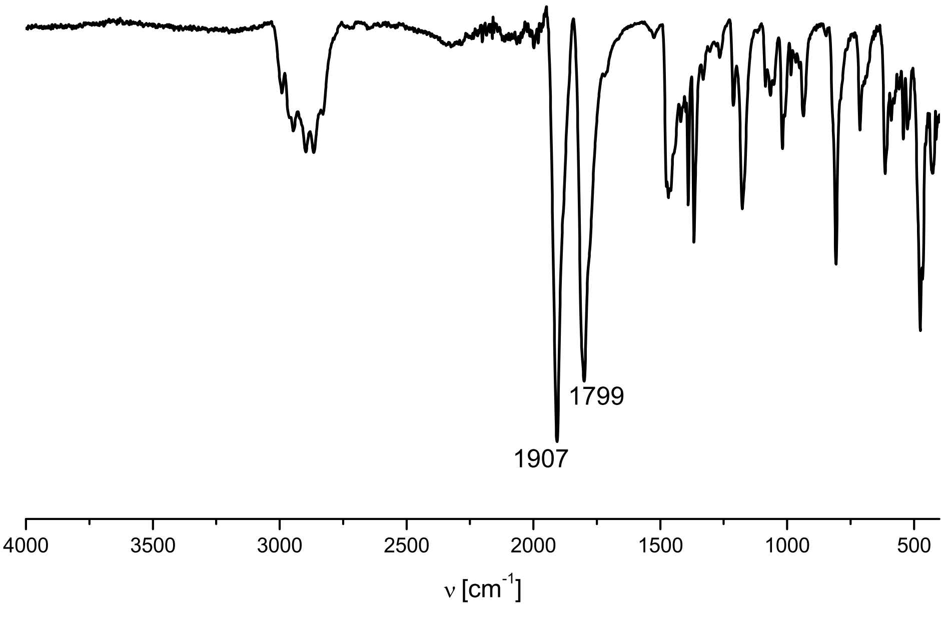

Figure 106: ATR-IR Spectrum of **18**.

6.1.14 [WCl(CO)$_2$(PNP)] (10)

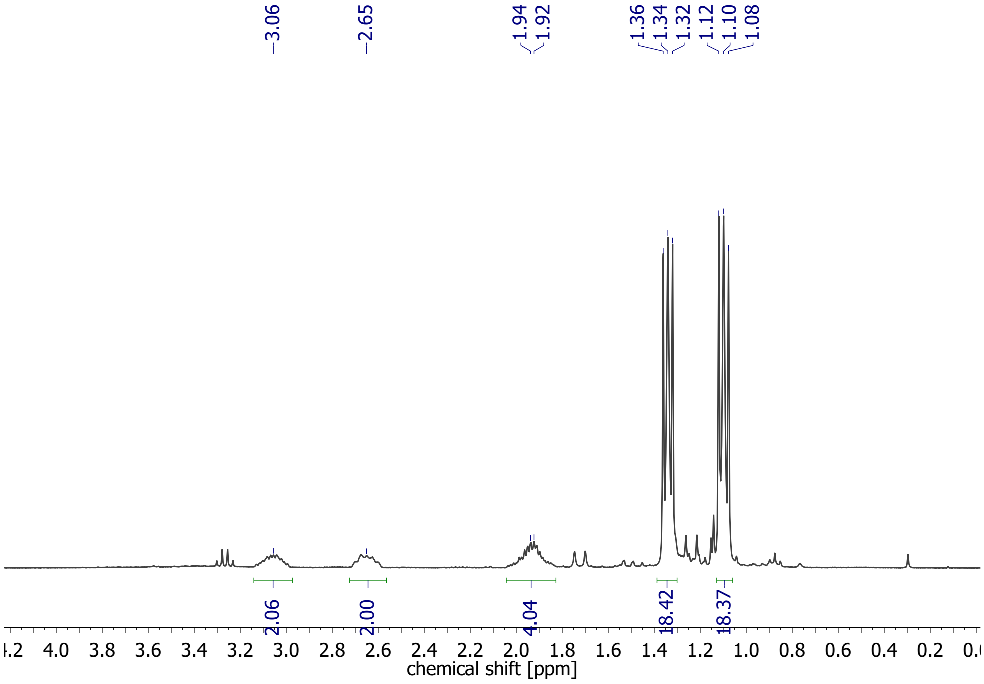

Figure 107: ^{1}H NMR Spectrum of **10** in C_6D_6 at r.t.

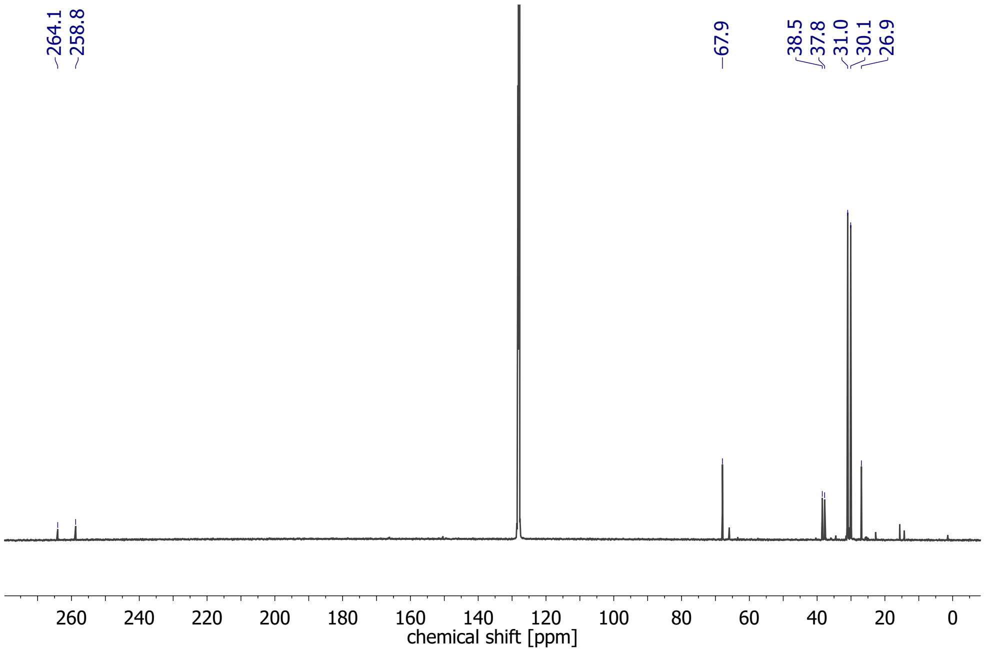

Figure 108: ^{13}C{^{1}H} NMR Spectrum of **10** in C_6D_6 at r.t.

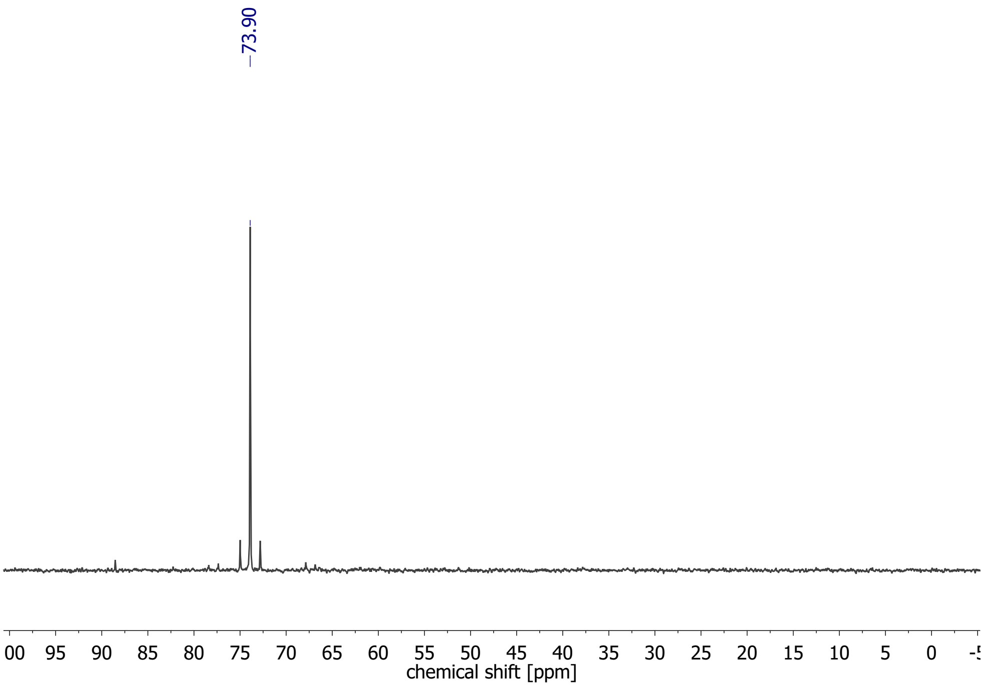

Figure 109: $^{31}P\{^{1}H\}$ NMR Spectrum of **10** in C_6D_6 at r.t.

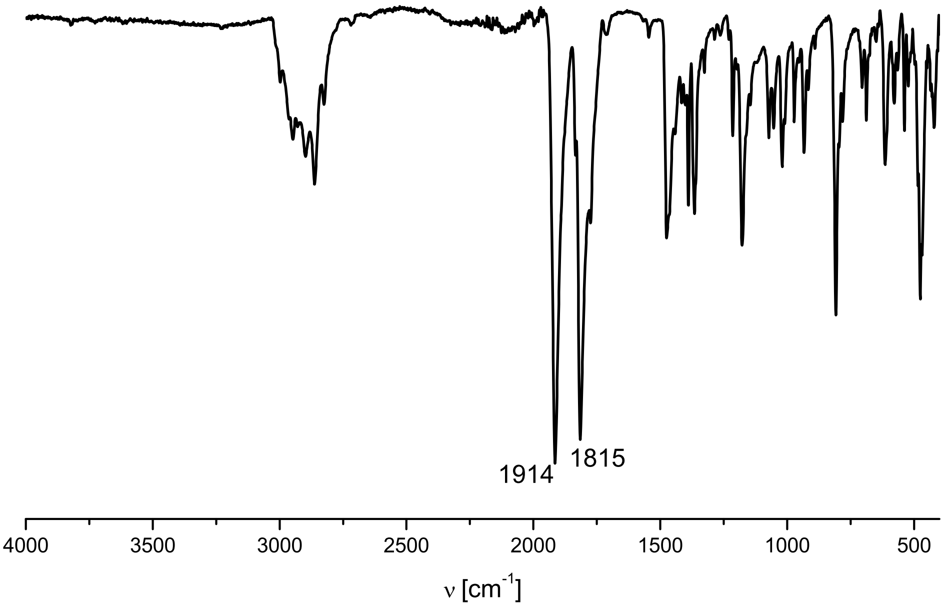

Figure 110: ATR-IR Spectrum of **10**.

6.1.15 Characterization of TMS—NCO

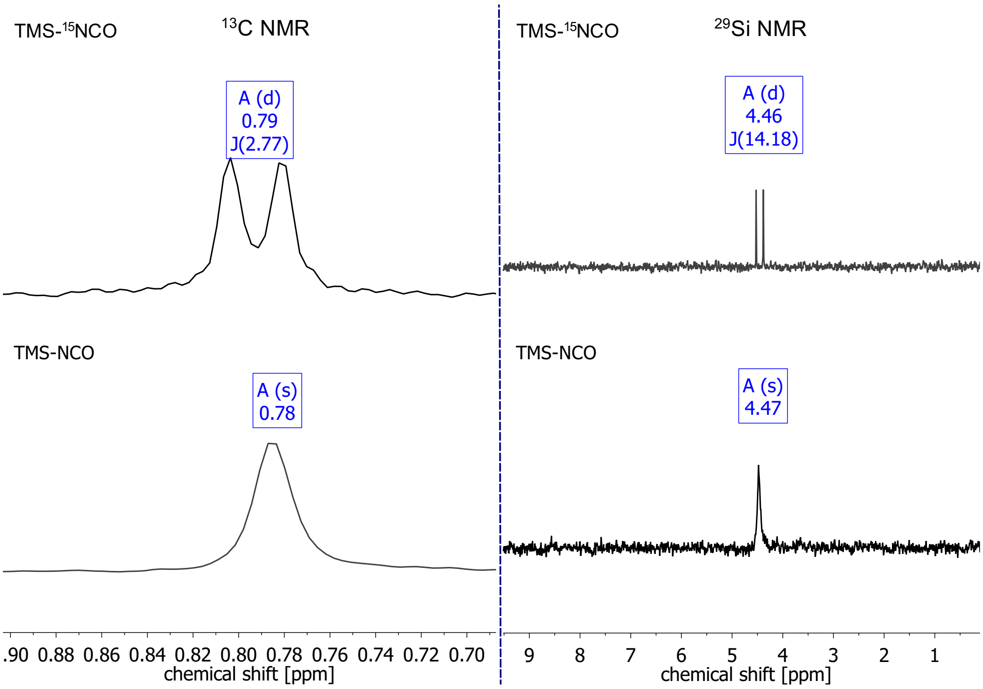

Figure 111: *left:* Comparison of the $^{13}C\{^{1}H\}$ NMR Spectra of TMS—^{15}NCO (*top*) and TMS—NCO (*bottom*). *right:* Comparison of the $^{29}Si\{^{1}H\}$ NMR Spectra of TMS—NCO (*top*) and TMS—^{15}NCO (*bottom*).

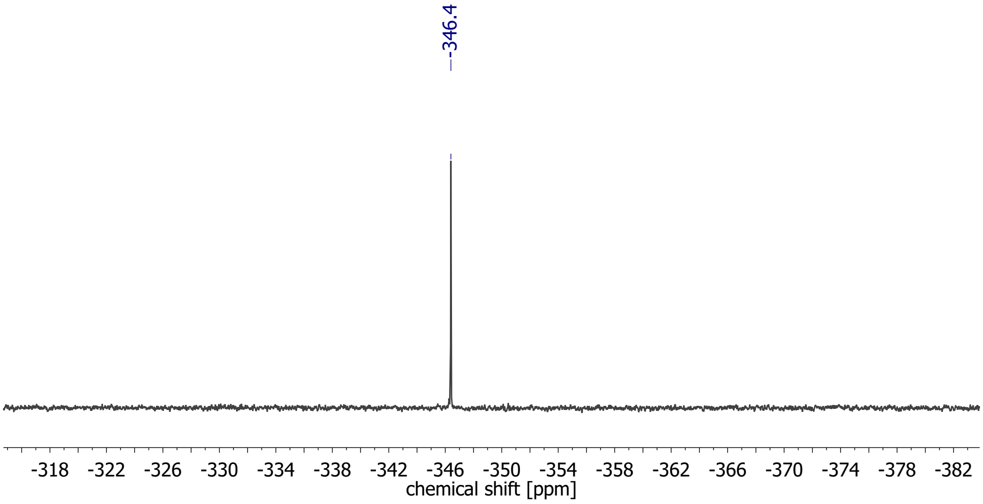

Figure 112: $^{15}N\{^{1}H\}$ NMR Spectrum of TMS—^{15}NCO in C_6D_6 at r.t.

6.1.16 [W(N_3)(CO)$_2$(PNP)] (19)

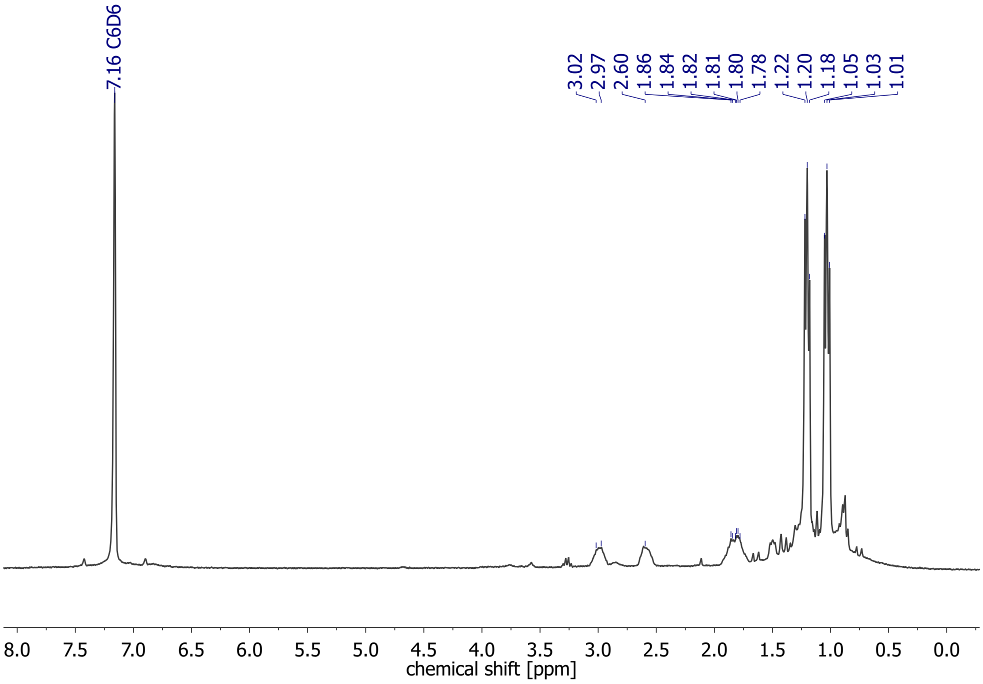

Figure 113: ^{1}H NMR Spectrum of **19** in C_6D_6 at r.t.

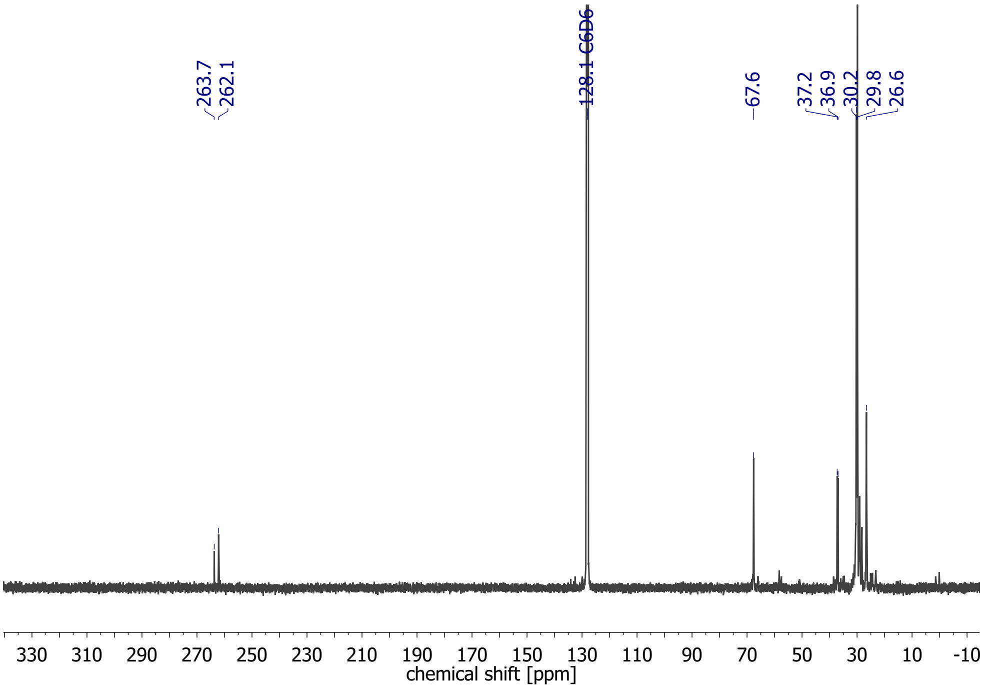

Figure 114: $^{13}C\{^1H\}$ NMR Spectrum of **19** in C_6D_6 at r.t.

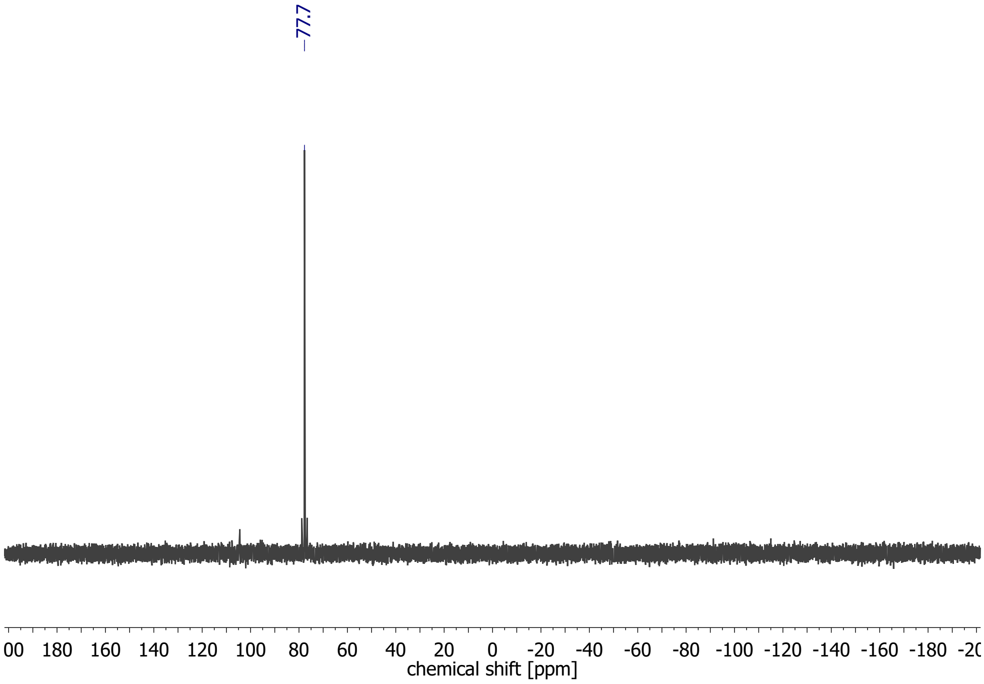

Figure 115: $^{31}P\{^{1}H\}$ NMR Spectrum of **19** in C_6D_6 at r.t.

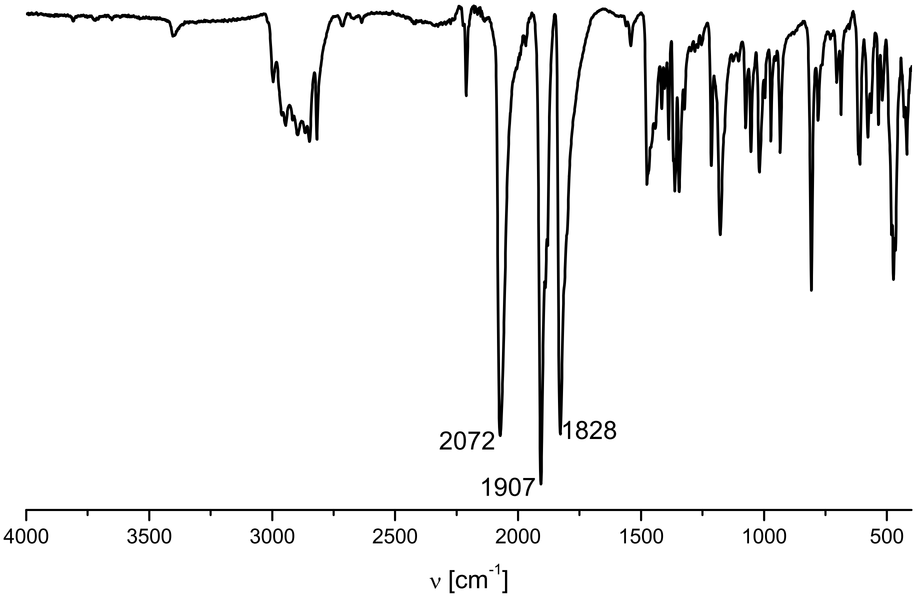

Figure 116: ATR-IR Spectrum of **19**.

6.1.17 [W(NCO)(CO)$_2$(PNP)] (21)

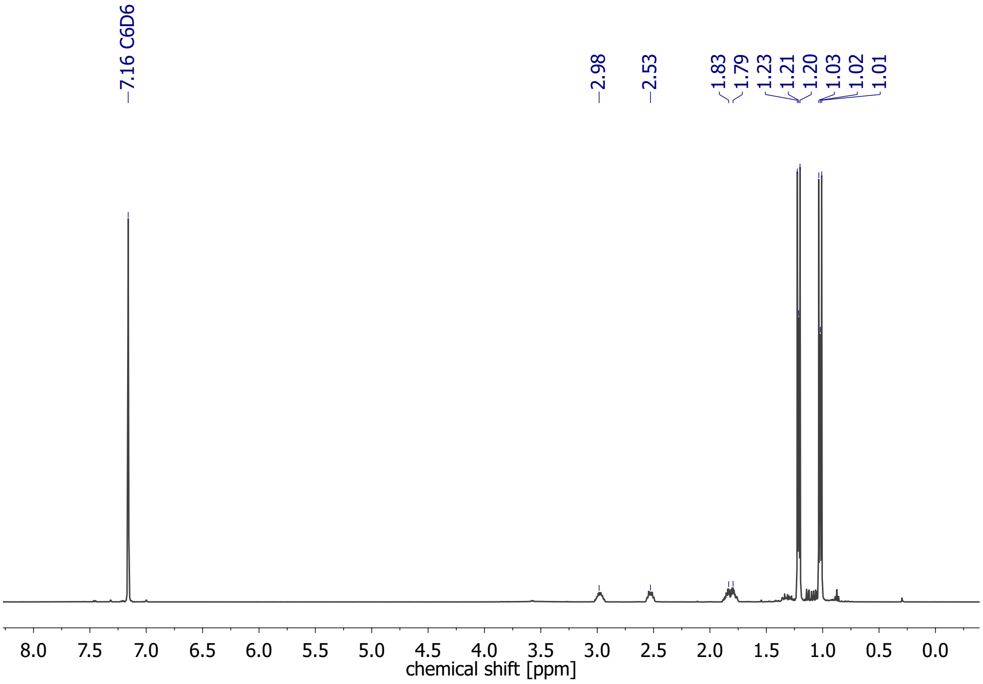

Figure 117: ^{1}H NMR Spectrum of **21** in C_6D_6 at r.t.

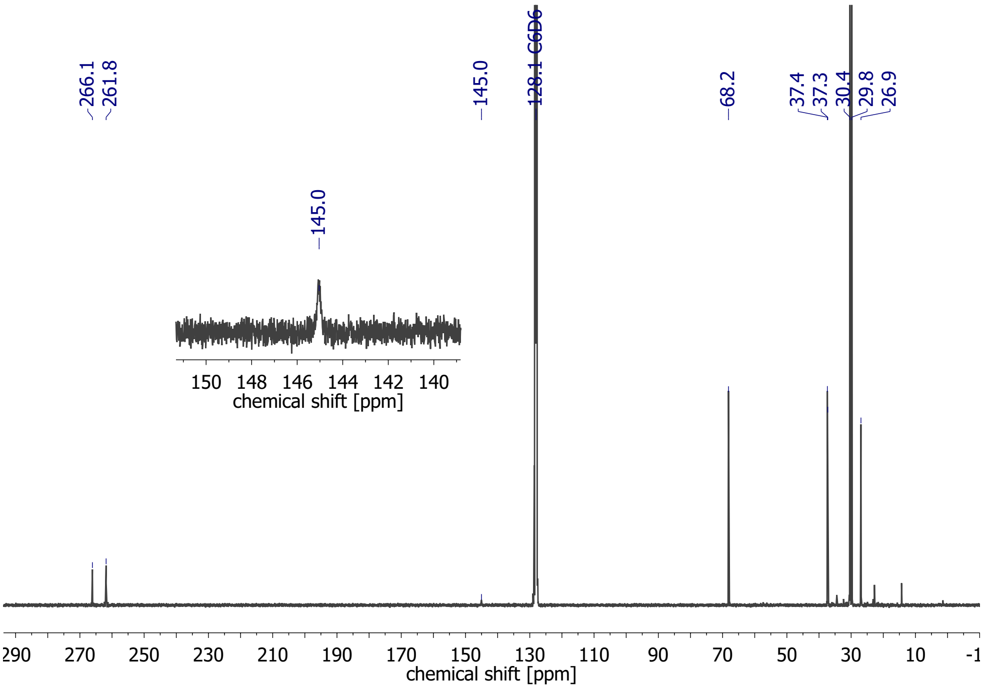

Figure 118: $^{13}C\{^1H\}$ NMR Spectrum of **21** in C_6D_6 at r.t.

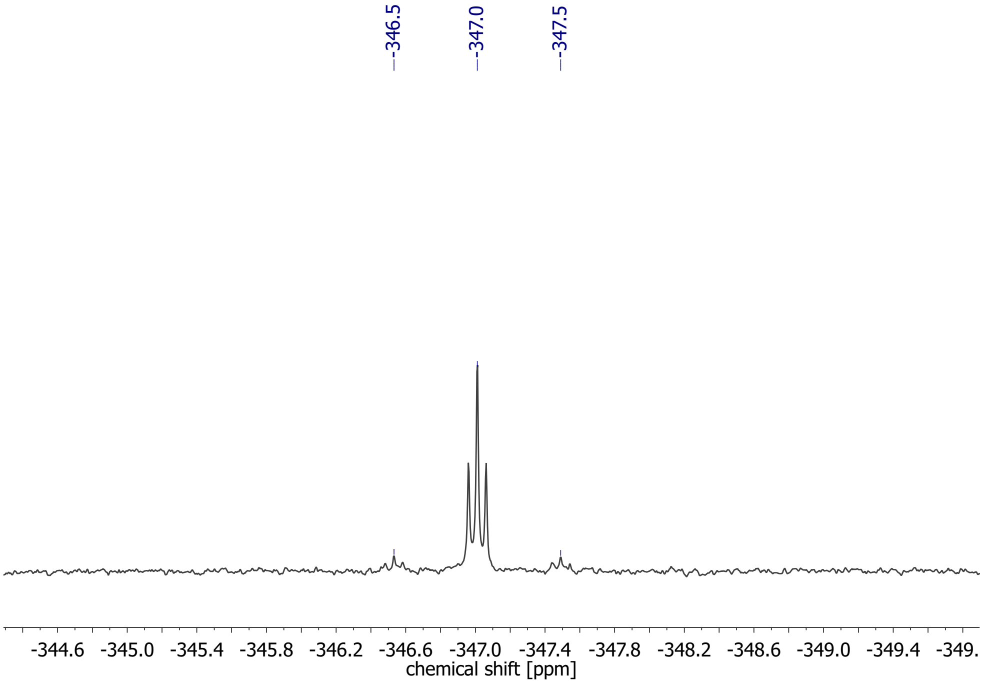

Figure 119: $^{15}N\{^1H\}$ NMR Spectrum of ^{15}N-**21** in C_6D_6 at r.t.

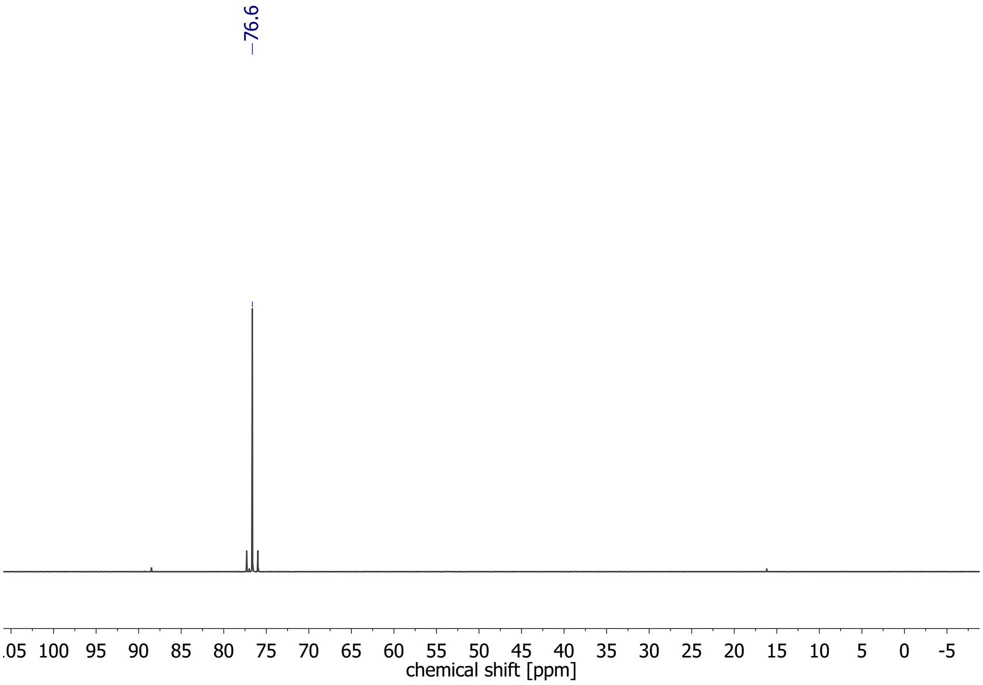

Figure 120: $^{31}P\{^1H\}$ NMR Spectrum of **21** in C_6D_6 at r.t.

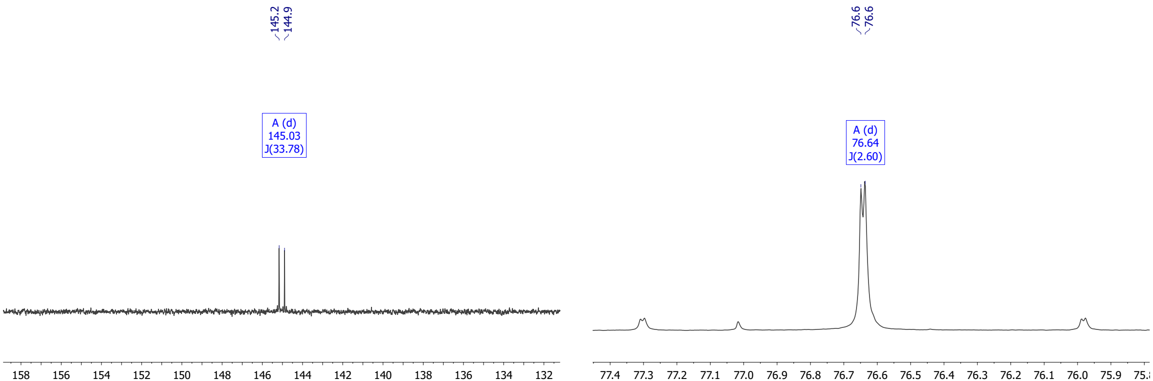

(a) $^{13}C\{^{1}H\}$ NMR

(b) $^{31}P\{^{1}H\}$ NMR

Figure 121: $^{13}C\{^{1}H\}$ (*left*) and $^{31}P\{^{1}H\}$ (*right*) NMR spectra of ^{15}N-**21** in C_6D_6 at r.t.

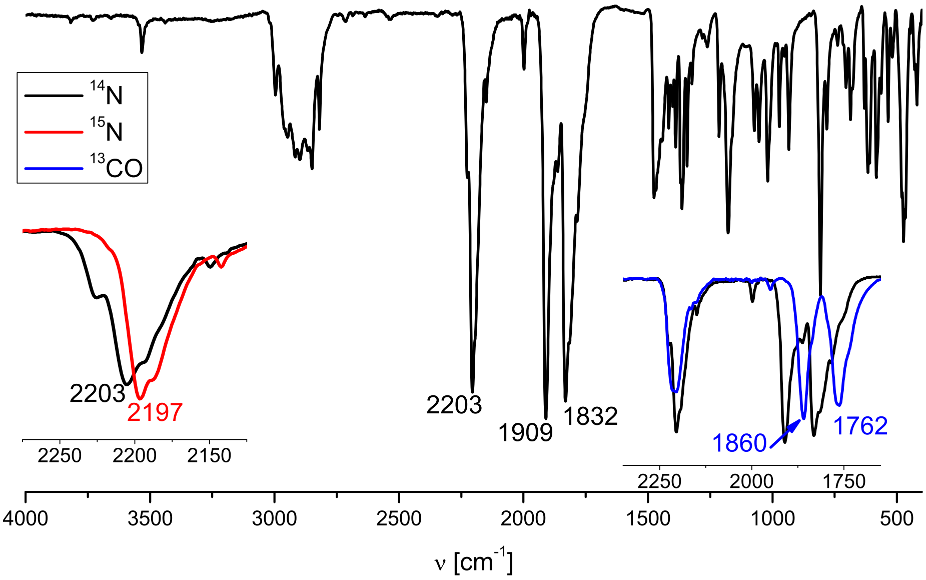

Figure 122: ATR-IR spectrum of **21**. The red line represents the ATR-IR spectrum of ^{15}N-**21**, the blue line shows the spectrum of $(^{13}CO)_2$-**21**.

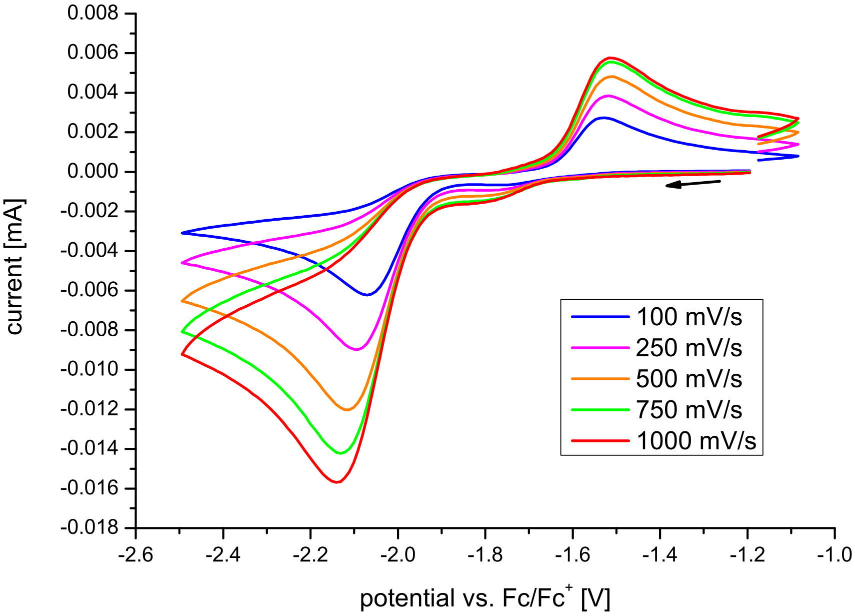

Figure 123: CV of the reduction of **21** in 0.1 M solution of [^{n}Bu$_4$N][PF$_6$] in THF (WE = GC, RE = Ag/Ag$^+$, CE = Pt) at different scan rates.

6.1.18 [W(NCO)(CN^{t}Bu)$_2$(PNP)] (22)

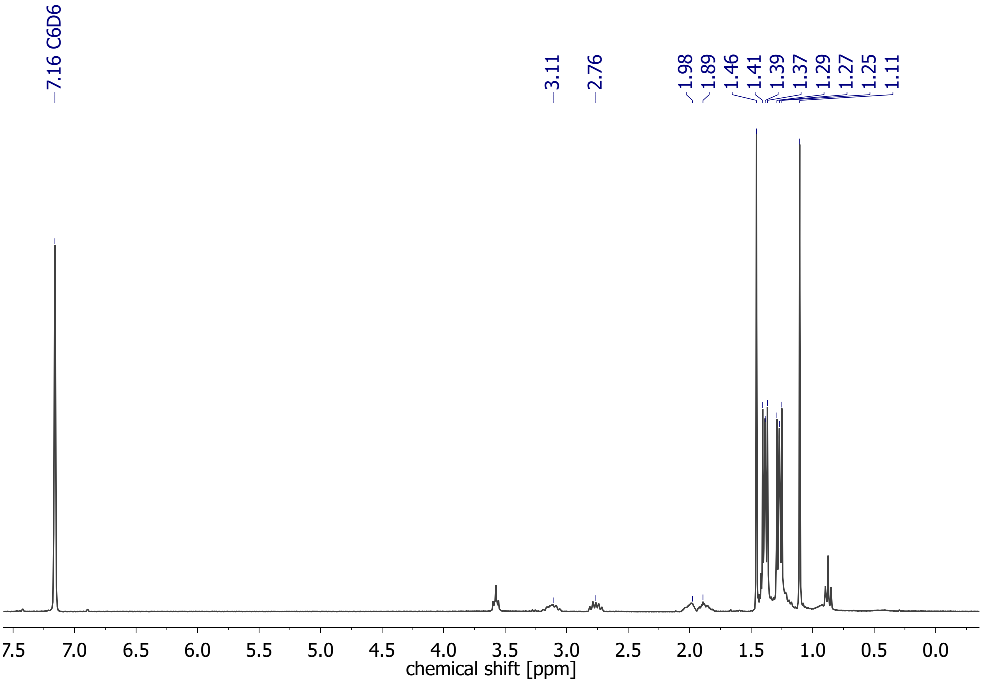

Figure 124: ^{1}H NMR Spectrum of **22** in C_6D_6 at r.t.

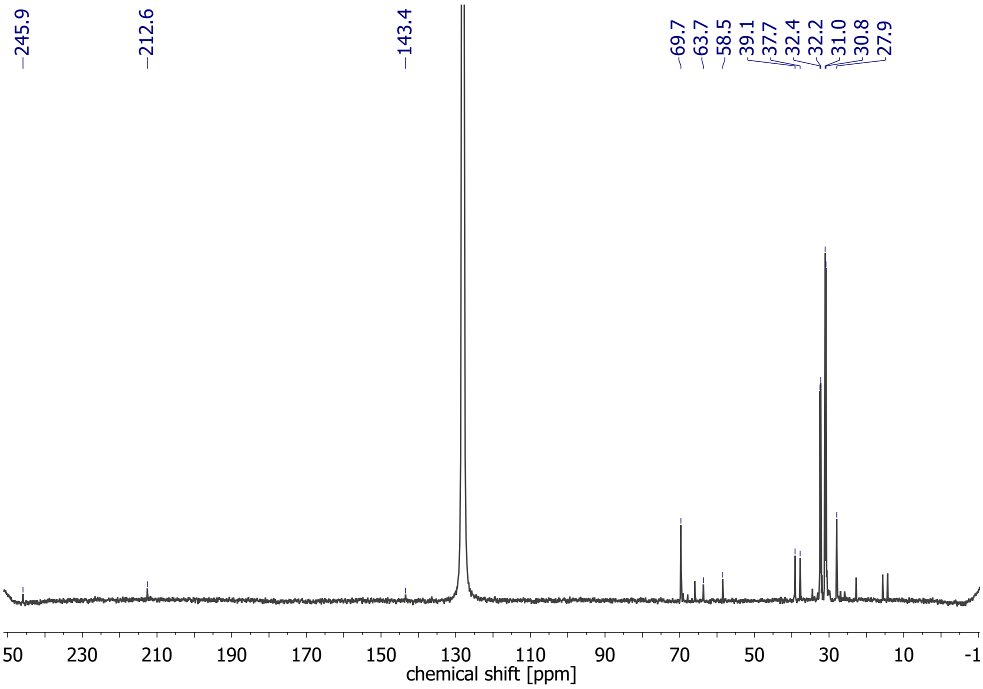

Figure 125: $^{13}C\{^1H\}$ NMR Spectrum of **22** in C_6D_6 at r.t.

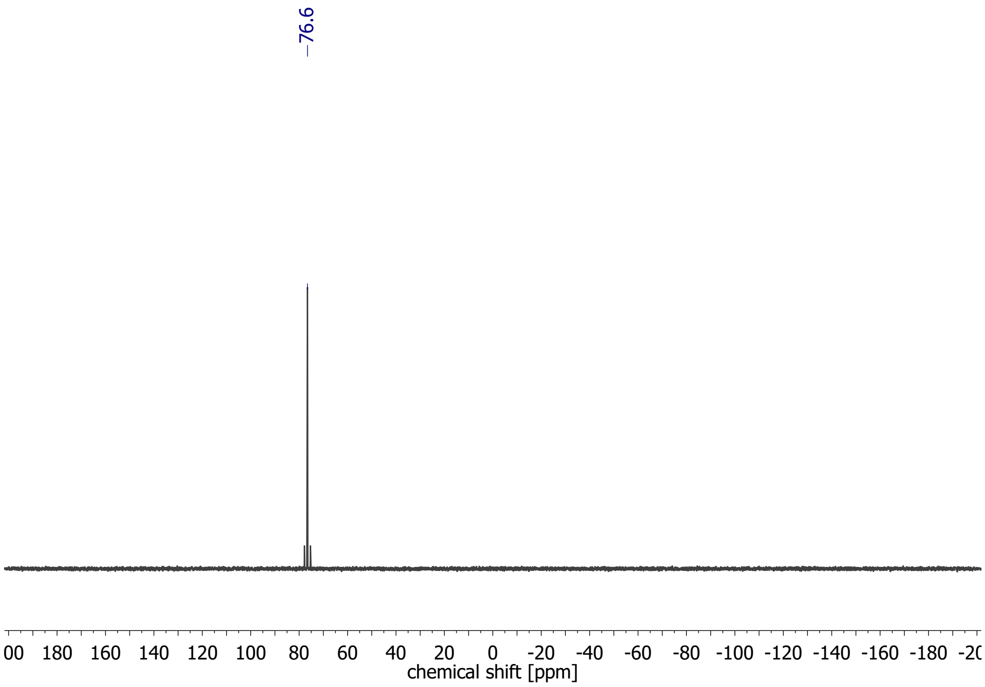

Figure 126: $^{31}P\{^{1}H\}$ NMR Spectrum of **22** in C_6D_6 at r.t.

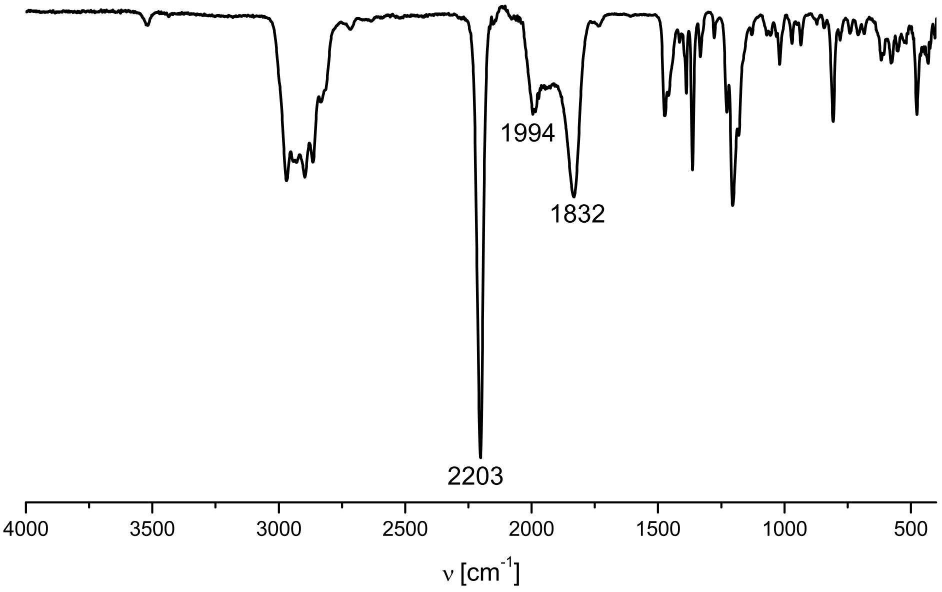

Figure 127: ATR-IR Spectrum of **22**.

6.1.19 [W(NCO)(CN–C_6H_4–OMe)$_2$(PNP)] (23)

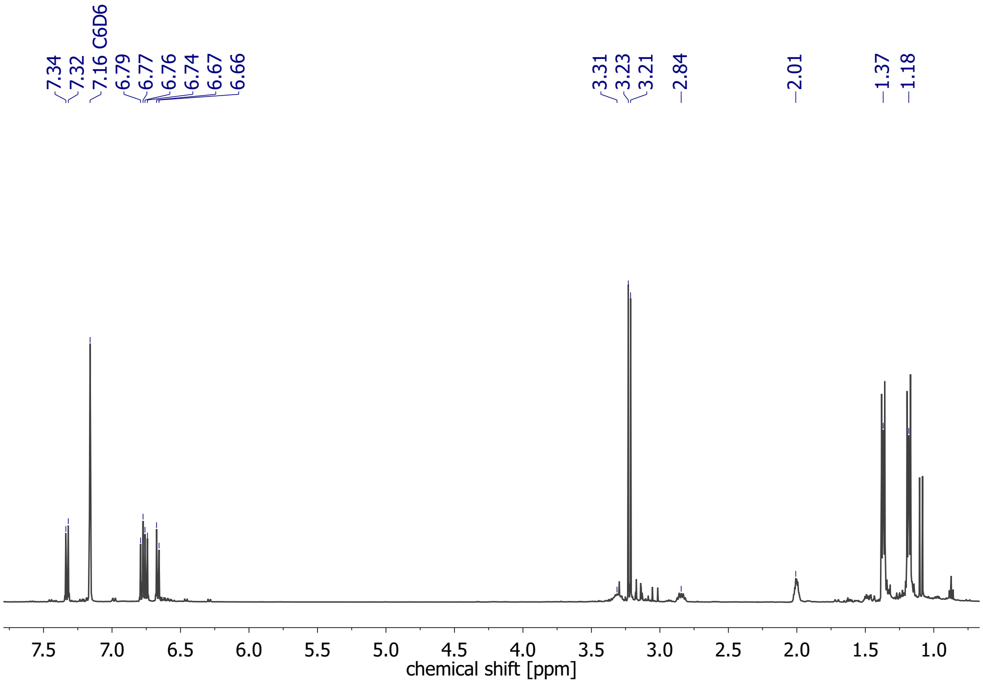

Figure 128: ^{1}H NMR Spectrum of **23** in C_6D_6 at r.t.

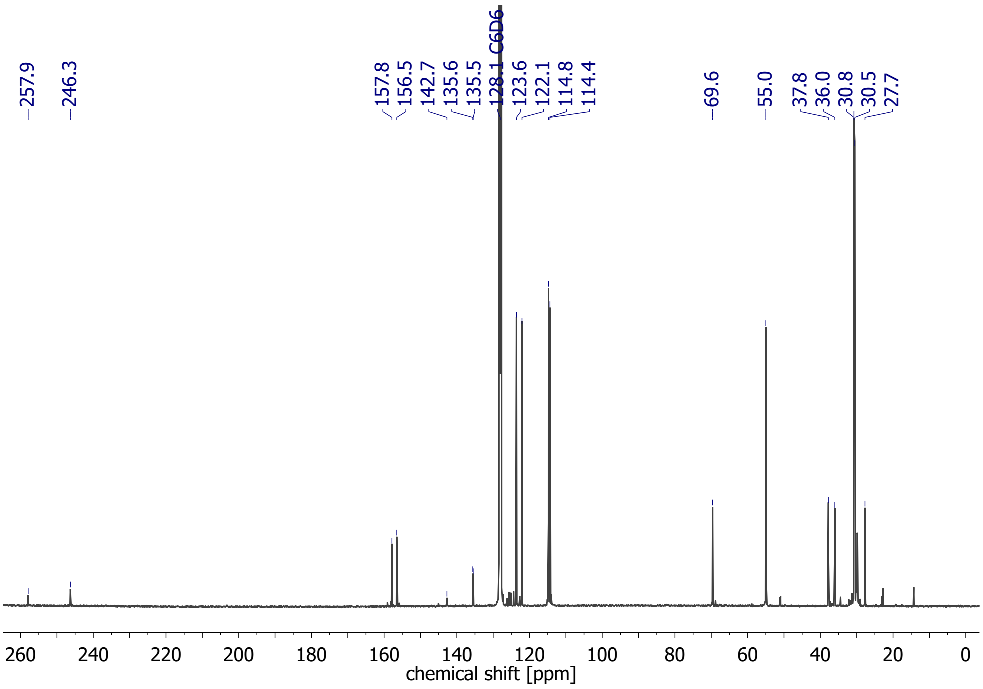

Figure 129: ^{13}C{^{1}H} NMR Spectrum of **23** in C_6D_6 at r.t.

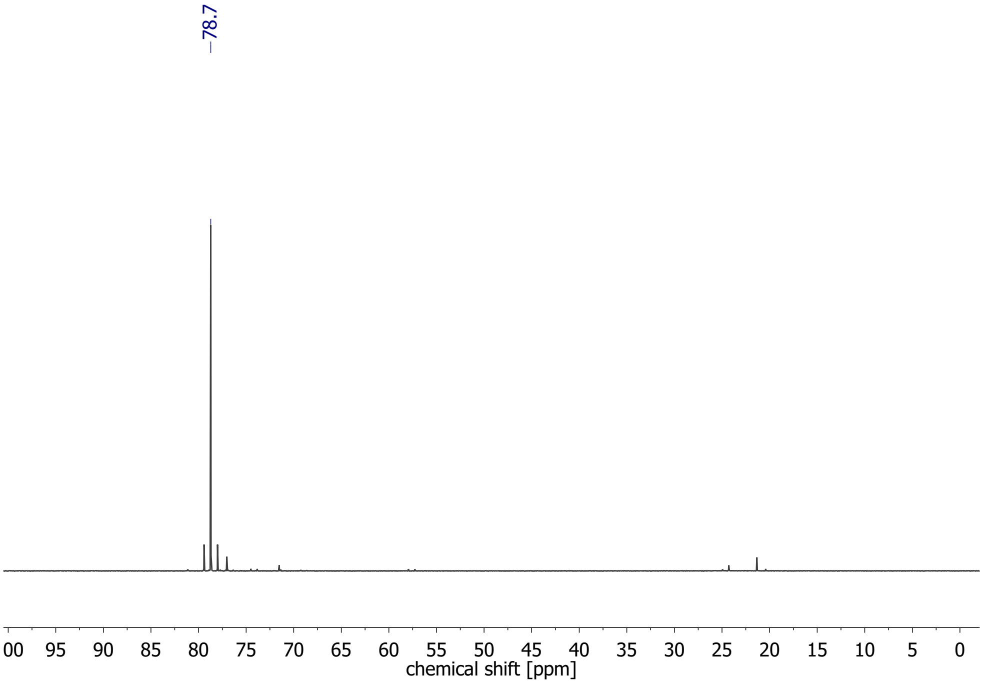

Figure 130: $^{31}P\{^1H\}$ NMR Spectrum of **23** in C_6D_6 at r.t.

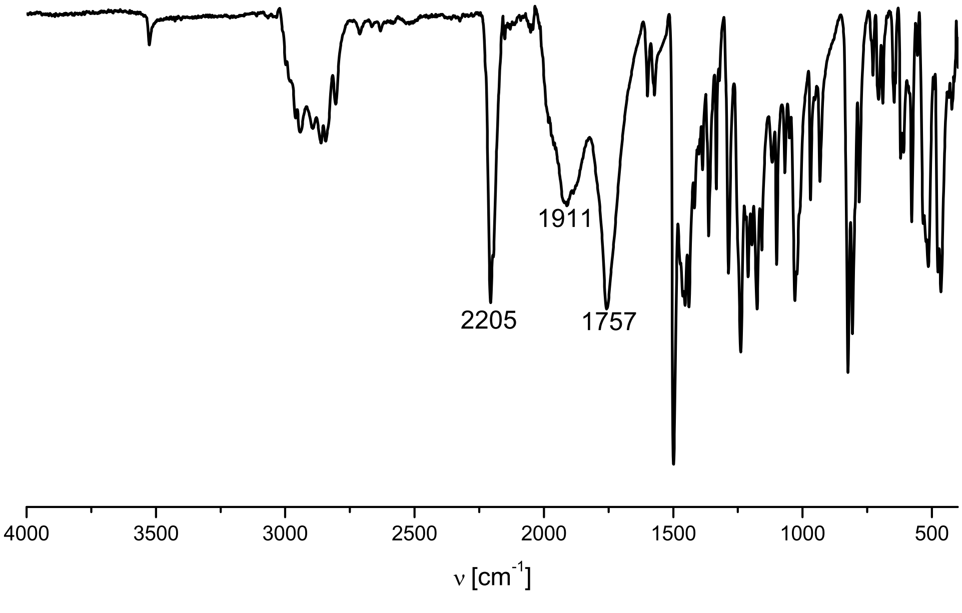

Figure 131: ATR-IR Spectrum of **23**.

6.1.20 [WCl(CN^{t}Bu)$_2$(PNP)] (6)

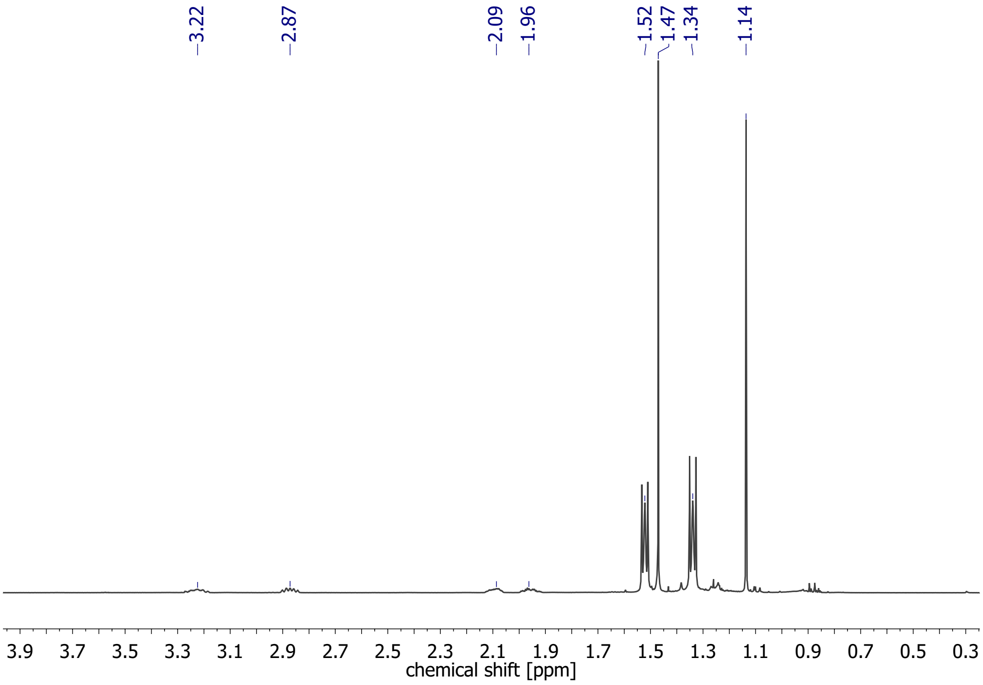

Figure 132: ^{1}H NMR Spectrum of **6** in D$_6$D$_6$ at r.t.

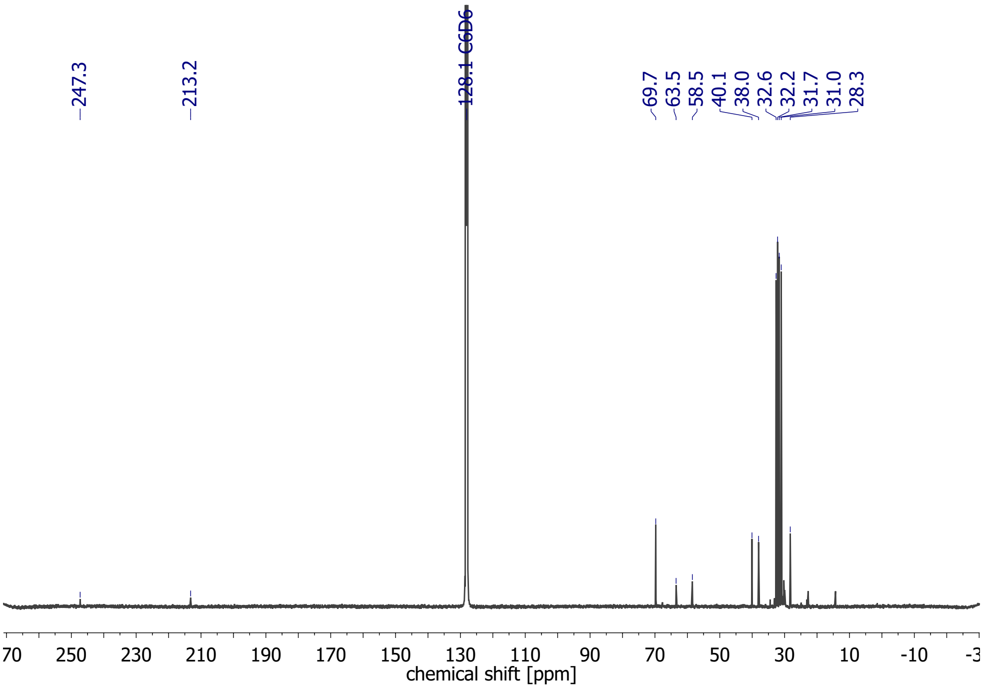

Figure 133: ^{13}C{^{1}H} NMR Spectrum of **6** in D$_6$D$_6$ at r.t.

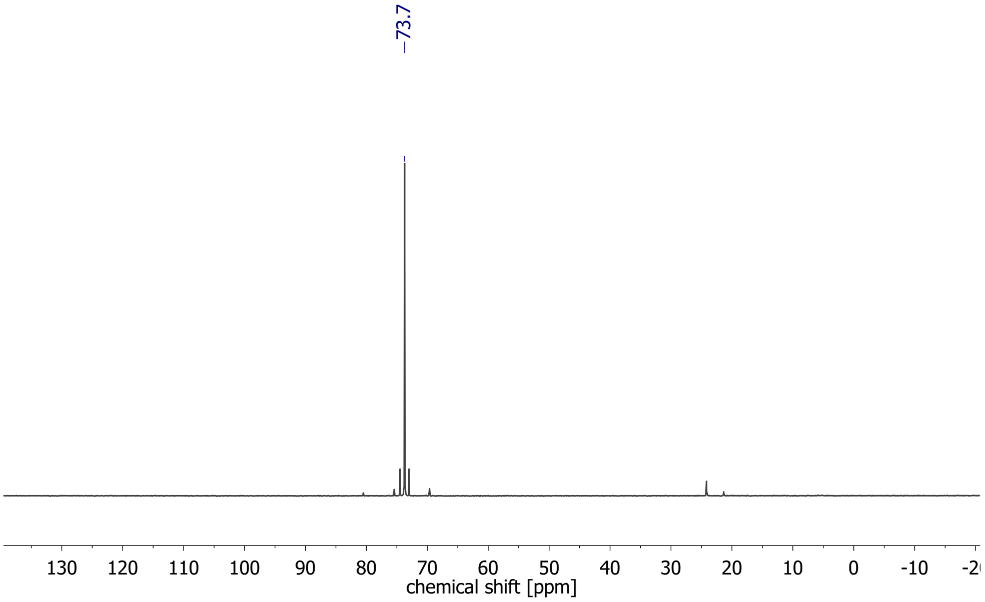

Figure 134: $^{31}P\{^{1}H\}$ NMR Spectrum of **6** in D_6D_6 at r.t.

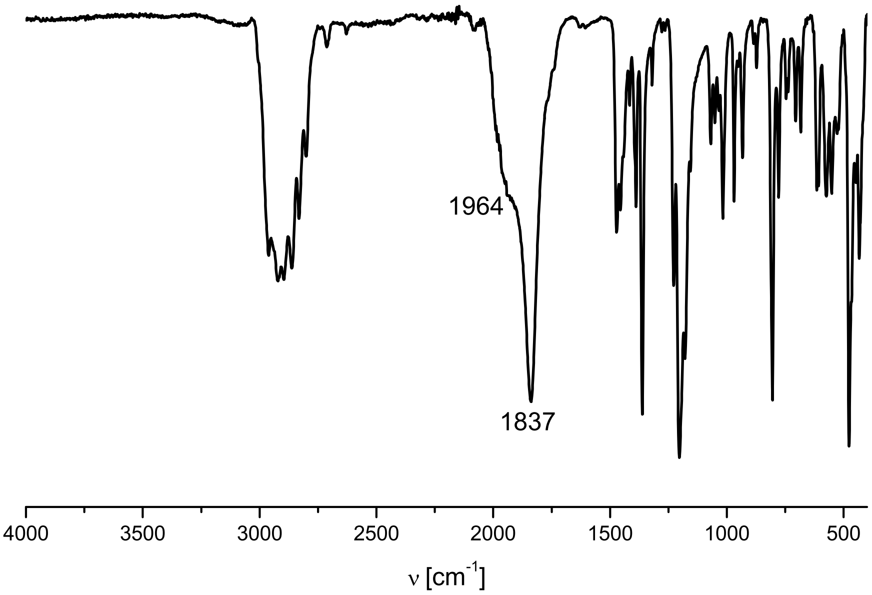

Figure 135: ATR-IR Spectrum of **6**.

6.1.21 Na[W(CO)$_2$(PNP)] (24)

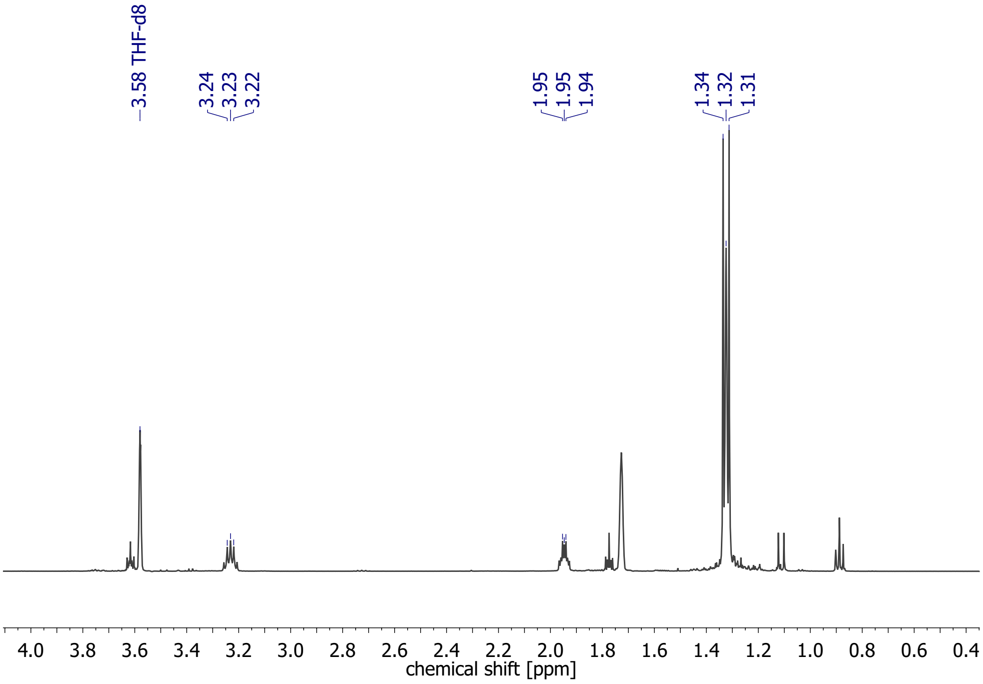

Figure 136: ^{1}H NMR Spectrum of **24** in THF—d$_8$ at r.t.

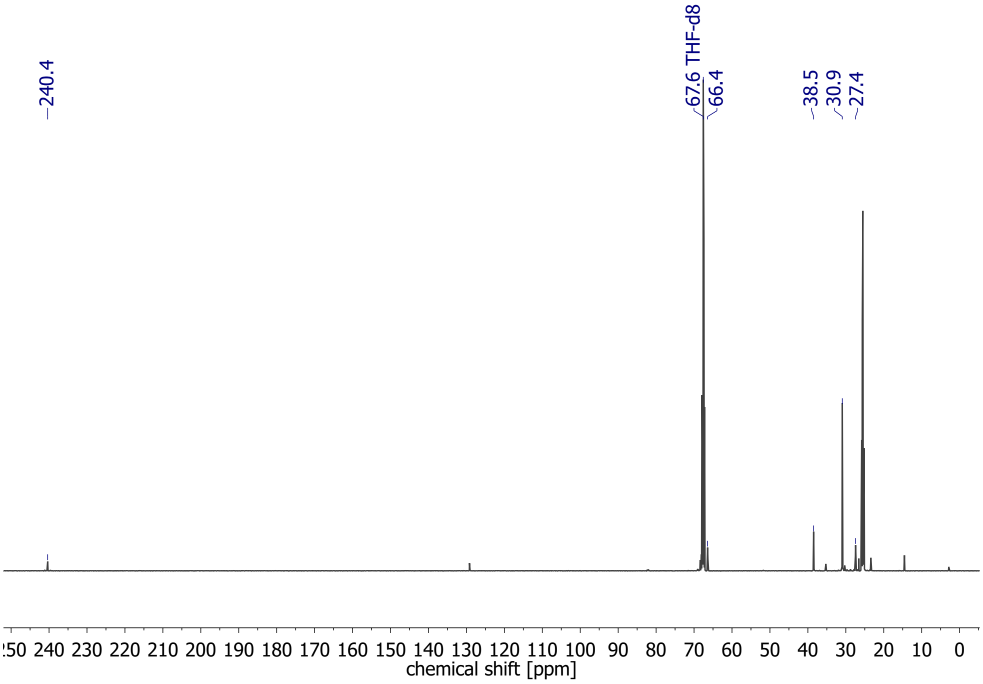

Figure 137: ^{13}C{^{1}H} NMR Spectrum of **24** in THF—d$_8$ at r.t.

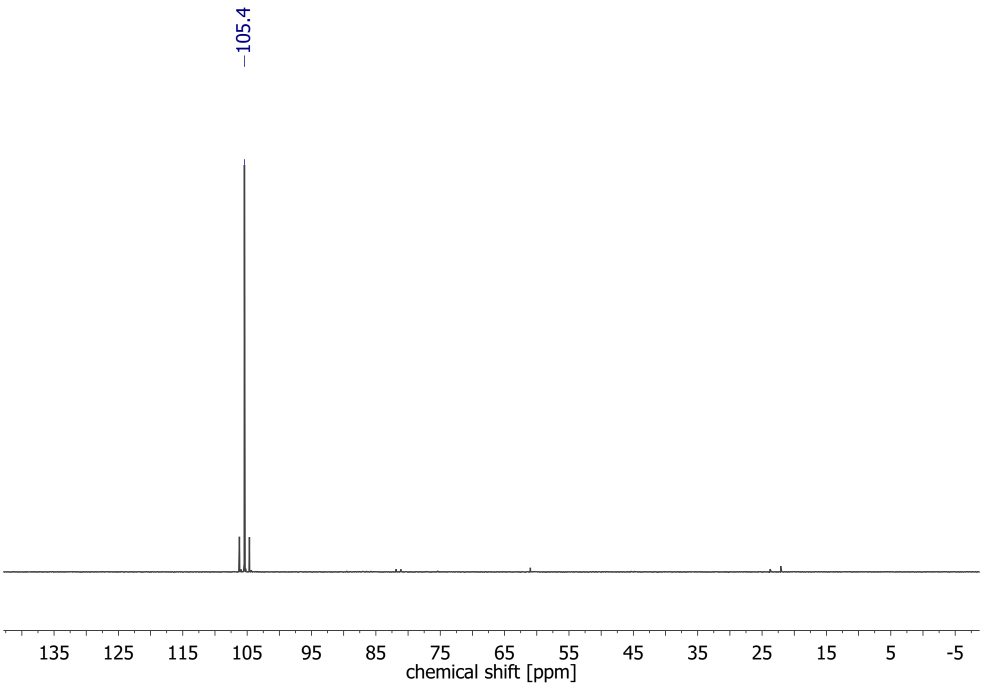

Figure 138: $^{31}P\{^1H\}$ NMR Spectrum of **24** in THF—d_8 at r.t.

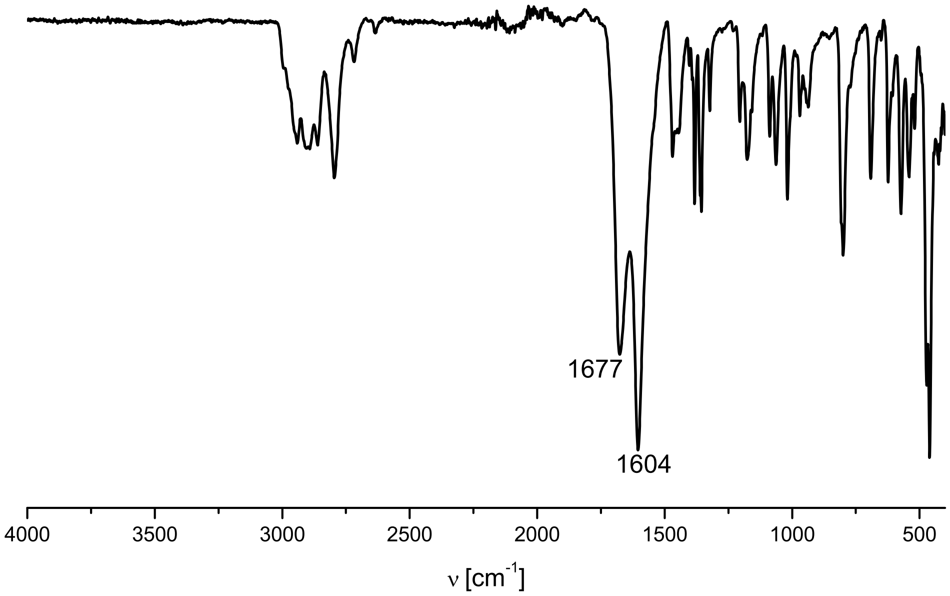

Figure 139: ATR-IR Spectrum of **24**.

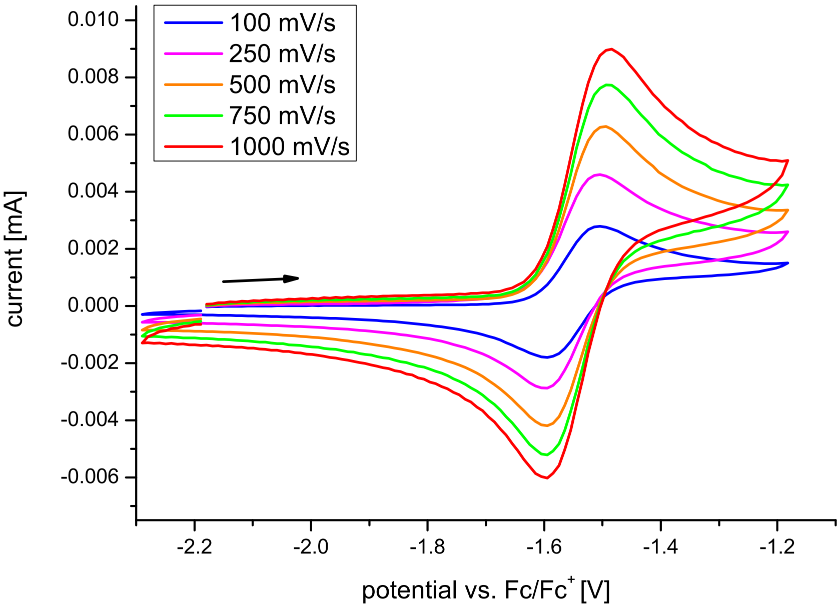

Figure 140: CV of the first oxidation event of **24** in 0.1 M solution of [^{n}Bu$_4$N][PF$_6$] in THF (WE = GC, RE = Ag/Ag$^+$, CE = Pt) at different scan rates.

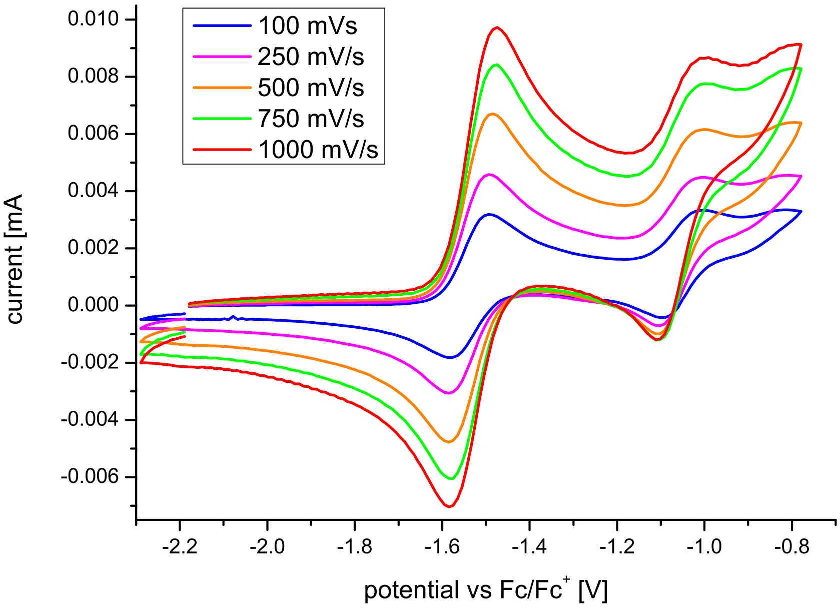

Figure 141: CV of the first two oxidation events of **24** in 0.1 M solution of [^{n}Bu$_4$N][PF$_6$] in THF (WE = GC, RE = Ag/Ag$^+$, CE = Pt) at different scan rates.

6.2 Crystal Structures

6.2.1 [WCl_3(PNP)] (5)

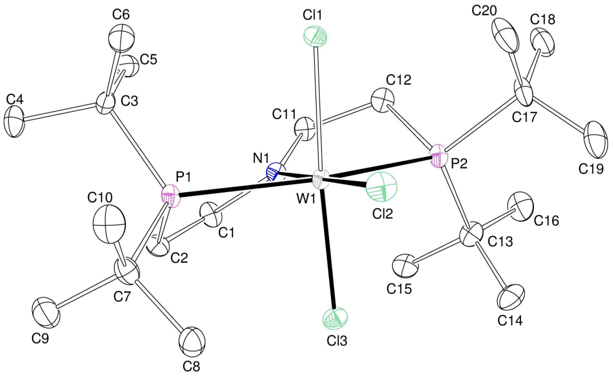

Figure 142: Thermal ellipsoid plot of **5** with the anisotropic displacement parameters drawn at the 50% probability level. The asymmetric unit contains one complex molecule.

Table 9: Crystal data and structure refinement for **5**.

Identification code	**5**	
Empirical formula	$C_{20}H_{44}Cl_3NP_2W$	
Formula weight	650.70	
Temperature	100(2) K	
Wavelength	0.71073 Å	
Crystal system	Orthorhombic	
Space group	Pbca	
Unit cell dimensions	a = 13.1751(7) Å	α = 90°
	b = 14.2709(8) Å	β = 90°
	c = 28.3358(16) Å	γ = 90°
Volume	5327.7(5) Å^3	
Z	8	
Density (calculated)	1.622 Mg/m^3	
Absorption coefficient	4.765 mm^{-1}	
F(000)	2608	
Crystal size	0.185 x 0.129 x 0.074 mm^3	
Crystal shape and color	Block, clear light orange-yellow	
Theta range for data collection	2.111 to 27.174°	
Index ranges	-16<=h<=16, -18<=k<=18, -36<=l<=36	
Reflections collected	213569	
Independent reflections	5908 [R(int) = 0.1012]	
Completeness to theta = 25.242°	100.0%	
Max. and min. transmission	0.7455 and 0.6750	
Refinement method	Full-matrix least-squares on F2	
Data / restraints / parameters	5908 / 0 / 256	
Goodness-of-fit on F^2	1.081	
Final R indices [I>2σ(I)]	R1 = 0.0291,	wR2 = 0.0473
R indices (all data)	R1 = 0.0451,	wR2 = 0.0507
Largest diff. peak and hole	1.018 and -1.379 eÅ^{-3}	

6.2.2 [(N_2){WCl(PNP)}$_2$] (1)

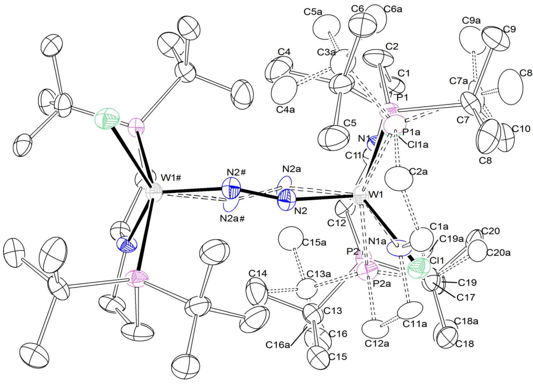
C5a
C6
C6a
C9a
C9
C4
C3a
C2
C1
C8a
C7a
C4a
P1
C7
C5
P1a
C10
N1
Cl1a
C11
C8
C2a
W1#
N2#
N2a
W1
N2
N2a#
C12
C1a
C20
N1a
C19a
C15a
P2
C20a
Cl1
C14
C13a
P2a
C19
C17
C13
C11a
C18a
C16
C16a
C12a
C18
C15

Figure 143: Thermal ellipsoid plot of **1** with the anisotropic displacement parameters drawn at the 50% probability level. The asymmetric unit contains a half disordered complex molecule. The disordered complex molecule was refined with population of 0.670(3) on the main domain using some restraints (SADI, RIGU).

Table 10: Crystal data and structure refinement for **1**.

Identification code	**1**	
Empirical formula	$C_{40}H_{88}Cl_2N_4P_4W_2$	
Formula weight	1187.62	
Temperature	100(2) K	
Wavelength	0.71073 Å	
Crystal system	Monoclinic	
Space group	C2/c	
Unit cell dimensions	a = 23.0363(8) Å	α = 90°
	b = 9.8057(3) Å	β = 111.350(2)°
	c = 23.3255(8) Å	γ = 90°
Volume	4907.3(3) $Å^{-3}$	
Z	4	
Density (calculated)	1.607 Mg/m^3	
Absorption coefficient	4.955 mm^{-1}	
F(000)	2392	
Crystal size	0.168 x 0.128 x 0.088 mm^3	
Crystal shape and color	Block, clear intense green	
Theta range for data collection	2.128 to 28.358°	
Index ranges	-30<=h<=30, -13<=k<=13, -30<=l<=31	
Reflections collected	53392	
Independent reflections	6110 [R(int) = 0.0747]	
Completeness to theta = 25.242°	100.0%	
Max. and min. transmission	0.7457 and 0.5543	
Refinement method	Full-matrix least-squares on F2	
Data / restraints / parameters	6110 / 217 / 456	
Goodness-of-fit on F2	1.089	
Final R indices [I>2sigma(I)]	R1 = 0.0303,	wR2 = 0.0482
R indices (all data)	R1 = 0.0473,	wR2 = 0.0518
Largest diff. peak and hole	1.434 and -1.253 $eÅ^{-3}$	

6.2.3 $[(N_2)\{WCl(PNP)\}_2]^+$ (2)

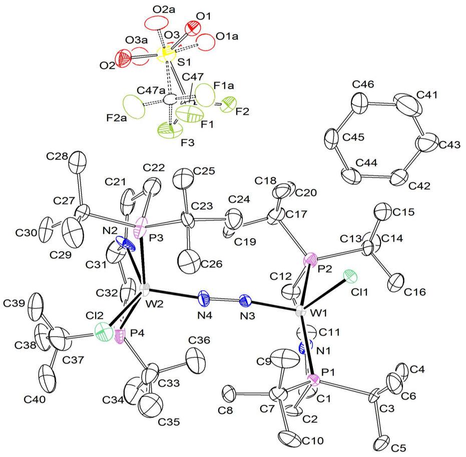
O2a
O1
O3a
O3
O1a
O2
S1
C47
C47a
F1a
F2a
F1
F2
F3
C46
C41
C45
C43
C44
C42
C28
C22
C25
C21
C18
C20
C27
C23
C24
C17
C15
C13
C14
C30
N2
P3
C19
C29
C31
C26
P2
C12
Cl1
C16
C32
W2
N4
N3
W1
C39
Cl2
C11
N1
C38
P4
C36
C37
C9
P1
C4
C6
C40
C34
C33
C1
C3
C8
C7
C2
C35
C10
C5

Figure 144: Thermal ellipsoid plot of **2** with the anisotropic displacement parameters drawn at the 50% probability level. The asymmetric unit contains one complex molecule, one benzene solvent molecule and one disordered $CF_3SO_3^-$ anion with a population of 0.67(1) on the main domain. The structure was refined as twin using the twin law -100 010 00-1 (BASF: 0.47(1)) and some restraints and constrains (SADI, RIGU, EADP). .

Table 11: Crystal data and structure refinement for **2**.

Identification code	**2**	
Empirical formula	$C_{47}H_{94}Cl_2F_3N_4O_3P_4SW_2$	
Formula weight	1414.80	
Temperature	100(2) K	
Wavelength	0.71073 Å	
Crystal system	Orthorhombic	
Space group	$Pna2_1$	
Unit cell dimensions	a = 19.7515(9) Å	α = 90°
	b = 13.2485(6) Å	β = 90°
	c = 22.2689(10) Å	γ = 90°
Volume	5827.3(5) $Å^3$	
Z	4	
Density (calculated)	1.613 Mg/m^3	
Absorption coefficient	4.232 mm^{-1}	
F(000)	2852	
Crystal size	0.370 x 0.096 x 0.033 mm^3	
Crystal shape and color	Needle, clear intense brown	
Theta range for data collection	2.256 to 28.397°	
Index ranges	-26<=h<=26, -17<=k<=17, -29<=l<=29	
Reflections collected	175705	
Independent reflections	14544 [R(int) = 0.1450]	
Completeness to theta = 25.242°	99.9%	
Refinement method	Full-matrix least-squares on F2	
Data / restraints / parameters	14544 / 232 / 651	
Goodness-of-fit on F2	1.081	
Final R indices [I>2sigma(I)]	R1 = 0.0513,	wR2 = 0.0968
R indices (all data)	R1 = 0.0683,	wR2 = 0.1029
Largest diff. peak and hole	2.428 and -1.729 $eÅ^{-3}$	

6.2.4 $[(N_2)\{WCl(PNP)\}_2]^{2+}$ (3)

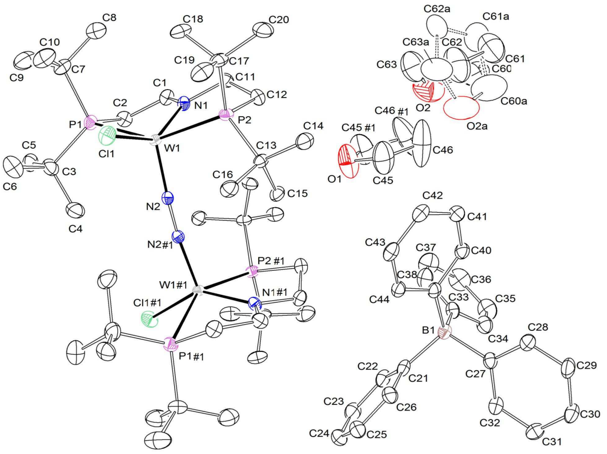
C8
C18
C20
C62a
C61a
C10
C63a
C62
C61
C9
C7
C19
C17
C63
C60
C11
C1
C12
O2
C60a
C2
N1
P2
C46 #1
O2a
P1
C45 #1
C14
Cl1
W1
C13
C46
C5
C3
O1
C45
C6
C16
C15
N2
C42
C4
C41
N2#1
C43
C37
C40
P2 #1
W1#1
C38
C36
N1#1
Cl1#1
C44
C33
C35
B1
C34
C28
P1#1
C22
C21
C27
C29
C23
C26
C32
C30
C24
C25
C31

Figure 145: Thermal ellipsoid plot of **3** with the anisotropic displacement parameters drawn at the 50% probability level. The asymmetric unit contains a half complex molecule, a half THF solvent molecule, one BPh_4 anion and one disordered THF solvent molecule. The disordered THF molecule was refined with population of 0.506(6) on the main domain using some restraints (SADI, RIGU)..

Table 12: Crystal data and structure refinement for **3**.

Identification code	**3**	
Empirical formula	$C_{100}H_{152}B_2Cl_2N_4O_3P_4W_2$	
Formula weight	2042.35	
Temperature	101(2) K	
Wavelength	0.71073 Å	
Crystal system	Monoclinic	
Space group	C2/c	
Unit cell dimensions	a = 35.4758(14) Å	α = 90°
	b = 14.6906(6) Å	β = 131.4330(10)°
	c = 24.6143(17) Å	γ = 90°
Volume	9617.5(9) Å^3	
Z	4	
Density (calculated)	1.411 Mg/m^3	
Absorption coefficient	2.563 mm^{-1}	
F(000)	4224	
Crystal size	0.200 x 0.101 x 0.076 mm^3	
Crystal shape and color	Plate, clear intense yellow-brown	
Theta range for data collection	2.201 to 30.605°	
Index ranges	-50<=h<=50, -20<=k<=20, -34<=l<=35	
Reflections collected	139562	
Independent reflections	14725 [R(int) = 0.1073]	
Completeness to theta = 25.242°	100.0%	
Refinement method	Full-matrix least-squares on F2	
Data / restraints / parameters	14725 / 90 / 586	
Goodness-of-fit on F2	1.018	
Final R indices [I>2sigma(I)]	R1 = 0.0373,	wR2 = 0.0618
R indices (all data)	R1 = 0.0714,	wR2 = 0.0700
Largest diff. peak and hole	1.601 and -1.376 eÅ^{-3}	

6.2.5 [W(N)Cl(^{H}PNP)]$^+$ (11)

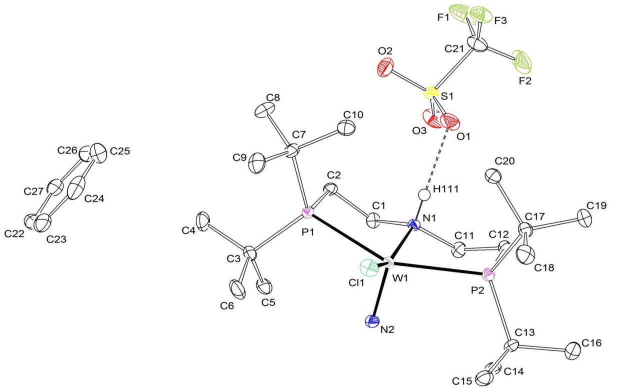

Figure 146: Thermal ellipsoid plot of **11** with the anisotropic displacement parameters drawn at the 50% probability level. The asymmetric unit contains one cationic complex molecule, one CF_3COO^- anion and one benzene solvent molecule. The N-H hydrogen atom was found from the residual density map and isotropically refined.

Table 13: Crystal data and structure refinement for **11**.

Identification code	**11**	
Empirical formula	$C_{27}H_{51}ClF_3N_2O_3P_2SW$	
Formula weight	821.99	
Temperature	100(2) K	
Wavelength	0.71073 Å	
Crystal system	Monoclinic	
Space group	$P2_{1/c}$	
Unit cell dimensions	a = 19.1996(8) Å	α = 90°
	b = 10.9562(4) Å	β = 99.585(2)°
	c = 16.6152(7) Å	γ = 90°
Volume	3446.3(2) Å^3	
Z	4	
Density (calculated)	1.584 Mg/m^3	
Absorption coefficient	3.629 mm^{-1}	
F(000)	1660	
Crystal size	0.336 x 0.327 x 0.178 mm^3	
Crystal shape and color	Plate, clear intense green	
Theta range for data collection	2.236 to 28.437°	
Index ranges	-25<=h<=25, -14<=k<=14, -22<=l<=22	
Reflections collected	130600	
Independent reflections	8680 [R(int) = 0.0796]	
Completeness to theta = 25.242°°	100.0%	
Refinement method	Full-matrix least-squares on F2	
Data / restraints / parameters	8680 / 0 / 377	
Goodness-of-fit on F2	1.058	
Final R indices [I>2sigma(I)]	R1 = 0.0261,	wR2 = 0.0470
R indices (all data)	R1 = 0.0371,	wR2 = 0.0495
Largest diff. peak and hole	1.456 and -1.350 eÅ^{-3}	

6.2.6 [(N_2){WCl(CO)(PNP)}$_2$] (8)

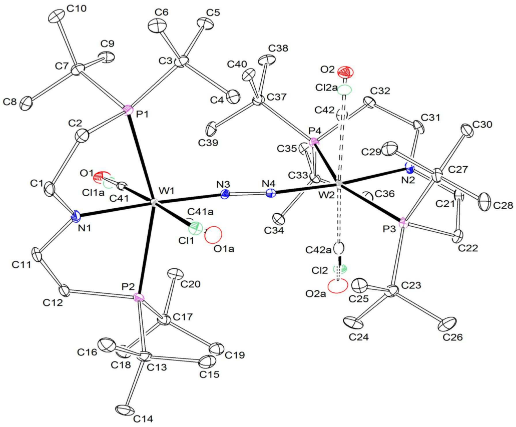
C10
C6
C5
C9
C7
C3
C38
C40
O2
C8
C4
C37
Cl2a
C32
C42
C2
P1
C31
C30
C39
P4
C35
C29
C1
O1
C33
N2
C27
Cl1a
W1
N3
N4
C41
W2
C36
C28
C21
C41a
N1
P3
C34
Cl1
O1a
C22
C42a
C11
Cl2
C20
P2
C23
O2a
C25
C12
C17
C24
C26
C16
C19
C18
C13
C15
C14

Figure 147: Thermal ellipsoid plot of **8** with the anisotropic displacement parameters drawn at the 50% probability level. The asymmetric unit contains one disordered complex molecule. The disordered complex molecule was refined with population of 0.845(5) and 0.724(8) on their main domains using some restraints and constraints (SADI, EADP). The structure was refined as an inversion twin using the twin law -100 0-10 00-1 (BASF: 0.307(4)). Reflection 0 2 1 was removed from the refinement using OMIT commands.

Table 14: Crystal data and structure refinement for **11**.

Identification code	**8**	
Empirical formula	$C_{42}H_{88}Cl_2N_4O_2P_4W_2$	
Formula weight	1243.64	
Temperature	101(2) K	
Wavelength	0.71073 Å	
Crystal system	Orthorhombic	
Space group	$P2_12_12_1$	
Unit cell dimensions	a = 12.2138(5) Å	α = 90°
	b = 18.6597(8) Å	β = 90°
	c = 23.1169(9) Å	γ = 90°
Volume	5268.5(4) $Å^3$	
Z	4	
Density (calculated)	1.568 Mg/m^3	
Absorption coefficient	4.622 mm^{-1}	
F(000)	2504	
Crystal size	0.284 x 0.165 x 0.134 mm^3	
Crystal shape and color	Block, dark blue	
Theta range for data collection	2.179 to 28.357°	
Index ranges	-16<=h<=16, -24<=k<=24, -30<=l<=30	
Reflections collected	163801	
Independent reflections	13100 [R(int) = 0.0659]	
Completeness to theta = 25.242°	99.9%	
Refinement method	Full-matrix least-squares on F2	
Data / restraints / parameters	13100 / 24 / 568	
Goodness-of-fit on F2	1.056	
Final R indices [I>2sigma(I)]	R1 = 0.0187,	wR2 = 0.0312
R indices (all data)	R1 = 0.0233,	wR2 = 0.0321
Largest diff. peak and hole	0.495 and -0.783 $eÅ^{-3}$	

6.2.7 [(N_2){W(CO)(PNP)}$_2$] (4)

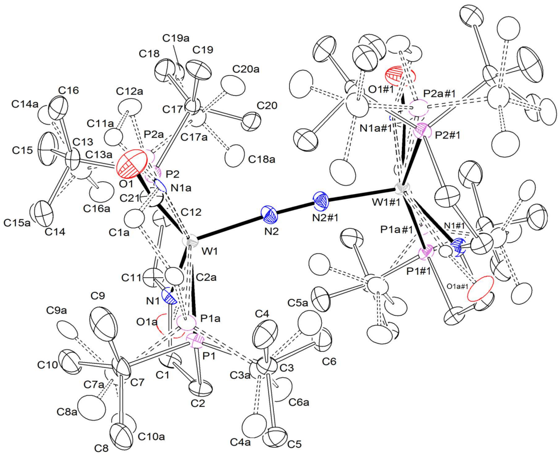
C19a
C18
C19
C20a
C16
C12a
C14a
C11a
C17
C20
P2a
C17a
C15
C13
C13a
C18a
P2
O1
N1a
C21
C12
C16a
C15a
C14
C1a
N2
N2#1
W1
C11
C2a
C9
N1
C9a
O1a
P1a
C4
C5a
C10
P1
C3a
C3
C6
C7a
C7
C1
C2
C6a
C8a
C10a
C8
C4a
C5
O1#1
P2a#1
N1a#1
P2#1
W1#1
P1a#1
N1#1
P1#1
O1a#1

Figure 148: Thermal ellipsoid plot of **4** with the anisotropic displacement parameters drawn at the 25% probability level. The asymmetric unit contains a half disordered complex molecule. The disordered complex molecule was refined with population of 0.799(6) on the main domain using some restraints (SADI, RIGU).

Table 15: Crystal data and structure refinement for **4**.

Identification code	**4**	
Empirical formula	$C_{42}H_{88}N_4O_2P_4W_2$	
Formula weight	1172.74	
Temperature	100(2) K	
Wavelength	0.71073 Å	
Crystal system	Monoclinic	
Space group	C2/c	
Unit cell dimensions	a = 27.147(3) Å	α= 90 °
	b = 9.8359(11) Å	β= 109.232(4)°
	c = 19.638(2) Å	γ = 90°
Volume	4951.0(10) Å^3	
Z	4	
Density (calculated)	1.573 Mg/m^3	
Absorption coefficient	4.809 mm^{-1}	
F(000)	2368	
Crystal size	0.219 x 0.169 x 0.070 mm3	
Crystal shape and color	Block, dark blue	
Theta range for data collection	2.218 to 25.388°	
Index ranges	-29<=h<=32, -11<=k<=11, -23<=l<=23	
Reflections collected	33664	
Independent reflections	4465 [R(int) = 0.0579]	
Completeness to theta = 25.242°	98.0%	
Refinement method	Full-matrix least-squares on F2	
Data / restraints / parameters	4465 / 646 / 494	
Goodness-of-fit on F2	1.224	
Final R indices [I>2sigma(I)]	R1 = 0.0478,	wR2 = 0.1012
R indices (all data)	R1 = 0.0555,	wR2 = 0.1058
Largest diff. peak and hole	2.492 and -1.568 eÅ $^{-3}$	

6.2.8 [WI(CO)$_2$(PNP)] (18)

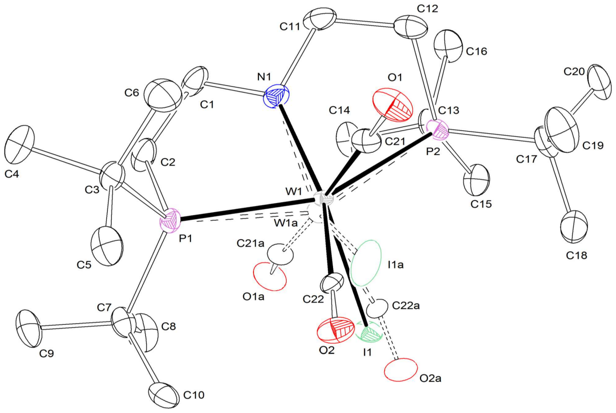

Figure 149: Thermal ellipsoid plot of **18** with the anisotropic displacement parameters drawn at the 50% probability level. The asymmetric unit contains one disordered complex molecule. The disordered complex molecule was refined with population of 0.9311(9) on the main domain using some restraints and constraints (SADI, EADP).

Table 16: Crystal data and structure refinement for **18**.

Identification code	**18**	
Empirical formula	$C_{22}H_{44}INO_2P_2W$	
Formula weight	727.27	
Temperature	100(2) K	
Wavelength	0.71073 Å	
Crystal system	Monoclinic	
Space group	$P2_{1/c}$	
Unit cell dimensions	a = 13.6443(6) Å	α = 90°
	b = 12.7207(5) Å	β = 91.120(2)°
	c = 15.7397(7) Å	γ = 90°
Volume	2731.3(2) Å^3	
Z	4	
Density (calculated)	1.769 Mg/m^3	
Absorption coefficient	5.494 mm^{-1}	
F(000)	1424	
Crystal size	0.242 x 0.074 x 0.051 mm^3	
Crystal shape and color	Plate, intense orange	
Theta range for data collection	2.189 to 28.376°	
Index ranges	-18<=h<=18, -16<=k<=16, -20<=l<=21	
Reflections collected	84964	
Independent reflections	6817 [R(int) = 0.0800]	
Completeness to theta = 25.242°	99.9%	
Refinement method	Full-matrix least-squares on F2	
Data / restraints / parameters	6817 / 15 / 305	
Goodness-of-fit on F2	1.132	
Final R indices [I>2sigma(I)]	R1 = 0.0300,	wR2 = 0.0443
R indices (all data)	R1 = 0.0439,	wR2 = 0.0469
Largest diff. peak and hole	0.957 and -0.994 eÅ^{-3}	

6.2.9 [W(N)(CO)(^{H}PNP)]$^+$ (20)

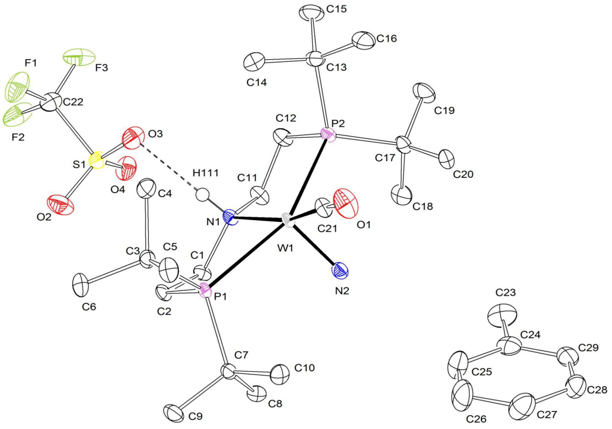

Figure 150: Thermal ellipsoid plot of **20** with the anisotropic displacement parameters drawn at the 50% probability level. The asymmetric unit contains one complex molecule one $CF_3SO_3^-$ anion and one toluene solvent molecule. The N-H hydrogen atom was found from the residual density map and isotropically refined.

Table 17: Crystal data and structure refinement for **20**.

Identification code	**20**	
Empirical formula	$C_{29}H_{53}F_3N_2O_4P_2SW$	
Formula weight	828.58	
Temperature	100(2) K	
Wavelength	0.71073 Å	
Crystal system	Triclinic	
Space group	P-1	
Unit cell dimensions	a = 10.1515(5) Å	α = 89.010(2)°
	b = 12.4018(5) Å	β = 84.707(2)°
	c = 14.1176(6) Å	γ = 84.964(2)°
Volume	1762.88(14) Å^3	
Z	2	
Density (calculated)	1.561 Mg/m^3	
Absorption coefficient	3.476 mm^{-1}	
F(000)	840	
Crystal size	0.296 x 0.287 x 0.162 mm^3	
Crystal shape and color	Plate, clear intense red	
Theta range for data collection	2.205 to 30.628°	
Index ranges	-14<=h<=14, -17<=k<=17, -20<=l<=20	
Reflections collected	113344	
Independent reflections	10868 [R(int) = 0.0773]	
Completeness to theta = 25.242°	99.9%	
Refinement method	Full-matrix least-squares on F2	
Data / restraints / parameters	10868 / 0 / 396	
Goodness-of-fit on F2	1.033	
Final R indices [I>2sigma(I)]	R1 = 0.0265,	wR2 = 0.0417
R indices (all data)	R1 = 0.0393,	wR2 = 0.0444
Largest diff. peak and hole	1.700 and -0.765 eÅ^{-3}	

6.2.10 [W(NCO)(CO)$_2$(PNP)] (21)

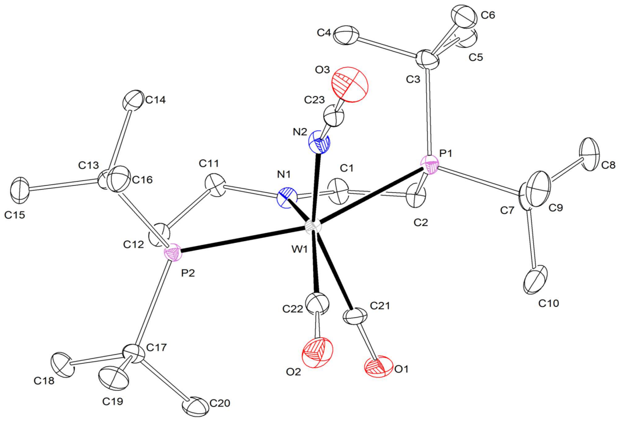

Figure 151: Thermal ellipsoid plot of **21** with the anisotropic displacement parameters drawn at the 50% probability level. The asymmetric unit contains one complex molecule. The reflections 2 0 0 and 8 9 16 are removed from the refinement using OMIT commands.

Table 18: Crystal data and structure refinement for **21**.

Identification code	**21**	
Empirical formula	$C_{23}H_{44}N_2O_3P_2W$	
Formula weight	642.39	
Temperature	100(2) K	
Wavelength	0.71073 Å	
Crystal system	Orthorhombic	
Space group	Pbca	
Unit cell dimensions	a = 16.8071(14) Å	α = 90°
	b = 13.5576(11) Å	β = 90°
	c = 23.5209(17) Å	γ = 90°
Volume	5359.6(7) $Å^3$	
Z	8	
Density (calculated)	1.592 Mg/m^3	
Absorption coefficient	4.455 mm^{-1}	
F(000)	2592	
Crystal size	0.231 x 0.093 x 0.051 mm^3	
Crystal shape and color	Plate, clear intense purple	
Theta range for data collection	2.593 to 27.927°	
Index ranges	-22<=h<=21, -17<=k<=17, -30<=l<=30	
Reflections collected	45436	
Independent reflections	6275 [R(int) = 0.0687]	
Completeness to theta = 25.242°°	97.8%	
Refinement method	Full-matrix least-squares on F2	
Data / restraints / parameters	6275 / 0 / 292	
Goodness-of-fit on F2	1.025	
Final R indices [I>2sigma(I)]	R1 = 0.0288,	wR2 = 0.0647
R indices (all data)	R1 = 0.0462,	wR2 = 0.0726
Largest diff. peak and hole	2.639 and -2.055 $eÅ^{-3}$	

6.2.11 [W(NCO)(CN^{t}Bu)$_2$(PNP)] (22)

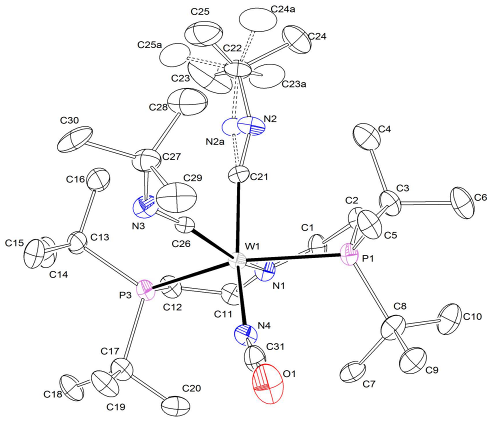

Figure 152: Thermal ellipsoid plot of **22** with the anisotropic displacement parameters drawn at the 50% probability level. The asymmetric unit contains one disordered complex molecule. The disordered complex molecule was refined with population of 0.67(1) on the main domain using some restraints (RIGU, SADI). The structure was refined as an inversion twin using the twin law -100 0-10 00-1 (BASF: 0.03(1)).

Table 19: Crystal data and structure refinement for **22**.

Identification code	**22**	
Empirical formula	$C_{31}H_{62}N_4OP_2W$	
Formula weight	752.63	
Temperature	100(2) K	
Wavelength	0.71073 Å	
Crystal system	Orthorhombic	
Space group	$Pna2_1$	
Unit cell dimensions	a = 13.5380(9) Å	α = 90°
	b = 18.3332(12) Å	β = 90°
	c = 14.4776(9) Å	γ = 90°
Volume	3593.3(4) Å^3	
Z	4	
Density (calculated)	1.391 Mg/m^3	
Absorption coefficient	3.331 mm^{-1}	
F(000)	1552	
Crystal size	0.357 x 0.252 x 0.208 mm^3	
Crystal shape and color	Block, dark green	
Theta range for data collection	2.340 to 30.602°	
Index ranges	-19<=h<=19, -26<=k<=26, -20<=l<=20	
Reflections collected	59367	
Independent reflections	11011 [R(int) = 0.1325]	
Completeness to theta = 25.242°	99.7%	
Refinement method	Full-matrix least-squares on F2	
Data / restraints / parameters	11011 / 94 / 409	
Goodness-of-fit on F2	1.003	
Final R indices [I>2sigma(I)]	R1 = 0.0431,	wR2 = 0.0698
R indices (all data)	R1 = 0.0833,	wR2 = 0.0811
Absolute structure parameter	0.036(12)	
Largest diff. peak and hole	2.271 and -1.198 eÅ^{-3}	

6.2.12 [W(NCO)(CN-C_6H_4-OMe)$_2$(PNP)] (23)

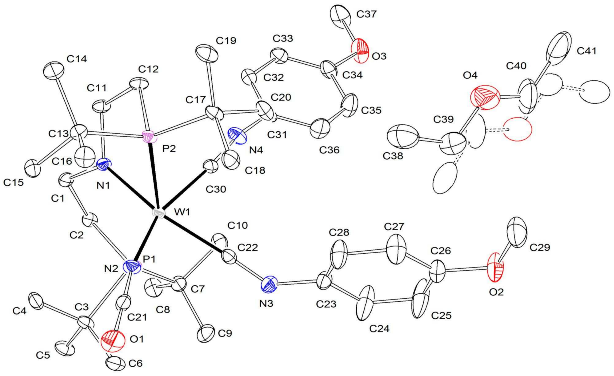
C37
C41
C33
O3
C19
C14
C12
C34
O4
C40
C11
C32
C17
C20
C35
C39
C13
P2
C31
N4
C36
C38
C16
C18
C15
N1
C30
C1
W1
C10
C28
C27
C26
C2
C22
C29
P1
N2
C7
N3
O2
C8
C23
C4
C3
C21
C24
C25
C9
O1
C5
C6

Figure 153: Thermal ellipsoid plot of **23** with the anisotropic displacement parameters drawn at the 50% probability level. The asymmetric unit contains one complex molecule and a half disordered diethyl ether solvent molecule. The disorder was refined using PART -1 command.

Table 20: Crystal data and structure refinement for **23**.

Identification code	**23**	
Empirical formula	$C_{37}H_{58}N_4O_3P_2W \cdot 0.5\,C_4H_{10}O$	
Formula weight	889.72	
Temperature	100(2) K	
Wavelength	0.71073 Å	
Crystal system	Triclinic	
Space group	P-1	
Unit cell dimensions	a = 9.4010(6) Å	α = 104.902(2)°
	b = 11.0756(7) Å	β = 94.164(3)°
	c = 20.7216(14) Å	γ = 101.531(3)°
Volume	2025.3(2) Å^3	
Z	2	
Density (calculated)	1.459 Mg/m^3	
Absorption coefficient	2.972 mm^{-1}	
F(000)	914	
Crystal size	0.391 x 0.113 x 0.094 mm^3	
Crystal shape and color	Plate, dark brown	
Theta range for data collection	2.230 to 28.394°	
Index ranges	-12<=h<=12, -14<=k<=14, -27<=l<=27	
Reflections collected	140974	
Independent reflections	10120 [R(int) = 0.0882]	
Completeness to theta = 25.242°	99.9%	
Refinement method	Full-matrix least-squares on F2	
Data / restraints / parameters	10120 / 0 / 485	
Goodness-of-fit on F2	1.090	
Final R indices [I>2sigma(I)]	R1 = 0.0244,	wR2 = 0.0468
R indices (all data)	R1 = 0.0343,	wR2 = 0.0501
Largest diff. peak and hole	1.922 and -1.107 eÅ^{-3}	

6.2.13 [WCl(CN^{t}Bu)$_2$(PNP)] (6)

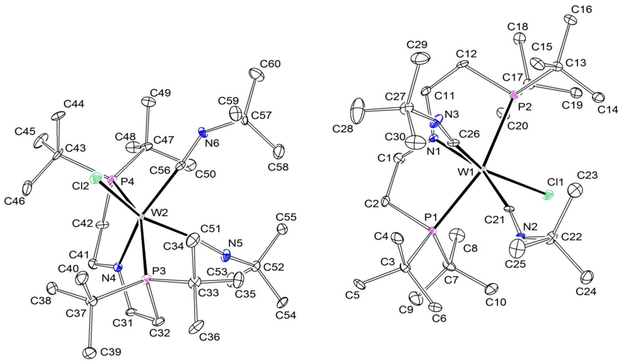
C44
C45
C43
C46
Cl2
C48
C47
C49
P4
C56
C50
N6
C59
C57
C60
C58
W2
C42
C51
C55
N5
C34
C52
C41
C40
N4
P3
C53
C33
C35
C38
C37
C31
C32
C36
C54
C39
C16
C18
C15
C13
C29
C12
C17
C19
C14
C27
C11
P2
C28
N3
C26
C20
C30
N1
C1
W1
Cl1
C23
C2
P1
C21
N2
C22
C4
C8
C25
C3
C7
C24
C5
C9
C6
C10

Figure 154: Thermal ellipsoid plot of **6** with the anisotropic displacement parameters drawn at the 50% probability level. The asymmetric unit contains two complex molecules.

Table 21: Crystal data and structure refinement for **6**.

Identification code	**6**	
Empirical formula	$C_{30}H_{62}ClN_3P_2W$	
Formula weight	746.06	
Temperature	101(2) K	
Wavelength	0.71073 Å	
Crystal system	Orthorhombic	
Space group	$P2_12_12_1$	
Unit cell dimensions	a = 17.4654(9) Å	α = 90°
	b = 17.9198(9) Å	β = 90°
	c = 22.6945(12) Å	γ = 90°
Volume	7102.8(6) Å^3	
Z	8	
Density (calculated)	1.395 Mg/m^3	
Absorption coefficient	3.440 mm^{-1}	
F(000)	3072	
Crystal size	0.426 x 0.314 x 0.125 mm^3	
Crystal shape and color	Block, clear intense blue-green	
Theta range for data collection	2.273 to 30.562°	
Index ranges	-24<=h<=22, -24<=k<=25, -32<=l<=32	
Reflections collected	111814	
Independent reflections	21707 [R(int) = 0.1530]	
Completeness to theta = 25.242°	99.9%	
Refinement method	Full-matrix least-squares on F2	
Data / restraints / parameters	21707 / 0 / 703	
Goodness-of-fit on F2	0.995	
Final R indices [I>2sigma(I)]	R1 = 0.0489,	wR2 = 0.0749
R indices (all data)	R1 = 0.0871,	wR2 = 0.0850
Absolute structure parameter	0.010(6)	
Largest diff. peak and hole	2.581 and -2.121 eÅ^{-3}	

6.2.14 Na[W(CO)$_2$(PNP)] (24)

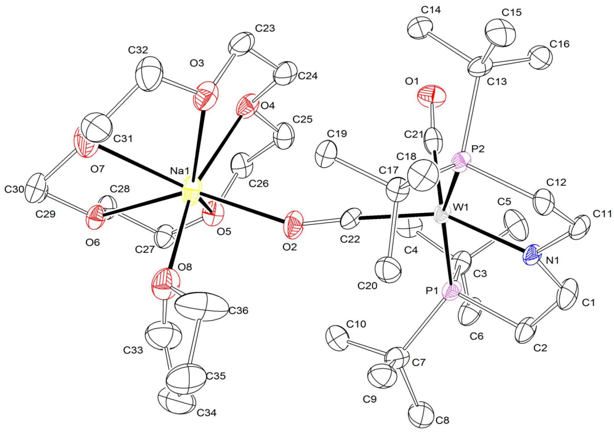
C14
C15
C16
C23
C32
O3
C24
O1
C13
O4
C25
C19
C21
C31
C18
P2
O7
Na1
C17
C12
C30
C28
C26
W1
C5
C11
C29
O5
O6
C27
O2
C22
C4
N1
C3
O8
C20
P1
C1
C36
C10
C6
C2
C33
C7
C35
C9
C8
C34

Figure 155: Thermal ellipsoid plot of **24** with the anisotropic displacement parameters drawn at the 50% probability level. The asymmetric unit contains one complex molecule. The reflections -5 5 6 and -5 5 8 are removed from the refinement using OMIT commands.

Table 22: Crystal data and structure refinement for **24**.

Identification code	**24**	
Empirical formula	$C_{36}H_{72}NNaO_8P_2W$	
Formula weight	915.72	
Temperature	100(2) K	
Wavelength	0.71073 Å	
Crystal system	Monoclinic	
Space group	$P2_{1/n}$	
Unit cell dimensions	a = 10.2148(9) Å	α = 90°
	b = 21.2618(17) Å	β = 93.444(3)°
	c = 19.0681(17) Å	γ = 90°
Volume	4133.8(6) Å^3	
Z	4	
Density (calculated)	1.471 Mg/m^3	
Absorption coefficient	2.929 mm−1	
F(000)	1896	
Crystal size	0.451 x 0.231 x 0.068 mm^3	
Crystal shape and color	Plate, clear intense orange	
Theta range for data collection	2.194 to 25.759°	
Index ranges	-12<=h<=12, -25<=k<=22, -23<=l<=23	
Reflections collected	114649	
Independent reflections	7903 [R(int) = 0.0962]	
Completeness to theta = 25.242°	99.9%	
Refinement method	Full-matrix least-squares on F2	
Data / restraints / parameters	7903 / 0 / 454	
Goodness-of-fit on F2	1.350	
Final R indices [I>2sigma(I)]	R1 = 0.0521,	wR2 = 0.1305
R indices (all data)	R1 = 0.0601,	wR2 = 0.1345
Largest diff. peak and hole	2.155 and -1.946 e Å^{-3}	

References

[1] Hoffman, B. M.; Dean, D. R.; Seefeldt, L. C. *Accounts of Chemical Research* **2009**, *42*, 609–619.

[2] Hoffman, B. M.; Lukoyanov, D.; Yang, Z.-Y.; Dean, D. R.; Seefeldt, L. C. *Chemical Reviews* **2014**, *114*, 4041–4062.

[3] Haber, F. *Die Naturwissenschaften* **1922**, *10*, 1041–1049.

[4] Ertl, G. *Angewandte Chemie International Edition* **2008**, *47*, 3524–3535.

[5] Erisman, J. W.; Sutton, M. A.; Galloway, J.; Klimont, Z.; Winiwarter, W. *Nature Geoscience* **2008**, *1*, 636.

[6] Bezdek, M. J.; Chirik, P. J. *Angewandte Chemie International Edition* **2016**, *55*, 7892–7896.

[7] van der Ham, C. J. M.; Koper, M. T. M.; Hetterscheid, D. G. H. *Chem. Soc. Rev.* **2014**, *43*, 5183–5191.

[8] Yandulov, D. V.; Schrock, R. R. *Science* **2003**, *301*, 76–78.

[9] Arashiba, K.; Miyake, Y.; Nishibayashi, Y. *Nature Chemistry* **2011**, *3*, 120–125.

[10] Anderson, J. S.; Rittle, J.; Peters, J. C. *Nature* **2013**, *501*, 84–87.

[11] Ertl, G. *Catalysis Reviews* **1980**, *21*, 201–223.

[12] Laplaza, C. E.; Cummins, C. C. *Science* **1995**, *268*, 861–863.

[13] Rodriguez, M. M.; Bill, E.; Brennessel, W. W.; Holland, P. L. *Science* **2011**, *334*, 780–783.

[14] Hebden, T. J.; Schrock, R. R.; Takase, M. K.; Müller, P. *Chemical Communications* **2012**, *48*, 1851.

[15] Klopsch, I.; Finger, M.; Würtele, C.; Milde, B.; Werz, D. B.; Schneider, S. *Journal of the American Chemical Society* **2014**, *136*, 6881–6883.

[16] Miyazaki, T.; Tanaka, H.; Tanabe, Y.; Yuki, M.; Nakajima, K.; Yoshizawa, K.; Nishibayashi, Y. *Angewandte Chemie International Edition* **2014**, *53*, 11488–11492.

[17] Liao, Q.; Cavaillé, A.; Saffon-Merceron, N.; Mézailles, N. *Angewandte Chemie International Edition* **2016**, *55*, 11212–11216.

[18] Falcone, M.; Chatelain, L.; Scopelliti, R.; Živković, I.; Mazzanti, M. *Nature* **2017**, *547*, 332–335.

[19] Ashida, Y.; Arashiba, K.; Nakajima, K.; Nishibayashi, Y. *Nature* **2019**, *568*, 536–540.

[20] Katayama, A.; Ohta, T.; Wasada-Tsutsui, Y.; Inomata, T.; Ozawa, T.; Ogura, T.; Masuda, H. *Angewandte Chemie International Edition* **2019**, *58*, 11279–11284.

[21] Bruch, Q. J.; Connor, G. P.; Chen, C.-H.; Holland, P. L.; Mayer, J. M.; Hasanayn, F.; Miller, A. J. M. *Journal of the American Chemical Society* **2019**, *141*, 20198–20208.

[22] Klopsch, I.; Yuzik-Klimova, E. Y.; Schneider, S. *Topics in Organometallic Chemistry*; Elsevier, 2017; Vol. 60; pp 71–112.

[23] Sellmann, D. *Angewandte Chemie International Edition in English* **1974**, *13*, 639–649.

[24] Jia, H.-P.; Quadrelli, E. A. *Chem. Soc. Rev.* **2014**, *43*, 547–564.

[25] Bazhenova, T.; Shilov, A. *Coordination Chemistry Reviews* **1995**, *144*, 69–145.

[26] Allen, A. D.; Senoff, C. V. *Chemical Communications (London)* **1965**, 621.

[27] Badger, R. M. *The Journal of Chemical Physics* **1934**, *2*, 128–131.

[28] Fryzuk, M. D.; Johnson, S. A. *Coordination Chemistry Reviews* **2000**, *200-202*, 379–409.

[29] MacKay, B. A.; Fryzuk, M. D. *Chemical Reviews* **2004**, *104*, 385–402.

[30] Evans, W. J.; Fang, M.; Zucchi, G.; Furche, F.; Ziller, J. W.; Hoekstra, R. M.; Zink, J. I. *Journal of the American Chemical Society* **2009**, *131*, 11195–11202.

[31] Marinkas, P. L.; Bartram, R. H. *The Journal of Chemical Physics* **1968**, *48*, 927–930.

[32] Gelerinter, E.; Silsbee, R. H. *The Journal of Chemical Physics* **1966**, *45*, 1703–1709.

[33] Brailsford, J. R.; Morton, J. R.; Vannotti, L. E. *The Journal of Chemical Physics* **1969**, *50*, 1051–1055.

[34] Shaver, M. P.; Fryzuk, M. D. *Advanced Synthesis & Catalysis* **2003**, *345*, 1061–1076.

[35] Peters, J. C.; Cherry, J.-P. F.; Thomas, J. C.; Baraldo, L.; Mindiola, D. J.; Davis, W. M.; Cummins, C. C. *Journal of the American Chemical Society* **1999**, *121*, 10053–10067.

[36] Lindley, B. M.; van Alten, R. S.; Finger, M.; Schendzielorz, F.; Würtele, C.; Miller, A. J. M.; Siewert, I.; Schneider, S. *Journal of the American Chemical Society* **2018**, *140*, 7922–7935.

[37] Armor, J. N.; Taube, H. *Journal of the American Chemical Society* **1970**, *92*, 2560–2562.

[38] Kane-Maguire, L. A. P.; Sheridan, P. S.; Basolo, F.; Pearson, R. G. *Journal of the American Chemical Society* **1970**, *92*, 5865–5872.

[39] Buhr, J. D.; Taube, H. *Inorganic Chemistry* **1979**, *18*, 2208–2212.

[40] Che, C.-m.; Lam, H.-w.; Tong, W.-f.; Lai, T.-f.; Lau, T.-c. *Journal of the Chemical Society, Chemical Communications* **1989**, 1883.

[41] Ware, D. C.; Taube, H. *Inorganic Chemistry* **1991**, *30*, 4605–4610.

[42] Lam, H.-w.; Che, C.-M.; Wong, K.-y. *Journal of the Chemical Society, Dalton Transactions* **1992**, 1411.

[43] Demadis, K. D.; Meyer, T. J.; White, P. S. *Inorganic Chemistry* **1997**, *36*, 5678–5679.

[44] Seymore, S. B.; Brown, S. N. *Inorganic Chemistry* **2002**, *41*, 462–469.

[45] Betley, T. A.; Peters, J. C. *Journal of the American Chemical Society* **2004**, *126*, 6252–6254.

[46] Schöffel, J.; Rogachev, A. Y.; George, S. D. B.; Burger, P. *Angewandte Chemie - International Edition* **2009**, *48*, 4734–4738.

[47] Scheibel, M. G.; Askevold, B.; Heinemann, F. W.; Reijerse, E. J.; de Bruin, B.; Schneider, S. *Nature Chemistry* **2012**, *4*, 552–558.

[48] Scheibel, M. G.; Wu, Y.; Stückl, A. C.; Krause, L.; Carl, E.; Stalke, D.; de Bruin, B.; Schneider, S. *Journal of the American Chemical Society* **2013**, *135*, 17719–17722.

[49] Krahe, O.; Bill, E.; Neese, F. *Angewandte Chemie International Edition* **2014**, *53*, 8727–8731.

[50] Abbenseth, J.; Finger, M.; Würtele, C.; Kasanmascheff, M.; Schneider, S. *Inorganic Chemistry Frontiers* **2016**, *3*, 469–477.

[51] Keener, M.; Peterson, M.; Hernández Sánchez, R.; Oswald, V. F.; Wu, G.; Ménard, G. *Chemistry - A European Journal* **2017**, *23*, 11479–11484.

[52] Chisholm, M. H.; Cotton, F. A.; Frenz, B. A.; Reichert, W. W.; Shive, L. W.; Stults, B. R. *Journal of the American Chemical Society* **1976**, *98*, 4469–4476.

[53] Hahn, J.; Nasluzov, V. A.; Neyman, K. M.; Rösch, N. *Inorganic Chemistry* **2002**, *36*, 3947–3951.

[54] Johnson, M. J. A.; Lee, P. M.; Odom, A. L.; Davis, W. M.; Cummins, C. C. *Angewandte Chemie International Edition in English* **1997**, *36*, 87–91.

[55] Cummins, C. C. *Chemical Communications* **1998**, *29*, 1777–1786.

[56] Laplaza, C. E.; Johnson, A. R.; Cummins, C. C. *Journal of the American Chemical Society* **1996**, *118*, 709–710.

[57] Tsai, Y.-C.; Johnson, M. J. A.; Mindiola, D. J.; Cummins, C. C.; Klooster, W. T.; Koetzle, T. F. *Journal of the American Chemical Society* **1999**, *121*, 10426–10427.

[58] Chatt, J.; Fay, R. C.; Richards, R. L. *J. Chem. Soc. A* **1971**, 702–704.

[59] Fryzuk, M. D.; Haddad, T. S.; Mylvaganam, M.; McConville, D. H.; Rettig, S. J. *Journal of the American Chemical Society* **1993**, *115*, 2782–2792.

[60] Laplaza, C. E.; Johnson, M. J. A.; Peters, J. C.; Odom, A. L.; Kim, E.; Cummins, C. C.; George, G. N.; Pickering, I. J. *Journal of the American Chemical Society* **1996**, *118*, 8623–8638.

[61] Curley, J. J.; Cook, T. R.; Reece, S. Y.; Mueller, P.; Cummins, C. C. *Journal of the American Chemical Society* **2008**, *130*, 9394–9405.

[62] Mindiola, D. J.; Meyer, K.; Cherry, J.-p. F.; Baker, T. A.; Cummins, C. C. *Organometallics* **2000**, *19*, 1622–1624.

[63] Ferguson, R.; Solari, E.; Floriani, C.; Osella, D.; Ravera, M.; Re, N.; Chiesi-Villa, A.; Rizzoli, C. *Journal of the American Chemical Society* **1997**, *119*, 10104–10115.

[64] Ferguson, R.; Solari, E.; Floriani, C.; Chiesi-Villa, A.; Rizzoli, C. *Angewandte Chemie International Edition in English* **1993**, *32*, 396–397.

[65] Re, N.; Rosi, M.; Sgamellotti, A.; Floriani, C. *Inorganic Chemistry* **1995**, *34*, 3410–3417.

[66] Shih, K.-Y.; Schrock, R. R.; Kempe, R. *Journal of the American Chemical Society* **1994**, *116*, 8804–8805.

[67] Pucino, M.; Allouche, F.; Gordon, C. P.; Wörle, M.; Mougel, V.; Coperet, C. *Chemical Science* **2019**,

[68] Doyle, L. R.; Wooles, A. J.; Jenkins, L. C.; Tuna, F.; McInnes, E. J. L.; Liddle, S. T. *Angewandte Chemie International Edition* **2018**, *57*, 6314–6318.

[69] Doyle, L. R.; Wooles, A. J.; Liddle, S. T. *Angewandte Chemie International Edition* **2019**, *58*, 6674–6677.

[70] Silantyev, G. A.; Förster, M.; Schluschaß, B.; Abbenseth, J.; Würtele, C.; Volkmann, C.; Holthausen, M. C.; Schneider, S. *Angewandte Chemie International Edition* **2017**, *56*, 5872–5876.

[71] Schendzielorz, F.; Finger, M.; Abbenseth, J.; Würtele, C.; Krewald, V.; Schneider, S. *Angewandte Chemie International Edition* **2019**, *58*, 830–834.

[72] Treitel, I. M.; Flood, M. T.; Marsh, R. E.; Gray, H. B. *Journal of the American Chemical Society* **1969**, *91*, 6512–6513.

[73] Mercer, M.; Crabtree, R. H.; Richards, R. L. *J. Chem. Soc., Chem. Commun.* **1973**, *1*, 808–809.

[74] Smith, J. M.; Sadique, A. R.; Cundari, T. R.; Rodgers, K. R.; Lukat-Rodgers, G.; Lachicotte, R. J.; Flaschenriem, C. J.; Vela, J.; Holland, P. L. *Journal of the American Chemical Society* **2006**, *128*, 756–769.

[75] Holland, P. L.; Smith, J. M.; Lachicotte, R. J.; Pittard, K. a.; Cundari, T. R.; Lukat-Rodgers, G.; Rodgers, K. R. *Journal of the American Chemical Society* **2001**, *123*, 9222.

[76] Ding, K.; Pierpont, A. W.; Brennessel, W. W.; Lukat-Rodgers, G.; Rodgers, K. R.; Cundari, T. R.; Bill, E.; Holland, P. L. *Journal of the American Chemical Society* **2009**, *131*, 9471–9472.

[77] Pfirrmann, S.; Limberg, C.; Herwig, C.; Stößer, R.; Ziemer, B. *Angewandte Chemie International Edition* **2009**, *48*, 3357–3361.

[78] McWilliams, S. F.; Rodgers, K. R.; Lukat-Rodgers, G.; Mercado, B. Q.; Grubel, K.; Holland, P. L. *Inorganic Chemistry* **2016**, *55*, 2960–2968.

[79] McWilliams, S. F.; Bill, E.; Lukat-Rodgers, G.; Rodgers, K. R.; Mercado, B. Q.; Holland, P. L. *Journal of the American Chemical Society* **2018**, *140*, 8586–8598.

[80] Stoian, S. A.; Vela, J.; Smith, J. M.; Sadique, A. R.; Holland, P. L.; Münck, E.; Bominaar, E. L. *Journal of the American Chemical Society* **2006**, *128*, 10181–10192.

[81] Grubel, K.; Brennessel, W. W.; Mercado, B. Q.; Holland, P. L. *Journal of the American Chemical Society* **2014**, *136*, 16807–16816.

[82] Hirotsu, M.; Fontaine, P. P.; Epshteyn, A.; Sita, L. R. *Journal of the American Chemical Society* **2007**, *129*, 9284–9285.

[83] Fontaine, P. P.; Yonke, B. L.; Zavalij, P. Y.; Sita, L. R. *Journal of the American Chemical Society* **2010**, *132*, 12273–12285.

[84] Keane, A. J.; Yonke, B. L.; Hirotsu, M.; Zavalij, P. Y.; Sita, L. R. *Journal of the American Chemical Society* **2014**, *136*, 9906–9909.

[85] Duman, L. M.; Farrell, W. S.; Zavalij, P. Y.; Sita, L. R. *Journal of the American Chemical Society* **2016**, *138*, 14856–14859.

[86] Hirotsu, M.; Fontaine, P. P.; Zavalij, P. Y.; Sita, L. R. *Journal of the American Chemical Society* **2007**, *129*, 12690–12692.

[87] Bezdek, M. J.; Guo, S.; Chirik, P. J. *Inorganic Chemistry* **2016**, *55*, 3117–3127.

[88] MacLachlan, E. A.; Fryzuk, M. D. *Organometallics* **2006**, *25*, 1530–1543.

[89] Jonas, K. *Angewandte Chemie International Edition in English* **1973**, *12*, 997–998.

[90] Krüger, C.; Tsay, Y.-H. *Angewandte Chemie International Edition in English* **1973**, *12*, 998–999.

[91] Evans, W. J.; Ulibarri, T. A.; Ziller, J. W. *Journal of the American Chemical Society* **1988**, *110*, 6877–6879.

[92] Fryzuk, M. D.; Haddad, T. S.; Rettig, S. J. *Journal of the American Chemical Society* **1990**, *112*, 8185–8186.

[93] Falcone, M.; Barluzzi, L.; Andrez, J.; Fadaei Tirani, F.; Zivkovic, I.; Fabrizio, A.; Corminboeuf, C.; Severin, K.; Mazzanti, M. *Nature Chemistry* **2019**, *11*, 154–160.

[94] Lv, Z.-J.; Huang, Z.; Zhang, W.-X.; Xi, Z. *Journal of the American Chemical Society* **2019**, jacs.9b04293.

[95] Clentsmith, G. K. B.; Bates, V. M. E.; Hitchcock, P. B.; Cloke, F. G. N. *Journal of the American Chemical Society* **1999**, *121*, 10444–10445.

[96] Monillas, W. H.; Yap, G. P. A.; MacAdams, L. A.; Theopold, K. H. *Journal of the American Chemical Society* **2007**, *129*, 8090–8091.

[97] Hanna, T. E.; Keresztes, I.; Lobkovsky, E.; Chirik, P. J. *Inorganic Chemistry* **2007**, *46*, 1675–1683.

[98] Manriquez, J. M.; Bercaw, J. E. *Journal of the American Chemical Society* **1974**, *96*, 6229–6230.

[99] Bobadova-Parvanova, P.; Wang, Q.; Morokuma, K.; Musaev, D. G. *Angewandte Chemie International Edition* **2005**, *44*, 7101–7103.

[100] Chirik, P. J. *Organometallics* **2010**, *29*, 1500–1517.

[101] Pool, J. A.; Lobkovsky, E.; Chirik, P. J. *Nature* **2004**, *427*, 527–530.

[102] Pool, J. A.; Bernskoetter, W. H.; Chirik, P. J. *Journal of the American Chemical Society* **2004**, *126*, 14326–14327.

[103] Fryzuk, M. D. *Science* **1997**, *275*, 1445–1447.

[104] Bobadova-Parvanova, P.; Wang, Q.; Quinonero-Santiago, D.; Morokuma, K.; Musaev, D. G. *Journal of the American Chemical Society* **2006**, *128*, 11391–11403.

[105] Morello, L.; Love, J. B.; Patrick, B. O.; Fryzuk, M. D. *Journal of the American Chemical Society* **2004**, *126*, 9480–9481.

[106] Bernskoetter, W. H.; Lobkovsky, E.; Chirik, P. J. *Angewandte Chemie - International Edition* **2007**, *46*, 2858–2861.

[107] Knobloch, D. J.; Lobkovsky, E.; Chirik, P. J. *Nature Chemistry* **2010**, *2*, 30–35.

[108] Semproni, S. P.; Chirik, P. J. *Journal of the American Chemical Society* **2013**, *135*, 11373–11383.

[109] Burford, R. J.; Fryzuk, M. D. *Nature Reviews Chemistry* **2017**, *1*, 0026.

[110] Ma, X.; Zhang, X.; Zhang, W.; Lei, M. *Phys. Chem. Chem. Phys.* **2013**, *15*, 901–910.

[111] Chatt, J.; Heath, G. A.; Richards, R. L. *Journal of the Chemical Society, Chemical Communications* **1972**, *0*, 1010.

[112] Chatt, J.; Pearman, A. J.; Richards, R. L. *Nature* **1975**, *253*, 39–40.

[113] Chatt, J.; Pearman, A. J.; Richards, R. L. *Journal of the Chemical Society, Dalton Transactions* **1977**, 1852–1860.

[114] Chatt, J.; Richards, R. L. *Journal of Organometallic Chemistry* **1982**, *239*, 65–77.

[115] Schrock, R. R. *Angewandte Chemie - International Edition* **2008**, *47*, 5512–5522.

[116] Yandulov, D. V.; Schrock, R. R. *Inorganic Chemistry* **2005**, *44*, 1103–1117.

[117] Schenk, S.; Le Guennic, B.; Kirchner, B.; Reiher, M. *Inorganic Chemistry* **2008**, *47*, 3634–3650.

[118] Smythe, N. C.; Schrock, R. R.; Müller, P.; Weare, W. W. *Inorganic Chemistry* **2006**, *45*, 7111–7118.

[119] Yandulov, D. V.; Schrock, R. R. *Canadian Journal of Chemistry* **2005**, *83*, 341–357.

[120] Smythe, N. C.; Schrock, R. R.; Müller, P.; Weare, W. W. *Inorganic Chemistry* **2006**, *45*, 9197–9205.

[121] Anderson, J. S.; Cutsail, G. E.; Rittle, J.; Connor, B. A.; Gunderson, W. A.; Zhang, L.; Hoffman, B. M.; Peters, J. C. *Journal of the American Chemical Society* **2015**, *137*, 7803–7809.

[122] Thompson, N. B.; Green, M. T.; Peters, J. C. *Journal of the American Chemical Society* **2017**, *139*, 15312–15315.

[123] Nesbit, M. A.; Oyala, P. H.; Peters, J. C. *Journal of the American Chemical Society* **2019**, *141*, 8116–8127.

[124] Rittle, J.; Peters, J. C. *Journal of the American Chemical Society* **2016**, *138*, 4243–4248.

[125] Chalkley, M. J.; Del Castillo, T. J.; Matson, B. D.; Roddy, J. P.; Peters, J. C. *ACS Central Science* **2017**, *3*, 217–223.

[126] Chalkley, M. J.; Del Castillo, T. J.; Matson, B. D.; Peters, J. C. *Journal of the American Chemical Society* **2018**, *140*, 6122–6129.

[127] Kolmar, S. S.; Mayer, J. M. *Journal of the American Chemical Society* **2017**, *139*, 10687–10692.

[128] Kuriyama, S.; Arashiba, K.; Nakajima, K.; Tanaka, H.; Kamaru, N.; Yoshizawa, K.; Nishibayashi, Y. *Journal of the American Chemical Society* **2014**, *136*, 9719–9731.

[129] Tanaka, H.; Arashiba, K.; Kuriyama, S.; Sasada, A.; Nakajima, K.; Yoshizawa, K.; Nishibayashi, Y. *Nature Communications* **2014**, *5*, 3737.

[130] Arashiba, K.; Eizawa, A.; Tanaka, H.; Nakajima, K.; Yoshizawa, K.; Nishibayashi, Y. *Bulletin of the Chemical Society of Japan* **2017**, *90*, 1111–1118.

[131] Smith, J. M. *Progress in Inorganic Chemistry*; 2014; Vol. 58; pp 417–470.

[132] Cui, Q.; Musaev, D. G.; Svensson, M.; Sieber, S.; Morokuma, K. *Journal of the American Chemical Society* **1995**, *117*, 12366–12367.

[133] Solari, E.; Da Silva, C.; Iacono, B.; Hesschenbrouck, J.; Rizzoli, C.; Scopelliti, R.; Floriani, C. *Angewandte Chemie (International ed. in English)* **2001**, *40*, 3907–3909.

[134] Kol, M.; Schrock, R. R.; Kempe, R.; Davis, W. M. *Journal of the American Chemical Society* **1994**, *116*, 4382–4390.

[135] Fischler, I.; von Gustorf, E. K. *Naturwissenschaften* **1975**, *62*, 63–70.

[136] Huss, A. S.; Curley, J. J.; Cummins, C. C.; Blank, D. A. *The Journal of Physical Chemistry B* **2013**, *117*, 1429–1436.

[137] Rafiq, S.; Bezdek, M. J.; Koch, M.; Chirik, P. J.; Scholes, G. D. *Journal of the American Chemical Society* **2018**, *140*, 6298–6307.

[138] Reiher, M.; Kirchner, B.; Hutter, J.; Sellmann, D.; Hess, B. A. *Chemistry - A European Journal* **2004**, *10*, 4443–4453.

[139] Rafiq, S.; Bezdek, M. J.; Chirik, P. J.; Scholes, G. D. *Chem* **2019**, *5*, 402–416.

[140] Keane, A. J.; Farrell, W. S.; Yonke, B. L.; Zavalij, P. Y.; Sita, L. R. *Angewandte Chemie International Edition* **2015**, *54*, 10220–10224.

[141] Kunkely, H.; Vogler, A. *Angewandte Chemie International Edition* **2010**, *49*, 1591–1593.

[142] Krewald, V.; González, L. *Chemistry - A European Journal* **2018**, *24*, 5112–5123.

[143] Krewald, V. *Dalton Transactions* **2018**, *47*, 10320–10329.

[144] Krewald, V. *Frontiers in Chemistry* **2019**, *7*, 352.

[145] Rupp, S.; Plasser, F.; Krewald, V. *European Journal of Inorganic Chemistry* **2020**, *2020*, 728–735.

[146] Klopsch, I.; Kinauer, M.; Finger, M.; Würtele, C.; Schneider, S. *Angewandte Chemie International Edition* **2016**, *55*, 4786–4789.

[147] Fritzsche, J.; Struve, H. *Journal für Praktische Chemie* **1847**, *41*, 97–113.

[148] Dehnicke, K.; Strähle, J. *Angewandte Chemie - International Edition* **1992**, *31*, 955–978.

[149] Che, C.-M. *Pure and Applied Chemistry* **1995**, *67*, 225–232.

[150] Abram, U.; Schmidt-Brücken, B.; Hagenbach, A.; Hecht, M.; Kirmse, R.; Voigt, A. *Zeitschrift für anorganische und allgemeine Chemie* **2003**, *629*, 838–852.

[151] Eikey, R. A.; Abu-Omar, M. M. *Coordination Chemistry Reviews* **2003**, *243*, 83–124.

[152] Strähle, J. *Zeitschrift für anorganische und allgemeine Chemie* **2003**, *629*, 828–837.

[153] Mehn, M. P.; Peters, J. C. *Journal of Inorganic Biochemistry* **2006**, *100*, 634–643.

[154] Strähle, J. *Zeitschrift für anorganische und allgemeine Chemie* **2007**, *633*, 1757–1761.

[155] Berry, J. F. *Comments on Inorganic Chemistry* **2009**, *30*, 28–66.

[156] Smith, J. M.; Subedi, D. *Dalton Trans.* **2012**, *41*, 1423–1429.

[157] Ballhausen, C. J.; Gray, H. B. *Inorganic Chemistry* **1962**, *1*, 111–122.

[158] Mayer, J. M. *Comments on Inorganic Chemistry* **1988**, *8*, 125–135.

[159] Hoffmann, R. *Angewandte Chemie International Edition in English* **1982**, *21*, 711–724.

[160] Vogel, C.; Heinemann, F. W.; Sutter, J.; Anthon, C.; Meyer, K. *Angewandte Chemie - International Edition* **2008**, *47*, 2681–2684.

[161] Scepaniak, J. J.; Fulton, M. D.; Bontchev, R. P.; Duesler, E. N.; Kirk, M. L.; Smith, J. M. *Journal of the American Chemical Society* **2008**, *130*, 10515–10517.

[162] Walstrom, A.; Pink, M.; Yang, X.; Tomaszewski, J.; Baik, M. H.; Caulton, K. G. *Journal of the American Chemical Society* **2005**, *127*, 5330–5331.

[163] Sieh, D.; Schöffel, J.; Burger, P. *Dalton Transactions* **2011**, *40*, 9512–9524.

[164] Hedegård, E. D.; Bendix, J.; Sauer, S. P. *Journal of Molecular Structure: THEOCHEM* **2009**, *913*, 1–7.

[165] Crevier, T. J.; Mayer, J. M. *Journal of the American Chemical Society* **1998**, *120*, 5595–5596.

[166] Crevier, T. J.; Bennett, B. K.; Soper, J. D.; Bowman, J. A.; Dehestani, A.; Hrovat, D. A.; Lovell, S.; Kaminsky, W.; Mayer, J. M. *Journal of the American Chemical Society* **2001**, *123*, 1059–1071.

[167] Crevier, T. J.; Mayer, J. M. *Angewandte Chemie - International Edition* **1998**, *37*, 1891–1893.

[168] Bendix, J.; Meyer, K.; Weyhermüller, T.; Bill, E.; Metzler-Nolte, N.; Wieghardt, K. *Inorganic Chemistry* **1998**, *37*, 1767–1775.

[169] Enemark, J.; Feltham, R. *Coordination Chemistry Reviews* **1974**, *13*, 339–406.

[170] Espada, M. F.; Bennaamane, S.; Liao, Q.; Saffon-Merceron, N.; Massou, S.; Clot, E.; Nebra, N.; Fustier-Boutignon, M.; Mézailles, N. *Angewandte Chemie International Edition* **2018**, *57*, 12865–12868.

[171] Liao, Q.; Saffon-Merceron, N.; Mézailles, N. *ACS Catalysis* **2015**, *5*, 6902–6906.

[172] Bennaamane, S.; Espada, M. F.; Yagoub, I.; Saffon-Merceron, N.; Nebra, N.; Fustier-Boutignon, M.; Clot, E.; Mézailles, N. *European Journal of Inorganic Chemistry* **2020**, *2020*, 1499–1505.

[173] Connor, G. P.; Mercado, B. Q.; Lant, H. M. C.; Mayer, J. M.; Holland, P. L. *Inorganic Chemistry* **2019**, *58*, 10791–10801.

[174] Sceats, E. L.; Figueroa, J. S.; Cummins, C. C.; Loening, N. M.; Van der Wel, P.; Griffin, R. G. *Polyhedron* **2004**, *23*, 2751–2768.

[175] Curley, J. J.; Cozzolino, A. F.; Cummins, C. C. *Dalton Transactions* **2011**, *40*, 2429.

[176] Curley, J. J.; Sceats, E. L.; Cummins, C. C. *Journal of the American Chemical Society* **2006**, *128*, 14036–14037.

[177] Figueroa, J. S.; Piro, N. A.; Clough, C. R.; Cummins, C. C. *Journal of the American Chemical Society* **2006**, *128*, 940–950.

[178] Klopsch, I.; Schendzielorz, F.; Volkmann, C.; Würtele, C.; Schneider, S. *Zeitschrift für anorganische und allgemeine Chemie* **2018**, *644*, 916–919.

[179] Cozzolino, A. F.; Silvia, J. S.; Lopez, N.; Cummins, C. C. *Dalton Trans.* **2014**, *43*, 4639–4652.

[180] Schalke, P. M. *Ullmann's Encyclopedia of Industrial Chemistry*; Wiley-VCH Verlag GmbH & Co. KGaA: Weinheim, Germany, 2006; Vol. 10; pp 673–710.

[181] Meessen, J. H. *Ullmann's Encyclopedia of Industrial Chemistry*; Wiley-VCH Verlag GmbH & Co. KGaA: Weinheim, Germany, 2010; Vol. 37; pp 425–474.

[182] Malcolm W. Chase, J. *NIST-JANAF Thermochemical Tables Fourth Edition Part I, Al-Co*; Journal of Physical and Chemical Reference Data: Gaithersburg, Maryland, 1998.

[183] Vanderzee, C. E.; Myers, R. A. *The Journal of Physical Chemistry* **1961**, *65*, 153–158.

[184] Askevold, B.; Nieto, J. T.; Tussupbayev, S.; Diefenbach, M.; Herdtweck, E.; Holthausen, M. C.; Schneider, S. *Nature Chemistry* **2011**, *3*, 532–537.

[185] Tran, B. L.; Pink, M.; Gao, X.; Park, H.; Mindiola, D. J. *Journal of the American Chemical Society* **2010**, *132*, 1458–1459.

[186] Silvia, J. S.; Cummins, C. C. *Journal of the American Chemical Society* **2009**, *131*, 446–447.

[187] Scepaniak, J. J.; Bontchev, R. P.; Johnson, D. L.; Smith, J. M. *Angewandte Chemie - International Edition* **2011**, *50*, 6630–6633.

[188] Cleaves, P. A.; King, D. M.; Kefalidis, C. E.; Maron, L.; Tuna, F.; McInnes, E. J.; McMaster, J.; Lewis, W.; Blake, A. J.; Liddle, S. T. *Angewandte Chemie - International Edition* **2014**, *53*, 10412–10415.

[189] Buss, J. A.; Cheng, C.; Agapie, T. *Angewandte Chemie International Edition* **2018**, *57*, 9670–9674.

[190] Ishida, Y.; Kawaguchi, H. *Journal of the American Chemical Society* **2014**, *136*, 16990–16993.

[191] G. Fickes, M.; L. Odom, A.; C. Cummins, C. *Chemical Communications* **1997**, *041*, 1993.

[192] Benson, S. W. *Journal of Chemical Education* **1965**, *42*, 502.

[193] Addison, A. W.; Rao, T. N.; Reedijk, J.; van Rijn, J.; Verschoor, G. C. *J. Chem. Soc., Dalton Trans.* **1984**, 1349–1356.

[194] Bistoni, G.; Rampino, S.; Scafuri, N.; Ciancaleoni, G.; Zuccaccia, D.; Belpassi, L.; Tarantelli, F. *Chemical Science* **2016**, *7*, 1174–1184.

[195] Chatt, J.; Leigh, G. J.; Mingos, D. M. P. *Journal of the Chemical Society A: Inorganic, Physical, Theoretical* **1969**, 1674.

[196] Palion-Gazda, J.; Gryca, I.; Machura, B.; Lloret, F.; Julve, M. *RSC Advances* **2015**, *5*, 101616–101622.

[197] Abbenseth, J.; Diefenbach, M.; Bete, S. C.; Würtele, C.; Volkmann, C.; Demeshko, S.; Holthausen, M. C.; Schneider, S. *Chem. Commun.* **2017**, *53*, 5511–5514.

[198] Kinauer, M.; Diefenbach, M.; Bamberger, H.; Demeshko, S.; Reijerse, E. J.; Volkmann, C.; Würtele, C.; van Slageren, J.; de Bruin, B.; Holthausen, M. C.; Schneider, S. *Chemical Science* **2018**, *9*, 4325–4332.

[199] Delony, D.; Kinauer, M.; Diefenbach, M.; Demeshko, S.; Würtele, C.; Holthausen, M. C.; Schneider, S. *Angewandte Chemie International Edition* **2019**, *58*, 10971–10974.

[200] Bleaney, B. *Journal of Magnetic Resonance (1969)* **1972**, *8*, 91–100.

[201] Figgis, B. N.; Hitchman, M. A. *Ligand Field Theory and Its Applications*; Wiley VHC: Weinheim, Germany, 2000.

[202] Dehnicke, K.; Strähle, J. *Angewandte Chemie International Edition in English* **1981**, *20*, 413–426.

[203] McClain, K. R.; O'Donohue, C.; Koley, A.; Bonsu, R. O.; Abboud, K. A.; Rev-

elli, J. C.; Anderson, T. J.; McElwee-White, L. *Journal of the American Chemical Society* **2014**, *136*, 1650–1662.

[204] Clough, C. R.; Greco, J. B.; Figueroa, J. S.; Diaconescu, P. L.; Davis, W. M.; Cummins, C. C. *Journal of the American Chemical Society* **2004**, *126*, 7742–7743.

[205] Chisholm, M. H.; Hoffman, D. M.; Huffman, J. C. *Inorganic Chemistry* **1983**, *22*, 2903–2906.

[206] Kütt, A.; Selberg, S.; Kaljurand, I.; Tshepelevitsh, S.; Heering, A.; Darnell, A.; Kaupmees, K.; Piirsalu, M.; Leito, I. *Tetrahedron Letters* **2018**, *59*, 3738–3748.

[207] Seeman, J. I. *Chemical Reviews* **1983**, *83*, 83–134.

[208] Atkins, P. W.; De Paula, J. *Physikalische Chemie. 4., vollständig überarbeitete Auflage.*; Wiley-VCH Verlag: Weinheim, Germany, 2006.

[209] Tausch, M. W. *Photochemie*; John Wiley & Sons, Ltd, 2005; Chapter 3, pp 83–112.

[210] Turro, N. J.; McVey, J.; Ramamurthy, V.; Lechtken, P. *Angewandte Chemie International Edition in English* **1979**, *18*, 572–586.

[211] Eyring, H. *The Journal of Chemical Physics* **1935**, *3*, 107–115.

[212] Wingard, L. A.; White, P. S.; Templeton, J. L. *Dalton Transactions* **2012**, *41*, 11438.

[213] Meiners, J.; Friedrich, A.; Herdtweck, E.; Schneider, S. *Organometallics* **2009**, *28*, 6331–6338.

[214] Abdur-Rashid, K.; Fong, T. P.; Greaves, B.; Gusev, D. G.; Hinman, J. G.; Landau, S. E.; Lough, A. J.; Morris, R. H. *Journal of the American Chemical Society* **2000**, *122*, 9155–9171.

[215] Krossing, I.; Reisinger, A. *European Journal of Inorganic Chemistry* **2005**, *2005*, 1979–1989.

[216] Jordan, R. F.; Echols, S. F. *Inorganic Chemistry* **1987**, *26*, 383–386.

[217] Curley, J. J.; Bergman, R. G.; Tilley, T. D. *Dalton Trans.* **2012**, *41*, 192–200.

[218] Demadis, K. D.; Meyer, T. J.; White, P. S. *Inorganic Chemistry* **1998**, *37*, 3610–3619.

[219] Martinsen, A.; Songstad, J.; Larsson, R.; Pouchard, M.; Hagenmuller, P.; Andresen, A. F. *Acta Chemica Scandinavica* **1977**, *31a*, 645–650.

[220] APEX3 V2016.9-0 (SAINT/SADABS/SHELXT/SHELXL).

[221] Sheldrick, G. M. *Acta Crystallographica Section A Foundations of Crystallography* **2008**, *64*, 112–122.

[222] Sheldrick, G. M. *Acta Crystallographica Section C Structural Chemistry* **2015**, *71*, 3–8.

[223] Sheldrick, G. M. *Acta Crystallographica Section A Foundations and Advances* **2015**, *71*, 3–8.

[224] Elgrishi, N.; Rountree, K. J.; McCarthy, B. D.; Rountree, E. S.; Eisenhart, T. T.; Dempsey, J. L. *Journal of Chemical Education* **2018**, *95*, 197–206.

[225] Belford, R. L.; Nilges, M. J. *EPR Symposium, 21st Rocky Mountain Conference, Denver, Colorado* **1979**,

[226] Sur, S. K. *Journal of Magnetic Resonance* **1989**, *82*, 169–173.

[227] Haberditzl, W. *Angewandte Chemie International Edition in English* **1966**, *5*, 288–298.

[228] Bain, G. A.; Berry, J. F. *Journal of Chemical Education* **2008**, *85*, 532.

[229] Bill, E. *julX, Program for Simulation of Molecular Magnetic Data,*; 2008.

[230] Fulmer, G. R.; Miller, A. J. M.; Sherden, N. H.; Gottlieb, H. E.; Nudelman, A.; Stoltz, B. M.; Bercaw, J. E.; Goldberg, K. I. *Organometallics* **2010**, *29*, 2176–2179.

[231] Schneck, F.; Ahrens, J.; Finger, M.; Stückl, A. C.; Würtele, C.; Schwarzer, D.; Schneider, S. *Nature Communications* **2018**, *9*, 1161.

[232] Kaindl, R. A.; Wurm, M.; Reimann, K.; Hamm, P.; Weiner, A. M.; Woerner, M. *Journal of the Optical Society of America B* **2000**, *17*, 2086.

[233] Hoops, S.; Sahle, S.; Gauges, R.; Lee, C.; Pahle, J.; Simus, N.; Singhal, M.; Xu, L.; Mendes, P.; Kummer, U. *Bioinformatics* **2006**, *22*, 3067–3074.

7 Curriculum Vitae

Personal

Name	Bastian Schluschaß
Nationality	German
Date of Birth	19.10.1989
Place of Birth	Frankfurt am Main
E-mail	bschlus@gwdg.de

Education

since May 2016	**Graduate Student**, *Georg-August-University, Göttingen (Germany)* Institute for Inorganic Chemistry, Research-group of Prof. Dr. Sven Schneider
2013-2016	**Master of Science**, *Georg-August-University, Göttingen (Germany)* Final Grade: 1.6 Thesis title: "Reactivity of Co(PNP)-Pincer-Complexes" (Grade 1.0) Institute for Inorganic Chemistry, Research-group of Prof. Dr. Sven Schneider
2010-2013	**Bachelor of Science**, *Georg-August-University, Göttingen (Germany)* Final Grade: 1.6 Thesis title: "Reactivity of Ru(PNP)-Nitrido-Pincer-Complexes" (Grade 1.7) Institute for Inorganic Chemistry, Research-group of Prof. Dr. Sven Schneider

Experience

Traineeships

Jul - Oct 2017	**Internship**, *Indiana University, Indiana (USA)* Department of Chemistry, Research-group of Prof. Dr. Kenneth Caulton
Mar - Jun 2015	**Erasmus Internship**, *Stockholm University, Stockholm (Schweden)* Department of Organic Chemistry, Research-group of Dr. Eric V. Johnson

Contributions at Conferences

2019	15. Koordinationschemie-Treffen, Munich (Germany), *Talk*
2018	28th ICOMC, Florence (Italy), *Talk*
2018	14. Koordinationschemie-Treffen, Heidelberg (Germany), *Poster*
2017	9. Göttinger Chemie Forum, Göttingen (Germany), *Talk*
2017	5th COST Carisma Meeting, Lisbon (Portugal), *Talk*
2016	12. Koordinationschemie-Treffen, Kiel (Germany), *Poster*

Publications

- "Selectivity of tungsten mediated dinitrogen splitting *vs.* proton reduction", Bastian Schluschaß, Josh Abbenseth, Serhiy Demeshko, Markus Finger, Alicija Franke, Christian Herwig, Christian Würtele, Ivana Ivanovic-Burmazovic, Christian Limberg, Joshua Telser and Sven Schneider, *Chemical Science*, **2019**, *10*, 10275-10282.
- "Dinitrogen Splitting Coupled to Protonation", Gleb A. Silantyev, Moritz Förster, Bastian Schluschaß, Josh Abbenseth, Christian Würtele, Christian Volkmann, Max C. Holthausen and Sven Schneider, *Angewandt Chemie International Edition*, **2017**, *57*, 5872-5876.
- "Water oxidation mediated by ruthenium oxide nanoparticles supported on siliceous mesocellular foam" Karl P. J. Gustafson, Andrey Shatskiy, Oscar Verho, Markus D. Kärkäs, Bastian Schluschaß, Cheuk-Wai Tai, Björn Åkermark, Jan-Erling Bäckvall and Eric V. Johnston, *Catalysis, Science and Technology*, **2017**, *7*, 293-299.
- "Square-Planar Cobalt(III) Pincer Complex", Paraskevi O. Lagaditis, Bastian Schluschaß, Serhiy Demeshko, Christian Würtele and Sven Schneider, *Inorganic Chemistry*, **2016**, *55*, 4529-4536.
- "Electron-rich, Nitrido-bridged Ruthenium Complexes", Arne Glüer, Bjorn Askevold, Bastian Schluschaß, Frank W. Heinemann and Sven Schneider, *Zeitschrift für anorganische und allgemeine Chemie*, **2015**, *641*, 49-51.